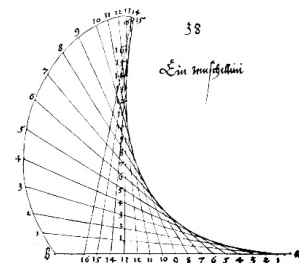


Groundwater Flow and Transport in Complex Real Systems



Groundwater Flow and Transport in Complex Real Systems

Anke Schneider (GRS)
Susan Britz (GRS)
Anne Gehrke (GRS)
Klaus-Peter Kröhn (GRS)
Michael Lampe (G-CSC)
Arne Nägel (G-CSC)
Sebastian Reiter (G-CSC)
Gabriel Wittum (G-CSC)
Hong Zhao (GRS)

May 2020

Remark:

This study has been funded by the German Federal Ministry for Economic Affairs and Energy (BMWi) under the support code no 02E11476A-B.

The work was conducted by Gesellschaft für Anlagen- und Reaktorsicherheit (GRS) gGmbH and the Goethe Center for Scientific Computing (G-CSC) of Goethe University Frankfurt.

The authors are responsible for the content of the report.

Keywords:

Crystalline, Density-driven Flow, Diffusion, Grid Generation, Modelling, Multigrid

Acknowledgement

This report summarizes the work in the joint project “Groundwater Flow and Transport in Complex Real Systems“ (GRUSS) of the project partners from the University of Frankfurt and the GRS. The project was funded by the German Federal Ministry for Economic Affairs and Energy (BMWi) under the contract no’s 02E11476A, and 02E11476B.

We would like to thank all our colleagues of the working group of Prof. Gabriel Wittum (University of Frankfurt) who contributed to this final report and to the successful conclusion of the project. Our very special thanks is due to Dmitrij Logashenko (currently KAUST, Saudi Arabia) who helped us with his advice and support throughout the entire project. Finally, we would like to express our thanks to the colleagues of the Repository Safety Research Division of GRS that were not directly concerned with the project, for their consultation.

Abstract

The code d^{3f++} has been developed for modelling density-driven flow and nuclide transport in the far field of repositories for hazardous material in deep geological formations. It is applicable in porous media as well as in fractured rock or mudstone, for modelling salt- and heat transport as well as a free groundwater surface.

The growing and varying demands on groundwater flow and transport modelling evoke constantly rising requirements for code enhancement and improvement. With the objective to enable d^{3f++} for the modelling of short-term field-scale experiments with pressure-influenced transient processes the flow equation is extended by a storage term. New projectors for an intelligent grid refinement with better resolution of the model geometry were implemented to improve pre-processing and grid generation.

Improving speed-up and robustness of the multigrid solvers is a permanent task. To speed-up solving of the nonlinear problem, two versions of LIMEX methods were investigated. Very promising results could be achieved for various test cases. Additionally, new types of smoothers using downwind numbering ILU and ILU_{β} were tested. The coarse grid correction was enhanced by implementing a Galerkin projection and a special matrix dependent interpolation. Additionally, Filtering Algebraic Multi-Grid Methods (FAMG) were adapted to thermohaline flow and implemented in d^{3f++} . To strengthen the robustness of the parallelization, ideas from computer graphics were adapted to get an adaptive anisotropic refinement strategy, and downward numbering algorithms were parallelized to improve load balancing. Special attention was spent to a substantially stabilization of the levelset method and, therefore, the modelling of free groundwater surfaces.

A short review of various concepts of diffusion and sorption of radioactive nuclides in crystalline rock is presented. As a result of this process a two-zone approach is used for modelling the transport of four different tracers in Task 9b of the SKB Task Force on Groundwater Flow and Transport of Solutes.

In the scope of this work d^{3f++} was applied to three 3d groundwater flow models at regional scale, in porous media as well as in crystalline rock. These are the Äspö Site Descriptive Model (SDM), the overburden of the Waste Isolation Pilot Plant (WIPP) site,

a repository for transuranic waste in bedded salt in New Mexico, and the Čihadlo candidate site in the Czech Republic.

Zusammenfassung

Der Code d^{3f++} wurde für die Modellierung von Dichteströmung und Nuklidtransport im Fernfeld von Endlagern für gefährliche Stoffe in tiefen geologischen Formationen entwickelt. Er kann sowohl in porösen Medien als auch im Kluffgestein oder Ton, für die Modellierung von Salt- und Wärmetransport sowie für Modelle mit freier Grundwasseroberfläche eingesetzt werden.

Die wachsenden und sich ändernden Anforderungen an die Grundwasserströmungs- und Transportmodellierung erfordern eine ständige Weiterentwicklung der Rechenprogramme. Mit dem Ziel, d^{3f++} für die Modellierung von Feldexperimenten zu ertüchtigen, in denen druckbeeinflusste, transiente Prozesse eine Rolle spielen, wurde das Gleichungssystem um einen Speicherterm erweitert. Die Entwicklung und Implementierung von Projektoren für eine intelligentere Gitterverfeinerung ermöglichen eine bessere Auflösung der geologischen Strukturen.

Die Verbesserung von Robustheit und Geschwindigkeit der Mehrgitterlöser ist eine ständige Herausforderung. Zur Beschleunigung der Lösung des nichtlinearen Problems wurden zwei Arten von LIMEX-Methoden untersucht und verglichen. Ihre Anwendung auf mehrere aus der Literatur bekannte Testfälle lieferte vielversprechende Resultate. Als Glättungsverfahren wurden ILU und ILU _{β} -Verfahren getestet. Eine Galerkin-Projektion und eine spezielle Matrix-abhängige Interpolation zur Verbesserung der Grobgitterkorrektur wurden implementiert. Filternde Algebraische Mehrgitterverfahren (FAMG) wurden für die thermohaline Strömung weiterentwickelt und implementiert. Methoden aus der Computergrafik wurden benutzt, um eine adaptive anisotrope Verfeinerungsstrategie zu entwickeln und so die Parallelisierung robuster zu machen. Besondere Aufmerksamkeit wurde der Stabilisierung der Modellierung der freien Grundwasseroberfläche gewidmet.

Motiviert durch die Teilnahme an Task 9b der SKB Task Force on Groundwater Flow and Transport of Solutes wurden verschiedene Konzepte zur Erklärung von Diffusions- und Sorptionsprozessen im Kristallin gegenübergestellt.

Ein bedeutender Teil der Arbeiten bestand in der Anwendung von d^{3f++} auf drei großräumige 3d Anwendungsfälle, das Äspö Site Descriptive Model (SDM), das Deckgebirge

der WIPP-Site, einem Endlager für transurane Abfälle in New Mexico, und den potentiellen Endlagerstandort Čihadlo in der Tschechischen Republik.

Content

1	Introduction.....	1
2	Extension and improvement of the applicability of d^{3f++}	5
2.1	Utilization of d ^{3f++} for the modelling of field-scale experiments: extension of the flow equation by a storage term	5
2.1.1	Balance equation	5
2.1.2	Notes about specific storage.....	9
2.1.3	Pressure dependent density	9
2.1.4	Pressure dependent porosity	10
2.1.5	Comparison with an analytical solution	10
2.2	Enhancement of the preprocessor ProMesh	13
2.2.1	General Remarks.....	13
2.2.2	Overview and notation	14
2.2.3	Concepts	16
2.2.4	Meshing.....	19
2.2.5	Visualisation	20
2.2.6	Implementation	23
3	Advancement of the solvers in d^{3f++}	27
3.1	Adaption of the LIMEX method to thermohaline groundwater flow to speed-up the nonlinear solvers	27
3.1.1	Preliminary considerations.....	28
3.1.2	Numerical experiments	32
3.1.3	Conclusion.....	50
3.2	Robust smoothers for the geometric multigrid solver	51
3.3	Improvement of the coarse-grid correction.....	52
3.4	Adapting the FAMG method to thermohaline groundwater flow, parallel scalability	53
3.5	Parallel adaptive algorithms and appropriate grid structures.....	54
3.5.1	Adaptive anisotropic refinement.....	54

3.5.2	Adjusted load balancing for convection-dominated problems.....	56
3.5.3	General parallel-adaptive strategy	63
3.6	Stable modelling of free groundwater surfaces	63
3.6.1	Virtual elements for free surfaces at thermohaline flow	68
3.6.2	Improved PLIC-reconstruction for free surfaces	69
4	Applications and benchmarks	71
4.1	SKB Task Force on Groundwater Flow and Transport of Solutes, Task 9b.....	71
4.1.1	The LTDE experiment.....	71
4.1.2	Motivation	75
4.1.3	Explanations for the data	76
4.1.4	Workshop on the skin-effect	77
4.1.5	Approach	78
4.1.6	Data analysis	81
4.1.7	Homogeneous model.....	82
4.1.8	Fitting results for A-cores	83
4.1.9	Fitting results for D-cores.....	87
4.1.10	Summary and conclusions.....	90
4.2	Äspö Site Descriptive Model (SDM)	94
4.2.1	Background and motivation	94
4.2.2	Review of approaches and data.....	94
4.2.3	Pre-studies in a vertical cross-section for a regional-scale model	119
4.2.4	Regional-scale model in 3D	137
4.3	The WIPP Site, New Mexico	146
4.3.1	Hydrogeological situation.....	147
4.3.2	Model description.....	150
4.3.3	Numerical model.....	152
4.3.4	Results	154
4.3.5	Summary	157
4.4	Čihadlo groundwater flow model, Czech Republic	159
4.4.1	Hydrogeological model	160

4.4.2	Results	162
4.4.3	Discussion	166
5	Summary	169
	References	173
	Table of Figures	189
	List of Tables	195
A	Appendix: Data for modelling the LTDE.....	197
A.1	Tracer data	197
A.2	Experimental data during the tests.....	201
A.3	Conversion of tracer concentration units.....	203
A.4	Experimental data after the tests	205

1 Introduction

Long-term safety assessment for a radioactive waste repository requires a comprehensive system understanding and qualified high-performance tools. These tools have to be able to describe all relevant processes concerning nuclide transport through the host rock and the overlying geological formations.

The transport of radionuclides is mainly driven by groundwater flow. Groundwater flow and nuclide transport are depending on the properties of the geological rock formations as well as driving forces as hydraulic boundary conditions or the existence of density influencing materials. Therefore, the geological and hydrogeological situation of each potential repository site have to be well investigated. Successful numerical groundwater flow and transport modelling is based on a profound hydrogeological knowledge.

A growing amount of data and including more and more relevant physical processes lead to an increasing degree of approximation of the model representation to the real and thus induce a growing complexity of the numerical models. A proper definition of boundary conditions makes it necessary to choose the model boundaries correspondent to hydrogeological structures as watersheds. This leads to regional-scale models covering thousands of square kilometers. Climatic changes are to be regarded. Model and parameter uncertainties have to be taken into account and the demands for accuracy and grid resolution are growing. Additionally, according to the German safety case requirements for heat-generating radioactive waste an assessment time of one million years is regarded. All this implies a substantially increase of computational effort and makes it necessary to employ the most advanced hardware and cutting-edge numerical solvers have to be used at all times.

To meet the needs of modelling groundwater flow and nuclide transport, starting from 1994 the computer codes d^3f (distributed density-driven flow) and r^3t (radio-nuclides, reaction, retardation, and transport) were developed /FEI 99/, /FEI 04/, and afterwards step by step advanced as well as continuously adapted to the state-of-the-art of science and technology /SCH 12/, /SCH 13/, /NOS 12/. The codes d^3f and r^3t were based on version 3 of the UG toolbox, developed at the Frankfurt University /BAS 97/. Recently, they were adapted to the substantially updated, C++-based version UG4 /VOG 13/, and during this process the codes were combined to one conjoint code d^3f++ /SCH 16/. Furthermore, the code was, applied, qualified and enhanced in various projects, see e. g. /NOS 12/, /SCH 13a/, /JOB 16/, /SCH 17/. All these works were funded by the Federal Ministry of

Education and Research (BMBF) and by the Federal Ministry of Economics and Technology (BMWi), respectively

Today, d^{3f++} allows to simulate density-driven groundwater flow at regional scale in porous as well as fractured media and the transport of radionuclides or other substances with all processes relevant for safety assessment. The application of modern, parallelized numerical algorithms as well as the effective use of high-performance computers allow a relatively high number of grid elements, that means a high resolution in feasible computation times.

However, the growing extension and complexity of the models require steadily further speed-up and robustness of the solvers. At the other hand, recent scientific advances in the field of numerics have to be adopted, and code adaptations are crucial for profiting of new hardware developments. Section 3 outlines various advancements of the solvers. To speed-up the nonlinear solvers, linearly implicit extrapolation (LIMEX) methods were adapted to thermohaline groundwater flow and implemented in d^{3f++}. The robustness of the smoothers for the geometric multigrid (GMG) solvers was improved and filtering algebraic multigrid solvers (FAMG) were applied. Adaptive anisotropic refinement algorithms were implemented to improve the numerical properties of the computational grid. The parallelization was improved by an adjusted load balancing for convection-dominated problems using Downwind Numbering. At least, the modelling of free groundwater surfaces in d^{3f++} was substantially improved and stabilized.

Groundwater and transport modelling bases on a detailed understanding of physical and chemical processes, based on a comprehensive knowledge of geological facts and material properties. A well-founded, careful and reasonable model set-up is fundamental for a growing confidence in model results. Section 4.1 presents a short review of various concepts of diffusion and sorption of radioactive nuclides in crystalline rock. As a result of this process a two-zone approach is used for modelling the transport of four different tracers in Task 9b of the SKB Task Force on Groundwater Flow and Transport of Solutes.

A demonstration of the capability and efficiency of d^{3f++} in regional-scale modelling in sedimental as well as crystalline rock is important for a broad acceptance and application of the code. Section 4 outlines the application of d^{3f++} to three groundwater flow models at regional scale, in porous media as well as in crystalline rock, the Äspö Site

Descriptive Model, the WIPP site in New Mexico and the candidate site Čihadlo in the Czech Republic.

Section 2.1 describes the extension of the flow equation by a storage term. This extension enables the utilization of d^{3f}++ for the modelling of short-term field-scale experiments.

At least, user interfaces are an essential factor for the usability and the application of a code. Their importance is growing with extent and complexity of the models. Section 2.2 outlines the enhancement of the preprocessor ProMesh to facilitate model set-up, to improve grid properties the representation of complex geological structures or the digital elevation model avoiding high element numbers in the coarse grid.

Members of the joint project

Goethe Center for Scientific Computing (G-CSC)

University of Frankfurt

Kettenhofweg 139

60325 Frankfurt

Prof. Gabriel Wittum

Dr. Arne Nägel

Dr. Sebastian Reiter

Dr. Michael Lampe

Gesellschaft für Anlagen- und Reaktorsicherheit (GRS) gGmbH

Geological disposal division

Th.-Heuss-Str. 4

38122 Braunschweig

Anke Schneider

Dr. Susan Britz

Anne Gehrke

Dr. Klaus-Peter Kröhn

Dr. Hong Zhao

2 Extension and improvement of the applicability of d^{3f++}

2.1 Utilization of d^{3f++} for the modelling of field-scale experiments: extension of the flow equation by a storage term

2.1.1 Balance equation

The general balance equation for the mass of groundwater leads to the continuity equation which can be written as (e. g. /KRÖ 91/)

$$\frac{\partial(\rho \Phi)}{\partial t} + \text{div}(\rho v_f) = 0 \quad (2.1)$$

ρ - fluid density [kg m⁻³]

Φ - porosity [-]

t - time [s]

v_f - filter velocity [m s⁻¹]

or

$$\Phi \frac{\partial \rho}{\partial t} + \rho \frac{\partial \Phi}{\partial t} + \text{div}(\rho v_f) = 0 \quad (2.2)$$

With the goal of writing equation (2.2) in terms of the hydraulic pressure as the only independent variable, the time derivatives are modified to

$$\Phi \left(\frac{\partial \rho}{\partial p} \frac{\partial p}{\partial t} + \frac{\partial \rho}{\partial T} \frac{\partial T}{\partial t} + \frac{\partial \rho}{\partial c} \frac{\partial c}{\partial t} \right) + \rho \frac{\partial \Phi}{\partial p} \frac{\partial p}{\partial t} + \text{div}(\rho v_f) = 0 \quad (2.3)$$

assuming a dependence of the density on pressure p , temperature T and solute concentration c and a dependence of the porosity on the hydraulic pressure:

$$\rho = \rho(p, T, c) \quad (2.4)$$

p - hydraulic pressure [Pa]

T - temperature [K]

c - mass fraction [-]

$$\Phi = \Phi(p) \quad (2.5)$$

Rearranging (2.3) makes clear that the effect from temperature or concentration changes are formally handled like source terms in the flow equation.

$$\left(\Phi \frac{\partial \rho}{\partial p} + \rho \frac{\partial \Phi}{\partial p} \right) \frac{\partial p}{\partial t} + \text{div}(\rho v_f) = -\Phi \left(\frac{\partial \rho}{\partial T} \frac{\partial T}{\partial t} + \frac{\partial \rho}{\partial c} \frac{\partial c}{\partial t} \right) \quad (2.6)$$

With the definition of the compressibility of the rock (see /DAV 66/)

$$\alpha = \frac{1}{1 - \Phi} \frac{\partial \Phi}{\partial p} \quad (2.7)$$

α - compressibility of the rock [1/Pa]

equation (2.6) yields

$$\left(\Phi \frac{\partial \rho}{\partial p} + \rho \alpha (1 - \Phi) \right) \frac{\partial p}{\partial t} + \text{div}(\rho v_f) = -\Phi \left(\frac{\partial \rho}{\partial T} \frac{\partial T}{\partial t} + \frac{\partial \rho}{\partial c} \frac{\partial c}{\partial t} \right) \quad (2.8)$$

Introducing a general Darcy's law

$$v_f = -\frac{k}{\eta} (\nabla p - \rho g) \quad (2.9)$$

k - permeability [m²]

η - fluid viscosity [Pa s]

z - vertical coordinate [m]

g - vector of the gravitational acceleration [m s⁻²] ($g = -g \nabla z$)

leads to

$$\left(\Phi \frac{\partial \rho}{\partial p} + \rho \alpha (1 - \Phi) \right) \frac{\partial p}{\partial t} - \text{div} \left(\frac{k \rho}{\eta} (\nabla p + \rho g \nabla z) \right) = -\Phi \left(\frac{\partial \rho}{\partial T} \frac{\partial T}{\partial t} + \frac{\partial \rho}{\partial c} \frac{\partial c}{\partial t} \right) \quad (2.10)$$

Introducing the bulk modulus for water

$$\beta_p = \frac{1}{\rho} \frac{\partial \rho}{\partial p} \quad (2.11)$$

β_p - bulk modulus for water [Pa⁻¹]

the thermal expansion coefficient for water

$$\beta_T = \frac{1}{\rho} \frac{\partial \rho}{\partial T} \quad (2.12)$$

β_T - thermal expansion coefficient for water [K⁻¹]

and the gain of density by solute concentration

$$\beta_c = \frac{1}{\rho} \frac{\partial \rho}{\partial c} \quad (2.13)$$

β_c - gain of density by solute concentration [-]

simplifies (2.10) to

$$\rho \left(\Phi \beta_p + \alpha (1 - \Phi) \right) \frac{\partial p}{\partial t} - \text{div} \left(\frac{k \rho}{\eta} (\nabla p + \rho g \nabla z) \right) = -\Phi \rho \left(\beta_T \frac{\partial T}{\partial t} + \beta_c \frac{\partial c}{\partial t} \right) \quad (2.14)$$

Note that up to this point neither simplifying assumption concerning the balance equation nor assumptions concerning the function $\rho = \rho(p, T, c)$ have been introduced.

In order to identify the relation between (2.10) and the specific storage, eq. (2.10) must be transformed even further since specific storage refers to the continuity equation formulated in terms of hydraulic head instead of hydraulic pressure. In case of negligible density variations the hydraulic pressure can be substituted by the hydraulic head using

$$h = \frac{p}{\rho g} + z \quad (2.15)$$

h - hydraulic head [m]

g - gravitational acceleration [m s⁻²]

z - reference horizon [m]

$$\rho^2 g \left(\Phi \beta_p + \alpha (1 - \Phi) \right) \frac{\partial h}{\partial t} - \text{div} \left(\frac{k \rho}{\eta} (\rho g \nabla h) \right) = -\rho \Phi \left(\beta_T \frac{\partial T}{\partial t} + \beta_c \frac{\partial c}{\partial t} \right) \quad (2.16)$$

In case of strongly varying density the hydraulic pressure would have to be evaluated pointwise by the integral

$$p = p_{ref} + \int_{z_{ref}}^z \rho(z) g dz \quad (2.17)$$

which is highly unpractical. However, assuming that only limited density variations are considered, (2.16) can simply be divided by ρ leading to

$$\rho g (\Phi \beta_p + \alpha (1 - \Phi)) \frac{\partial h}{\partial t} - \text{div} \left(\frac{k \rho g}{\eta} \nabla h \right) = -\Phi \left(\beta_T \frac{\partial T}{\partial t} + \beta_c \frac{\partial c}{\partial t} \right) \quad (2.18)$$

where the final substitutions

$$S_0 = \rho g (\Phi \beta_p + (1 - \Phi) \alpha) \quad (2.19)$$

S_0 - specific storage [1/m]

and

$$K = \frac{k \rho g}{\eta} \quad (2.20)$$

K - hydraulic conductivity [m s^{-1}]

eventually yield the well-known simple form of the continuity equation

$$S_0 \frac{\partial h}{\partial t} - \text{div}(K \nabla h) = 0. \quad (2.21)$$

Data from the field are usually given in terms of specific storage S_0 . In the pressure-dependent formulation (2.14) it would thus be incorporated as

$$\frac{S_0}{g} \frac{\partial p}{\partial t} - \text{div} \left(\rho \frac{k}{\eta} (\nabla p - \rho \mathbf{g}) \right) = -\Phi \rho \left(\beta_T \frac{\partial T}{\partial t} + \beta_c \frac{\partial c}{\partial t} \right) \quad (2.22)$$

2.1.2 Notes about specific storage

Generally, the specific storage quantifies changes of fluid mass in a control volume. In the derivation above, changes of the pore volume as well as changes in the fluid density are considered. Conceivable but not easily quantified is also the effect of entrapped air bubbles in the pore space that would contribute to the fluid compressibility which is not considered here.

Even assuming a perfectly rigid matrix whose pores are fully filled with water, the density changing influence of the hydraulic pressure on water is always present and thus poses a lower limit for the specific storage. The bulk modulus of water for pressure induced volumetric changes amounts to $4.81 \cdot 10^{-10} \text{ Pa}^{-1}$ (at $10 \text{ }^\circ\text{C}$) which is very low but finite.

Finally, because of the assumption of negligible density variations, the continuity equation (2.21) may take eventually the form of Fick's second law

$$\frac{\partial h}{\partial t} - \text{div} \left(\frac{K}{S_0} \nabla h \right) = 0. \quad (2.23)$$

where the ratio K/S_0 is often referred to with a term containing "diffusivity" like "aquifer hydraulic diffusivity" in /SIN 17/. The equivalent formulation in terms of pressure and permeability can be found by inserting eqs. (2.15) and (2.20) in (2.23):

$$\frac{\partial p}{\partial t} - \text{div} \left(\frac{\rho g k}{\eta S_0} \nabla p \right) = 0. \quad (2.24)$$

2.1.3 Pressure dependent density

The dependence of density on hydraulic pressure is usually given as

$$\rho = \rho_0 e^{\beta_p (p - p_0)} \quad (2.25)$$

p_0 - reference hydraulic pressure [Pa]

ρ_0 - reference fluid density [kg m^{-3}]

which, according to /BEA 87/, can be used "for all practical purposes" in its linearized form

$$\rho = \rho_0 (1 + \beta_p (p - p_0)) \quad (2.26)$$

A more complex formulation covering additionally the influence of temperature and solute concentration is given in /KRÖ 91/.

2.1.4 Pressure dependent porosity

In the same way in which the pressure-dependent density can be derived (see above) the dependence of the porosity on hydraulic pressure can be determined as

$$\Phi = 1 - (1 - \Phi_0) e^{-\alpha(p-p_0)} \quad (2.27)$$

2.1.5 Comparison with an analytical solution

Due to the similarity of equation (2.23) to the heat equation i. e. the law of heat conduction in materials

$$\frac{\partial T}{\partial t} - \text{div}(D_T \nabla T) = 0 \quad (2.28)$$

D_T - thermal diffusivity [$\text{m}^2 \text{s}^{-1}$]

the abundance of analytical solutions to equation (2.28) as compiled in /CAR 59/ can be used to qualify the implementation of the storage term in d³f++. For this purpose the temperature T has to be exchanged with the hydraulic head h and the thermal diffusivity D_T with the ratio K/S_0 .

Used here is the one-dimensional solution for a slab of the length $2l$ ($-l < x < +l$) to the instantaneous drop of temperature/hydraulic pressure at both ends from the initial value to zero (/CAR 59/, eq. (9), page 97, using the original notation):

$$v(x,t) = v_0 - v_0 \sum_{n=0}^{\infty} (-1)^n \left\{ \text{erfc} \frac{(2n+1)l - x}{2\sqrt{\kappa t}} + \text{erfc} \frac{(2n+1)l + x}{2\sqrt{\kappa t}} \right\} \quad (2.29)$$

- v_0 - initial temperature [K]
- l - half length of slab [m]
- κ - thermal diffusivity [$\text{m}^2 \text{s}^{-1}$]
- x - spatial coordinate [m]
- t - time [s]

This solution describes the temperature evolution in a slab of the initial temperature v_0 , where the boundary temperature is spontaneously changed to $v(x = \pm l, t) = 0$ at $t = 0$. With a few simple modifications this solution can be used to solve the problem of a slab of the length l ($0 < x < l$) where the boundary temperature is spontaneously increased from an arbitrary initial value v_0 to an arbitrary boundary value $v(x = 0, t) = v_b$.

As a test case, a basically one-dimensional model, realised with 3D elements, according to the following specifications has been used:

- length: 100 m
- cross-section: 2 m²
- permeability: 10⁻¹² m²
- porosity: 0.10
- rock compressibility: 2·10⁻⁸ Pa⁻¹
- initial hydraulic pressure: 0 Pa
- boundary pressure: 1000 Pa
- gravitational acceleration: 10 m² s⁻¹
- fluid density: 1000 kg m⁻³
- viscosity: 10⁻³ Pa·s

From these data follows a thermal/hydraulic diffusion coefficient of 0.05 m²/s. The results from d^{3f++} and the analytical solution are depicted in Fig. 2.1. The fit is satisfying and thus qualifying the implementation of the storage term in d^{3f++}.

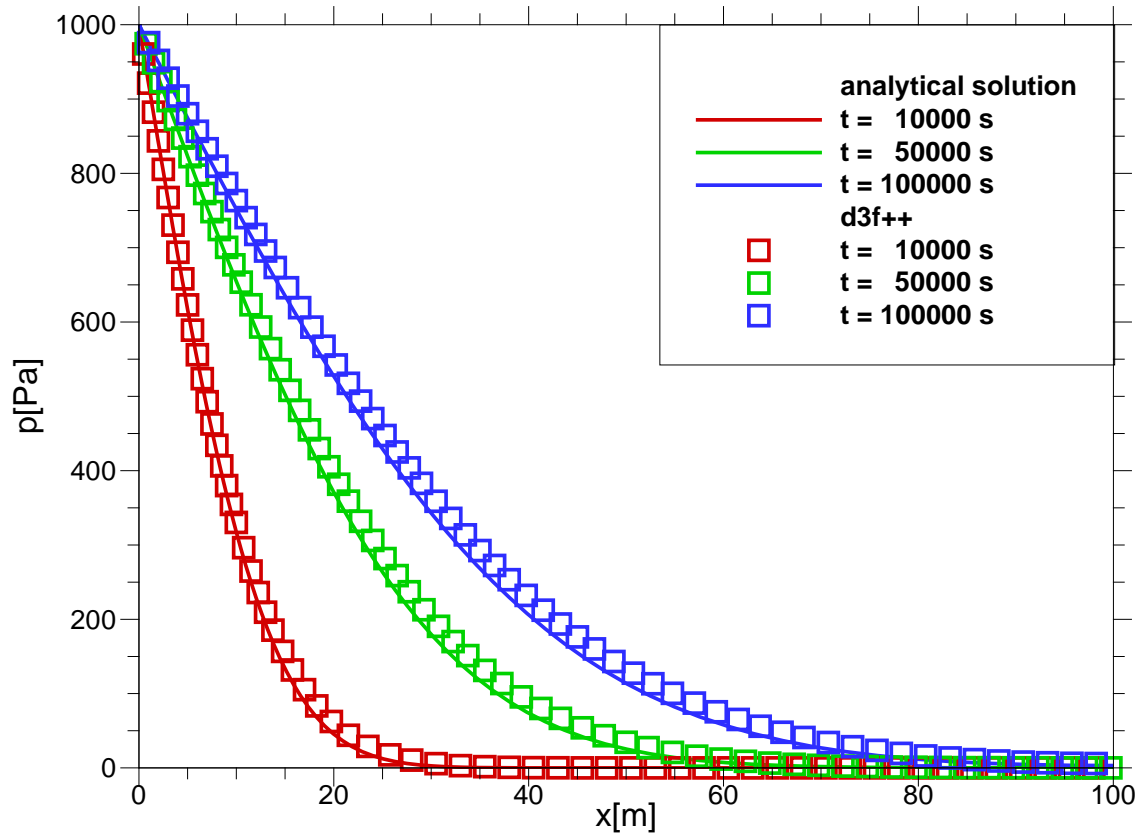


Fig. 2.1 Comparison of results from d^{3f++} and a referring analytical solution

2.2 Enhancement of the preprocessor ProMesh

2.2.1 General Remarks

Meshing of complex geometries for the purpose of scientific computing can be a challenging and time-consuming task. Not only the shape of modelled objects but also the quality of individual elements play an important role for the applicability and efficiency of different discretisation and solution strategies. Both commercial and open source packages exist that allow users to generate grids for simulations. Some are executed from the command line and others feature extensive graphical user interfaces. While open source packages typically focus on specific features of grid generation and therefore are often restricted to specific use cases, commercial products tend to obfuscate the algorithms involved and limit the user influence on the generation process. This may be beneficial for typical use cases in industry and production environments, however, it is not satisfying for the specific needs of scientists who develop new discretisation or solution strategies or which address uncommon or new problems from other fields (e. g. fractured flow in porous media, signal propagation in neural cells, etc.).

Current developments in high performance computing have highlighted the importance of hierarchical multigrid approaches as an efficient strategy for massively parallel solvers on distributed grids, /REI 14/. In those studies, it was shown that both algebraic and geometric multigrid approaches were able to handle billions of unknowns on hundred thousands of processes. One of the difficulties in such massively parallel applications is the construction of the required highly detailed meshes for simulations on realistic domains. Especially for geometric multigrid, a parallel grid generation approach driven by repeated refinement and redistribution of an initially coarse mesh has been shown to be very efficient /REI 14/. Besides efficient parallel refinement and redistribution, a coarse grid with good element qualities is paramount for such approaches. In order to achieve a good approximation of the original domains and to maintain good element qualities during refinement, a transformation of newly generated vertices both on the boundary and inside a refined grid may be necessary. ProMesh features tools to generate such coarse grids and to define projectors on those grids which transform refined grids to improve geometric approximation while maintaining good element qualities. Those projectors are exported and can be used by simulation environments to construct distributed grid hierarchies consisting of billions of elements, as required by massively parallel simulation setups.

In section 2.2.2 some basic definitions and notation are given that is used throughout the article. In section 2.2.3 the most important concepts of ProMesh are described which serve as the foundation for the interplay of the various algorithms. A selection of commonly used meshing algorithms is given in section 2.2.4. Finally, different applications are presented in section 2.2.5, which underline the applicability of the presented approach to relevant scientific problems.

2.2.2 Overview and notation

2.2.2.1 Grid structure

The basic structure on which ProMesh operates is the grid. In ProMesh, a grid \mathcal{G} is a collection of vertex ($\mathcal{E}_{\mathcal{G}}^0$), edge ($\mathcal{E}_{\mathcal{G}}^1$), face ($\mathcal{E}_{\mathcal{G}}^2$), and volume elements ($\mathcal{E}_{\mathcal{G}}^3$):

$$\mathcal{G} := \bigcup_{d=0}^3 \mathcal{E}_{\mathcal{G}}^d \quad (2.30)$$

For $\mathcal{E}_{\mathcal{G}}^d$, d denotes the dimension of the respective elements of that set, as detailed below. In order to keep the definitions simple, yet accurate, only very basic assumptions on the shape of the individual elements are made.

Topology

Vertices ($\mathcal{E}_{\mathcal{G}}^0$)

Vertices are the most basic element type of a grid. All other elements are defined by specifying the set of their corner vertices. For each vertex $v \in V_{\mathcal{G}}$ is called

$$\Phi_v \in \mathbb{R}^3 \quad (2.31)$$

the geometric representation (or simply position) of v .

Edges, faces, and volumes

The properties of edges, faces, and volumes of a grid \mathcal{G} can be defined recursively as follows. For $d = 1, 2, 3$ and for all $e \in \mathcal{E}_{\mathcal{G}}^d$ a mapping

$$[\cdot, \cdot, \dots, \cdot]_d \rightarrow \mathcal{E}_G^d \quad (2.32)$$

associates the element e with its corner vertices $v_1, \dots, v_m \in \mathcal{E}_G^0$:

$$e = [v_1, v_2, \dots, v_m]_d = [v_{\pi(1)}, v_{\pi(2)}, \dots, v_{\pi(m)}]_d \quad (2.33)$$

for each permutation π on $\{1, 2, \dots, m\}$, where $m = 2$ for $d = 1$ and $m \geq d + 1$ for $d > 1$.

Furthermore, for each $e \in \mathcal{E}_G^d$, $e = [v_1, \dots, v_m]_d$ with $v_1, \dots, v_m \in \mathcal{E}_G^0 \in$ a homomorphism

$$\phi_e: \{x \in \mathbb{R}^e \mid \|x\| \leq 1\} \rightarrow \overline{\Omega}_e \subset \mathbb{R}^3 \quad (2.34)$$

and elements $s_0, \dots, s_k \in \cup_{i=1}^{d-1} \mathcal{E}_G^i$, $k \in \mathbb{N}$ exist, such that

$$\partial\Omega_e = \bigcup_{i=1}^k \Omega_{s_i} \cup \bigcup_{j=1}^m \Phi_{v_j} \quad (2.35)$$

and

$$\bigcap_{i=1}^k \Omega_{s_i} \cap \bigcap_{j=1}^m \Phi_{v_j} = \emptyset \quad (2.36)$$

$\Omega_e \in \mathbb{R}^3$ is then called the geometric representation of e . An overview over the specialised element types used in ProMesh is given in Tab. 2.1.

As a consequence of the postulated properties for the geometric representation of individual elements, sides and sides of sides are contained in a grid as elements themselves. The following operations allow to easily access associated element sides and to define element neighbourhoods.

For two elements $e_1 \in \mathcal{E}_G^{d_1}$, $e_2 \in \mathcal{E}_G^{d_2}$ is written

$$e_1 \in e_2: \Leftrightarrow \begin{cases} e_1 \in \mathcal{S}_G^{e_2} & \text{for } d_2 - d_1 = 1, \\ \exists e' \in \mathcal{S}_G^{e_2}: e_1 \in \mathcal{S}_G^{e'} & \text{for } d_2 - d_1 = 2, \\ \exists e' \in \mathcal{S}_G^{e_2}: e'' \in \mathcal{S}_G^{e'}: e_1 \in \mathcal{S}_G^{e''} & \text{for } d_2 - d_1 = 3. \end{cases} \quad (2.37)$$

Tab. 2.1 Element types available in ProMesh

	#vertices	#edges	#triangles	#quadrilaterals
vertex	1	-	-	-
edge	2	1	-	-
triangle	3	3	1	-
quadrilateral	4	4	-	1
tetrahedron	4	6	4	-
pyramid	5	8	4	1
prism	6	9	2	3
hexahedron	8	12	-	6
octahedron	6	12	8	-

Element connectivity

Sides

For $d > 0$ the set of sides of an element $e \in \mathcal{E}_G^d$ is denoted by

$$\mathcal{S}_G^e := \{s \in \mathcal{E}_G^{d-1} \mid s = [v_1, \dots, v_k]_{d-1} \text{ and } e = [v_1, \dots, v_k, v_{k+1}, \dots, v_l]_d\} \quad (2.38)$$

with $k, l \in \mathbb{N}, k < l, v_1, \dots, v_l \in \mathcal{E}_G^0$ and $v = [v]_0 \forall v \in \mathcal{E}_G^0$.

2.2.3 Concepts

2.2.3.1 Selections

A central part of ProMesh's user interactions are element selections. At any time, elements of a grid are considered to be either selected or unselected. Formally, a mapping $sel_G: \mathcal{G} \rightarrow \{0,1\}$ is defined, so that for each $e \in \mathcal{G}$:

$$sel_G(e) = \begin{cases} 1, & e \text{ is selected,} \\ 0, & e \text{ is not selected.} \end{cases} \quad (2.39)$$

Elements can be freely marked as selected or unselected. Most algorithms in ProMesh operate on selected elements only. Selections are especially useful during adaptive refinement, where only selected elements will be refined, during vertex transformations, like translations, rotations or scaling, or when it comes to assigning elements to subsets.

Selections are most often performed through direct user input. The user selects elements in the grid visualisation widget by simply clicking on them or by dragging the mouse, thus performing a rectangular selection.

Many algorithms exist, which assist in performing selections on complicated geometries, e. g. algorithms which extend the selection to a neighbourhood of the current selection or which select areas of the grid with specific geometric or topological properties. Some examples of such algorithms can be found in section 2.2.3.2.

2.2.3.2 Subsets

Partitioning a grid into subsets has many benefits when it comes to using a grid in a simulation. The concept of subsets is used with differing names by several simulation packages (c.f. /BAS 94a/, /REI 14/) It is possible to assign different material properties to different subsets, like different permeabilities of different soil types in groundwater flow problems. Of course, one also could define entirely different problems on different subsets of a grid. Subsets are also very useful for defining boundary sections and interior low dimensional interfaces, where special processes have to be modelled or boundary conditions are to be set.

A grid element $e \in \mathcal{G}$ is assigned to at most one subset. Subsets are identified by an index. If an element is not assigned to a subset, the pseudo-index 1 is assigned. Formally the mapping $sub_{\mathcal{G}}: \mathcal{G} \rightarrow \{-1\} \cup \mathbb{N}_0$ is defined, so that

$$sub_{\mathcal{G}}(e) = \begin{cases} i \in \mathbb{N}_0 & e \text{ is assigned to subset } i \\ -1 & e \text{ is not assigned to a subset} \end{cases} \quad (2.40)$$

Algorithms exist, which assist in assigning elements to subsets. Most commonly, one simply assigns the current selection to a subset. However, automated algorithms exist, which e. g. separate groups of volumes into different subsets, e. g. by assigning two

volumes to the same subset, if a path between them exists, which only traverses faces $f \in \mathcal{E}_G^2$ with $sub_G(f) = -1$.

A path between volumes $v_a, v_b \in \mathcal{E}_G^3$ is thereby a sequence $p := v_0, \dots, v_m$ with $v_i \in \mathcal{E}_G^3, v_0 = v_a, v_m = v_b$, so that faces $f_0, \dots, f_{m-1} \in \mathcal{E}_G^2$ exist with $f_i = v_i \cap v_{i+1}, i = 0, \dots, m - 1$. Those faces f_i are then said to be crossed by the path p .

2.2.3.3 Projectors

The generation of multi-grid hierarchies by repeated refinement is a powerful tool to construct highly detailed meshes with adapted resolution. Especially when considering the mesh detail typically found in massively parallel computations of numerical PDE based simulations. Using this technique has the advantage that a relatively coarse mesh can be the starting point for a simulation. Besides reducing the hardware requirements for mesh generation, this significantly eases parallel loading and distribution.

During refinement, however, one has to make sure that the sequence of generated grids converges towards the underlying original domain. To this end, ProMesh allows to specify so called projectors for each subset. Whenever a vertex is generated during refinement, the appropriate projector is called to compute the coordinate at which the vertex should be placed, based on the vertices of the new vertex's parent element.

The difficulty hereby lies in maintaining a good element quality. To this end not only vertices on the boundary of a grid are relocated but also relocate inner vertices. This may in effect even lead to improved element ratios during refinement, /STE 11/.

To allow different projectors to operate on the same mesh, each projector not only calculates a new position for newly generated vertices, but also computes a weight with which the new position shall be weighted with a common underlying projector (e. g. classical linear interpolation). Using this weight, one could also specify multiple projectors for a single subset. This may be explored in future revisions of the software.

2.2.3.4 Marks

Similarly to selections, element marks provide a way to mark parts of a grid for special treatment for various algorithms. During remeshing, marks can for example be used, to

define crease-edges or fixed-vertices, which have to be treated with special care. Again a mapping $mark_{\mathcal{G}}: \mathcal{G} \rightarrow \{0,1,2\}$ is defined, so that for each $e \in \mathcal{G}$:

$$mark_{\mathcal{G}}(e) = \begin{cases} 0, & e \text{ is not marked,} \\ 1, & e \text{ is a crease element,} \\ 2, & e \text{ is fixed.} \end{cases} \quad (2.41)$$

Let $M_{\mathcal{G}}^C := \{e \in \mathcal{G} | mark_{\mathcal{G}}(e) = 1\}$ be the set consisting of all crease elements in \mathcal{G} , and $M_{\mathcal{G}}^F := \{e \in \mathcal{G} | mark_{\mathcal{G}}(e) = 2\}$ be the set consisting of all fixed elements in \mathcal{G} .

Marks are either created manually from the current selection or can be assigned automatically based on features of the geometry. One could for example mark all edges, at which triangles meet in a given angle.

2.2.4 Meshing

Meshes are either imported into ProMesh through various interchange formats (e. g. 'stl', 'exodus', 'vtu') or are generated directly in ProMesh. Besides free-form line drawing, ProMesh features several basic parameterised geometric primitives, e. g., circles, boxes, spheres, etc. Those can be combined to meshes using either manual or automated intersection algorithms. Through several remeshing algorithms, triangle qualities can be improved and meshes can be coarsened or refined.

Once a hull is generated, 2d or 3d triangulation algorithms can be employed to automatically generate volume meshes using, e. g., constrained Delaunay triangulation.

By extrusion, it is furthermore possible to generate prism- and hexahedra-based meshes. A combination of extrusion and triangulation algorithms allows for the creation of hybrid meshes.

2.2.4.1 Basic Operations

Edge-Split

During an Edge-Split an edge $e \in \mathcal{E}_{\mathcal{G}}^1$, $e = [v_1, v_2]$ is replaced by a vertex v^* and two new edges $[v_1, v^*]$ and $[v^*, v_2]$, with $p(v^*) := \frac{p(v_1) + p(v_2)}{2}$. Each adjacent triangle $[v_1, v_2, v_3^i] \in$

$\mathcal{E}_G^2, i = 1, \dots, k$ is replaced by two triangles $[v_1, v^*, v_3^i]$ and $[v^*, v_2, v_3^i]$. Furthermore, new edges $[v^*, v_3^i], i = 1, \dots, k$ are introduced (cf. Fig. 2.2).

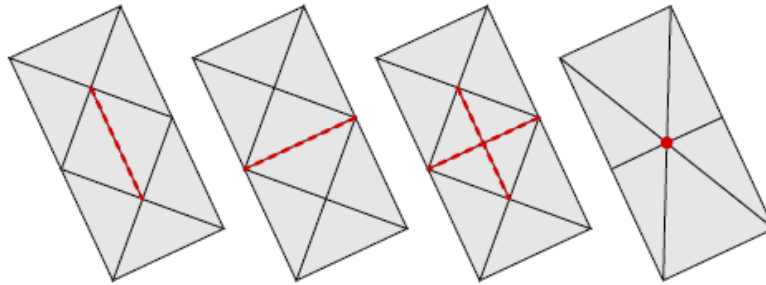


Fig. 2.2 Edge operations

Left: Original geometry with selected edge (red). Middle left: Edge-Swap. Middle right: Edge-Split. Right: New Edges

Face-Split

During a Face-Split a face $f \in \mathcal{E}_G^2, f = [v_1, \dots, v_k]$ is replaced by a new vertex v^* , with $p(v^*) := \frac{1}{k} \sum_{i=1}^k p(v_i)$, triangles $[v_i, v_{i+1}, v^*], i = 1, \dots, k$, and edges $[v^*, v_i], i = 1, \dots, k$ as shown in Fig. 2.3.

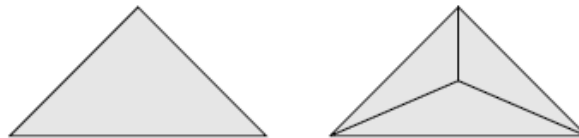


Fig. 2.3 Face-Split executed on the left triangle

The resulting triangulation (right) features one new vertex, three new edges and two new triangles.

2.2.5 Visualisation

Visualisation is a crucial part of each interactive meshing software. Besides allowing users to manually select elements of the grid for further processing, visualisation helps in quickly spotting problematic geometrical or topological issues in a grid.

Especially in 3d volume meshes, important inner structures in a grid are often obscured by surrounding elements. In order to inspect and modify those structures, it is crucial to provide techniques to visualise them.

In the following section, a short overview is given over the terminology and techniques used for 3d volume mesh visualisation with customisable element visibilities at interactive rates.

2.2.5.1 Element visibilities

Since element visibilities are most important for 3d volume meshes, considerations will be focussed on this special case. However, the concepts are also valid for 3d manifold meshes or any mesh of lower dimension.

An element $e \in \mathcal{G}$ is considered visible, if all of the following conditions are met:

1. The associated subset is set to “visible”. Individual subsets can be toggled between visible and invisible by the user.
2. The element is not in front of any active clipping plane. Clipping Planes are defined by the user by specifying a point on the plane and the planes normal. They allow to easily hide large parts of a geometry. They do not depend on the current camera or world transform and should not be confused with OpenGL’s near- and far-clipping-planes.
3. The element has not been assigned to the set of hidden elements $\mathcal{H}_{\mathcal{G}} := \{e \in \mathcal{G} | e \text{ is hidden}\}$. ProMesh provides commands to hide all selected elements and to reveal all hidden elements.

2.2.5.2 Rendering

Hardware accelerated rendering of vertices, edges, and faces (triangles and quadrilaterals) is accomplished through the cross platform OpenGL library. However, no hardware accelerated rendering is available for volume elements. Instead of drawing all visible volume elements, thus only the shell of the set of visible volume elements is drawn, together with visible lower dimensional elements which are not enclosed by hidden volumes. More precisely, let

$$\mathcal{VJS}_{\mathcal{G}}^{\mathcal{F}} := \{f \in \mathcal{E}_{\mathcal{G}}^2 | \exists v_1, v_2 \in \mathcal{E}_{\mathcal{G}}^3 \setminus \mathcal{H}_{\mathcal{G}}, v_1 \neq v_2, f \in \text{sides}_{\mathcal{G}}(v_1) \cap \text{sides}_{\mathcal{G}}(v_2)\} \quad (2.42)$$

be the set of potentially visible faces. Furthermore, let

$$\mathcal{VJS}_G^V := \{v \in \mathcal{E}_G^3 \setminus \mathcal{H}_G \mid \exists f \in \mathcal{VJS}_G^F : f \in v\} \quad (2.43)$$

be the set of potentially visible volumes, i. e., all volumes which are contained in the set of visible volumes and have a potentially visible side. Analogously, the set of potentially visible edges is then given by

$$\mathcal{VJS}_G^N := \{n \in \mathcal{E}_G^0 \setminus \mathcal{H}_G \mid \exists v \in \mathcal{E}_G^3 : n \in v\} \cup \{v \in \mathcal{E}_G^0 \mid \exists e \in \mathcal{VJS}_G^E : n \in e\} \quad (2.44)$$

Finally, the set of potentially visible nodes is given by

$$\mathcal{VJS}_G^E := \{e \in \mathcal{E}_G^1 \setminus \mathcal{H}_G \mid \exists v \in \mathcal{E}_G^3 : e \in v\} \cup \{e \in \mathcal{E}_G^1 \mid \exists f \in \mathcal{VJS}_G^F : e \in f\} \quad (2.45)$$

Visualization is now performed by drawing the nodes, edges, and faces from the sets \mathcal{VJS}_G^E , \mathcal{VJS}_G^N , and \mathcal{VJS}_G^F using OpenGL. As long as the camera stays outside of the visualised object, the resulting image from the outlined algorithm is the same as if all sides of all visible volume elements were rendered. However, the amount of rendered elements is drastically reduced by the chosen approach.

Since the conditions for element visibility are independent of the current camera orientation, those elements can be efficiently cached and rendered at interactive rates, even if the camera is moved or rotated. The lists have to be refreshed after operations have been performed on the mesh which altered the geometry or topology.

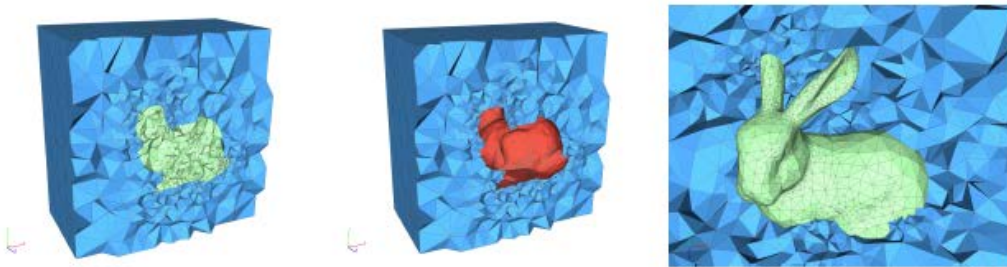


Fig. 2.4 Several visibility configurations for a tetrahedrization of the Stanford Bunny in a box

Left: Clip-plane; Middle: Clip-plane and hidden subset; Right: Hidden elements

2.2.6 Implementation

The concepts given above have been implemented in the grid library libGrid, which is part of the ug4 simulation framework (cf. /VOG 14/, /REI 14/). Implementing those concepts seems rather straight forward on first sight. However, a straight forward implementation, which e. g. simply stores a subset index in each element, has the great disadvantage, that the burden of handling and maintaining selections or subsets would be on the implementor of each individual algorithm which adds/deletes elements to/from a grid. This is not only cumbersome and prone to error, it furthermore severely restricts the usage of the introduced concepts. For example, an actual implementation should allow programmers to construct several independent partitions of a domain into subsets, e. g., to define a process map during parallelisation. However, an algorithm which, e. g., refines elements of a grid shouldn't have to worry about potentially existing subset partitions, let alone having to assign new elements to those subsets.

Grid Observers

Therefore it was decided to introduce an abstract grid observer class, modelled after the observer pattern given in /W3S 19/. Instances of derived classes of those observers can be registered at instances of the grid class and are from then on informed about changes to the grid's elements, including the creation of new elements, or an issued deletion or merge of existing elements.

When a new element in a grid is created, a parent element can optionally be specified. When the grid informs associated observers on the creation of an element, it then passes the specified parent element as a parameter to the corresponding callback. Observers use this parent parameter to, e. g., assign child elements to the same subset as their parent element or to copy the selection state from a parent element to a child element. Several different observers exist in libGrid, most notably the Selector and the SubsetHandler, which manage selections and subsets respectively. One SubsetHandler thereby provides one partitioning of a grid into subsets, as defined in section 2.2.3.2. Multiple SubsetHandlers may however exist at the same time, thus allowing to create different co-existing partitions.

Attachments

Data has to be associated with the elements of a grid, e. g., coordinates with vertices or a flag with all elements, that indicates whether an element is selected or not. While one could add member variables directly to the C++ classes which represent vertices, edges, faces or volume elements, this would result in a rather rigid setup. Another option in C++ could be template arguments to the different element types, defining the data that shall be stored in the elements. This data-template however would have to be a superset of all the data that any algorithm which potentially might be executed accesses. This would lead to bloated element types, and to the danger that unrelated algorithms corrupt the data on which other algorithms rely. Instead it was chosen to use a very flexible, yet efficient mechanism to associate arbitrary data with grid elements at runtime.

Through so called attachments an identifier is described, associated with a given data type. By attaching such attachments to, e. g., vertices of a grid, the grid is caused to provide instances of the attachments data type for all vertices of the grid. Attachments are present either for all elements of a given type (vertices, edges, faces or volumes) or for none. If new elements are created or deleted, the attached data will automatically be adjusted. This allows for a very efficient and cache friendly implementation using one consecutive array for each attachment.

Data associated with an attachment can then be accessed through so called attachment accessors. Those accessors are light weight classes which store a reference to the data which a grid provides for a given attachment and which feature methods to return the corresponding data entry for a given element. This abstraction allows fast, secure, and type safe access to attached data entries.

Attachments can, e. g., be used by algorithms to store temporary data in the elements of a grid. The Selector attaches a selection state and linked list entries to the grids elements, thus providing an efficient way to iterate over all selected elements and to query their selection state. Since each instance of a Selector defines its own attachment identifiers, multiple selectors can operate on a given grid at the same time.

Similarly, the SubsetHandler attaches a subset index and linked list entries to the grids elements. Furthermore, it stores a list of subset descriptors, which provide begin and end iterators to the elements in the different subsets. Again, by using separate attachment

identifiers for each instance of a `SubsetHandler`, it can be allowed for multiple `SubsetHandlers` to operate on a given grid at the same time. Element marks, as introduced in section 2.2.3.4, are for example simply maintained by an additional `SubsetHandler`.

Performance Considerations

The described implementation of course introduces a slight overhead on the element creation and removal process, as well as during data access. While the overhead for data access is a simple array lookup and therefore very small, a slightly higher overhead is introduced for the element creation and removal process, since for each element created in a grid, callbacks in associated observers have to be executed. While the functionality in those callbacks can not be considered as overhead, since it represents a part of the functionality of the whole program, the function call itself can be. However, the overhead of such a virtual method call is rather small, too, especially if one considers other task like neighbourhood information updates, boundary projections etc., which potentially also are executed during element creation.

In any case, the provided tools allow programmers to write clean and modular code, in which algorithms don't have to care about data concerning other algorithms, since observers can do this instead. In the grand scheme this is a crucial aspect in writing a comprehensive and extendible software framework, which here more than justifies the small overhead.

3 Advancement of the solvers in d^{3f++}

3.1 Adaption of the LIMEX method to thermohaline groundwater flow to speed-up the nonlinear solvers

The governing equations for density driven flow are the conservation of salt mass and fluid, which read

$$\frac{\partial}{\partial t}(\phi\rho\omega) + \nabla \cdot [\omega\rho\vec{q} - \rho\mathbb{D}\nabla\omega] = \omega\rho Q \quad (3.1)$$

$$\frac{\partial}{\partial t}(\phi\rho) + \nabla \cdot [\rho\vec{q}] = \rho Q \quad (3.2)$$

where ω denotes the salt-mass-fraction, and ϕ and Q denote spatially dependent porosity and fluid sources and sinks respectively. The system is closed by constitutive laws for the Darcy flow

$$\vec{q} = -\frac{k}{\mu}(\nabla p - \rho\vec{g}) \quad (3.3)$$

which introduces the gradient of the pressure p as the second unknown into the system. Moreover, mechanical dispersion (Scheidegger-type) is given by

$$\mathbb{D} = \phi\mathbb{D}_{mol} + \alpha_T|\vec{q}| + (\alpha_L - \alpha_T)\frac{\vec{q} \cdot \vec{q}^T}{|\vec{q}|} \quad (3.4)$$

Here, \mathbb{D}_{mol} is the molecular diffusion coefficient, while α_T and α_L denote the dispersion lengths in transversal and lateral direction, respectively.

The density ρ and the viscosity μ depend on the salt mass fraction ω and are given by empirical relations. For the density this work considers the linear relationship

$$\rho(\omega) = \rho_0 + (\rho_1 - \rho_0)\frac{\omega}{\omega_{max}} \quad (3.5)$$

where ω_{max} denotes the salt mass fraction of a saturated haline solution. The viscosity is given by either of the following:

$$\mu_{\text{const}}(\omega) = \mu_0 \quad (3.6)$$

$$\mu_{\text{real}}(\omega) = \mu_0(1 + 1.85\omega - 4.1\omega^2 + 44.5\omega^3) \quad (3.7)$$

Upon combining all these relations, the PDE system (3.1), (3.2) is nonlinearly coupled.

Resulting system after spatial discretization

Due to the lack of time derivatives in the equation for the pressure p the PDE system appears to be *degenerate*. After discretization of this PDE system by the *method of lines* one arrives at a differential algebraic (DAE) system of the kind

$$M(u) u' = f(u), \quad u(0) = u_0 \quad (3.8)$$

wherein $M(u)$ represents a solution dependent matrix, which is *singular* due to the fact that the PDE system is degenerate. In view of uniqueness of the solution the matrix pencil $\{M(u) - \tau J(u)\}$ must be regular, where J means

$$J(u) = J_f(u) - \Gamma[u, u'] \quad (3.9)$$

with

$$J_f(u) := \left(\frac{\partial f(u)}{\partial u} \right) \quad \text{and} \quad \Gamma[u, z] := \left(\frac{\partial M(u)}{\partial u} z \right) \quad (3.10)$$

3.1.1 Preliminary considerations

In this section, the most important algorithmic parts that are necessary to attack the challenging class of problems are shown.

3.1.1.1 Choice of Stiff Integrator

Suppose focusing on the regime where the PDE systems appear to be parabolic and large scale. As for the choice of a stiff integrator, typically exist the following options, see, e. g., the textbooks by Hairer/Wanner /HAI 02/ or Deuffhard/Bornemann /DEU 02/.

- *Implicit one-step or multistep methods:*

This class of algorithms covers the BDF method as a multistep method or the Radau method as a one-step method. In both cases, the realization of three nested loops is needed: the *outer* discretization loop (adaptive time step), the *medium-level* Newton-like iteration loop for the solution of the nonlinear system, and the *inner* loop for solving the linear equations to compute the Newton corrections.

- *Implicit Euler discretization:*

In an earlier algorithmic approach /NAE 15/, the problem class of interest here had been attacked by the simplest implicit one-step method, an implicit Euler discretization. That approach had been combined with extrapolation of order 2 and a heuristic time step control. In passing note that with that version of stiff integrator the Gorleben problem addressed in Section 3.1.2.4 could not be solved.

In contrast, the code IMPEX included in the numerical experiments in Section 3.1.2 below uses the same implicit discretization, but an adaptive order and time step control based on extrapolation, see, e. g. /DEU 02/. Convergence of the Newton-type iteration in each discretization step has been assumed, as soon as the outer residual has been reduced by 7 orders of magnitude.

- *Linearly implicit methods of Rosenbrock-Wanner type (ROW):*

This class of algorithms only requires two loops, the outer loop for an (adaptive) time step discretization and the inner loop for the numerical solution of the arising linear systems. An exact Jacobian matrix is required, an information that enters into the derivation of the algebraic equations for the coefficients.

- *Linearly implicit W-methods:*

This class of algorithms also only requires two loops, the *outer* loop for an (adaptive) time step discretization and the *inner* loop for the numerical solution of the arising linear systems. In contrast to the ROW class above, only a reasonable approximation of the Jacobian is needed. Unfortunately, the construction of this class of methods leads to a blow-up in the number of the arising algebraic conditions for the coefficients. For this reason, only low orders have been developed by the scientific community.

- *Linearly implicit extrapolation methods:*

These algorithms can be formally subsumed under W-methods, but do not require any algebraic conditions for coefficients. They, too, realize a certain freedom of choice of the Jacobian approximation.

Specification of the integrator LIMEX

In view of the challenging differential-algebraic problem class (3.8), the popular integrator LIMEX is selected here, based on a linearly implicit Euler method with adaptive time step and order control. The corresponding discretization has been worked out in detail in /DEU 87/ and /DEU 02/. In the numerical experiments below, the notation $\text{LIMEX}_{q_{\max}}$ is used to indicate the maximum permitted number q_{\max} of columns in the extrapolation table. Throughout the paper, the error tolerance for time integration has been set to $TOL = 0.001$. All of the LIMEX variants feature the usual sub-diagonal error criterion (see /DEU 02/). In order to estimate the error of the variable $u(t) = (\omega, p)^T(t)$, the scaled norm

$$\| |(\omega, p) | \|^2 := \left\| \frac{\kappa}{\mu_0} \nabla p(t) \right\|_{\rho}^2 + \left\| \vec{k} \omega(t) \right\|_{\rho}^2, \quad (3.11)$$

is used, where $\| \vec{v} \|_{\rho}^2 := \int_{\Omega} \rho^* \vec{v}^2$ measures the kinetic energy of a velocity field \vec{v} w.r.t a reference density ρ^* . The scaling in the second term is provided by the filter velocity

$$\vec{k}(x) := \frac{\kappa(x)}{\mu_0} \alpha \vec{g}, \quad (3.12)$$

where $\alpha \approx \frac{\partial \rho}{\partial \omega}$. This choice can be motivated by the Darcy velocity (3.3): For the linear density (3.6) and constant viscosity (3.7) one readily verifies

$$\| \vec{q}_1 - \vec{q}_2 \|_{\rho} \leq \sqrt{2} \max \left(1, \frac{\rho_1 - \rho_0}{\alpha \omega_{\max}} \right) \| | \omega_1 - \omega_2, p_1 - p_2 | \| . \quad (3.13)$$

Thus convergence w.r.t. $\| | \cdot \|$ directly induces convergence of the Darcy velocity.

Order reduction

As theoretically analyzed by Lubich/Ostermann /LUB 95/, LIMEX as a W -method will exhibit an order reduction to an “effective” order $p^* = 2$, as soon as the quasi-stationary solution has been reached, for more details see also Section 9.3.1 in the textbook /DEU 12/. It is not that easy to algorithmically identify the neighborhood of the quasi-stationary solution in a nonlinear PDE system. In view of this feature, the following heuristic strategy has been implemented: As soon as the suggested order q has been successfully reduced for consecutive two (or three) time steps to $q = 2$, the future order is fixed to $q = p^* = 2$. For step size selection

$$\tau_{\text{new}} = \sqrt[q+1]{\rho \frac{\text{TOL}}{[[\epsilon]]}} \tau_{\text{old}}$$

Is used, where $\rho = 0.25$ is a safety factor, TOL is a user-provided tolerance, and $[[\epsilon]]$ is the estimate for the relative error w. r. t. (3.11). Note that this is a classic proportional controller. Experiments with controllers considering a longer time history (see, e. g., /GUS 88/, /LAN 01/) turned out to be less successful in the tests.

3.1.1.2 Computation of full and reduced Jacobian

For the DAE system (3.8) Deuffhard/Nowak /DEU 87/suggest the following step:

$$(M_k - \tau J_0)(u_{k+1} - u_k) = \tau f(u_k) \quad (3.14)$$

where $M_k = M(u_k)$ and $J_0 = J(u_0)$ according to (3.9).

In the PDE context, the Jacobian J_0 will be most easily computed via solving the linearized perturbation equations. Upon inserting

$$(\omega, p)^T := (\omega_0, p_0)^T + (\delta\omega, \delta p)^T$$

and considering the linearization of equations (3.1), (3.2), a system for the increment $(\delta\omega, \delta p)^T$ is obtained that reads

$$\begin{aligned} & \frac{\partial}{\partial t} ((\rho_0 + \omega_0 \rho_{0,r}) \delta \omega) + \nabla \cdot \left[(\rho_0 \vec{q}_0) \delta \omega + \omega_0 \left\{ \frac{\partial}{\partial \omega} (\rho \vec{q}) \delta \omega + \frac{\partial}{\partial p} (\rho \vec{q}) \delta p \right\} \right. \\ & \quad \left. - (\rho_0 \mathbb{D}_0) \nabla \delta \omega - \left\{ \frac{\partial}{\partial \omega} (\rho \mathbb{D}) \delta \omega + \frac{\partial}{\partial p} (\rho \mathbb{D}) \delta p \right\} \nabla \omega_0 \right] \end{aligned} \quad (3.15)$$

$$\begin{aligned} & = (\rho_0 + \omega_0 \rho_{0,r}) Q \delta \frac{\partial}{\partial t} (\rho_0 \delta \omega) + \nabla \cdot \left[\frac{\partial}{\partial \omega} (\rho \vec{q}) \delta \omega + \frac{\partial}{\partial p} (\rho \vec{q}) \delta p \right] \\ & = (\rho' Q) \delta \omega \end{aligned} \quad (3.16)$$

The system decouples in the variables ω and p whenever

$$\omega_0 \frac{\partial}{\partial p} (\rho \vec{q}) \delta p = \omega_0 \rho_0 \frac{\partial \vec{q}}{\partial p} \delta p = 0$$

and

$$\frac{\partial}{\partial p} (\rho \mathbb{D}) \delta p \nabla \omega_0 = \rho_0 \frac{\partial \mathbb{D}(\vec{q})}{\partial \vec{q}} \frac{\partial \vec{q}}{\partial p} \delta p \nabla \omega_0 = 0.$$

Analogously, one can expect a block decoupling in the arising matrix after discretization, which will be beneficial for the linear solver. For a W -method like LIMEX, this can be achieved by using an inexact Jacobian $J_{reduced}$. $J_{reduced}$ is constructed as follows: While assembling (3.15), it is assumed that

$$\frac{\partial \vec{q}}{\partial p} = 0 \text{ and } \frac{\partial \vec{q}}{\partial \omega} = 0. \quad (3.17)$$

Note that, formally, the previous condition would be sufficient for the decoupling. However (3.17) proved to be more stable experimentally. In the remainder, a superscript indicates, how the Jacobian is approximated. LIMEX^{full} refers to an exact Jacobian, whereas LIMEX^{reduced} refers to an inexact Jacobian.

3.1.2 Numerical experiments

In this section, comparative numerical results are presented, obtained with the algorithms IMPEX and LIMEX. First three problems with homogeneous permeability

coefficients are considered, i. e. diffusion from a salt dome in 2D, as well as the Elder benchmark /VOS 87/ in slightly modified form, and the saltpool benchmark /OSW 04/ /JOH 02/ in 3D. The underlying geometry is given by rectangular quadrilateral and hexahedral grids respectively. These basic tests, which are documented in Subsections 3.1.2.1-3.1.2.3, were performed on a single cluster node of Intel Xeon Prozessor E5-2660 v2 @ 2200 MHz. As a final step, a complicated field test is considered with variable permeability on unstructured grids in 2D. The simulations were performed on the Hazel Hen supercomputer. For all problems, reasonable combinations of $q \leq q_{max}$ are explored. Consistent velocity approximation has been used in all experiments.

3.1.2.1 Diffusion from salt dome (2D)

For this problem, the domain is given by $\Omega_2 := (0,600) \times (0,150) \subset \mathbb{R}^2$. The Dirichlet condition $\omega(\vec{x}) = 1$ for $\vec{x} \in \Gamma_D^{BOT}$ is exploited on the part of the bottom boundary given by

$$\Gamma_{D,2}^{BOT} := \{(x_1, x_2) \in \partial\Omega: 150 \leq x_1 \leq 450, x_2 = 0\}.$$

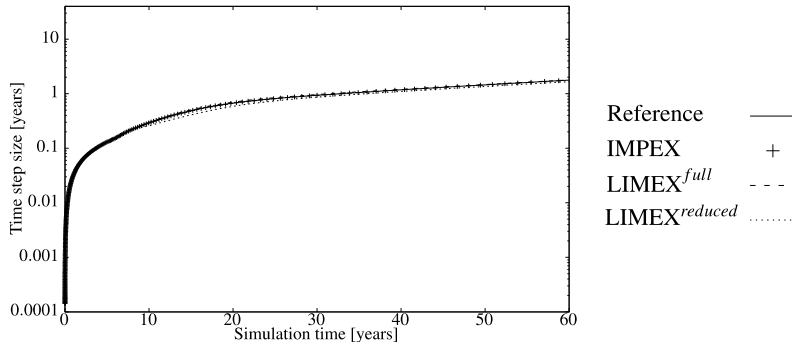
The initial condition is $\omega = 0$. For this setup, time-stepping strategies and two different preconditioners are compared. The geometry is given by $128 \times 512 = 65,536$ square elements, corresponding to 132,354 degrees of freedom.

SuperLU preconditioner

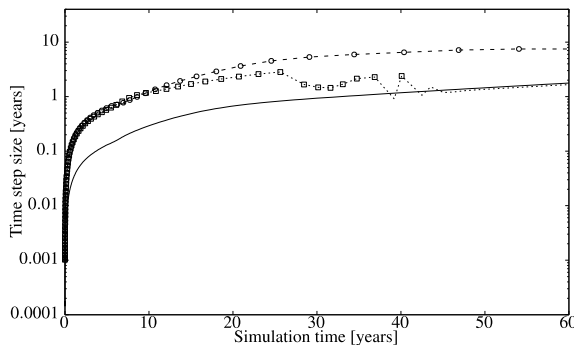
The time stepping history is provided in Fig. 3.1: The methods IMPEX, LIMEX₂^{full} and LIMEX₂^{reduced} suggest similar time step sizes (Fig. 3.1) and thus require almost identical number of time steps (Tab. 3.1). As can be expected, the SuperLU preconditioner is always convergent. Since LIMEX avoids an additional linearization loop, its computational effort is reduced. The factor is slightly larger than the factor ≈ 0.5 that can be deduced from the number of iteration calls. This is due to additional assembly calls for the Jacobian. LIMEX₃^{full} and LIMEX₄^{full} are efficient over the whole time interval, which may be an indicator for the high regularity of the regularity of the problem. The algorithms with reduced Jacobian perform slightly worse: LIMEX₃^{reduced} takes slightly smaller time steps than LIMEX₃^{full}. Similarly, LIMEX₄^{reduced} is almost on par with LIMEX₄^{full} initially. However, within a few time steps after $t = 10a$, the order first degradates to $q = 3$, and then to $q = 2$, even before the asymptotic order reduction phase (cf. Fig. 3.1c).

Multigrid preconditioner

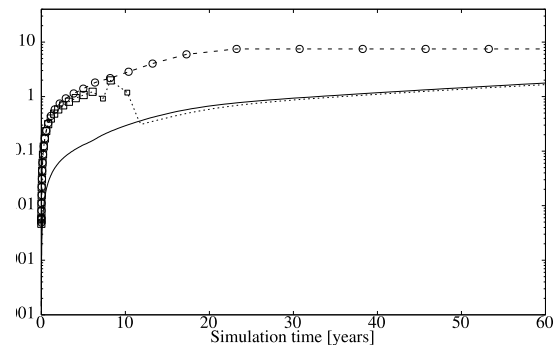
Employing multigrid yields almost identical results (Fig. 3.2). Only in two instances for LIMEX_4^{full} , the multigrid solver does not converge. Note that even for this small number of degrees of freedom, the multigrid solver is 3-4 times faster than SuperLU w. r. t. wall clock timing in the experiments.



(a) $q_{max} = 2$



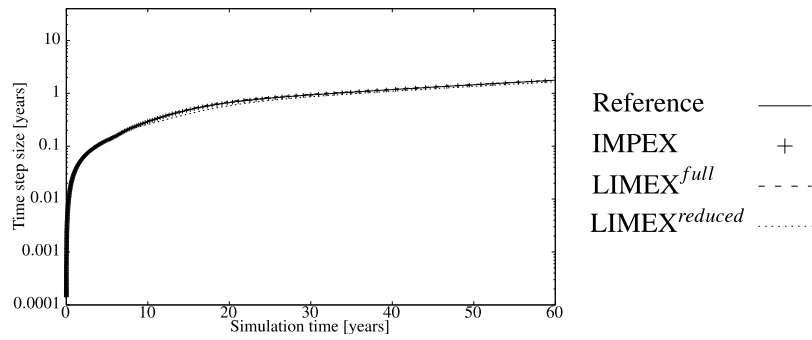
(b) $q_{max} = 3$



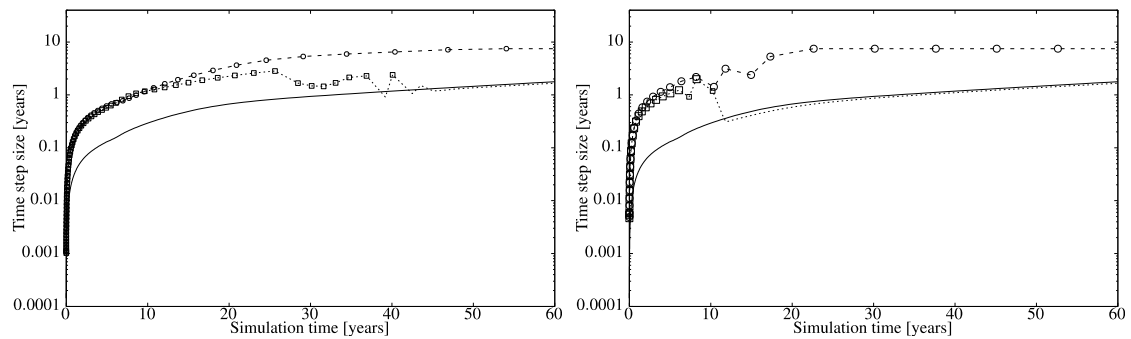
(c) $q_{max} = 4$

Fig. 3.1 Diffusion from salt dome (2D) with SuperLU preconditioner:

Time step size [yrs] vs. simulated time [yrs] for IMPEX, $\text{LIMEX}_{q_{max}}^{full}$, and $\text{LIMEX}_{q_{max}}^{reduced}$. The reference line is a continuous representation of IMPEX. It is identical in all figures to provide a guide to the eye. For LIMEX, the dashed lines represent steps with order $q = 2$, whereas symbols with different sizes indicate steps with order $2 < q \leq q_{max}$.



(a) $q_{max} = 2$



(b) $q_{max} = 3$

(c) $q_{max} = 4$

Fig. 3.2 Diffusion from salt dome (2D) with multigrid preconditioner:

Time step size [yrs] vs. simulated time [yrs] for IMPEX, $\text{LIMEX}_{q_{max}}^{full}$, and $\text{LIMEX}_{q_{max}}^{reduced}$. The reference line is a continuous representation of IMPEX. It is identical in all figures to provide a guide to the eye. For LIMEX, the dashed lines represent steps with order $q = 2$, whereas symbols with different sizes indicate steps with order $2 < q \leq q_{max}$

Tab. 3.1 Diffusion from salt dome (2D):

Iteration counts (for time stepping and linear solver), and CPU wall clock time when using (a) SuperLU or (b) Multigrid as a preconditioner.

(a) SuperLU

Method	Time steps				Linear solver		Timing	
	q=2	q=3	q=4	reject	success	fail	CPU [s]	Effort
IMPEX	322	—	—	2	2094	0	18977,11	1
LIMEX ₂ ^{full}	311	—	—	2	941	0	8798,4	0,46
LIMEX ₃ ^{full}	0	68	—	4	434	0	4009,62	0,21
LIMEX ₄ ^{full}	0	0	33	5	382	0	3500,73	0,18
LIMEX ₂ ^{reduced}	320	—	—	2	968	0	9275,06	0,49
LIMEX ₃ ^{reduced}	22	70	—	10	548	0	5003,89	0,26
LIMEX ₄ ^{reduced}	68	2	24	7	528	0	4888,33	0,26

(b) Multigrid

Method	Time steps				Linear solver		Timing	
	q=2	q=3	q=4	reject	success	fail	CPU [s]	Effort
IMPEX	322	—	—	2	2094	0	4937,6	1
LIMEX ₂ ^{full}	311	—	—	2	941	0	2657,97	0,54
LIMEX ₃ ^{full}	0	68	—	4	434	0	1138,44	0,23
LIMEX ₄ ^{full}	0	0	34	7	392	2	1020,37	0,21
LIMEX ₂ ^{reduced}	320	—	—	2	968	0	2649,58	0,54
LIMEX ₃ ^{reduced}	5	80	—	8	545	0	1416,93	0,29
LIMEX ₄ ^{reduced}	55	3	27	5	505	0	1323,16	0,27

3.1.2.2 Modified Elder (3D)

The next test is a variation of the Elder problem /VOS 87/ in the three-dimensional domain $\Omega_3 := (0,600) \times (0,600) \times (0,150) \subset \mathbb{R}^3$. The transient solution is sensitive w. r. t. the grid and discretisation (see, e. g., /JOH 03/). Following Schwarz /SCH 99/ modified

boundary and initial conditions are used: Dirichlet boundary conditions are provided on the upper part

$$\Gamma_D^{TOP} = \{(x_1, x_2, x_3)^T \in \partial\Omega \mid 150 \leq x_1, x_2 \leq 450, x_3 = 0\}$$

with values given by $\omega(x_1, x_2, x_3) := \omega_0 \phi(x_1) \phi(x_2)$ where

$$\phi(x) := \frac{9}{10} + \frac{1}{10} \cos\left(5\pi \frac{x - 300}{150}\right).$$

For the initial value $\omega \equiv 0$, this provides an array of initially 25 fingers that collapses rapidly. Due to this convection induced fingering the problem is more challenging than the previous problem. This will be observed in the convergence of the linear solver. The geometry is given by $64 \times 64 \times 16 = 65,536$ cubic elements, corresponding to 143,650 degrees of freedom.

SuperLU preconditioner

The time stepping history shown in Fig. 3.3 illustrates a very smooth behavior for LIMEX^{full}. An order reduction is only observed in the very last steps of the highest order method LIMEX₄^{full}. This is also reflected by Tab. 3.2a. As in the previous results, LIMEX^{reduced} selects smaller time steps and the order reduction is activated earlier. In this sense, the results are similar to those from the previous section in Fig. 3.1. Note that the SuperLU preconditioner did not obtain a solution for IMPEX within 30 days. Hence, the computation was interrupted at this point. In all plots, LIMEX₂^{full} is used as a reference to provide a guide to the eye.

Multigrid preconditioner

When switching to the multigrid preconditioner, the methods using an exact Jacobian (IMPEX and LIMEX^{reduced}) suffer from a severe drawback. As is illustrated in Fig. 3.4 and Tab. 3.2b both methods are now limited by lack of convergence convergence of the iterative method, which leads to reduction time step. Although LIMEX^{reduced} tends to select smaller time steps, it essentially revocers the results obtained with the SuperLU solver. As a consequence, the method provides greater robustness in particular towards the end of the simulation.

With respect to the total timings in Tab. 3.2b, the LIMEX-variants outperform IMPEX and are essentially on par with each other. Considering the asymptotic behavior, however, LIMEX *reduced* should be preferred.

Tab. 3.2 Modified Elder (3D):

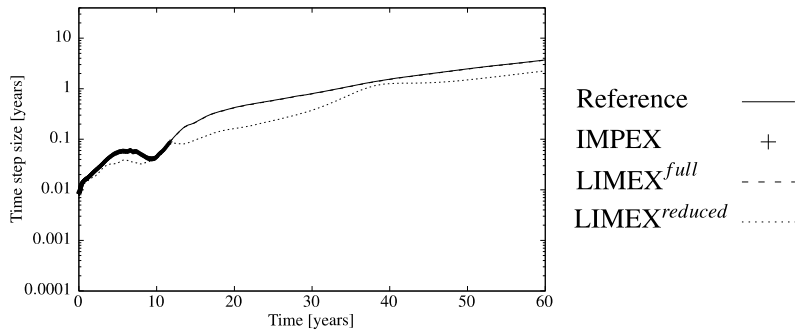
Iteration counts (for time stepping and linear solver), and CPU time when using (a) SuperLU, or (b) Multigrid as preconditioner for the linear problems.

(a) SuperLU

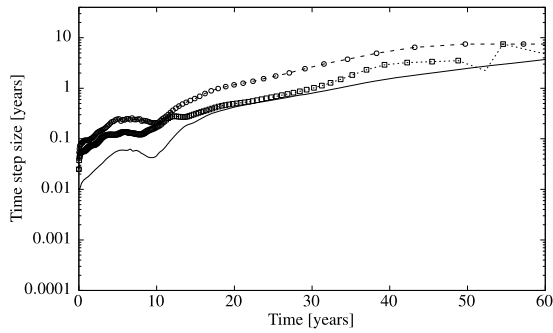
Method	Time steps				Linear solver		Timing
	q=2	q=3	q=4	reject	success	fail	CPU [s]
IMPEX	(Aborted after 1 month.)						
LIMEX $\frac{full}{2}$	408	—	—	1	1230	0	1508625,38
LIMEX $\frac{full}{3}$	0	98	0	0	591	0	732320,94
LIMEX $\frac{full}{4}$	0	3	50	3	551	2	680860,07
LIMEX $\frac{reduced}{2}$	578	0	0	1	1742	0	2164447,66
LIMEX $\frac{reduced}{3}$	3	159	0	0	968	0	1212680,52
LIMEX $\frac{reduced}{4}$	35	2	63	4	785	0	981973,82

(a) Multigrid

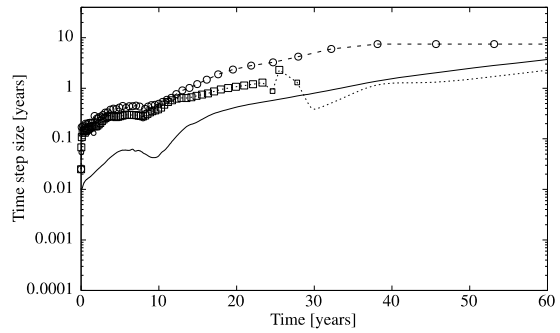
Method	Time steps				Linear solver		Timing	
	q=2	q=3	q=4	reject	success	fail	CPU [s]	Effort
IMPEX	461	—	—	37	3075	36	21228,19	1
LIMEX $\frac{full}{2}$	455	—	—	130	1371	129	13564,55	0,64
LIMEX $\frac{full}{3}$	75	90	—	131	768	131	7984,37	0,38
LIMEX $\frac{full}{4}$	81	7	40	136	708	134	7510,61	0,35
LIMEX $\frac{reduced}{2}$	578	—	—	1	1742	0	14375,54	0,68
LIMEX $\frac{reduced}{3}$	3	159	—	0	968	0	7464,05	0,35
LIMEX $\frac{reduced}{4}$	35	2	63	4	785	0	6115,75	0,29



(a) $q_{max} = 2$



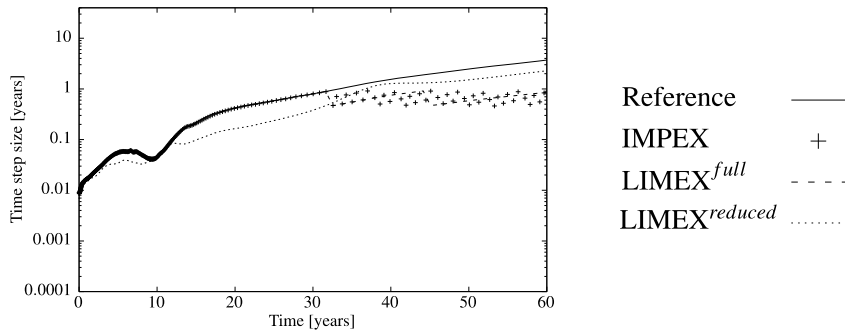
(b) $q_{max} = 3$



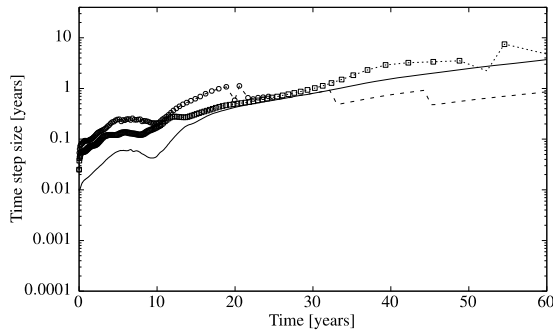
(c) $q_{max} = 4$

Fig. 3.3 Modified Elder (3D) with SuperLU:

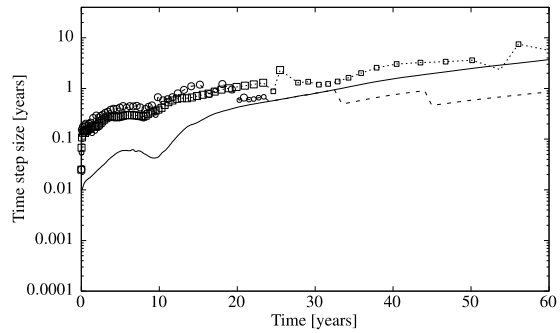
Time step size [yrs] vs. simulated time [yrs] for IMPEX, $LIMEX_{q_{max}}^{full}$, and $LIMEX_{q_{max}}^{reduced}$. The reference line is a continuous representation of $LIMEX_2^{full}$. It is identical in all figures to provide a guide to the eye. For LIMEX, the dashed lines represent steps with order $q = 2$, whereas symbols with different sizes indicate steps with order $2 < q \leq q_{max}$.



(a) $q_{max} = 2$



(b) $q_{max} = 3$



(c) $q_{max} = 4$

Fig. 3.4 Modified Elder (3D) with multi-grid:

Time step size [yrs] vs. simulated time [yrs] for IMPEX, $LIMEX_{q_{max}}^{full}$, and $LIMEX_{q_{max}}^{reduced}$. The reference line is a continuous representation of $LIMEX_2^{full}$. It is identical in all figures to provide a guide to the eye. For LIMEX, the dashed lines represent steps with order $q = 2$, whereas symbols with different sizes indicate steps with order $2 < q \leq q_{max}$.

3.1.2.3 Saltpool Problem (3D)

The saltpool problem, suggested by Oswald and Kinzelbach /OSW 04/ is an experimental benchmark for an upcoming process. In this laboratory scale experiment, a cubic box containing homogeneously shaped and distributed glass beads is filled with water. A stable brine layer with a given salt mass fraction is placed at the bottom. By injecting fresh water in one corner and simultaneously extracting fluid in the opposite corner, an upconing of the brine is induced. Injection and extraction occur with a controlled rate and the breakthrough curves, i. e., the salinity of the extracted brine at the outlet, were monitored.

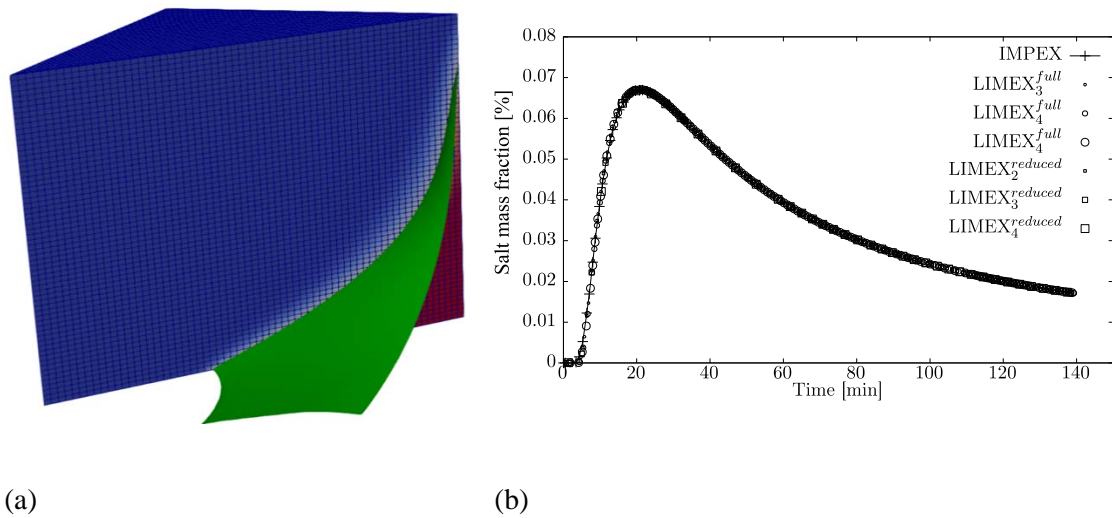


Fig. 3.5 Saltpool problem (3D): Simulated results for (a) the solution at the end of experiment; (b) breakthrough curve at outlet (for all simulations).

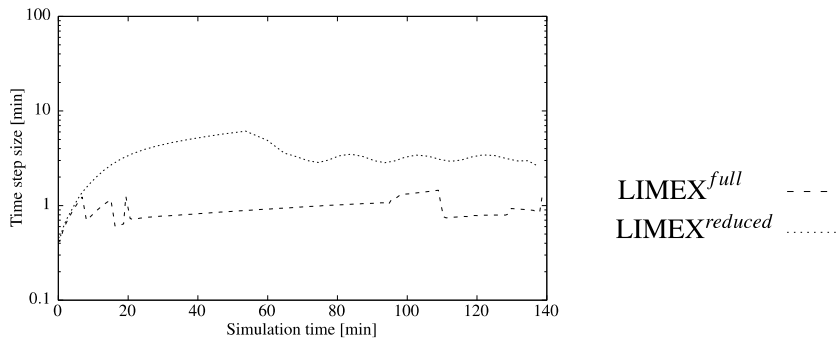
This problem imposes a challenge to time integration, as identified by Johannsen and coworkers /JOH 02/. In this work is focussed in particular on the low concentration case with only 1% salt mass fraction in the brine. In this case, the salinity at the outlet first rises rapidly to a peak 20min, before the system relaxes towards the end of the experiment. Of course, these dynamics must be captured correctly. Fig. 3.5 shows the salt distribution at the end of the experiments as well as the breakthrough curves computed by all methods.

Treatment of the dispersive terms

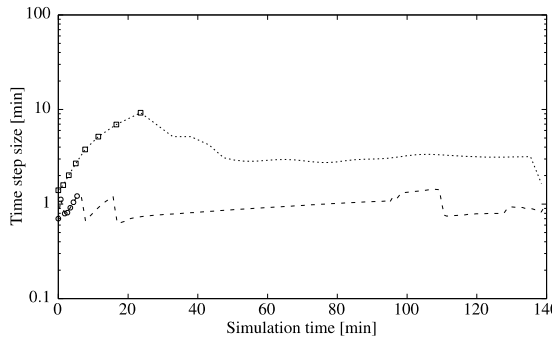
Unfortunately, the dispersion (3.4) leads to undesired properties of the discrete linear systems. As a consequence LIMEX^{full} is inefficient, as the multi-grid method is not converging properly with the consequence that time steps must be reduced. The same holds for LIMEX^{reduced}, when only the derivatives w. r. t. convection are neglected. However, disabling derivatives w. r. t. dispersion as well mitigates this problem.

Iteration statistics and time-stepping history for a uniform refinement with 2,097,152 hexahedral fine grid elements (4,293,378 degrees of freedom) are shown in Tab. 3.3 and Fig. 3.6, respectively. Timings are for a parallel multigrid solver executed on 20 cores. Due to the problem size, the problem could not be solved by SuperLU. The IMPEX scheme failed after 38 steps (corresponding to 30 min simulated), with a time step contracting to zero. For LIMEX^{full}, the time step is restricted by the linear solver.

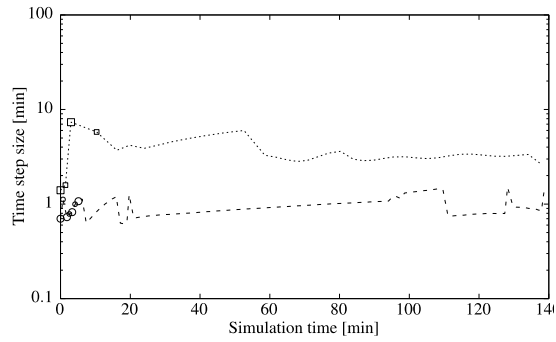
LIMEX *reduced* permits larger time steps. In all cases the number of stages is rapidly reduced to $q = 2$, however.



(a) $q_{max} = 2$



(b) $q_{max} = 3$



(c) $q_{max} = 4$

Fig. 3.6 Saltpool problem (3D) with multi-grid:

Time step size [yrs] vs. simulated time [yrs] for LIMEX $_{q_{max}}^{full}$ and LIMEX $_{q_{max}}^{reduced}$. IMPEX failed for non-obvious reasons. The dashed lines represent steps with order $q = 2$, whereas symbols with different sizes indicate steps with order $2 < q \leq q_{max}$.

Tab. 3.3 Saltpool problem (3D) with multigrid: Iteration counts (for time stepping and linear solver), and CPU time.

Method	Time steps				Linear solver		Timing
	q=2	q=3	q=4	reject	success	fail	CPU [s]
IMPEX	(Failed after 38 steps.)						
LIMEX ₂ ^{full}	157	0	0	318	478	316	39135,5
LIMEX ₃ ^{full}	148	97	0	323	487	323	39924,5
LIMEX ₄ ^{full}	146	3	4	320	497	320	39877,0
LIMEX ₂ ^{reduced}	49	0	0	5	163	0	3674,7
LIMEX ₃ ^{reduced}	34	8	0	7	181	0	4028,6
LIMEX ₄ ^{reduced}	35	3	2	7	169	0	3757,5

3.1.2.4 Gorleben problem (2D)

The last problem is taken from a field test first suggested in /KEE 05/. The task is to compute the ground water flow over a saltdome in the North German Plain, close to the village of Gorleben. The computational domain is a 2D cross section from geological data taken in north-south direction. It is given by an elongated strip with physical dimensions 16,370 in horizontal direction and 395 in vertical direction. The domain including the coarse grid triangulation is shown in Fig. 3.7. Mesh statistics are provided in Tab. 3.4.

Tab. 3.4 Gorleben problem (2D): Mesh statistics after uniform refinement.

Refinement level	# Elements	# Degrees of freedom
Base	4,924	8,506
3	315,136	498,954
4	1, 260,544	1,982,866
5	5,042,176	7,905,570

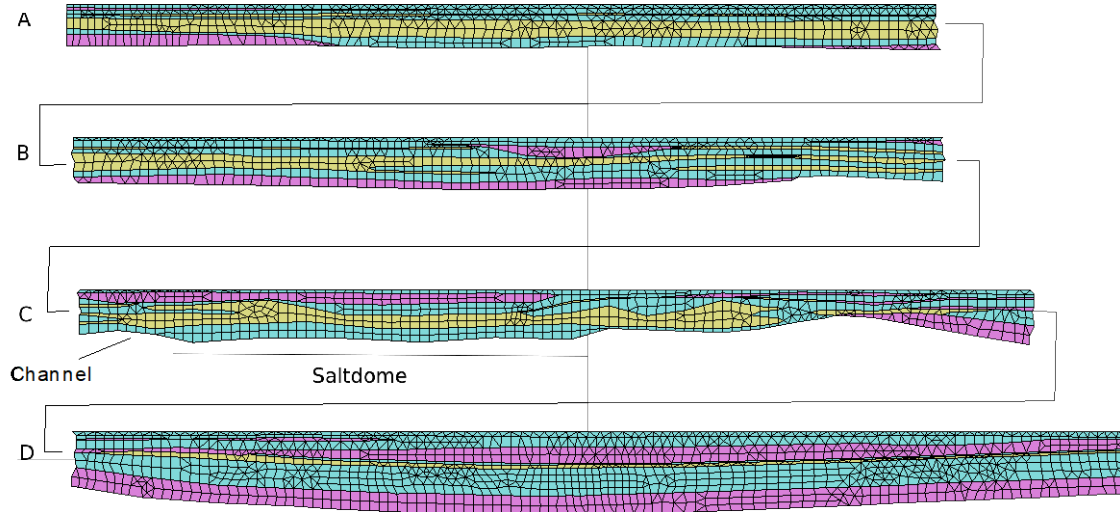


Fig. 3.7 Gorleben problem (2D):

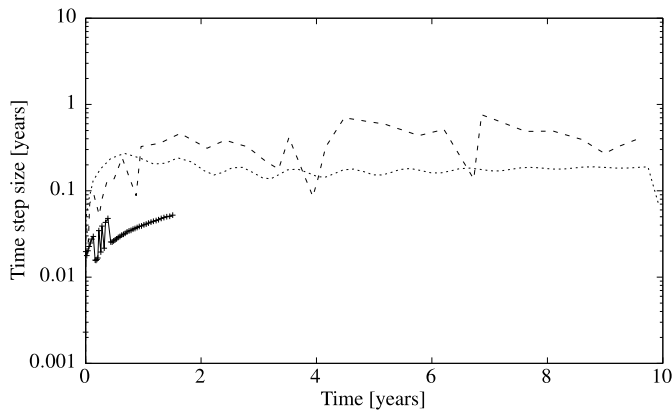
Permeability distribution in the computational domain indicated by colors (cyan : high permeability; magenta : medium permeability; yellow : low permeability). For the ease of presentation, the domain is presented broken into sections A (horizontal extension: 0 – 4.4) B (4.4 – 9.3), C (9.3 – 14.3), and D (14.3 – 19.8). The salt dome is located under Section C as indicated.

For the sake of simplification, the illustration is broken into four sections shown from top to bottom, that can be aligned from left to right. The shading of the elements indicates zones with three different permeabilities (cyan : high permeability, $\kappa = 10^{-12}$; magenta : medium permeability, $\kappa = 10^{-14}$; yellow : low permeability, $\kappa = 10^{-16}$). The salt dome is in contact with the domain in the middle of section C. In this region, a constant mass fraction $\omega = \omega_{max} = 0.26$ is assumed as a boundary condition. The boundary conditions on the upper part of the domain are given by the fresh water condition $\omega = 0$. Moreover, the pressure is given as a piecewise linear function derived from experiments. It starts from 173 on the southernmost tip (left) and decreases to 100 in the northernmost tip (right). The *linear density function* (5) is used (with $\rho_0 = 998.2^3$, $\rho_1 = 1197.2^3$ and $\omega_{max} = 0.26$), and the *real viscosity model* (7) (with $\mu_0 = \times 10^{-3} \text{ }^{-1}$). Diffusion and dispersion are characterized by porosity $\phi = 0.2$, molecular diffusion $D_m = 10^{-9}$, dispersion lengths $\alpha_L = 10$, and $\alpha_T = 1$. Initially, no salt is present in the domain ($\omega = 0$).

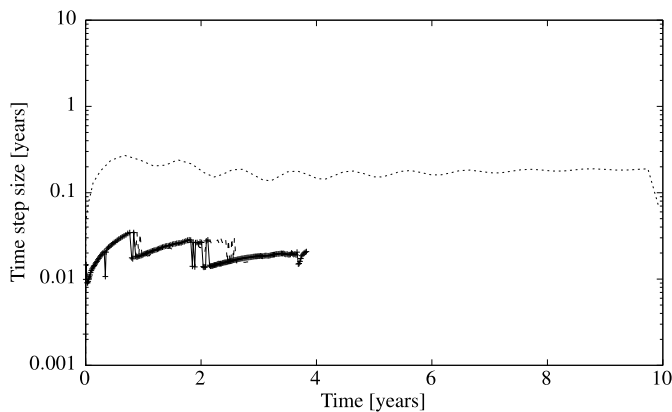
The scientific interest for the problem is in particular the long term evolution. Based on the experience from the previous tests, in particular from the salt pool benchmark, the number of stages shall be limited to $q_{max} = 2$. This is consistent with the low regularity, e. g., since $\mathbb{D}(\vec{q})$ is not differentiable at $\vec{q} = 0$, and jumping permeability coefficients.

Performance of the different solvers

As a preliminary step, solver performance is investigated in the small time interval of the first 10 years only on the rather coarse mesh at refinement level 3. The linear system for the corresponding 498,954 degrees of freedom is still small enough for the (serial) SuperLU solver. Results are provided in Fig. 3.8 and Tab. 3.5. After 12 of wall clock time unfinished jobs were terminated by the scheduler.



(a) SuperLU



(b) Multi-grid

Fig. 3.8 Gorleben problem (2D) – initial phase:

Time stepping history for the first 10 years with both preconditioners. Due to the interest in long term behavior, results are provided for $q_{max} = 2$ stages only. Wall clock time was restricted to 12. IMPEX (both preconditioners) and LIMEX^{full} (with multi-grid) did not finish within this limit. For these instances, data is provided until termination.

Tab. 3.5 Gorleben problem (2D) – initial phase:

Iteration counts (for time stepping and linear solver), and CPU time when using (a) SuperLU, or (b) Multigrid as preconditioner for the linear problems.

(a) SuperLU

Method	Time steps				Linear solver		Timing
	q=2	q=3	q=4	reject	success	fail	CPU [s]
IMPEX	(Did not terminate within 12h)						
LIMEX ₂ ^{full}	36	0	0	3	122	0	2447.12
LIMEX ₂ ^{reduced}	60	0	0	0	185	0	3766,7

(b) Multigrid

Method	Time steps				Linear solver		Timing
	q=2	q=3	q=4	reject	success	fail	CPU [s]
IMPEX	(Did not terminate within 12h)						
LIMEX ₂ ^{full}	(Did not terminate within 12h)						
LIMEX ₂ ^{reduced}	60	0	0	0	185	0	2250,1

For this problem, IMPEX showed unexpected behavior, since the the method did not succeed to compute the solution at $t = 10$ within the wall-clock time limit of twelve hours. For large time steps, only linear convergence of the Newton method was observed, and the desired tolerance was not achieved within the prescribed maximum number of $n = 10$ iterations. As a result, the time step had to be recomputed with bisected step size. At the end, the computational cost for this strategy turned out to be too high.

LIMEX^{full} successfully computed a solution using the SuperLU preconditioner. However, when switching to multigrid, linear solver turned out to be the limiting factor. Again, this could be avoided using LIMEX^{reduced}, which generated identical time stepping histories independent of the preconditioner. In passing note that even for this small problem size, using multigrid resulted in smaller wall clock times.

Computational results

Results computed with $\text{LIMEX}_2^{\text{reduced}}$ over 10.000 years are shown in Fig. 3.9 and Fig. 3.10. The illustration is centered around region 3 above the salt dome. The grid has been obtained by 4 uniform refined steps, which is accurate enough for this purposes. The brine distribution far away from the salt dome is almost independent of the grid size h (data not shown). The pressure distribution at the top surface induces a flow from left to right, which is observed in the highly conductive layers close to the surface. The solution was obtained within ≈ 12 wall clock time on HazelHen using 192 cores in 9885 time steps (and corresponding 29656 calls of a parallel multgrid solver).

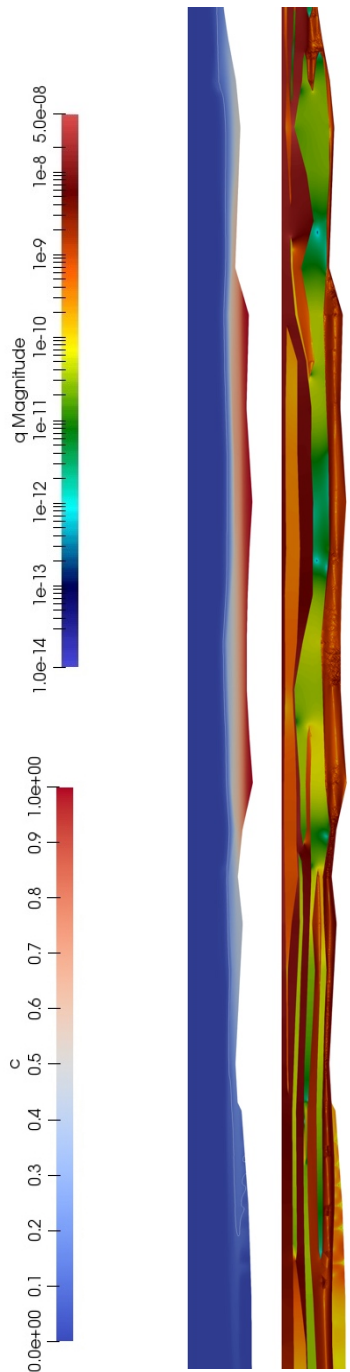
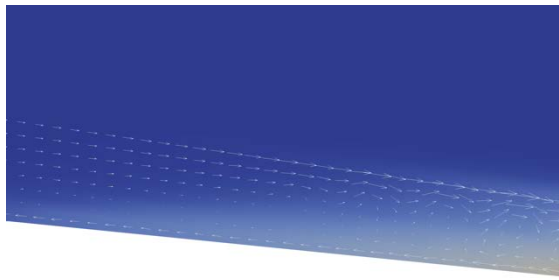
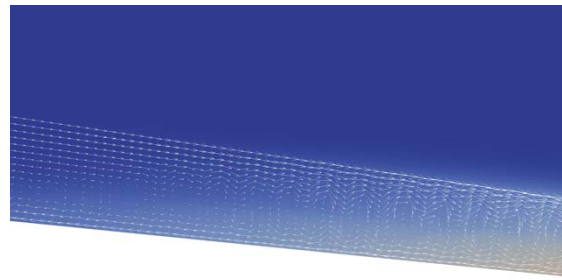


Fig. 3.9 Gorleben problem (2D):

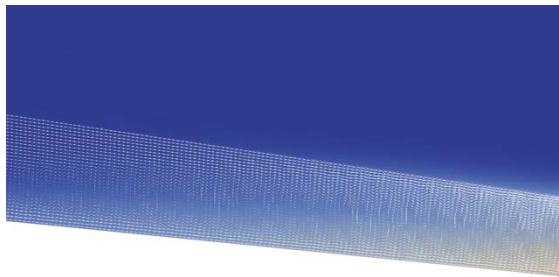
Results at $t = 10,000$ years. Top: Salt mass distribution. The white line indicates the isoline for $\omega = 0.1$. Bottom: Magnitude of \vec{q} . All results are at refinement level 4.



(a) Refinement level 3



(b) Refinement level 4



(c) Refinement level 5

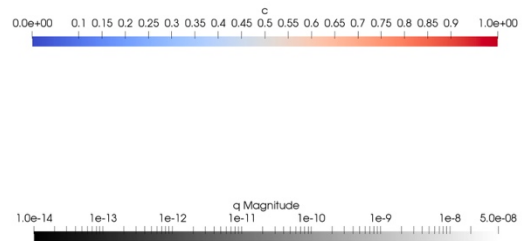


Fig. 3.10 Gorleben problem:

Magnification of the bidirectional flow pattern in the channel region in section 3 left of the salt dome ($t \approx 1,000$ years; refinement levels 3-5): Brine with high density is removed from the salt dome on the bottom, whereas fluid with lower density is transported towards the salt dome in the upper region of the channel. This gives rise to convective cells. Their size depends on the mesh size.

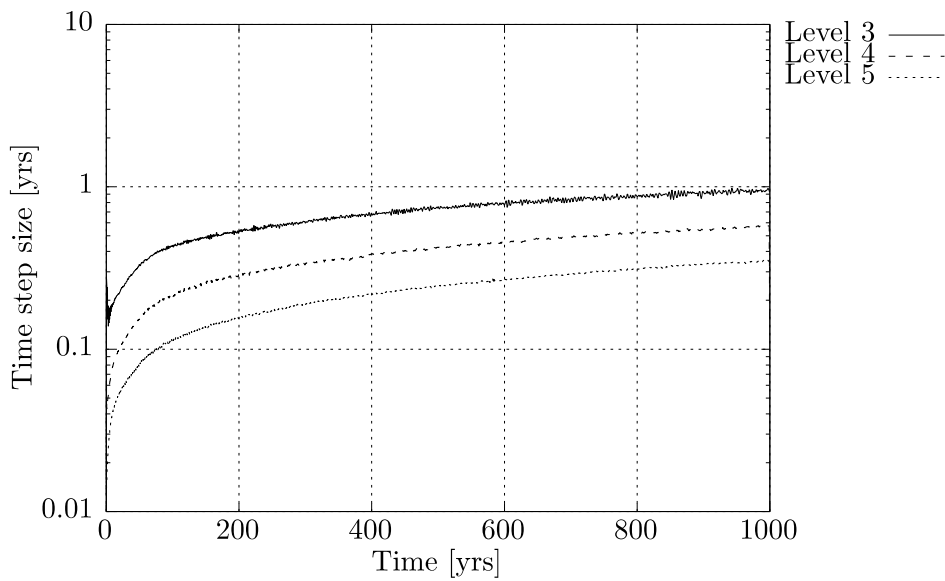


Fig. 3.11 Gorleben problem (2D): Time step size [yrs] vs. time [yrs] for LIMEX₂^{reduced} (omitting derivatives w. r. t. convection and diffusion).

Mesh size dependent time stepping

In the deeper strata in proximity of the salt dome a bidirectional flow pattern is observed: In the upper region of these strata, fresh water flows towards the salt dome, while brine is transported away from the salt dome at the bottom of the strata. Both regions are well separated by a region of small velocity, giving rise to transient convective cells. This depends on the mesh size h is visualized in Fig. 30 for $t = 1,000$ years in a magnified region at the southern (left) end of the aquifer above the salt dome. The mesh size dependence is also reflected in the corresponding LIMEX time stepping history in Fig. 3.11.

3.1.3 Conclusion

For density-driven flow problems LIMEX -methods have been demonstrated as an attractive and efficient alternative to standard time-stepping strategy. To that end, two versions were devised, differing in the approximation of the Jacobian:

In principle, the basic version LIMEX^{full} with an exact Jacobian is the method of choice. It is the most efficient method w. r. t. time stepping. In some cases, however, convergence of the linear multi-grid solver may be poor, and thus total efficiency is deteriorating.

When this happens, the version LIMEX *reduced* may be an attractive alternative. This is constructed based on an inexact Jacobian. As demonstrated theoretically, neglecting certain terms of the Jacobian, leads to a linear system, where the variables ω and p decouple. This can be achieved by treating the partial derivatives of Darcy velocity \vec{q} in the transport equation explicitly. Even though the time steps turn out to be smaller than with LIMEX *full*, it was demonstrated that convergence problems of the linear solver can be avoided. With LIMEX *reduced*, the field test for the *Gorleben* problem could be solved robustly.

3.2 Robust smoothers for the geometric multigrid solver

Multigrid methods are fast solvers of optimal complexity, however, like sensible race horses, they require certain prerequisites. This is in particular the adequate resolution of the relevant scales. If, e. g., with highly anisotropic problems the anisotropy is not resolved by the grid, multigrid convergence will slow down a lot. Analogous problems exist with dominating convection and strong heterogeneities. There are workarounds for all these cases, however, they have to be used adequately, which is not easy in practice.

With anisotropic coefficients, asymptotically only resolving the scales will help. Often anisotropies are due to the geometry or the grid /HEI 95/, /HEI 96/. This is a particular problem on coarse grids, which can not resolve the scales by construction. Thus, special tools are necessary to handle this situation.

To that end robust multigrid methods are needed. Robustness refers to convergence behaviour, which is independent of critical model parameters, such as anisotropy, convection and heterogeneity. To that end, special components must be used in the algorithm.

One such tool is robust smoothing. The smoother is an essential part of a multigrid algorithm. It is designed to reduce the error of the high-frequency components and project it to a lower dimensional space. In case of singularly perturbed problem, i. e., e. g., anisotropies or convection, it is possible to devise smoothers which are exact in the limit case for model problems /WIT 89/, /BEY 95/, /BEY 97/. In some cases, e. g. for dominating convection, this can be transferred to the general case as explained below.

Applied are the smoothers, ILU_β for anisotropic diffusion and downwind numbering ILU for partially convection dominated problems mainly within a collective relaxation framework and optimised the parameters. It became soon clear that the smoother alone is not capable of solving the robustness problem, however, it proved to be a valuable component of an overall robustness strategy.

3.3 Improvement of the coarse-grid correction

The other approach to achieve robustness is to improve the coarse-grid correction. Multi-grid methods combine two algorithms, smoother and coarse-grid correction. If the smoother can not cover all the high-frequency error components, it is possible to apply coarse-grid corrections, catching the part not covered by the smoother. This is done by so-called semi-coarsening. Semi-coarsening works with an increased number of unknowns on the coarse grid, but it must still satisfy geometric reduction of the number of unknowns. For an anisotropic problem, semi coarsening means coarsening only the non-anisotropic directions. This is easy for model problems, however, not so easily accomplished for unstructured grids or highly varying coefficients. This was one of the main reasons leading to the development of Algebraic Multi-Grid Methods (AMG).

Other means to improve the coarse-grid correction are to modify the coarse grid operator and the grid-transfer functions. Usually, as coarse-grid operator just the differential equations are discretised on a coarse grid. However, without a reasonable resolution of the relevant scales on the coarse levels, this may not be appropriate. Instead the Galerkin projection can be used:

$$A_{l-1} = rA_l p \tag{3.18}$$

where A_l and A_{l-1} are fine and coarse-grid operator resp., r and p are the grid-transfer operators mapping coarse-grid functions to fine-grid ones or vice versa. This is typically used in AMG methods.

As grid-transfer functions r and p usually interpolation is taken and $r = p^*$, where p^* denotes the adjoint operator of p w. r. t. the underlying scalar product:

$$(u_l, pu_{l-1}) = (p^*u_l, u_{l-1}) = (ru_l, u_{l-1}) \tag{3.19}$$

where u_l and u_{l-1} are fine and coarse-grid functions resp. and $(.,.)$ is the underlying scalar product in the resp. Hilbert spaces. For p typically a geometric interpolation (e. g. linear) is used. To improve that, however, matrix dependent interpolation can be used, which uses the matrix stencil rather than the geometry to construct interpolation /ALC 81/.

In the project, both are implemented, the Galerkin projection and the matrix dependent grid transfers as part of the AMG methods. This is helpful as an additional tool together with special smoothers to develop a robustness strategy, however, just by themselves these methods are not sufficient to obtain a robust method.

3.4 Adapting the FAMG method to thermohaline groundwater flow, parallel scalability

The Filtering Algebraic Multi-Grid Method (FAMG) is an AMG method introduced by Wagner /WAG 00/ The main idea is to construct the prolongation such that it is exact on a small subspace spanned by some test or filter vectors, i. e.,

Construct p such that

$$A_l^{-1}S_l^*t_\mu = pA_{l-1}^{-1}p^*S_l^*t_\mu \text{ for } \mu = 1, \dots, \tau \quad (3.20)$$

where the coarse grid matrix A_{l-1} is defined by the Galerkin projection, S^* is a smoother and t_μ are the test or filter vectors resp. spanning the filter space of dimension τ . If the smoother S satisfies corresponding conditions:

$$S_l t_\mu = A_l^{-1} t_\mu \text{ for } \mu = 1, \dots, \tau \quad (3.21)$$

FAMG is an improved Algebraic Multigrid Method. It is exact on the filter space. Thus, the method allows for a (small) subspace to be treated exactly. Applying this method, this filter space is chosen as the span of the first eigenvectors of A_l , since this is the space causing problems in solving the linear system. In /WAG 97/ an algorithm to pick the filter vectors is given.

/NAE 07/ continued the development of the method and /RUP 20/ investigated it more thoroughly, modified it and generalised it for relevant applications. His results help the generalisation to the problem of density driven flow.

3.5 Parallel adaptive algorithms and appropriate grid structures

For challenging non-linear problems like thermohaline groundwater flow and transport considered here, the ability to solve with very fine resolution is decisive in order to achieve a correct description of the non-linear behaviour of the problem /JOH 04/. Talking about a time-dependent and non-linear problem in three space dimensions, one has to care about robust solvers in parallel. Further, the studies in Section 3.2-3.4 resulted in the insight, that it is decisive to tailor the grid tree in an appropriate way, in order to obtain a robust method. That is the reason for working on adaptive anisotropic refinement.

3.5.1 Adaptive anisotropic refinement

Adaptive anisotropic refinement is what is finally necessary to cope with critical problem phenomena due to unresolved scales. This needs to be combined with robust smoothing and improved coarse-grid corrections in order to form a robustness strategy. The construction of a sensible grid tree is the backbone of this strategy.

To that end, a special way to deal with the robustness problem is developed. The idea comes from computer graphics. There, people use the so-called subdivision-surfaces method to obtain gradually improving and smooth approximation of structures. This is achieved by specially constructed splines, see Fig. 3.12.

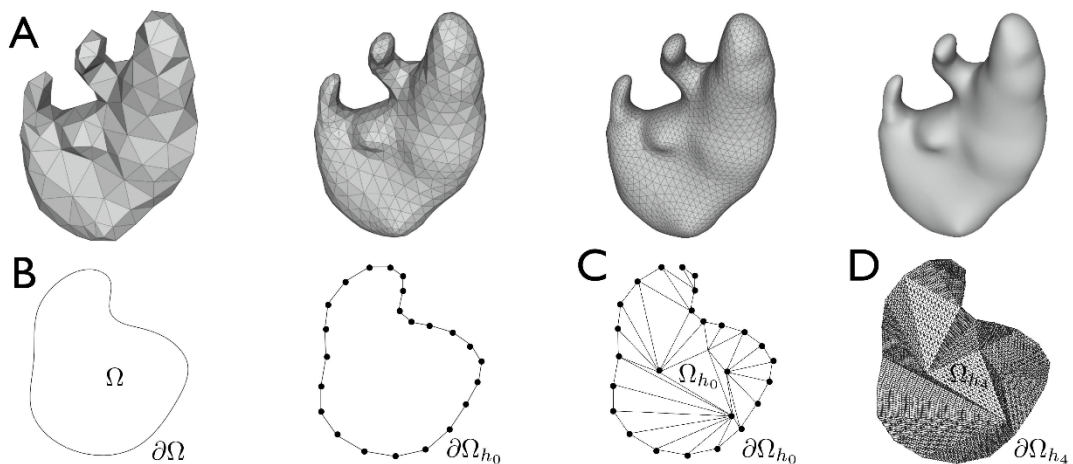


Fig. 3.12 Repeated refinements of an initial set of control vertices x^0 (far left) yields a sample subdivision surface $x^\infty := \lim_{j \rightarrow \infty} x^{j+1} = \lim_{j \rightarrow \infty} (Sx^j)$ of a reconstructed 3D nucleus geometry (far right), /STE 20/

Due to geometric convergence speed subdivision schemes provide a fast and reasonable piecewise linear approximation of the actual smooth limit subdivision curve, surface or volume resp. by the sequence of polytope complexes consisting of the control vertices x^j after only a few refinement steps featuring a high element regularity. This inherent hierarchical property makes the application of subdivision schemes particularly interesting in a multigrid setting. B: Given a domain $\Omega \subset \mathbb{R}^2$, a piecewise linear representation $\partial\Omega_{h_0}$ of the boundary $\partial\Omega$ is derived. C: Subsequent to (B), an initial triangulation is generated in such a manner that the triangulation boundary matches the polytope complex describing $\partial\Omega_{h_0}$. For a GMG solver, this triangulation can be used as base volume grid Ω^0 . D: Given the base volume grid Ω^0 generated in (C), successive linear refinement steps using edge bisection allow for the generation of a nested multigrid hierarchy $\Omega_{h_0} \subset \Omega_{h_1} \subset \dots \subset \Omega_{h_L}$ (exemplary illustration of Ω_{h_4}).

This technique is not only able to obtain a successively better approximation of a complicated geometric surface, a problem, with which one has to fight many times in past application projects, but moreover, it is able to smooth the volume grids and adaptively change grids according to given criteria, e. g., a objective function.

/STE 20/ developed this technique to be used as solvers for partial differential equations mainly with the example of modelling neurons, which have complex cell structures, e. g. neuron nuclei, see Fig. 3.13. Now this method is applied to the density driven flow problem and the structures typically obtained here in large application computations.

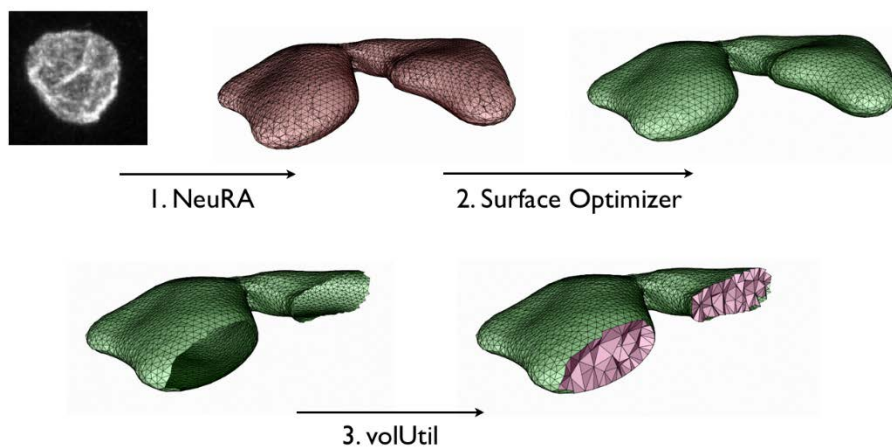


Fig. 3.13 Reconstruction of a neuron nucleus using subdivision surfaces using the subdivision surface method /STE 14/.

In /STE 20/ the authors introduced the Subdivision based Geometric Multi-Grid Method (SGMG) and showed that this technique is capable of generating robust multi-grid methods, just by modifying the grid in a systematic way according to subdivision surfaces. There, they applied the method to model problems. This step is absolutely necessary to fully understand the method, before applying it to very complex non-linear problems like the thermohaline flow. The generalisation to thermohaline flow will be done in the following project HYMNE (FKZ 02E11809A-B).

3.5.2 Adjusted load balancing for convection-dominated problems and ILU-T

For convection dominated problems developed the Downwind Numbering strategy (DN) for robust smoothing was developed /BEY 95/, /FRI 17/. This strategy is available in d³f++, but only for serial computations. It works fine there. However, a parallel version is not available up to now, since this requires special load balancing techniques, which still have to be developed. That is the issue of the current work item.

The idea of Downwind Numbering is that convection is typically discretised by an upwinding method, which is one sided. The upwind side is preferred vs. the downwind one. This makes perfect sense, since convective transport is coming from a source and going to a sink. There is no symmetry in convective transport.

The convection-diffusion equation

$$-\varepsilon \Delta u + \vec{v} \cdot \nabla u = f \tag{3.22}$$

is considered with $\nabla^T \cdot \vec{v} = 0$ and $\varepsilon > 0$. For discretisation a finite volume box method is used as described below.

A finite volume method (also called box method) is used for the discretisation of the convection diffusion equation, which can be interpreted as a conservation law. See e. g. the papers of /HAC 89/, for a detailed description in the 2d case, and /BEY 95/ for three dimensions. The 3d case is explained below.

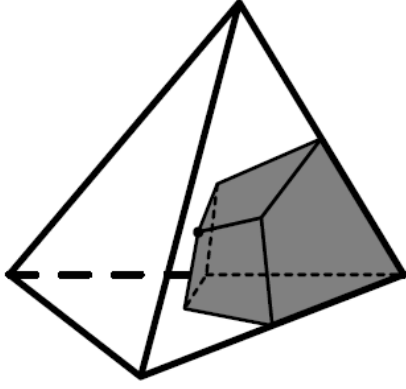


Fig. 3.14 Box portion of an elements corner.

For every triangulation $\mathfrak{T} = \mathfrak{T}_k$, a dual box mesh B is defined, consisting of boxes b_j for every node x_i of \mathfrak{T} in such a way that $x_i \in b_i$ and the boxes $b_i \subset B$ cover Ω and have pairwise empty inner intersection. The three-dimensional box mesh is constructed by connecting the center of mass of every element to the center of mass of all its faces and these again to the midpoints of their edges. Thus, four portions of the element are obtained, each of the same volume and one for each vertex. The box b_i belonging to x_i is then defined to be the union of all portions containing x_i in a tetrahedron which has x_i as corner.

According to /HAC 89/, the following second-order discretisation can be constructed under usual finite element assumptions. Using piecewise linear ansatz functions on \mathfrak{T} represented in terms of the corresponding nodal basis $\{\phi_i, i = 1 \dots, n\}$, integration of the convection-diffusion equation over the box b_i and Gauss' Theorem lead us to

$$\sum_j \int_{\partial b_i} (-\varepsilon \nabla \phi_j + c \cdot \phi_j) d\sigma = \int_{b_i} f(x) dx \quad (3.23)$$

This is the discrete linear system with respect to \mathfrak{T} , and the discrete solution u is given by

$$u(x) = \sum_j u_j \phi_j(x). \quad (3.24)$$

Unfortunately, finite volume as well as finite element discretisations are known to be unstable in the case of dominating convection, which is observable in strong oscillations in the discrete solution. These are explained by the fact that the stiffness matrix is nearly

skew symmetric and not an M-matrix. In special cases, the linear system can even be singular.

To avoid those stability problems, a first-order upwind scheme is used (see e. g. /BAS 94/), resulting in an $O(h)$ -discretization. In one dimension, this upwind method can be interpreted as the substitution of central by upstream differences or as introducing an artificial diffusion. In the following this 3d upwinding is described in detail.

The integrals along the boundary ∂b_i are calculated as follows: Let \mathfrak{T}_j be the set of tetrahedra $T \in \mathfrak{T}$ with corner x_i . Then b_i is a subset of the union of the elements $T \in \mathfrak{T}_j$ and the integrals can be splitted into

$$\int_{\partial b_i} (-\varepsilon \nabla \phi_j + c \phi_j) \cdot d\sigma = \sum_{T \in \mathfrak{T}_i} \int_{T \cap \partial b_i} (-\varepsilon \nabla \phi_j + c \phi_j) \cdot d\sigma \quad (3.25)$$

On account of the Dirichlet boundary conditions, it is sufficient to consider interior points x_i . In this case $T \cap \partial b_j$ consists of three plane segments that are located in the interior of \mathbb{T} , as can be seen from Fig. 3.14. Thus, each integral over a boundary portion $T \cap \partial b_j$ can be split again into a sum of three integrals running over the three plane segments. For simplicity assume that the corners of T are numbered as in Fig. 3.15. To each pair (i, k) satisfying $0 \leq i \neq k \leq 3$ a vector S_{ik} is associated with the following properties:

- (i) The length of S_{ik} is given by the area of the plane segment between b_i and b_k ,
- (ii) $S_{ik}/|S_{ik}|$ coincides with the outer normal of b_i at the plane segment between b_i and b_k .

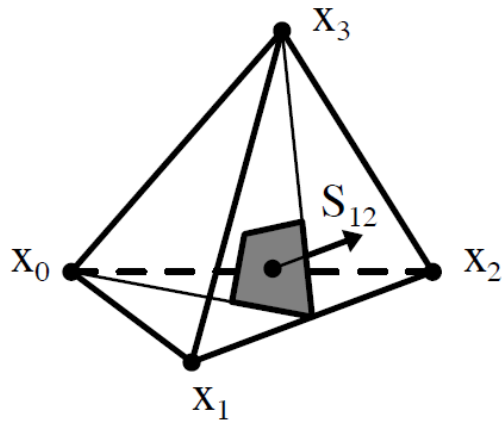


Fig. 3.15 Segment vector and center of mass.

Denoting by s_{ik} the center of mass of the segment between b_i and b_k , the quadrature formula

$$\int_{T \cap \partial b_j} (-\varepsilon \nabla \phi_j + c \phi_j) \cdot d\sigma \approx \sum_{k \neq i} (-\varepsilon s_{ik} \nabla \phi_j + c s_{ik} \phi_j s_{ik} \cdot S_{ik'}) \quad (3.26)$$

Is obtained. The vectors S_{ik} and the integration points s_k can be computed as follows: Let $0 \leq \ell, \ell' \leq 3$ be the remaining corner subscripts not equal to i, k . Then follows

$$s_{ik} = \frac{17}{48}(x_i + x_k) + \frac{7}{48}(x_\ell + x_{\ell'}) \quad (3.27)$$

and

$$S_{ik} = \frac{1}{12} \left(\frac{x_i + x_k}{2} - x_\ell \right) \times \left(\frac{x_i + x_k}{2} - x_{\ell'} \right) \quad (3.28)$$

where \times denotes the usual vector product in \mathbb{R}^3 and the direction of S_{ik} is chosen such that $S_{ik}(x_k - x_i) > 0$. In addition holds

$$\phi_j(s_{ik}) = \begin{cases} \frac{17}{48}, & \text{for } j = i \text{ or } j = k \\ \frac{7}{48}, & \text{for } j \neq i, k \end{cases} \quad (3.29)$$

After computing these values the quadrature formula (3.26) is easily applied to evaluate the integrals over the boundary of a box b_i .

The numbering process described below is based on the directed graph generated by upwinding. The application of the same process to higher order upwind schemes is straightforward.

This method is used to discretise the convective term and then downwind numbering is applied as follows.

Let the convection-diffusion equation be given as described above and be discretised by a finite volume method using an upwinding technique for the convective part as described above. By $A = (a_{ij}), ij \in \mathfrak{N}$, \mathfrak{N} denoting the set of nodes, where the unknowns

are localised. By A_{conv} the part of A corresponding to the discretisation of the convective term $v \cdot \nabla$ is denoted and by $\mathcal{G} = \{(K, L): K, L \in \mathfrak{N}, a_{conv, KL} \neq 0\}$ the matrix graph.

The main aim of the ordering process is to bring the stiffness matrix for the convective terms in triangular form. This can be performed easily, provided the flow field is vortex-free.

When the convective part is discretised by the upwind scheme mentioned before, each edge in the matrix graph is assigned a direction. If the graph generated this way is cycle-free, it defines a partial ordering of the unknowns. This partial ordering can be used to number the unknowns in streamwise direction. In the following, two algorithms are discussed which order the cycle-free part of \mathcal{G} .

Algorithm 1: Downwind_numbering_1

1. Assign the downwind direction from the discretisation of the convective term to each link in the stiffness matrix graph. Indifferent links are marked by 0.
2. Set $n =$ Number of unknowns;
3. Compute $I(K)$, the number of inflow edges of node K for all $K \in \mathfrak{N}$.
4. Find all minimal elements $K \in \mathfrak{N}$ with respect to the number of inflow edges $I(K)$ and put them into a fifo \mathfrak{F} .

5. Loop:

While \mathfrak{F} not empty repeat: Get E from \mathfrak{F} .

1. Put $\text{Index}(E) := 1$. Put E into a fifo \mathfrak{B} . Let $i := 1$.

2. Loop:

While \mathfrak{B} not empty and $i < n$: Get K from \mathfrak{B} .

Loop:

For all neighbours L of K do:

If (L is downwind from K) and ($\text{Index}(L) \leq \text{Index}(K)$), then

$i := \text{Index}(L) := \text{Index}(K) + 1$;

Put L into \mathfrak{B} .

Sort the vertex list such that $\text{Index}(L) < \text{Index}(K) \Rightarrow L < K$.

6. Output: Ordered vertex list.

Remark

- If the edge graph is cycle-free, loop (5.1) terminates in $O(n)$ steps with $\mathfrak{P} \neq \emptyset$. Loop (5) has complexity $O(q \cdot n)$ where q is the number of minimal elements in the edge graph, which is small.
- In step 6. nodes with the same index may be numbered in arbitrary order, caring that the number of a node with higher index is increased at the same time. This is possible with $O(n)$ complexity. Using quicksort for this purpose would spoil the optimal complexity.
- If loop (5.2) terminates with $\mathfrak{P} \neq \emptyset$ and $i \geq n$, then the edge graph contains a cycle.

The complexity of Algorithm 1 may be improved by the following algorithm. For the description, it is assumed that the matrix graph \mathfrak{G} does not contain cycles.

Algorithm 2: *Downwind_Numbering_2*

Downwind_Numbering_2 (matrix graph \mathfrak{G}) begin

1. Assign the downwind direction from the discretisation of the convective term to each link in the stiffness matrix graph. Indifferent links are marked by 0.
2. Compute $I(K)$, the number of inflow edges of node K for all nodes of matrix graph \mathfrak{G} .
3. $m := 0$; /* global counter */
4. For each $K \in \mathfrak{N}$ do: $\mu(K) := -1$;
/* $\mu(K)$ contains the number of node K .
 $\mu(K) = -1$ means node not yet numbered */
5. For each $K \in \mathfrak{N}$ do:
if ($I(K) = 0$ and $\mu(K) = -1$) Number(K);
end;
Number(node K);
begin
 $\mu(K) := m$;
 $m := m + 1$;
for all neighbours L of K do:
if (L is downwind from K) then

```

begin
   $l(L) := l(L) - 1;$ 
  if (  $l(L) = 0$  ) Number( $L$ );
end;
end;

```

This algorithm is of optimal complexity, since each edge and each node is processed only once. The correctness follows directly from the depth search applied here. In the case of cycles, one may use the algorithm described by /TAR 72/, to determine the strongly connected components containing cycles. Then apply the above algorithm to the cycle-free graph of the components. Using a block Gauss-Seidel smoother with blocks corresponding to the components, a robust smoother is obtained. This is reasonable for small cycles. The treatment of large cycles is discussed in /HAC 96/.

These algorithms have been applied very successfully for serial computations also in d³f++. Using them in parallel, however, requires a special type of load balancing. The partitioning has to follow the streamlines. Otherwise, the exactness in the limit case would be lost. If the grid is partitioned just perpendicular to the convection, the number of steps simply increases with the number of partitions, see Fig. 3.16.

BISECTIONX			
\mathcal{P}	Iter.	q_{dist}	Partitioning
2	2	1.0	
4	4	1.0	
8	8	1.0	
16	16	1.0	

Fig. 3.16 Dependence of the number of iteration steps on the number of partitions due to wrong partitioning. The colours show the domains given to the processors. The parallelisation then has no gain /FEH 18/.

The correct partitioning along the streamlines delivers the following results, see Fig. 3.17.

\mathcal{P}	STREAMLINEPARTITIONER			METIS(STR)		METIS	
	Iter.	q_{dist}	Level (Target)	Iter	q_{dist}	Iter	q_{dist}
2	75	1.00	18 (17)	75	1.00	40	1.00
4	78	0.59	17 (16)	79	1.00	42	1.00
8	84	0.82	16 (15)	81	0.99	64	0.99
16	103	0.71	15 (14)	87	0.96	63	0.98

Fig. 3.17 Number of iteration steps for different partitioners of the 2d channel, /FEH 18/

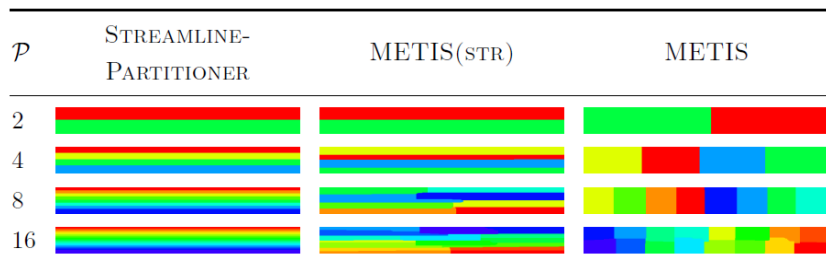


Fig. 3.18 Partitions used for the results from Fig. 3.17 /FEH 18/; The colours show the domains given to the processors.

The Streamline partitioner is visibly best, however, it still needs to be improved, so that also flow fields with cycles can be treated.

3.5.3 General parallel-adaptive strategy

In total, a strategy allowing for robust parallel adaptive computations is derived. Several components of the strategy, however, are still to be optimised in detail as well as their interplay. This remains as task of future projects.

3.6 Stable modelling of free groundwater surfaces

In nature, not the entire porous matrix of an aquifer is saturated with the fluid phase. Normally, the upper part is unsaturated, so that the density-driven flow model can be applied only to the lower, saturated part. The parts are separated by a transition zone. Due to the geological length and time scales, it is assumed that this zone is very narrow and its thickness may be neglected. Then it can be approximated by the so-called phreatic surface, a free upper boundary of the saturated zone, which is moving according to precipitation and other environmental conditions. Capturing its dynamics is important for

prediction of the correct water balance and planning the pumping strategies of water works with several wells.

Two approaches can be used for the simulation of the phreatic surface. One can consider the saturation as a variable and formulate the PDEs in the whole domain of the aquifer. This leads to the Richards equation [NUE 16]. The other approach is to represent the phreatic surface as a moving boundary of the subdomain Ω_2 where the density-driven flow model is applied for the simulation of the groundwater flow.

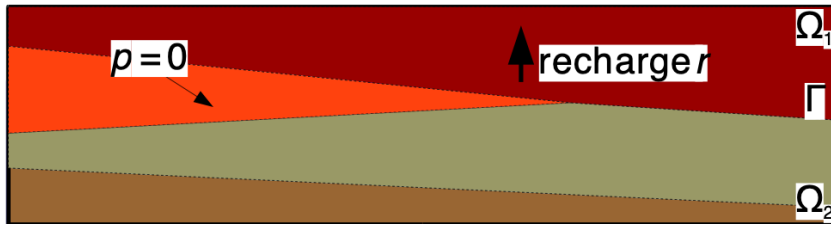


Fig. 3.19 Scheme of the domain of a partially saturated aquifer: Ω_1 is the unsaturated and Ω_2 the saturated parts separated by the phreatic surface Γ (blue line); the dotted lines are the boundaries of the geological layers.

Here, the latter method is followed and the original domain Ω of the aquifer is separated into two parts (cf. Fig. 3.19): $\Omega = \Omega_1 \cup \Omega_2$, where Ω_1 denotes the upper unsaturated part and Ω_2 the lower saturated one. In Ω_2 , the fluid phase is described by the pressure p and the mass fraction ω of the salt. (The implementation of d^{3f}++ supports the thermohaline flow. But as the treatment of the temperature is analogous to the mass fraction, therefore it is omitted here.) These fields satisfy the density-driven flow model:

$$\left. \begin{aligned} \partial_t(\Phi_k \rho \omega) + \nabla \cdot (\rho \omega \mathbf{q} - \rho \mathbf{D}_k \nabla \omega) &= 0 \\ \partial_k(\Phi_k \rho) + \nabla \cdot (\rho \mathbf{q}) &= 0 \end{aligned} \right\} \mathbf{q} \quad (3.30)$$

$$= -\frac{\mathbf{K}_k}{\mu} (\nabla p - \rho \mathbf{g})$$

where $\rho = \rho(\omega)$ and $\mu = \mu(\omega)$ are the density and the viscosity of the fluid phase, and k is the index of the geological layer. System (3.30) is extended with the boundary conditions on $\partial\Omega_2$. For $\partial\Omega_2 \cap \partial\Omega$, these are the typical boundary conditions imposed for the aquifer. On Γ , the “no stress” condition for the pressure

$$p = 0 \text{ on } \Gamma \quad (3.31)$$

Is imposed as well one of conditions

$$\frac{\partial \omega}{\partial \mathbf{n}} = 0 \text{ or } \omega = 0 \text{ on } \Gamma \quad (3.32)$$

for the mass fraction of the salt (\mathbf{n} being the outer normal for Ω_2). Initial conditions should be imposed only on the mass fraction ω .

To close the system (3.30)-(3.32), the dynamics of the moving boundary should be modelled. There are two factors determining the motion of the phreatic surface: The flow of the fluid phase in Ω_2 and the groundwater recharge through Ω_1 . The linear velocity of the fluid phase in Ω_2 is $\mathbf{q}(\omega, p)/\Phi_k$ and it depends on the fields ω and p in some neighborhood of Γ . The groundwater recharge r arises due to precipitation etc. that depends only on the geometric coordinates. The contribution of the recharge to the velocity of Γ is $r\mathbf{e}_z/\Phi_k$ where \mathbf{e}_z is the normalized z -direction. Furthermore, the motion of Γ is also influenced by the surficial channels and rivers. Their intensity c depends on the depth of Γ but the contribution to the velocity can be described by the same expression $c\mathbf{e}_z/\Phi_k$. The entire velocity of the moving boundary is therefore

$$\mathbf{v}_\Gamma = \frac{1}{\Phi_k} (\mathbf{q} + r\mathbf{e}_z + c\mathbf{e}_z). \quad (3.33)$$

Note that (3.33) defines \mathbf{v}_Γ only on Γ .

The implementation of d3f allows to take into account the surficial channels whose thickness is negligible w. r. t. the length scales of the aquifer. They are represented by a separate low-dimensional grid. At every point of this channel, the intensity is computed by the formula

$$c = -\frac{\mathbf{K}_{eff} \cdot \rho_{eff} \cdot \mathbf{g}}{\varepsilon \cdot \mu_{eff}} \cdot (h_s - h_{fs}) \cdot w \quad (3.34)$$

where \mathbf{g} is the gravity, w is the width of the channel, \mathbf{K}_{eff} and ε are the effective permeability and the thickness of the bottom of the channel, ρ_{eff} and μ_{eff} are the effective density and viscosity of the water in the channel, h_s is the specified water level in the channel, whereas h_{fs} is the depth of the groundwater table. For the numerical treatment,

the intensity (3.34) is smoothed in the xy -plane using a mollifier with a support of a prescribed radius. Note that the channels are often thought as sinks, and d^{3f++} may optionally cut positive values of C off.

The phreatic surface is often almost horizontal and near the top of Ω . It motivates the application of the “moving grids” technique for Ω_2 . However, the fine layered structure of the aquifer requires good resolution of the geological layers with the grid. This could be also important for the convergence of the iterative linear solvers.

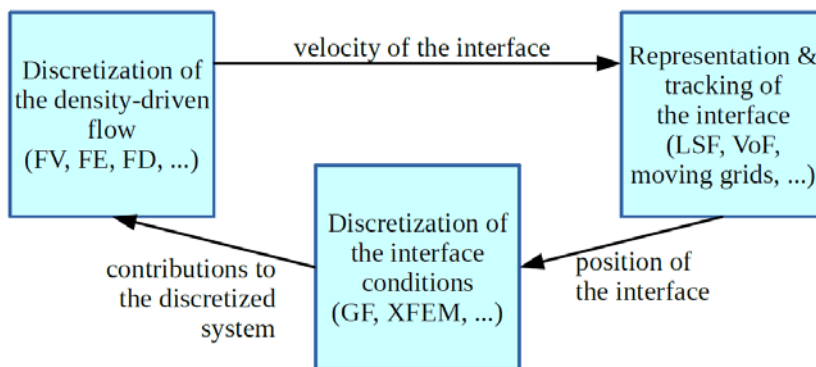


Fig. 3.20 Schematic numerical treatment of the free surface.

There are two basic approaches for the treatment of such free surface problems in the formulation give above, the level-set method and the volume of fluid method. Via (3.34), they are coupled to the flow in Ω_2 . Fig. 3.20 presents the general scheme of numerical treatment of this coupling. To compute the saline and thermohaline groundwater flow, unstructured grids are used to accommodate for complicated domain geometries and local solution behavior. Spatial discretization is accomplished by a vertex-centered collocated Finite Volume scheme, using linear and multi-linear shape functions. For time stepping, a number of implicit methods were implemented like implicit Euler scheme, diagonally implicit Runge-Kutta, fractional-step theta schemes and the LIMEX method described above (cf. also /NAE 19/). Besides Newton’s method, the LIMEX scheme also helps to solve the non-linearity in the problem. For solving the linearized systems, geometric and algebraic multi-grid methods are used, with Gauß-Seidel and ILU methods as smoothers. These solvers are typically accelerated with BiCGStab.

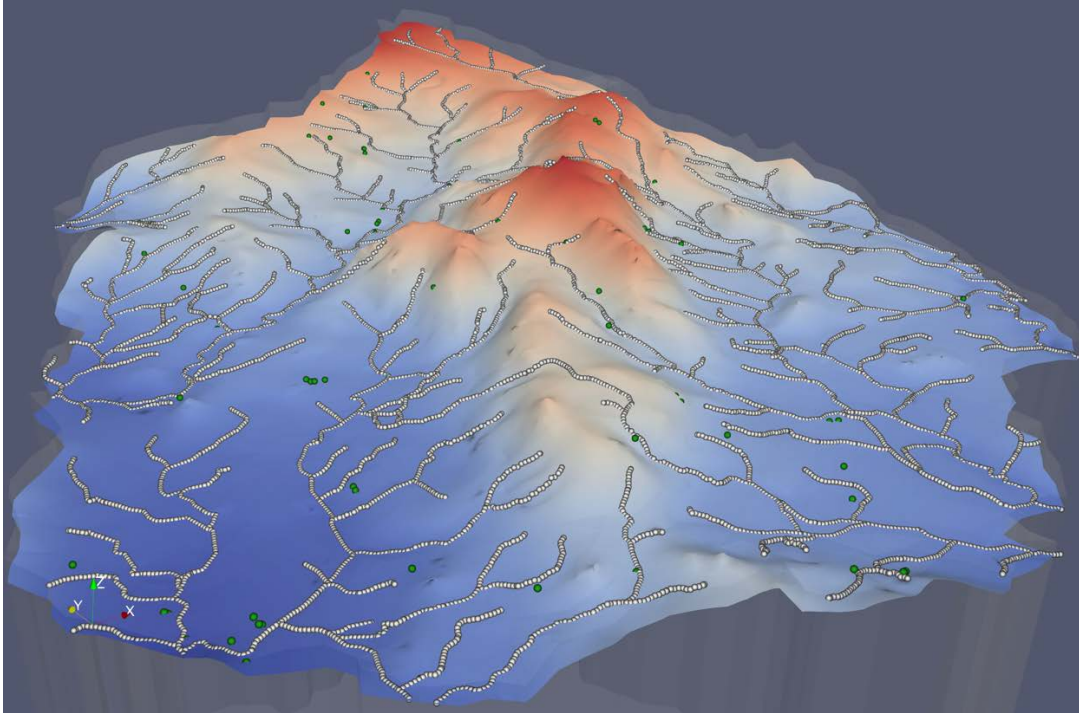


Fig. 3.21 Simulated position of the phreatic surface in the Cihadlo problem at $t \approx 1.5$ years; color: z -coordinate; white lines: channels; green points: measurements. The plot is scaled by 10 in z -direction.

Fig. 3.21 and Fig. 3.22 present results of the numerical experiments with this technique. The Cihadlo problem shown in Fig. 3.21 assumes $\omega = 0$ in the whole domain and has a very dense network of the 1d channels. The model is discretized on the grid with 1,352,295 vertices and computed on 32 cores. The WIPP problem presented in Fig. 3.21 is characterized by the strong anisotropy of the domain. It is discretized on the grid with 279,325 vertices and computed on 128 cores.

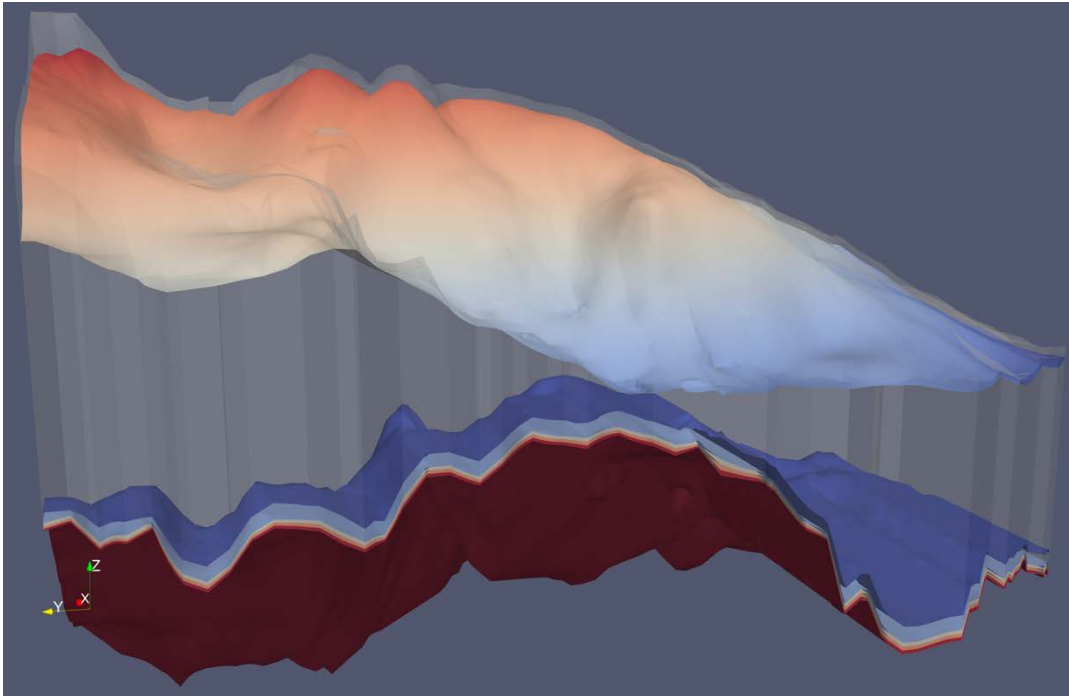


Fig. 3.22 Simulated position of the phreatic surface and the salt mass fraction field in the WIPP problem at $t \approx 453.3$ years; the upper isosurface presents the phreatic surface (color: z -coordinate); the lower ones correspond to $\omega = 0.01, 0.25, 0.5, 0.75, 0.99$. The plot is scaled by 100 in z -direction.

3.6.1 Virtual elements for free surfaces at thermohaline flow

Besides the level-set method used to approximate the free surface, a novel method for the treatment of free surfaces was developed. The idea goes back to /HOE 16/, /HOE 19a/ who developed it for the discretisation of particulate flows.

The basic idea is to discretise the flow using finite-volume methods, yielding balance equations of surface integrals, i. e. fluxes. This is the approach used for thermohaline groundwater flow too. Across the free surface, surfaces integrals are used to express the forces. This goes well with the finite-volume approach. Thus, the same approach is used here.

To describe the free surface, virtual elements are introduced by enriching the ansatz space with special flat-top basis functions

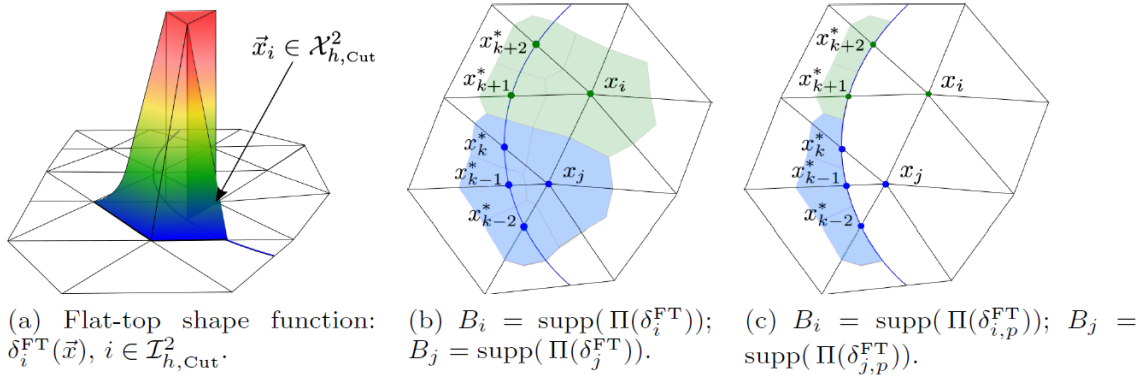


Fig. 3.23 Construction of the flat top basis functions

First, the elements, which are cut by the free surface, are selected. Then the points are used, where the free surface cuts the edges as additional points. By means of those, the additional basis functions are constructed, which approximate the free surfaces very well as shown in Fig. 3.24.

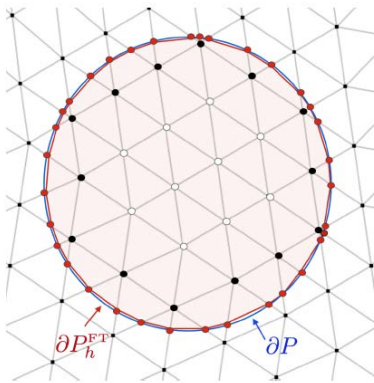


Fig. 3.24 Approximation of the free surface by the flat-top basis functions for a test problem

The method works as well in three dimensions. On tetrahedral grids, the tetrahedra is just cut analogously and introduce the additional basis functions. More details can be found in /HOE 19b/ and /HOE 20/. Enriching the ansatz spaces with these adapted basis functions, allows to include the free surface directly into the finite-volume formulation without moving grids.

3.6.2 Improved PLIC-reconstruction for free surfaces

This method relies on a reconstruction of the free surface. To accomplish that, the usual so-called PLIC method is used, where the interface is reconstructed using piecewise linear functions applying the conditions

1. The ratio of the two phases in each element shall be conserved.
2. The surface in each element is orthogonal to the gradient of the saturation.

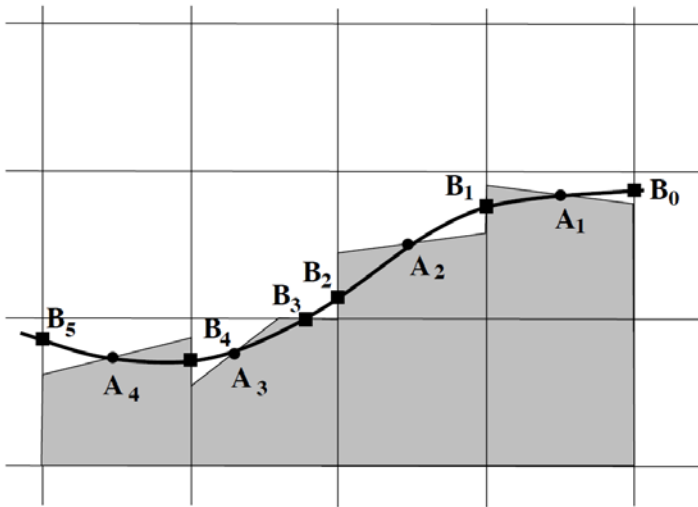


Fig. 3.25 PLIC reconstruction (grey) and subsequent spline reconstruction (smooth line)

In /GIN 01/ the PLIC reconstruction was improved using cubic splines for a 2d problem. In three dimensions, however, such an opportunity does not exist for unstructured grids. Therefore higher order polynomials are used and some reasonable conditions are added like continuity or smoothness of the interface in order to close the reconstruction problem.

This method shows nice properties and will be refined further in future projects.

4 Applications and benchmarks

4.1 SKB Task Force on Groundwater Flow and Transport of Solutes, Task 9b

4.1.1 The LTDE experiment

The Long-Term Diffusion Experiment (LTDE) – a sketch is shown in Fig. 4.1 – had been carried out at the Hard Rock Laboratory (HRL) Äspö in Sweden. Objective of the experiment was to check the concepts of diffusion and sorption of radioactive nuclides in crystalline rock. By a complex set of drilling stages and instrumentation (see Fig. 4.2 and Fig. 4.3), a solution containing 22 different solutes¹ was circulated across a circular part of a fracture surface as well as in a cylindrical borehole beyond the fracture. The cylindrically encased piece of rock at the fracture is called “stub”.

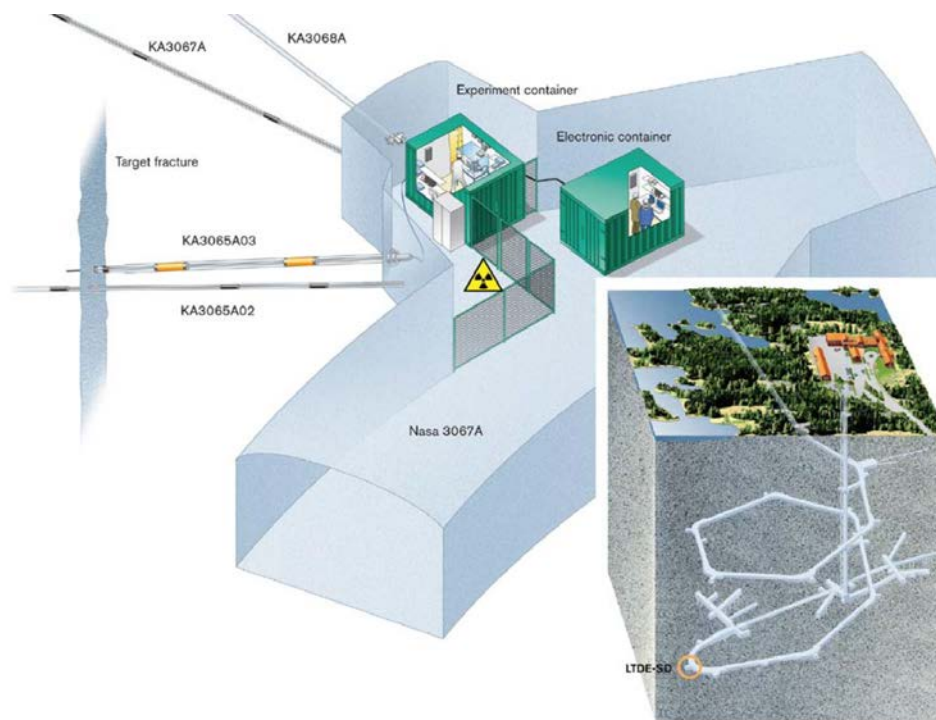


Fig. 4.1 Location of the LTDE-Experiment; from /WID 10a/

¹ $^{22}\text{Na}^+$, $^{35}\text{SO}_4^{2-}$, $^{36}\text{Cl}^-$, $^{57}\text{Co}^{2+}$, $^{63}\text{Ni}^{2+}$, $^{75}\text{SeO}_4^{2-}$, $^{85}\text{Sr}^{2+}$, $^{95}\text{NbO}^{2+}$, $^{95}\text{Zr(IV)}$, $^{99}\text{TcO}_4^-$, $^{102}\text{Pd}^{2+}$, $^{109}\text{Cd}^{2+}$, $^{110\text{m}}\text{Ag}^+$, $^{113}\text{Sn(IV)}$, $^{133}\text{Ba}^{2+}$, $^{137}\text{Cs}^+$, $^{153}\text{Gd(III)}$, $^{175}\text{Hf(IV)}$, $^{226}\text{Ra}^{2+}$, $^{233}\text{PaO(OH)}_3$, $^{236}\text{UO}_2$, and $^{237}\text{NpO}_2^+$. The tracer names written in bold were considered in Task 9b. Data relevant for modelling can be found in Appendix A, section A.1.

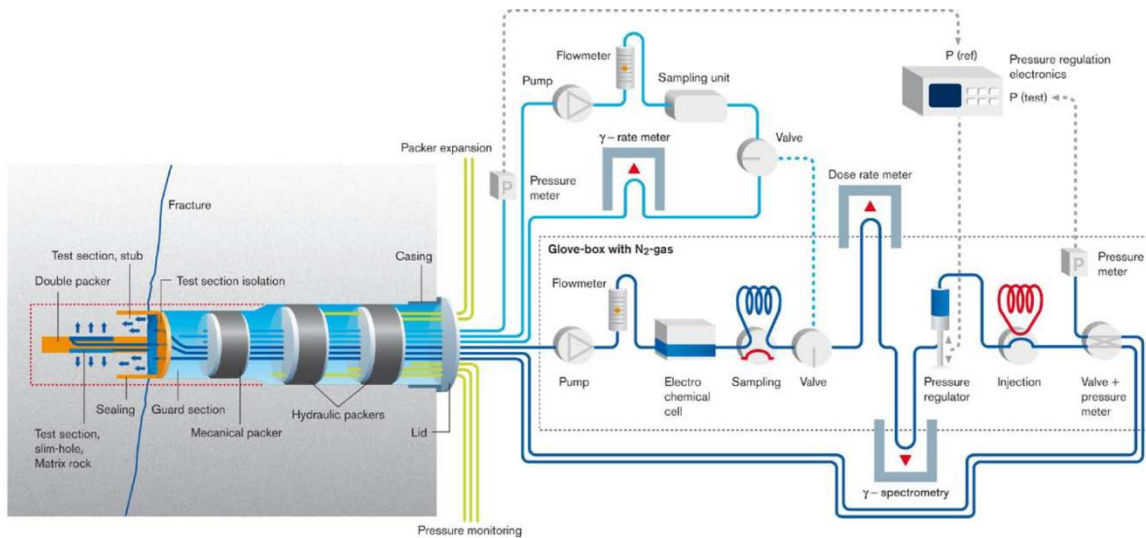


Fig. 4.2 Borehole instrumentation and test section design; from /WID 10b/

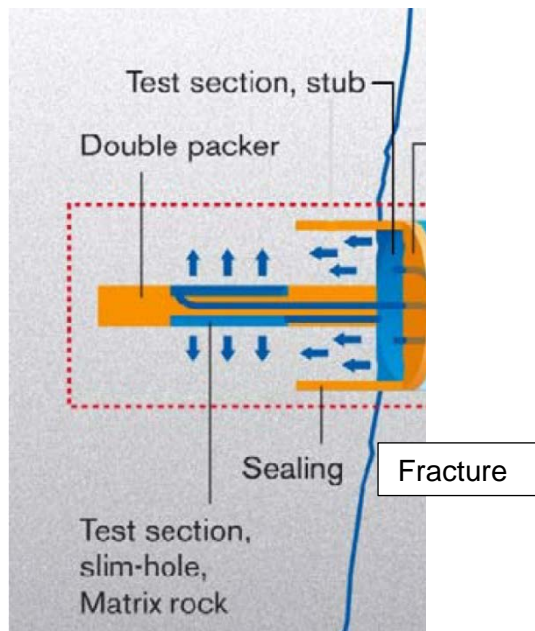


Fig. 4.3 Test sections, close-up from Fig. 4.2; modified from /WID 10b/

The tracer concentration in the test sections was monitored during the experiment. As the tracers were not replenished a decline in the concentration over time was expected. As it turned out, the concentration of the tracers $^{57}\text{Co}^{2+}$, $^{110\text{m}}\text{Ag}^+$, and $^{153}\text{Gd}(\text{III})$ decreased by several orders of magnitude while the concentration of the other tracers can reasonably well be approximated by a constant even if not necessarily the initial value. For details see Appendix A, section A.2.

When the experiment was terminated the inflow reservoir was filled with resin in order to avoid further diffusion of tracers into the rock. Borehole and stub were overcored. After a certain delay small cylindrical cores were drilled according to the pattern depicted in Fig. 4.4 and sealed. Relevant for the task at hand were the A-cores that were drilled through the fracture surface and were therefore arranged in parallel as well as the D-cores taken in radial direction from the borehole axis.

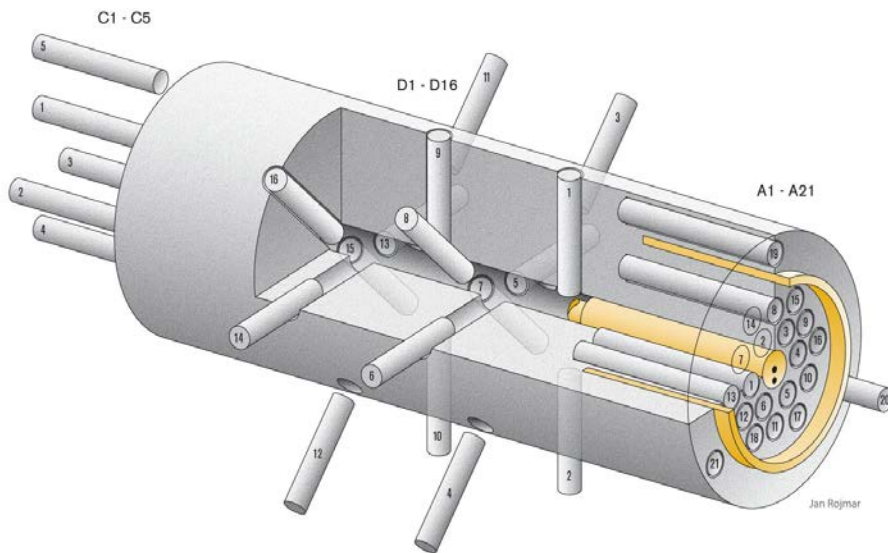


Fig. 4.4 Drill pattern of the overcored inflow reservoir

After another delay period the cores were sliced following a complex procedure which led to subsamples as illustrated in Fig. 4.5. The thickness of the slices varied and is listed in Tab. 4.1. The tracer concentrations were then determined in the subsamples by means of a number of analysis methods. These include autoradiography on intact samples, direct activity measurements on intact as well as crushed samples, and leaching or dissolution of intact and crushed samples, followed by water phase measurements.

The timeline of events that are relevant for modelling is given in Tab. 4.2 together with the duration of the periods and a related model time.

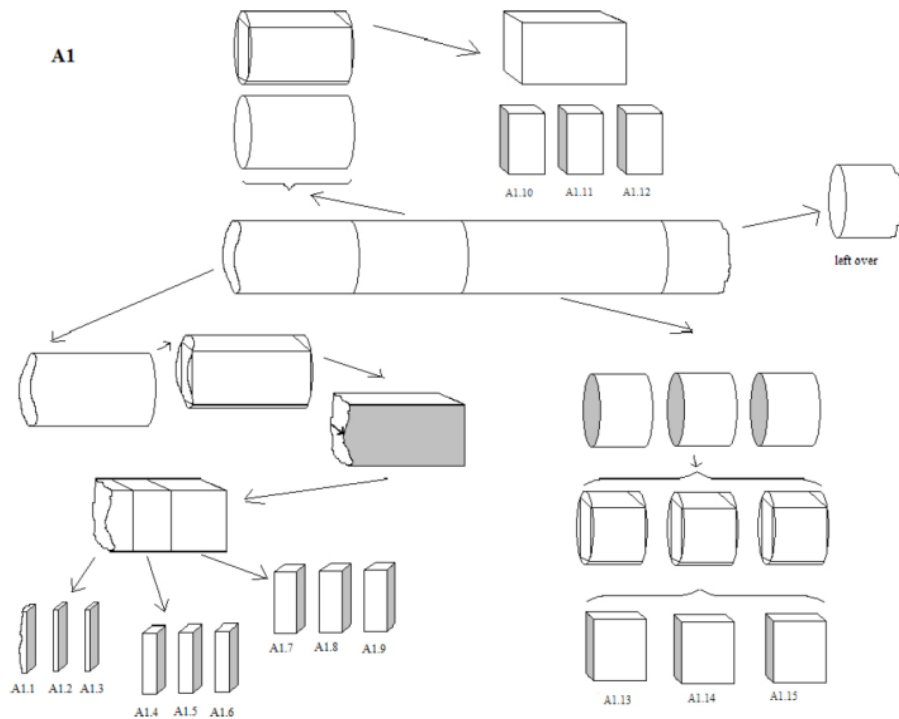


Fig. 4.5 Slicing pattern of the drill cores

Tab. 4.1 Thickness of slices according to slicing plan

Slice #	1 ²	2	3	4	5	6	7	8	9	10	11	12
Thickness [mm]	> 1	1	1	3	3	3	5	5	5	10	10	10
Data allocation [mm]	(>)0.5	1.5	2.5	4.5	7.5	10.5	14.5	19.5	24.5	32	42	52

Tab. 4.2 Timeline of the experiment, period lengths and resulting model times

date	action	duration [d]	model time [d]
27.09.2006			
27.09.2006	begin of LTDE		0
	LTDE	197	
12.04.2007	end of LTDE		197
	delay until drilling	120	
10.08.2007	middle of drilling		317
	delay until slicing	76	
25.10.2007	begin of slicing		393
	slicing	128	
01.03.2008	end of slicing		521

² Includes the rough core face surface

The resulting concentration profiles had not the anticipated shape. Up to three different characteristic parts of the curve were found. Mostly, the concentration decreased from the rock surface with a steep gradient over the first few millimetres into the rock. Subsequently, the gradient changed quite suddenly to a much lower slope followed eventually by a more or less horizontal plateau. A typical result is shown in Fig. 4.6 for $^{226}\text{Ra}^{2+}$. However, not all of the three parts could be observed in all activity curves.

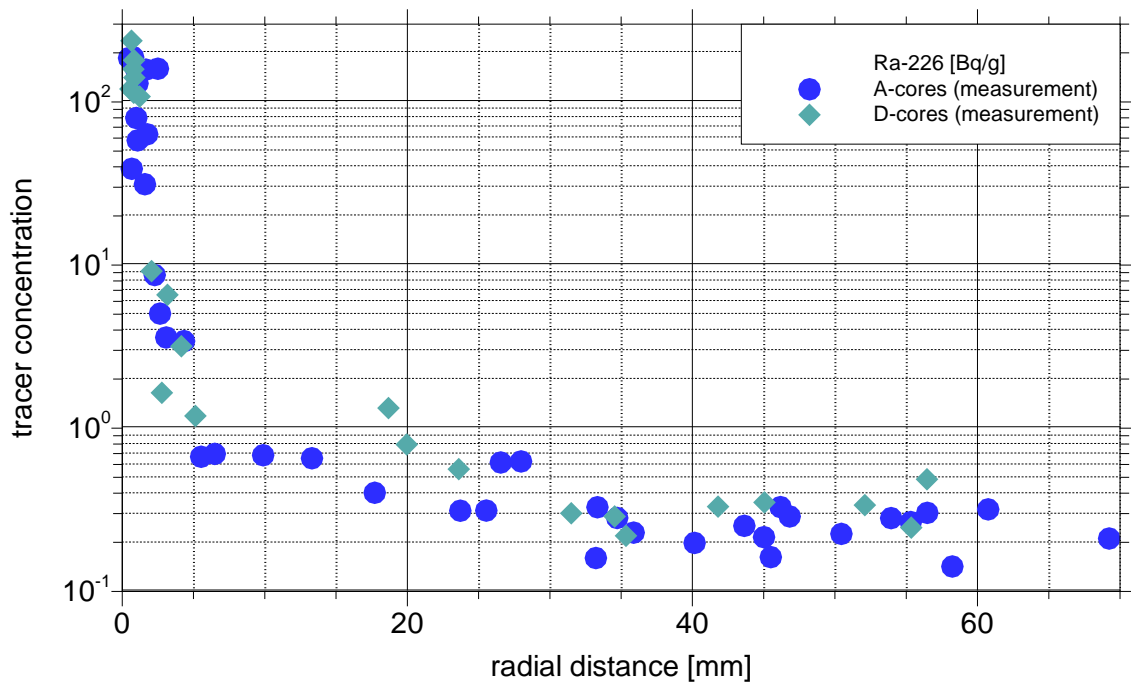


Fig. 4.6 $^{226}\text{Ra}^{2+}$ tracer profile found to be characteristic for the LTDE

4.1.2 Motivation

The reason for setting up the LTDE as Task 9b in the framework of the Task Force on Groundwater Flow and Transport of Solutes (TF GWFTS) of the Svensk Kärnbränslehantering (SKB) was that no obvious and convincing mechanism had been found to explain the curious concentration curves. The interest of GRS in joining Task 9b had been to check the own d^3f++ code using real data of advanced hydrochemical processes. In the run-up to Task 9 it had for instance been speculated that interaction of tracers might have played a role thus calling for a smart K_d -approach which is actually realised in the d^3f++ code. As it turned out, though, there was not enough data available to run the smart K_d -option. Apart from that there was a general bafflement about the physical explanation of the curious tracer profiles. The focus of GRS thus shifted towards finding a plausible mechanism.

4.1.3 Explanations for the data

Over time, many different approaches have been brought forward by the participants of the TF GWFTS. They are shortly described in the following to illustrate the great uncertainty that the LTDE-results had caused. The sequence in which the approaches are listed is not prioritising their credibility or their success. The suggesting party is labelled in brackets.

- **Homogeneous matrix with kinetic sorption** (KTH)
- **Multi-zone models**, optionally including the reservoir. Intuitively, one can assume that the tracers pass sequentially through two zones with different transport parameters. These zones could be interpreted as a skin zone and the undisturbed rock. The skin zone would have to show a much less apparent diffusivity than the neighbouring zone (see section 4.1.4) (TUL, KTH, JAEA, KAERI, LANL)

An interesting refinement has been brought forward by KAERI who combined the multi-zone model with a detailed description of the rock – including the disturbed zone – on the micro-scale (see also mineralogical heterogeneities on micro-scale) and above that with an additional microfracture.

By contrast, LANL postulated a disturbed zone represented by a micro-DFN (see below) in a continuous matrix, followed by a homogeneous matrix.

- **Double continuum models.** It has been speculated that there could be two parallel domains with different transport parameters that might be constituted by channels or fractures with different channel widths / fracture apertures as this would mathematically explain the concentration curves (HY, TUL)
- **Mineralogical heterogeneities on micro-scale.** These are grain scale models where the grains had been located and identified by X-ray tomography and each type of grain has a different sorption capacity. (CFE, AMPHOS, TUL, HYRL, KAERI (see also multi-scale models))
- **Micro-DFN** (ProGeo, LANL (see also multi-scale models))
- **Advection towards the borehole** (GRS)
- **Degassing.** Evolution of dissolved gases under decreasing hydraulic pressure (SU, GRS)

– **Artefacts**

- **Capillary transport** during drying of the overcored rock sample (KTH)
- **Contamination by drilling and sawing.** May have happened if drilling or sawing was done from high to low tracer concentrations (GeoSigma)
- **Challenge of the dispersion concept.** Applying Taylor-diffusion thus including effects on pore scale was suggested (KTH)
- **Electromigration.** Movement of ions along an electrical potential gradient like the one produced by the High Voltage Direct Current (HVDC) transmission between Gotland and the main land just 16 km away from Äspö (Niressa)

Abbreviations for the contributing teams

AMPHOS– AMPHOS²¹, Barcelona

CFE – Computer-aided Fluid Engineering (CFE) AB, Lyckeby

Geosigma – Geosigma AB, Uppsala

GRS – Gesellschaft für Anlagen- und Reaktorsicherheit gGmbH, Braunschweig

HY – Helsingin Yliopisto – Universität Helsinki

JAEA – Japan Atomic Energy Agency, Tokyo

KAERI – Korea Atomic Energy Research Institute, Daejeon

LANL – Los Alamos National Laboratory, Los Alamos

Niressa – Niressa AB, Norsborg

PROGEO – ProGeo, s.r.o., Prag

TUL – Technische Universität Liberec

4.1.4 Workshop on the skin-effect

In the framework of Task 8 GRS had used a narrow and flow impeding zone around geotechnical openings in order to explain the comparatively low outflow from the rock /KRÖ 18a/. This effect was included ad-hoc as it had already been observed during the Two-Phase Flow Project at the HRL Äspö /KUL 02/. The observation could not be explained but was later commonly referred to as the “skin-effect”.

Incorporating a skin in the GRS flow models for the BRIE and the Prototype Repository intrigued the participants of the TF GWFTS. Since a similar effect was suspected to in-

fluence the results from the LTDE in the parallel running Task 9b it was decided to organise a separate workshop on the skin-effect during the meeting in Prague in 2016 in order to benefit from the gathered knowledge among the TF participants. 13 contributions covered 20 examples from 7 underground laboratories (URL) in 5 countries worldwide, from laboratories and modelling exercises. The presentations were evaluated and the abstracts together with the results compiled in /KRÖ 18b/.

In the report the contents are divided according to the affected repository-relevant processes, namely groundwater flow and solute transport, because the spatial scale of the related observations is quite different. While a flow skin, as a general rule, appears to be associated with scales on the order of a metre, the observed transport skins have a thickness on the mm- to cm-scale.

From the compiled observations it is believed that no single cause explains all the observations and that in some cases it is possible that multiple processes and features of the flow system interact to cause observed skin effects. Unfortunately, the proposed explanations for skin can in many cases not be quantified for a specific situation. Often crucial information is missing, even in well-controlled environments. For these reasons typically only qualitative descriptions of the observed effects could be given and predictive models are (still) absent entirely. Spending a lot of effort, the workshop had thus brought forward valuable insight into the possibly “significantly under-reported” skin-effect(s) but not the much hoped-for conclusive explanation for the curious concentration profiles in the LTDE.

4.1.5 Approach

Left with no clear concept after some time of Task 9b had already elapsed and with the notion that sheer data fitting to an abstract model appeared to be pointless, it was no longer looked for a single convincing explanation of the tracer profiles. GRS therefore shifted the focus of the work towards a model that was potentially viable from an engineering point of view in order to check stringently the viability with the available data.

The skin-workshop had made clear that a transport skin might be caused by the drilling of the test borehole. The cooling fluid containing fine particles might have superficially clogged the pore space in the rock at the borehole wall. Also a borehole disturbed zone (BDZ) might have developed causing a larger surface area for sorption. The fracture

surface could clearly not have been affected by drilling but showed a coating from mineralisation. These considerations suggest a two-zone model with a narrow zone at the contact of rock and solution and an undisturbed matrix beyond as an appropriate representation of the situation at the LTDE. Further work is based on this assumption.

The strategy of choice was to fit the model results to the data and then to check if the resulting parameters make sense. The result of this exercise is obviously the more meaningful the less parameters are used for the fitting, meaning that the number of fitting parameters for the model should be as much as possible. It helped therefore that the properties of the undisturbed matrix are comparatively well-known thus leaving little leeway for fitting in this part of the model.

The envisaged modelling procedure was kept straightforward and thereby hopefully robust. It took place in a two steps. In the first step transport of a non-sorbing tracer was to be modelled in order to find out about the pore space topology. The only candidate was the anion $^{36}\text{Cl}^-$. All other tracers were cations that are prone to sorption because of the negative surface charge density of the crystalline rock. However, an effect from anion exclusion in narrow pore channels on the $^{36}\text{Cl}^-$ -tracer could not be ruled out entirely.

Without sorption, the only transport-relevant mechanism is diffusion. Fick's second law could therefore be applied in case of $^{36}\text{Cl}^-$:

$$\Phi \frac{\partial c}{\partial t} - \Phi \tau^+ \nabla \cdot (D \nabla c) = 0 \quad (4.1)$$

Φ - porosity [-]

c - tracer concentration [-]

t - time [s]

τ^+ - factor comprising diffusion limiting influences (tortuosity, constrictivity etc.) [-]

D - diffusion coefficient [m^2/s]

Assuming a homogeneous domain, only the diffusion limiting factor τ^+ remains for fitting since the diffusion coefficient is well-known and the porosity cancels out. Note that all activity data are given as decay corrected. Meaning and purpose are that the measured data was transformed to values as if no decay had taken place to allow for including codes that do not consider radioactive decay.

Adding a disturbed zone to the model increases the number of fitting parameters because the factor τ^+ cannot be expected to be the same in both parts of the model. The same applies to the porosity meaning that the porosity does not cancel out of the diffusion equation anymore. Two more parameters concern the disturbed zone. First, there is the unknown depth of the disturbed zone. Thinking of clogging from drilling fluid fines and/or mechanical disturbances from drilling, it appears to be highly improbable that the pore space geometry in disturbed zone is constant all over this zone and just simply switching at the zone boundary. Rather a transition of the parameters from the sample surface to the not affected matrix is expected. This transition can be formulated as a factor that depends on the distance from the surface and the depth of the disturbed zone:

$$\Phi_{matrix} + \left(\frac{l-x}{l} \right)^m \cdot \Delta\Phi = 0 \quad (4.2)$$

- l - depth of the disturbed zone [m]
- m - exponent [-]
- $\Delta\Phi$ - maximum difference of the porosity between BDZ and matrix [-]
- x - distance tot he sample surface [m]

The same can analogously be formulated for the parameter τ^+ . Different shapes of the transition function can be achieved by varying the exponent m . Examples for a normalised depth are given in Fig. 4.7.

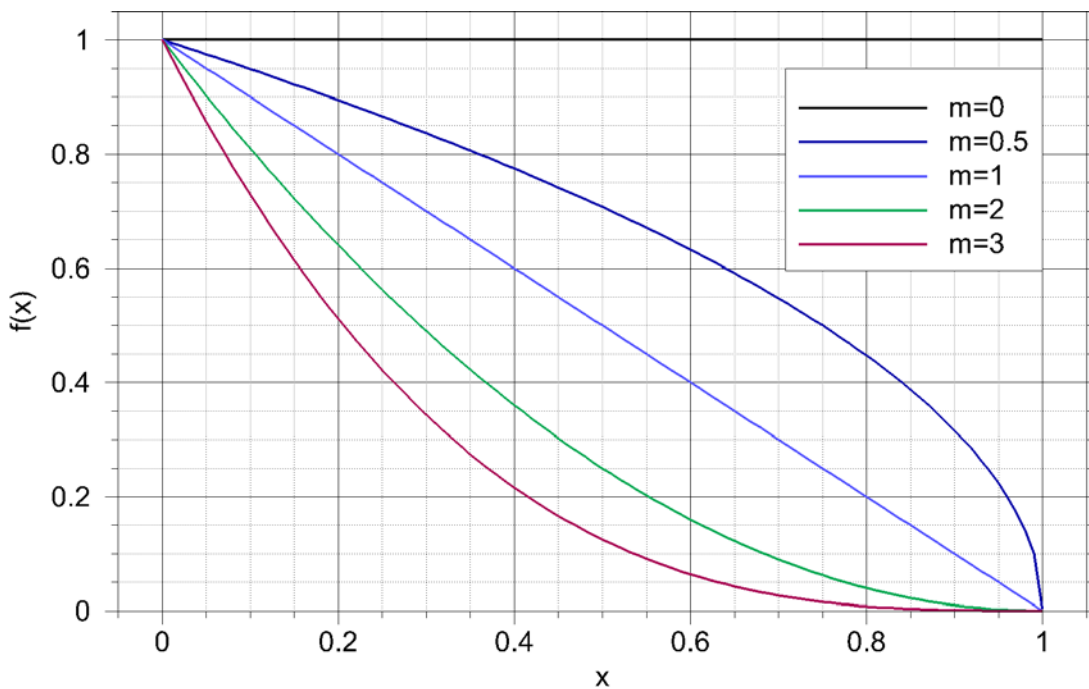


Fig. 4.7 Examples for the transition function for a normalised depth

Calibrating the model for ^{36}Cl -migration with respect to these six parameters takes care of the geometrical aspect of the porous transport system. Modelling migration of the cations should therefore add only sorption to the problem:

$$\left(\Phi + [1 - \Phi] \rho_s K_d\right) \frac{\partial c}{\partial t} - \Phi \tau^+ \nabla \cdot (D \nabla c) = 0 \quad (4.3)$$

K_d - distribution coefficient for equilibrium sorption [m^3/kg]

Step 2 is thus concerned with the cations thereby including sorption. As the K_d -value for all tracers has been determined in the laboratory this should not add a new fitting parameter. In an ideal case, the models for anion transport should immediately work with the known parameters from the calibrated model for ^{36}Cl . Note that the topological parameters for the matrix should be the same for the models of the A-cores and the D-cores.

4.1.6 Data analysis

Activity data for the eleven tracers chosen for investigation in Task 9b had been provided. A detailed and in-depth analysis of the data is given in Appendix A, section A.4. The main observations and conclusions from that analysis are:

(1): The detection limits are related to the subsample sizes as indicated in Fig. 4.8. If the activity values are in the same range and show the same trend as the detection limits as in case of $^{226}\text{Ra}^{2+}$ the activity data becomes meaningless. Concentration values that lie at the detection limits must therefore be considered to be at least comparatively badly known.

As scatter in the data at the detection limits might indicate an indeterminable continuation of the concentration distribution below the detection limits it is no use to discuss model results in the range of such data. This applies even more so to domain sections where all concentration values lie below the detection limits because they are entirely unknown and could even be zero if no tracer material has reached the particular position at all.

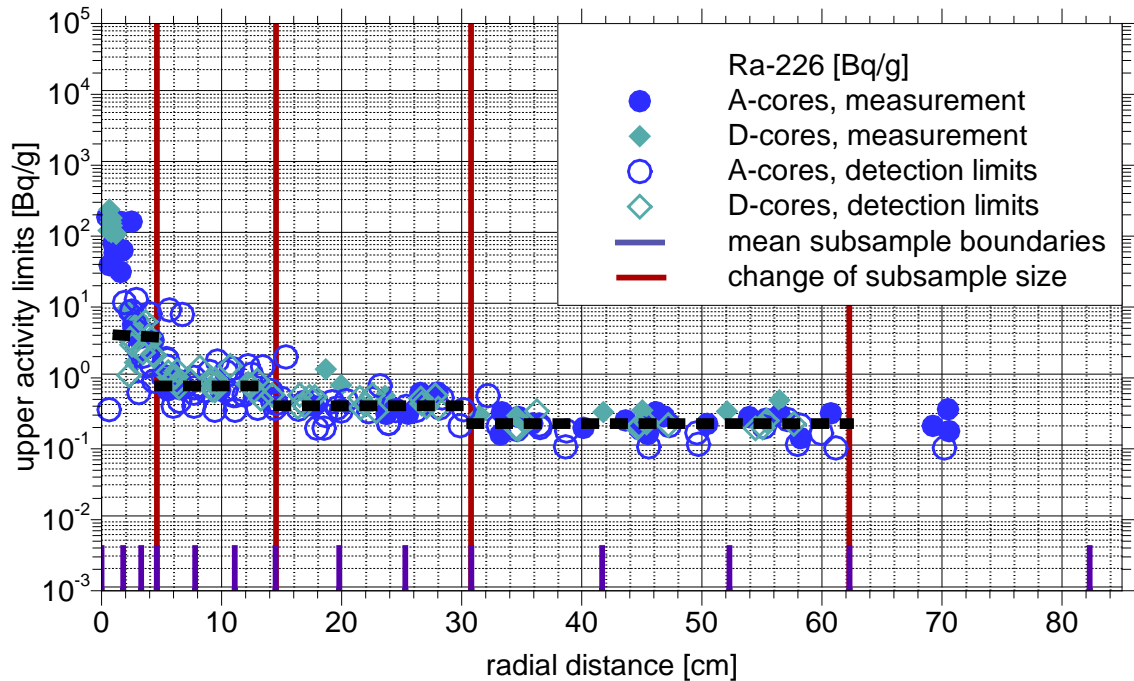


Fig. 4.8 $^{226}\text{Ra}^{2+}$ tracer profile, detection limits and subsample partitioning

(2): Only the activity data for $^{22}\text{Na}^+$, $^{36}\text{Cl}^-$, and $^{137}\text{Cs}^+$ are entirely and for $^{57}\text{Co}^{2+}$ and $^{133}\text{Ba}^{2+}$ at least partially relevant in that the data points lie clearly above the detection limits. All others show significant values only within a few millimeters from the borehole wall/fracture surface and are therefore not used for modelling.

(3): Data for $^{36}\text{Cl}^-$ and $^{22}\text{Na}^+$ from the D-cores do not show the steep concentration gradient in the immediate vicinity of the former reservoir. This observation is most significant as it indicates a principal difference between the fracture surface and the borehole wall and thus calls for different models for A- and D-cores.

(4): There is much less data uncertainty within a drill core than scatter between the cores. Apparently, there is already considerable local variation of material properties in the matrix on the scale of the LTDE. Fitting model results to the data can therefore not be done as stringent as it had been hoped for.

4.1.7 Homogeneous model

The attempt to fit model results and tracer data with a homogeneous model failed as in earlier modelling exercises (e. g. /NIL 10/). The only available fitting factor τ^+ (see section 4.1.5) just changes the curvature of the calculated curves and particularly not the

starting point at the sample surface, so the result shown in Fig. 4.9 is close to the best fit. Note that the tracer concentrations depicted in Fig. 4.9 to Fig. 4.18 as well as Fig. A.5 to Fig. A.14 in Appendix A are given in Bq per gram of rock.

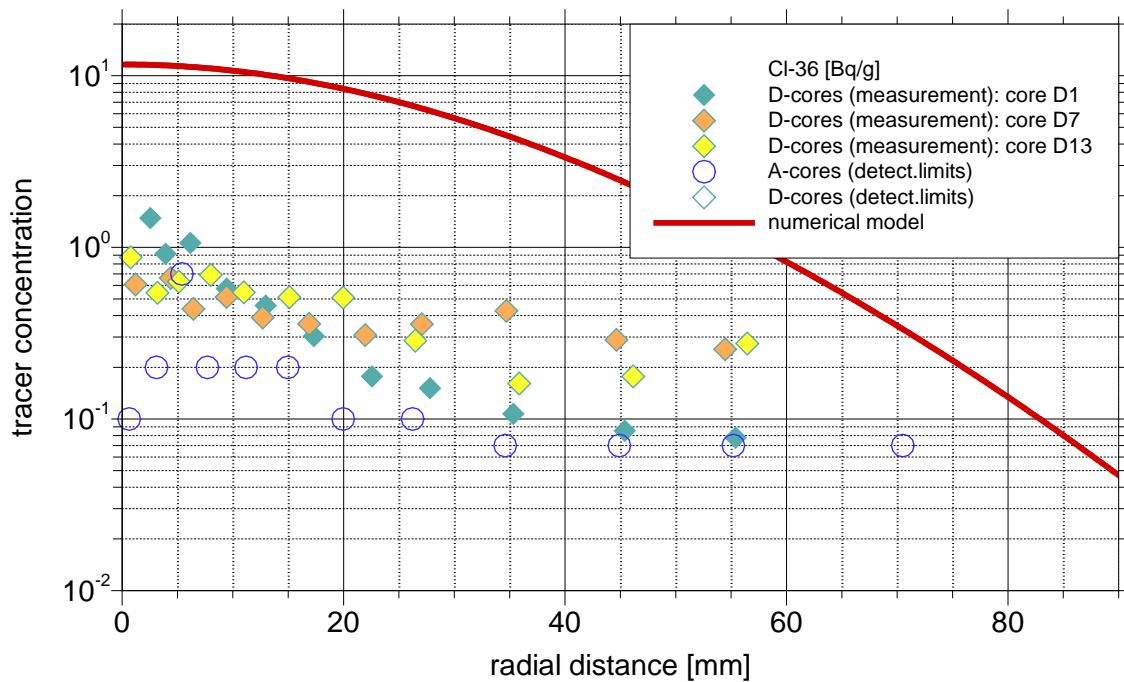


Fig. 4.9 Best model fit of a homogeneous model to the ³⁶Cl-data from the D-cores

4.1.8 Fitting results for A-cores

Since structural differences between the A-cores and the D-cores were suspected (see section 4.1.5) fitting was done for the A-cores and later separately for the D-cores. Step 1 – fitting the results for ³⁶Cl – resulted in the fit shown in Fig. 4.10.

As it turned out, though, this particular data set was the only one suggesting a disturbed zone as large as 5 mm. Moreover, the matrix porosity and tortuosity were extremely low (0.0004 and 0.005, respectively) which seems to indicate that there is actually some anion exclusion having effect in the matrix. What this means for the disturbed zone is not clear. For the fitting strategy, however, it means that the data for ³⁶Cl cannot be used as a basis for fitting the profiles for the cations.

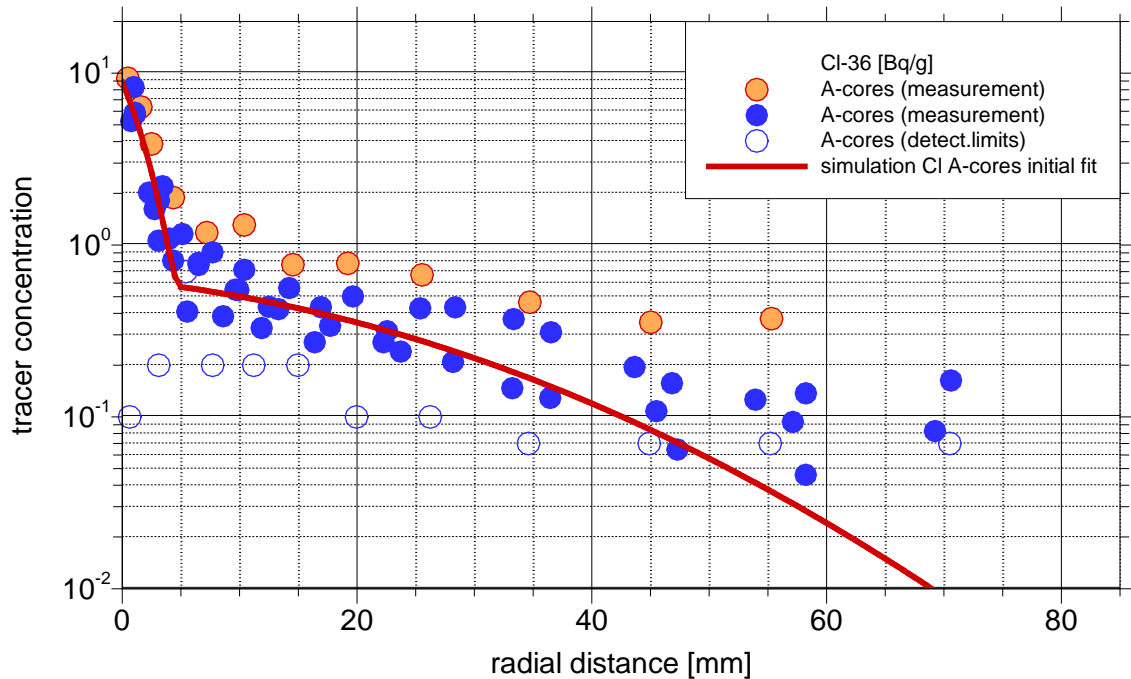


Fig. 4.10 Fit of the two-zone model to ^{36}Cl -data from the A-cores; initial fit

Since the goal was to use one and the same parameter set for all data, the models for the three cations in the A-cores were fitted next and then reconciled with the ^{36}Cl -profile. Fitting the results for the three cations (see Fig. 4.12 to Fig. 4.14) worked out well. In case of $^{137}\text{Cs}^+$ (see Fig. 4.13) re-evaluation of the data determination by Geosigma led to an increase of the detection limits as indicated by a dashed blue line which made the fitting a much better one. The topological parameters from the fitting exercise remained to be quite different for $^{36}\text{Cl}^-$ and the three cations as the compilation in Tab. 4.3 shows, confirming the suspicion of anion exclusion. The good fit for $^{36}\text{Cl}^-$ as in Fig. 4.10 could not be achieved after applying a data set common for all tracers even allowing for differences in the matrix as shown in Fig. 4.11.

Nevertheless, the data in Tab. 4.3 show reasonable values for matrix porosity and tortuosity (0.004 and 0.4, respectively). In comparison, the data for the disturbed zone a slightly decreased porosity (0.003) and a strongly decreased tortuosity (0.0006) which underpins the notion of a pore space filled with fines.

Tab. 4.3 Fitting parameters for the model results depicted in Fig. 4.10 to Fig. 4.14³

A-cores	³⁶ Cl ⁻	²² Na ⁺	¹³⁷ Cs ⁺	¹³³ Ba ²⁺
Φ_{BDZ} [-]	0,003	0,003	0,003	0,003
τ^+_{BDZ} [-]	0,0006	0,0006	0,0006	0,0006
l_{BDZ} [mm]	1	1	1	1
Φ_{matrix} [-]	0,0008	0,004	0,004	0,004
τ^+_{matrix} [-]	0,005	0,4	0,4	0,4
m [-]	2	2	2	2

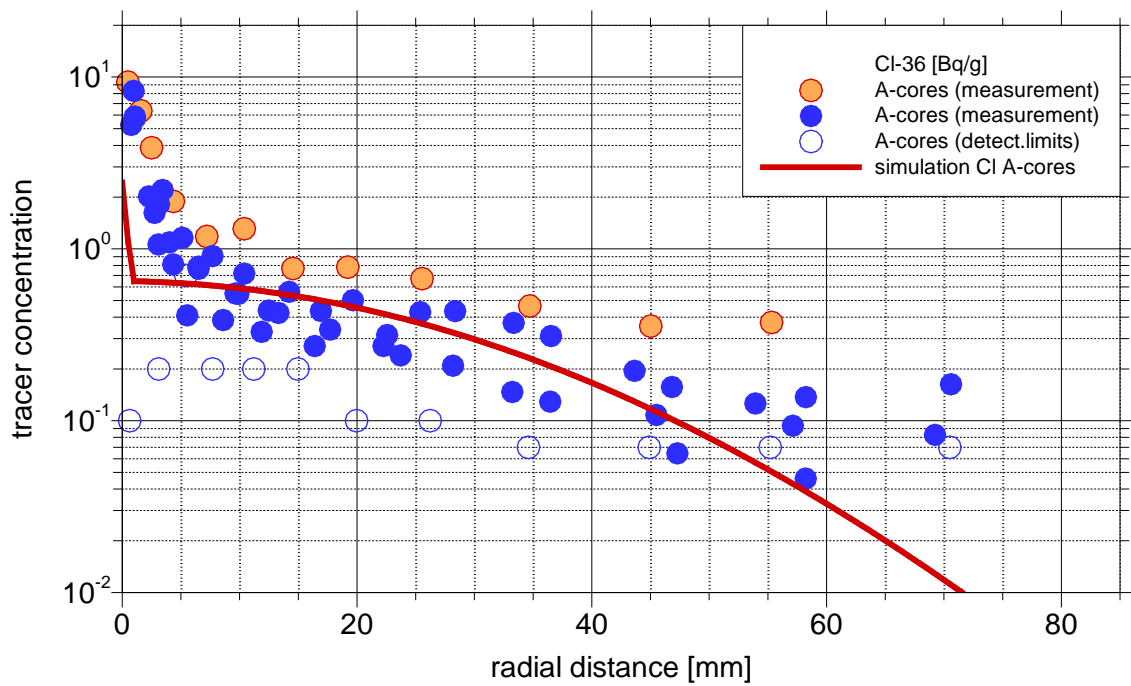


Fig. 4.11 Fit of the two-zone model to ³⁶Cl-data from the A-cores

³ The index “BDZ” denotes the narrow zone at the rock surface while the index “matrix” stands for the undisturbed matrix.

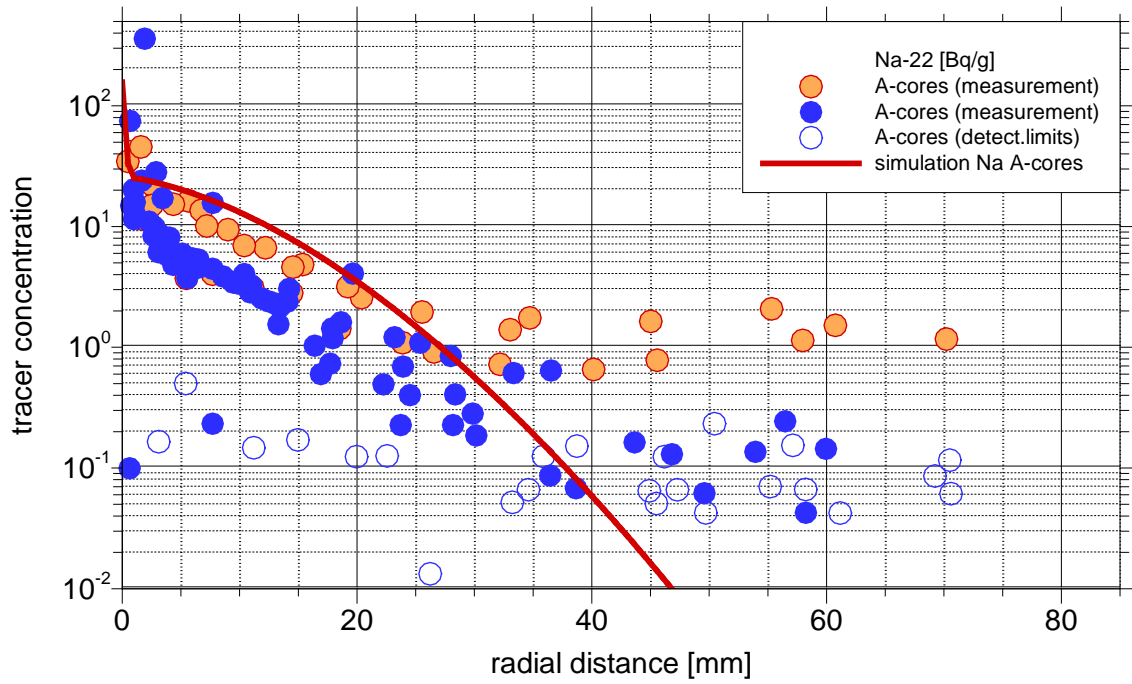


Fig. 4.12 Fit of the two-zone model to $^{22}\text{Na}^+$ -data from the A-cores

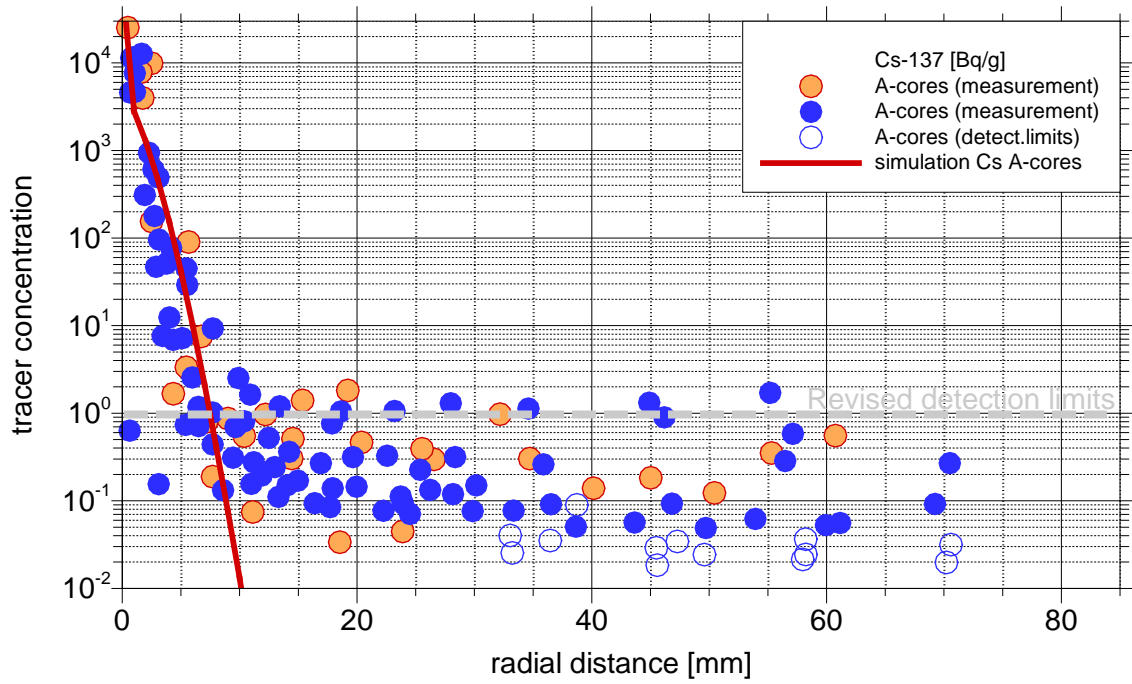


Fig. 4.13 Fit of the two-zone model to $^{137}\text{Cs}^+$ -data from the A-cores

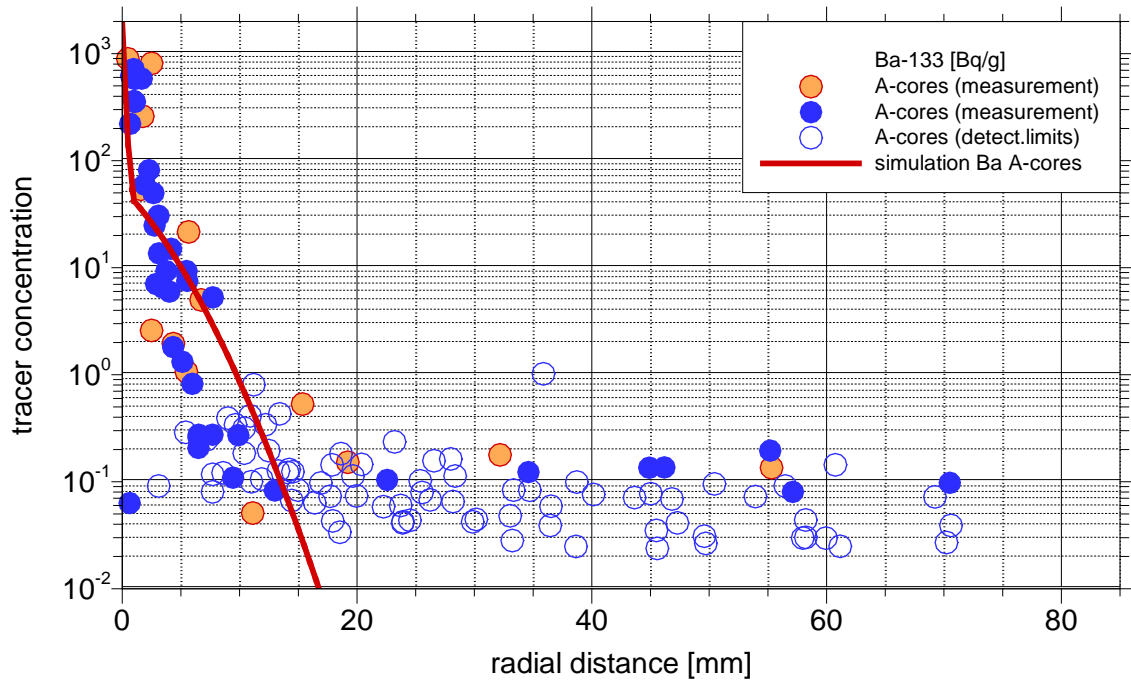


Fig. 4.14 Fit of the two-zone model to $^{133}\text{Ba}^{2+}$ -data from the A-cores

4.1.9 Fitting results for D-cores

The procedure described in the previous section was repeated for the D-cores. However, the results and conclusions are in principle the same as illustrated by Tab. 4.4 and Fig. 4.15 to Fig. 4.18. Note that the approach is more or less able also to account for the tracer profiles that do not show the initial steep concentration gradient as for $^{36}\text{Cl}^-$ and $^{22}\text{Na}^+$ (see Fig. 4.15 and Fig. 4.16).

Tab. 4.4 Fitting parameters for the model results depicted in Fig. 4.15 to Fig. 4.18

D-cores	$^{36}\text{Cl}^-$	$^{22}\text{Na}^+$	$^{137}\text{Cs}^+$	$^{133}\text{Ba}^{2+}$
Φ_{BDZ} [-]	0,001	0,001	0,001	0,001
τ_{BDZ}^+ [-]	0,001	0,001	0,001	0,001
l_{BDZ} [mm]	1	1	1	1
Φ_{matrix} [-]	0,0008	0,004	0,004	0,004
τ_{matrix}^+ [-]	0,005	0,4	0,4	0,4
m [-]	2	2	2	2

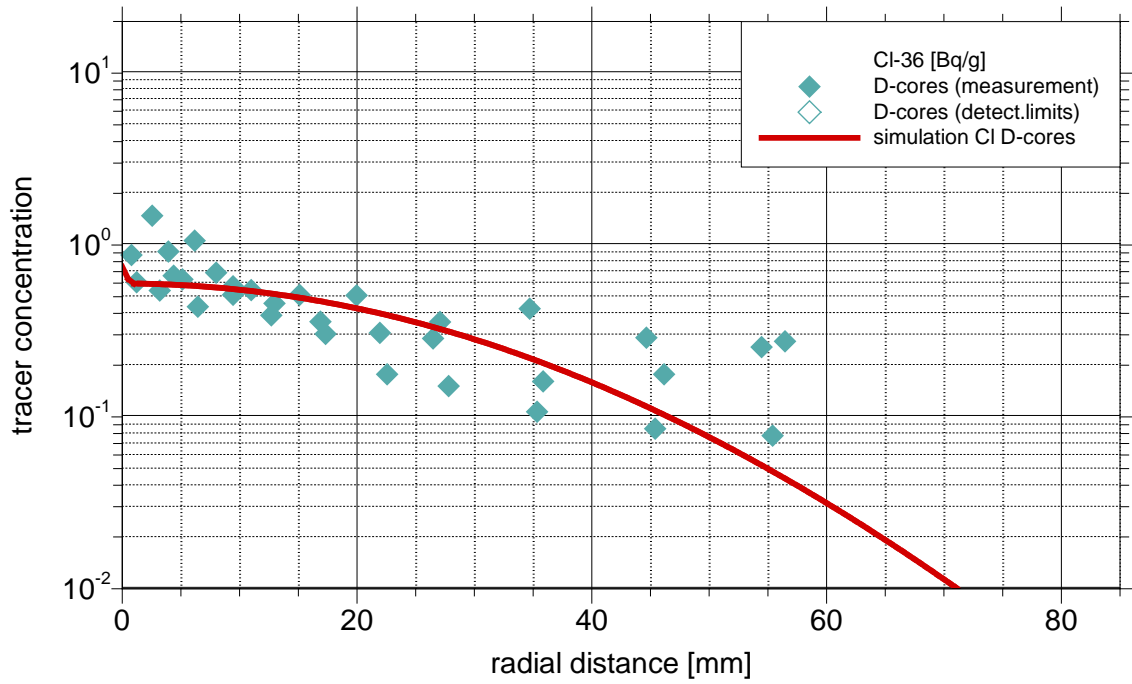


Fig. 4.15 Fit of the two-zone model to ^{36}Cl -data from the D-cores

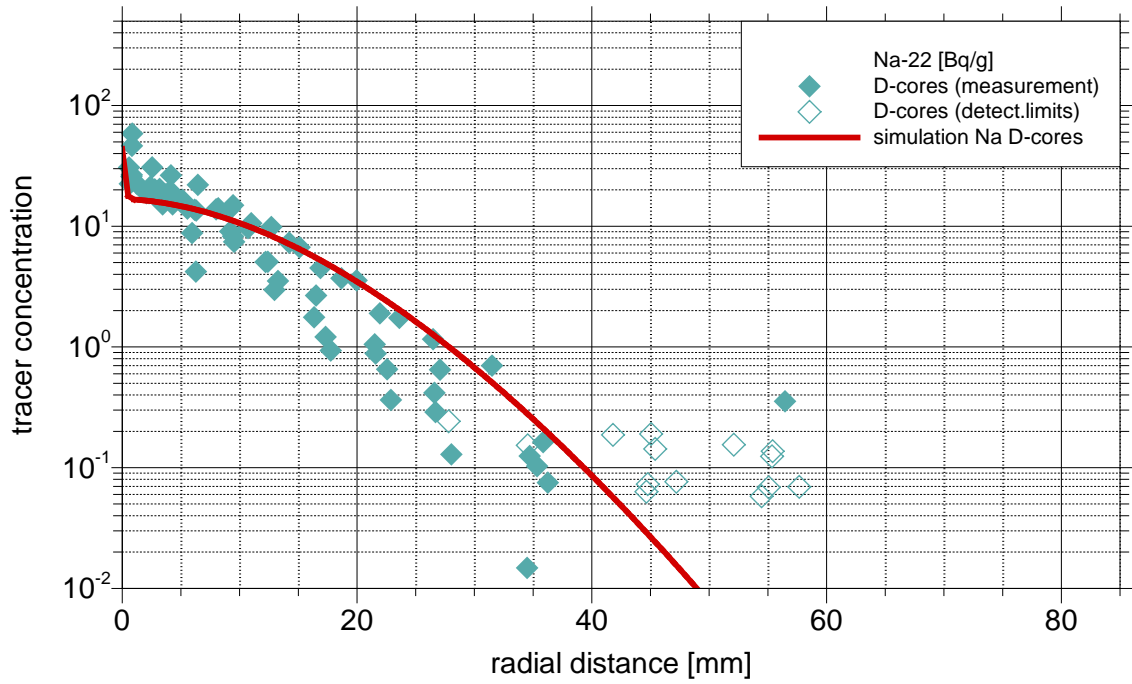


Fig. 4.16 Fit of the two-zone model to $^{22}\text{Na}^+$ -data from the D-cores

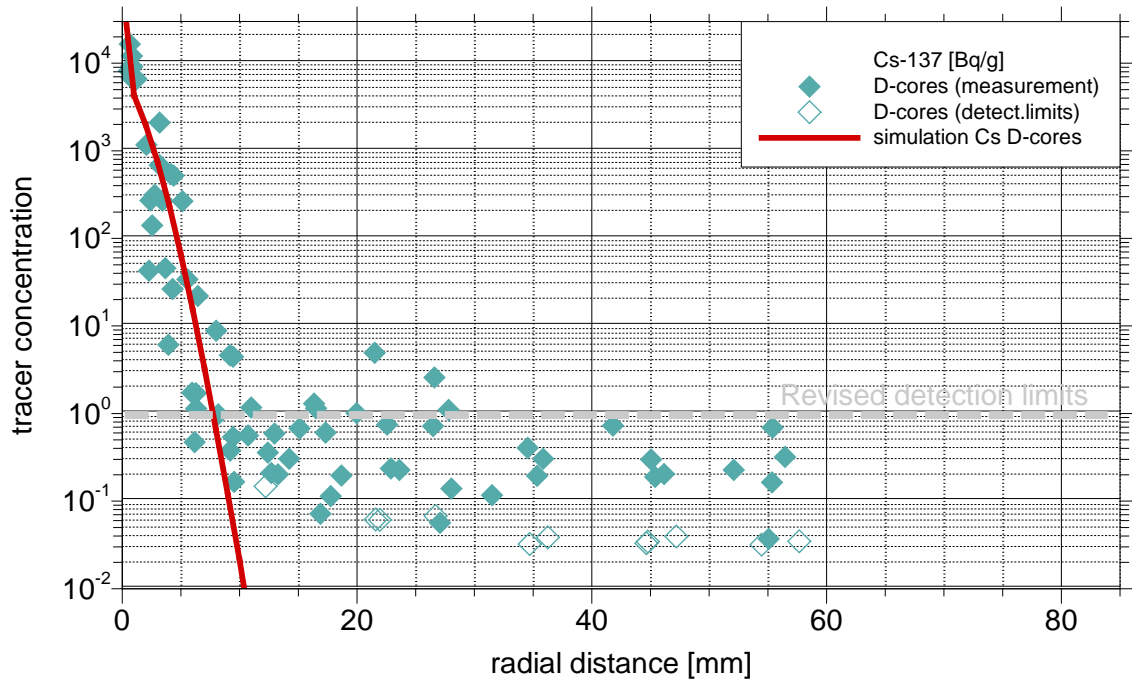


Fig. 4.17 Fit of the two-zone model to $^{137}\text{Cs}^+$ -data from the D-cores

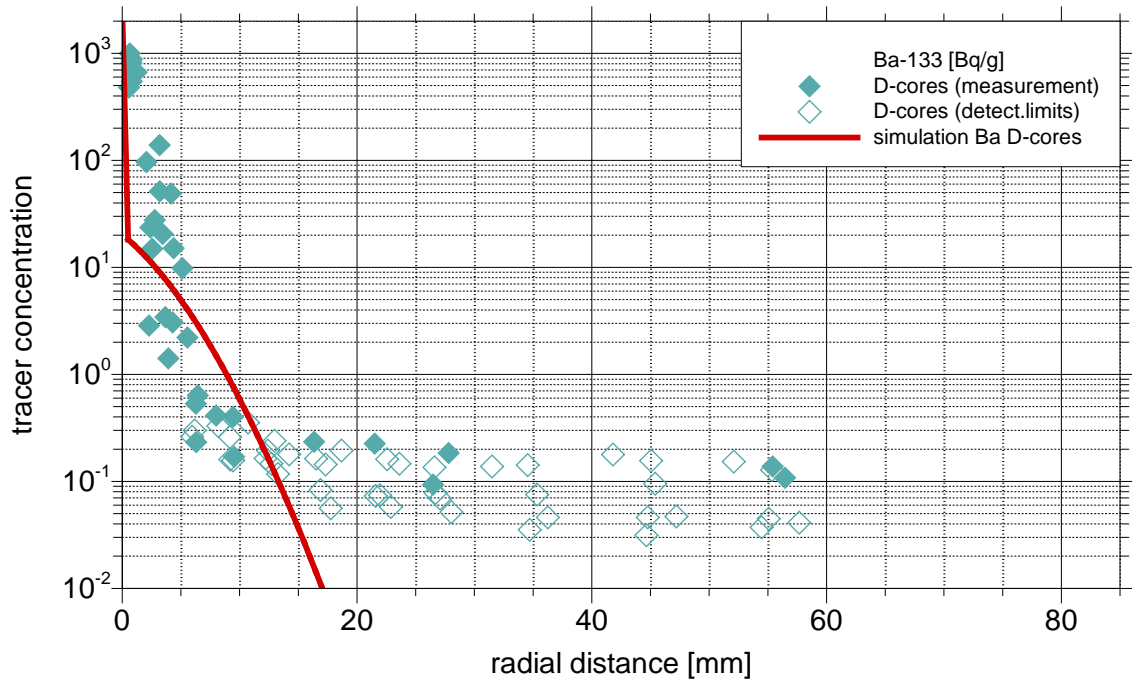


Fig. 4.18 Fit of the two-zone model to $^{133}\text{Ba}^{2+}$ -data from the D-cores

4.1.10 Summary and conclusions

The Long-Term Diffusion Experiment (LTDE) has been carried out at the Hard Rock Laboratory (HRL) Äspö in Sweden in order to check the concepts of diffusion and sorption of radioactive nuclides in crystalline rock. The test set-up was designed in such a way that 22 different solutes could enter the rock via a test borehole or from a controlled section of a natural fracture wall.

Tracer profiles were determined after the end of the test. They showed a peculiar shape, basically a steep gradient close to the rock surface followed by a subsequently much lower gradient without a significant transition zone. Task 9b of the Task Force on Groundwater Flow and Transport of Solutes (TF GWFTS) of the Svensk Kärnbränslehantering (SKB) had therefore become engaged in reproducing the curious concentration curves.

Initially, this had been considered to be a complex chemical problem, drawing the attention of GRS to a potential qualification of the referring options in d^{3f++}. However, despite the gathered expertise among the participants of Task 9b explanation attempts went into numerous entirely different directions. The focus of GRS thus shifted towards finding a plausible mechanism. A major attempt had been the co-organising of a workshop on the so-called “skin-effect”. The results encouraged GRS to check the plausibility of a two-zone model with a disturbed zone close to the rock surface and the undisturbed matrix beyond that.

A preceding data analysis provided valuable insight into reliability of the data as well as into the general structure of granite:

- In some cases the detection limits for the tracers appear to be related to the sub-sample sizes as indicated in Fig. 4.8.
- If the activity values are in the same range and show the same trend as the detection limits as in case of $^{226}\text{Ra}^{2+}$ the activity data becomes meaningless. Concentration values that lie at the detection limits or below must be considered to be at least comparatively badly known and should thus not be used for a comparison with model results.
- Only the activity data for $^{22}\text{Na}^+$, $^{36}\text{Cl}^-$, $^{137}\text{Cs}^+$, $^{57}\text{Co}^{2+}$, and $^{133}\text{Ba}^{2+}$ are entirely or at least partially relevant in that the data points lie clearly above the detection limits.

- Data for $^{36}\text{Cl}^-$ and $^{22}\text{Na}^+$ from the D-cores do not show the steep concentration gradient in the immediate vicinity of the former reservoir.
- Due to the different nature of the disturbed zones for A- and D-cores namely fracture coating and a BDZ, respectively, a principal difference is expected for A- and D-cores.
- There is much less data uncertainty within a drill core than scatter between the cores. This indicates considerable local variation of material properties in the matrix on the scale of the LTDE. Fitting model results to the data can therefore not be done as stringent as it had been hoped for.

As few parameters as possible were used to fit numerical results to the measurements. The fitting procedure was subject to several restrictions that followed from the approach of the two-zone model:

- The geometric parameters Φ and τ^+ for the undisturbed matrix should be the same for all eight models. A possible exception could be lower values for $^{36}\text{Cl}^-$ in case of anion exclusion. These would have to be the same for A- and D-cores, though.
- For the disturbed zone, these parameters should be equal for the A-cores as well as for the D-cores but may be different for A- and D-cores due to the different nature of the disturbed zone (fracture coating or BDZ).
- The same applies to the extension of the disturbed zone and the shape of the transition function for Φ and τ^+ across the disturbed zone.

Six parameters are thus required for each transport model. As four tracers are investigated here and since different models were used for the A- and for the D-cores, all in all eight models have been set up for the fitting procedure. The model parameters resulting from the fitting procedure are listed in Tab. 4.3 for the A-core models and in Tab. 4.4 for the D-core models.

All six models for the cations could be fit in such way that Φ_{matrix} and τ^+_{matrix} are the same (0.004 and 0.4, respectively). Moreover, the porosity derived for the cations as well as the tortuosity⁺-value is reasonably close to expectations for the undisturbed matrix.

For $^{36}\text{Cl}^-$, however, both parameters are considerably lower but nevertheless the same for A- and D-cores (0.0008 and 0.005, respectively). This observation indicates that the anions experienced anion exclusion by very narrow pore channels, indeed. Unfortunately, this means also that $^{36}\text{Cl}^-$ cannot be taken as an ideal tracer for deriving the topological parameters of the pore space. The parameters for the cations thus could not be confirmed by the fitting exercise in step 1 as planned. However, the resulting parameters concerning the undisturbed matrix obey the first condition listed above.

The four parameters concerning the disturbed zone Φ_{BDZ} , τ^+_{BDZ} , l_{BDZ} , and m satisfy the second and the third condition listed above as well. They show different values for Φ_{BDZ} and τ^+_{BDZ} between the A-cores (0.003 and 0.0006, respectively) and the D-cores (0.001 and 0.001, respectively) as expected from the different nature of the disturbed zone. Noteworthy are these parameters also since they seem to be reduced in comparison to the ones for the undisturbed matrix.

A bit unexpected, though, is the observation that l_{BDZ} and m are the same for all eight models (1 mm and exponent 2). Additionally, it has to be conceded that the $^{36}\text{Cl}^-$ -profile from the A-cores indicates rather a depth of 5 mm for the disturbed zone which is unique among the data sets investigated here. No explanation could be found for this observation.

By and large, the parameters derived from the fitting procedure explain the tracer profiles reasonably well, particularly considering that the tracer profiles for $^{36}\text{Cl}^-$ and $^{22}\text{Na}^+$ in the D-cores do not show the characteristic steep concentration gradient at the sample surface at all. At that, the results confirm the plausibility of the two-zone approach with a narrow disturbed zone and an undisturbed matrix. However, this cannot be mistaken for a proof of concept as there are many other explanations for the curious tracer profiles that may prove to viable as well. As long as the true reasons behind the strange tracer profiles are not known, correctness cannot be stated and the relevance for long-term safety cannot be evaluated.

What remains to be noted is certainly the surprisingly high degree of inhomogeneity among the drill cores that led to nice individual tracer profiles but a quite broad band when all data points were put together. It might be worthwhile to fit the curve parameters to each individual curve and to derive the uncertainty that is the consequence of the local inhomogeneity. Qualitatively, the data scatter between the different curves should also

be taken as a warning to be careful if using a homogeneous model for transport phenomena in crystalline rock.

4.2 Äspö Site Descriptive Model (SDM)

4.2.1 Background and motivation

The Hard Rock Laboratory (HRL) Äspö is in south-eastern Sweden and has operated since 1995. Local groundwater flow has an immediate impact on running the HRL in terms of mine drainage and the hydraulic conditions at the location of in-situ experiments. It is, however, only a comparatively small part of a much larger groundwater flow system that controls the local flow. Understanding of the local groundwater thus requires understanding flow on a regional scale and was sought from the beginning on.

A lot of effort in that direction has again been spent during the first decade of the third millennium when the nearby Laxemar region had been one of the two potential sites for the Swedish high-level waste repository. The work reported here can be seen as a rerun of these models with up-to-date methods, tools, and new aspects like thermally driven flow.

The work presented here is focused on establishing pre-excavation flow conditions as a prerequisite for a hydrogeologic description of the flow system during the operational phase of the HRL. It is divided into three parts, a review of approaches and data from the earlier exercises, 2-D pre-studies on the flow field to sharpen the view for possible problems and the 3-D regional scale model.

4.2.2 Review of approaches and data

Model domain

Previous studies have been considering different scales. Among them are

- the supra-regional models (SM) on the scale of 100 km by /ERI 06/, /ERI 10/ and
- regional scale models with a length of about
 - 50 km (RM1) by /HOL 08/
 - 20 km (RM2) by /RHÉ 08/, /RHÉ 09a/, /RHÉ 09b/ with focus on Laxemar
 - 20 km (ÄM) by /SVE 08/ with focus on Äspö.

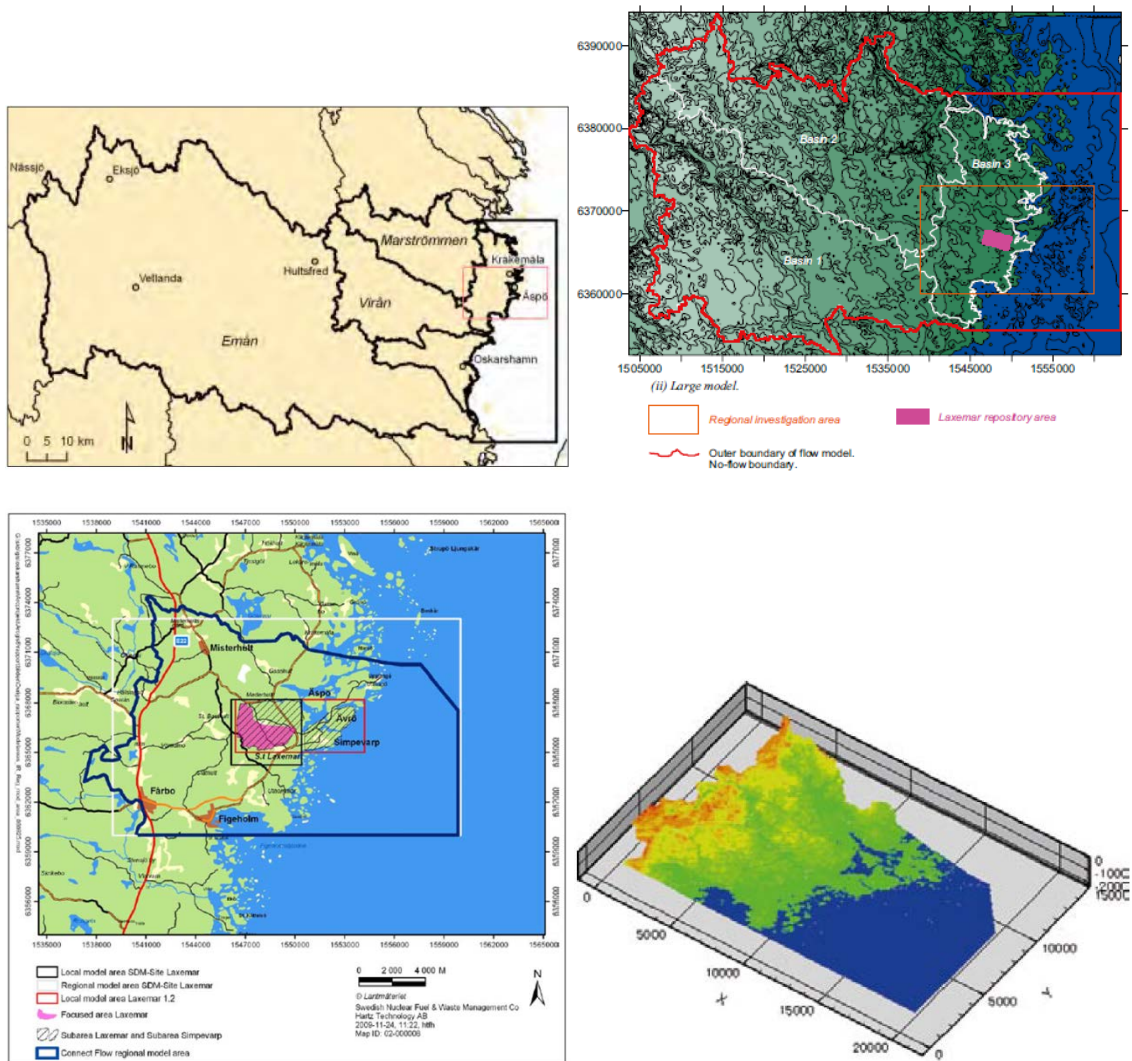


Fig. 4.19 Model areas for SM (top left), RM1 (top right), RM2 (lower left) and ÅM (lower right); from /ERI 06/, /HOL 08/, /RHÉ 09a/, and /SVE 08/

Generally, it has been tried to align the horizontal model boundaries with the known catchment areas. The work from /ERI 06/ shows that the catchment area Emån (see top left map in Fig. 4.19) is hydraulically separated from the neighbouring areas Virån and Oskarshamn because the water divide between these areas reaches even down to the deep groundwater. Contrary to this, the divide between the coastal catchment area and the Virån and the Maströmmen basin works only down to a certain depth. It appears that there is a hydraulic connection in the deep groundwater /HOL 08/. However, assuming a complete water divide for RM2 leads to longer travel times by a factor of 1.3 for the groundwater in comparison to RM1 with deep groundwater crossing this divide /RHÉ 09a/. RM2 does therefore not contain the Virån and the Maströmmen basin and only a part of the coastal catchment area. Note that the horizontal model boundary of

RM2 is basically identical to that of the ÄM. An even slightly smaller regional catchment area as shown in Fig. 4.20 is suggested by /WER 05/ and confirmed by /MOR 17/.

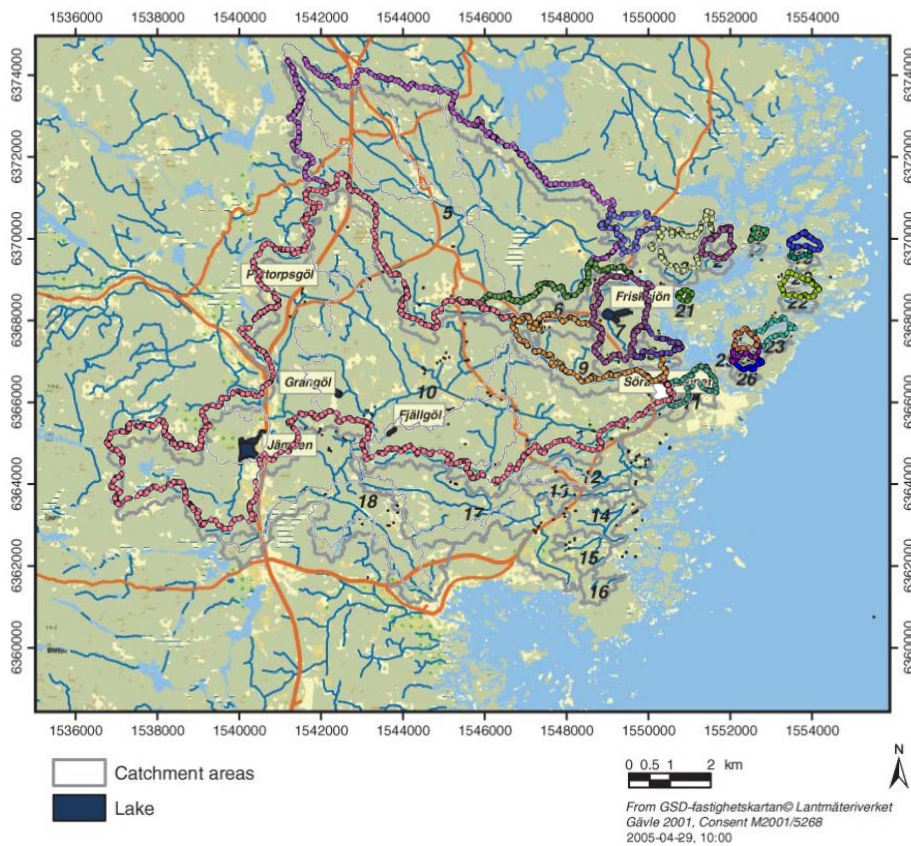


Fig. 4.20 Overlay of catchment areas in the coastal region; from /WER 05/ and /MOR 17/

A general impression of the surface topography is given by /RHÉ 09a/ for the RM2 as shown in Fig. 4.21. Later on, a very detailed Digital Elevation Model (DEM) has been provided by SKB.

There is no obvious known feature suggesting a possible position of the lower model boundary. The models are therefore simply horizontally cut at the bottom. The chosen depth varies from model to model, though:

- Supraregional models (SM): 2500 m and 6000 m, respectively
- Regional model 1 (RM1): depth: 2500 m
- Regional model 2 (RM2): depth: 2160 m
- Äspö regional model (ÄM): depth: 2100 m

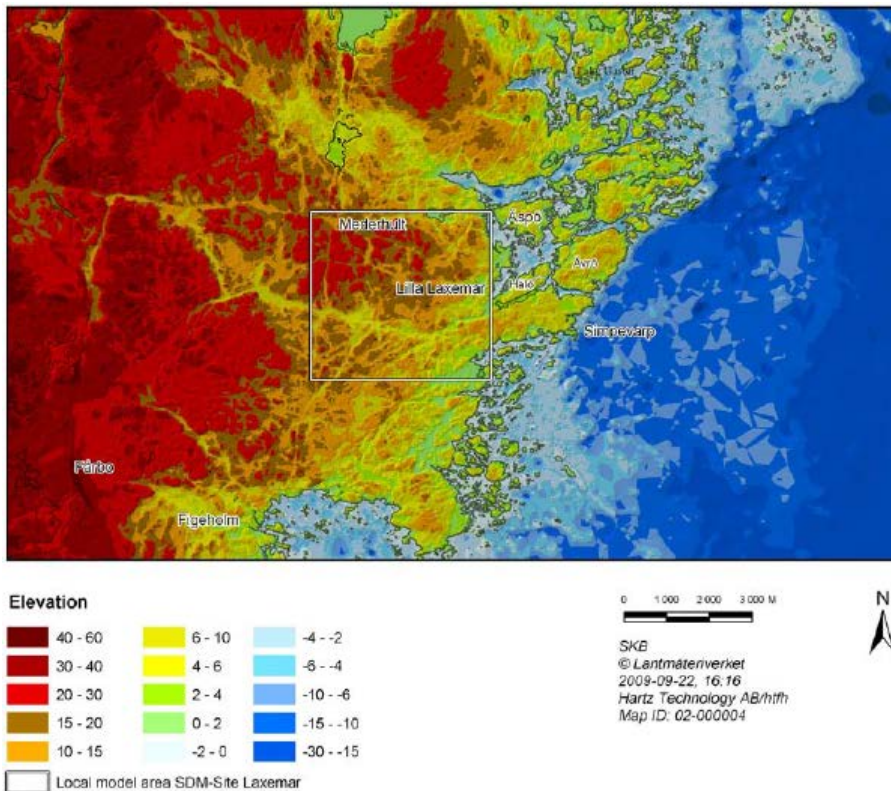


Fig. 4.21 Map of ground-surface topography in the area of RM2; from /RHÉ 09a/

The results from the model by /ERI 10/ with a depth of 6000 m confirmed the suspicion that considering a greater depth in the flow model would not change the outcome of the transport simulations considerably.

Upconing of salt water from a depth of 1,000 m to 1,200 m has been observed at Äspö /MOR 17/.

Basically, there are three hydrogeological features: the regolith on top, the bedrock below and fractures as well as fault zones in the rock. This generally accepted model concept is nicely illustrated in /RHÉ 09b/ by a 3D-graphic (see Fig. 4.22) and associated vertical cross-sections (Fig. 4.23).

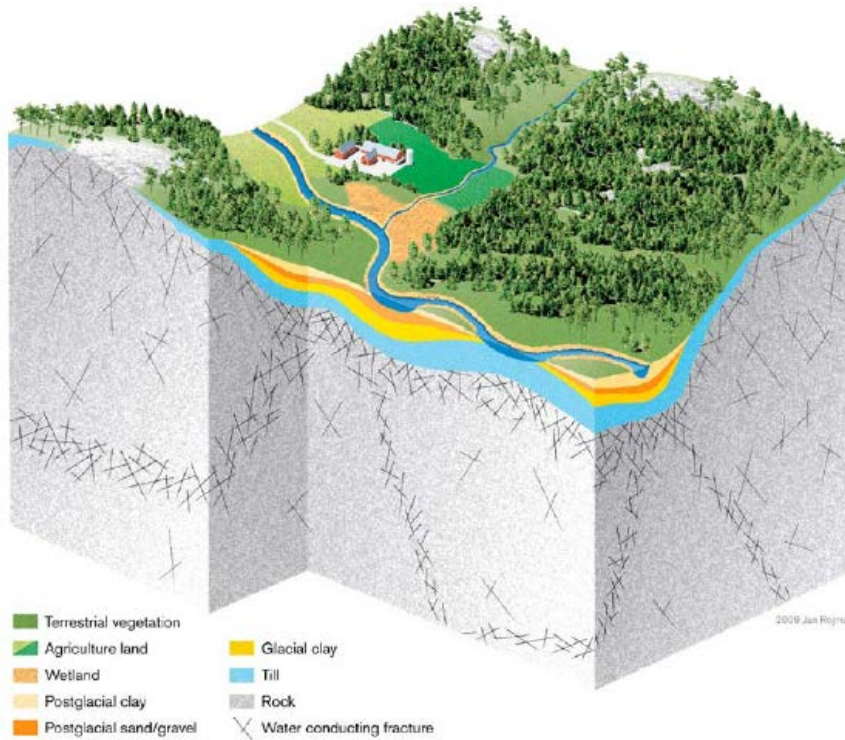


Fig. 4.22 Conceptual understanding of the underground at a typical valley at Laxemar; from /RHÉ 09b/

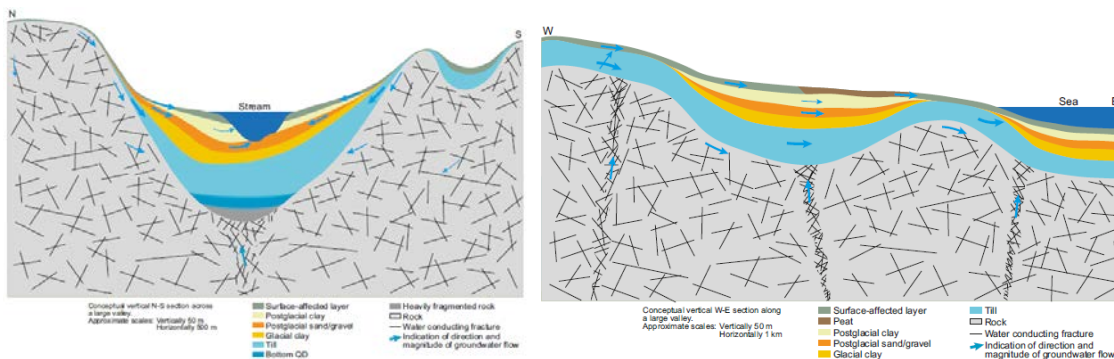


Fig. 4.23 North-west and west-east cross-section through the valley in Fig. 4.22, the graphics are exaggerated by a factor of 20 in the vertical direction; from /RHÉ 09b/

Regolith

The regolith consists of different kinds of unconsolidated quaternary deposits, such as till, clay and peat, together with artificial filling material /NYM 08/. They were formed dur-

ing the Quaternary period which is why the regolith is sometimes called Quaternary deposits in the reports. Generally, distribution and thickness of the regolith layer depends on the topography of the underlying bedrock (for details see /RHÉ 09a/).

The thickness of the regolith does not appear to be an entirely settled matter as reports addressing this property in the framework of the RM1 /HOL 08/ and the RM2 /RHÉ 09a/ are a bit contradictory. In general, the thickness can be expected to reach several meters only except for local “low-altitude ‘valley’ type areas” where the thickness might reach even 50 m /RHÉ 09a/ (cp. Fig. 4.23). Note, that Quaternary deposits have also been identified offshore.

For modelling, the regolith layer creates issues particularly in areas with little thickness. Several strategies for representing this layer have been adopted:

- Representation by a uniform 3 m thick layer of silty till (/HAR 06a/)
- Representation by a three layers model of varying vertical thickness and spatial variations in the soil types within each layer based on the Quaternary deposits (QD) model of /NYM 08/ (/HAR 07/).
- Representation by a layer with a uniform thickness but elementwise adapted effective hydraulic conductivity according to the spatial variability and anisotropy of the models of Quaternary deposits, as specified in /WER 08/ or /SOH 08/ (/FOL 07c/).
- Representation by an artificial layer whose hydraulic conductivity decreases with depth until the “bedrock characteristics” are reached at 20 m depth (/SVE 08/).

Hydraulic conductivity at the surface is dependent on the material and supposed to be in the range of 10^{-6} to 10^{-4} m s⁻¹ /ERI 06/, /HOL 08/. In the model of /SVE 08/ even a local value of 10^{-3} m s⁻¹ can be found.

The infiltration capacity of the Quaternary deposits in Laxemar is generally considered to exceed the rainfall intensity and the snowmelt intensity /WER 08/.

Bedrock

While a map of lithological units for SM looks quite complex (see /ERI 06/, /BER 03/) the situation appears to be much simpler when the view is restricted to the coastal areas as

shown exemplarily in Fig. 4.24. For all models except one it is assumed that the lithological units found at the surface are vertically extending to the bottom, see for instance Fig. 4.25. In case of the RM2 a true 3D-distribution by /WAH 08/ depicted in Fig. 4.26 has been used. This has been the only model with such a feature but, unfortunately, it could not be reproduced based on the published data.

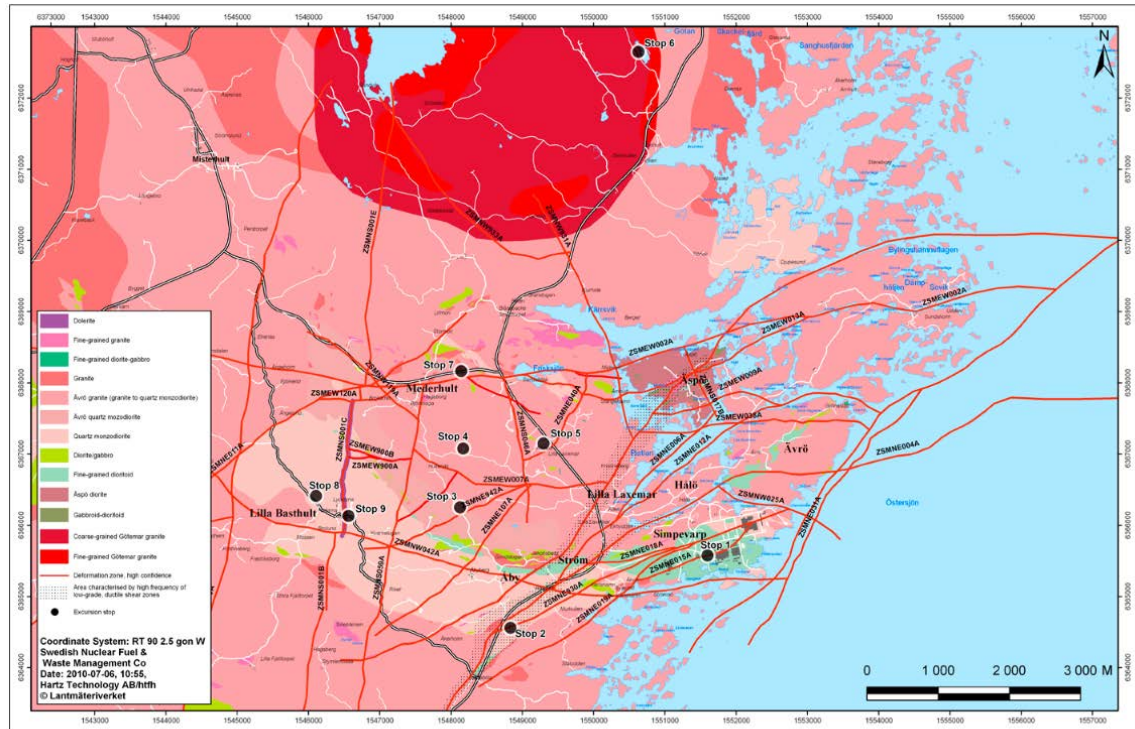


Figure 3-2. Combination of the bedrock geological map from the model version 0 /SKB 2002/ and the detailed bedrock geological map of the Laxemar-Simevarp area.

Fig. 4.24 Map of lithological units from /WAH 10/

Also the task of assigning the hydraulic properties to the lithological units has been handled differently in different models. /ERI 06/ (SM) and /HOL 08/ (RM1) use a continuum where the permeability is determined stochastically for several cells of each rock unit. A depth-dependence of the permeability is considered in RM1 /HOL 08/ as well as in all other models. For RM2 /RHÉ 09a/ derive permeabilities for an equivalent porous medium based on a DFN.

The hydraulic conductivity data for these models appear to be somewhat high. By contrast, background information for modelling groundwater flow at Äspö in the framework of Task 8 of the Task Force on Groundwater Flow and Transport of Solutes of SKB indicate very low hydraulic conductivities, e. g. 10^{-11} to 10^{-13} m s⁻¹ for granodiorite. According to on-site experience at Äspö, though, the rock at Äspö should be more permeable than the rock in the surrounding areas /MOR 17/.

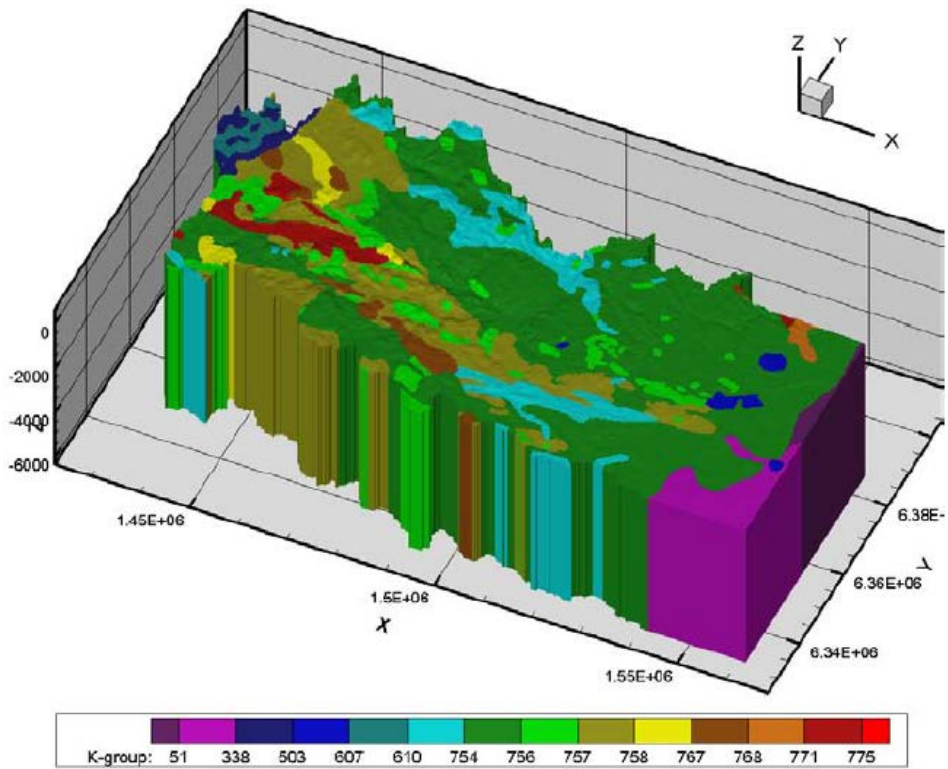


Fig. 4.25 3D-view of lithological units in the SM; from /ERI 10/

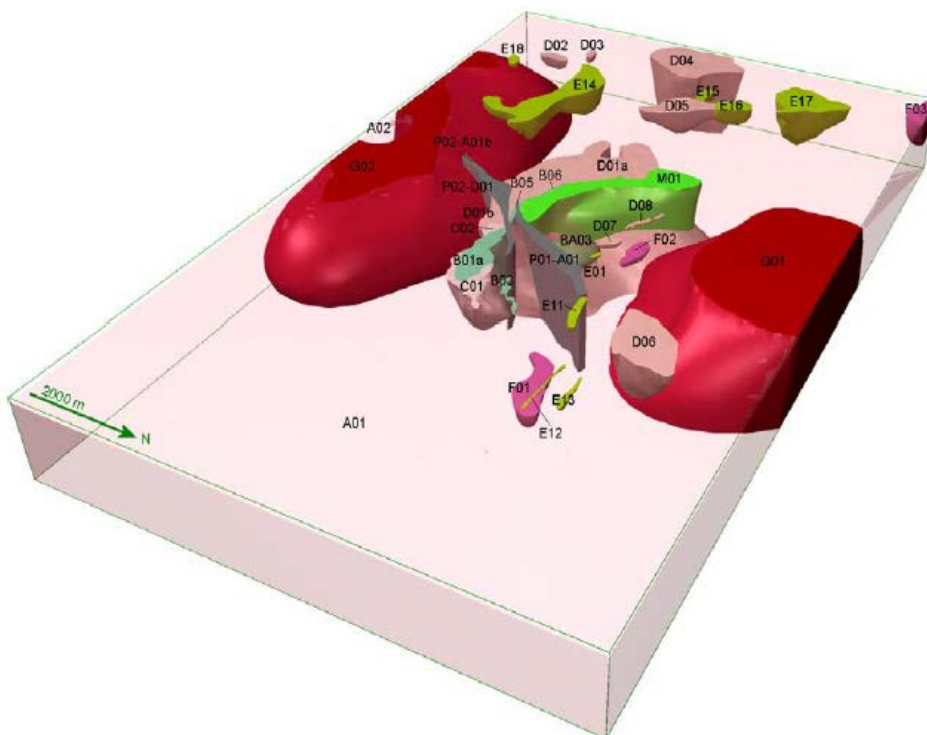


Fig. 4.26 Lithological units in the model for RM2; from /WAH 08/

This seeming contradiction has motivated an extensive study of the SKB-literature. Considered is as much material as possible concerning the general area of Äspö, Simpevarp and Laxemar (see appendix A). What is found is a vast amount of conductivity data covering an astonishing range of values, indeed. If applicable, the related data about location, borehole depth, depth of measurements, and length of test interval in the borehole (test-scale) are compiled as well. Subsequent analyses are performed with the help of Microsoft Excel.

The data has been divided into data sets for the locations of Äspö, Simpevarp and Laxemar. For each of the three data sets the test-scale is related to the determined hydraulic conductivity by defining length ranges (classes) according to the different test set-ups. All related conductivity values are geometrically averaged, first within each class for each site, then between the related classes for the three sites, if applicable.

The result is compiled in Tab. 4.5 showing the classes of test-scales and the resulting conductivity values. There is a clear trend to lower conductivities with decreasing test-scale except for a slight deviation for the scale 300 m. This data point is rather uncertain, though, as it is derived from eleven measurements between 600 m and 2000 m depth. Only one of these was done at Äspö. The origin of the other ten remains to be unclear. Included are also data from the Geological Survey of Sweden (SGU) Well Archive leading to the conclusion that the cited value might be biased /RHÉ 97c/.

Tab. 4.5 Relation of test-scales and the resulting hydraulic conductivity

Test-scale	Hydraulic conductivity [m s^{-1}]
300 m	4,7E-08
125 m	9,0E-08
100 m	6,0E-09
10 – 30 m	1,5E-09
0.5 – 10 m	7,1E-11
0.02-0.20 m	1,9E-12
0.005 m	4,7E-14

This result confirms the notion that an increasing test-scale would not only include an increasing number of fractures in the test but also increasing the chance of including the comparatively scarce fractures with high transmissivities.

The hydraulic conductivity data have also been examined with a view to depth dependence, ignoring all data with a test-scale of less than 100 m in order to avoid a bias from lower conductivity values. Note that in case of Simpevarp there were actually no tests below a test-scale of 100 m so that there is no change in the results from this restriction. In case of Äspö and Laxemar, though, where small-scale tests comprise more than the half of all tests, the mean hydraulic conductivity increases by a factor of 65 and 144, respectively, due to excluding the smaller test ranges from consideration.

The remaining data are depicted in Fig. 4.27. As the data appear to be a bit confusing, they are shown also in Fig. 4.28 separated according to their location. It becomes apparent that there is a clear distinction between the data for Äspö and the data for Laxemar and Simpevarp. While the plots for Laxemar and Simpevarp indicate a significant depth-dependence of the hydraulic conductivity this seems to be very slight at Äspö if there is such dependence at all.

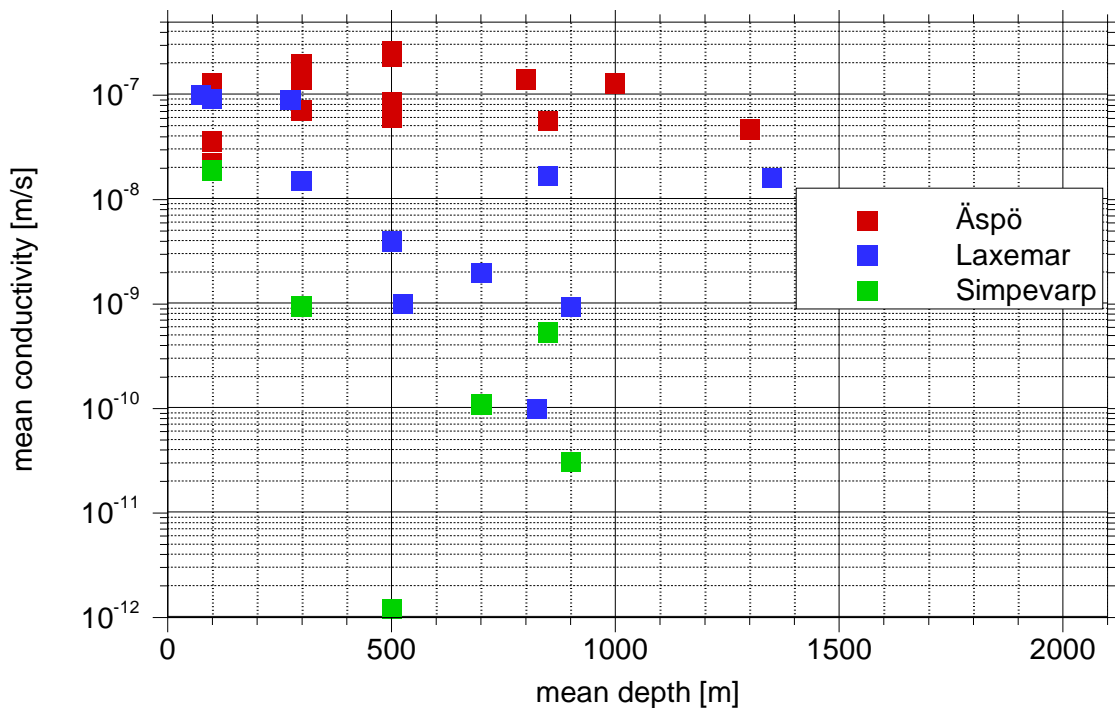


Fig. 4.27 Depth-dependent hydraulic conductivities for all three locations

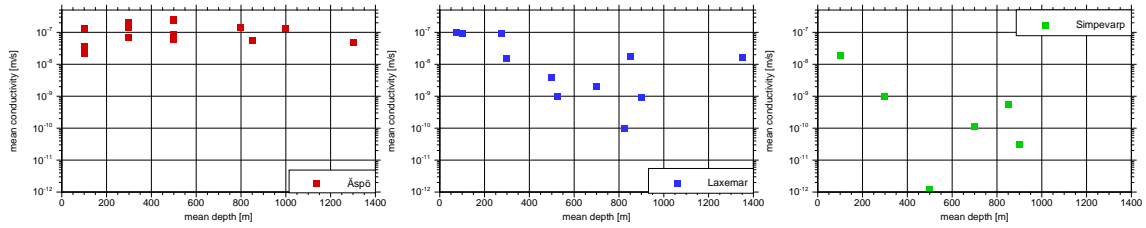


Fig. 4.28 Depth-dependent hydraulic conductivities separately for the three locations

For each of the three data sets a function is fitted to the data according to the approach that the permeability at the ground surface decreases by one order of magnitude over a depth of c [m]:

$$K = K_0 \cdot 10^{\left(\frac{z}{c}\right)} \quad (4.4)$$

K - hydraulic conductivity [m s^{-1}]

K_0 - reference hydraulic conductivity at $z=0$ m [m s^{-1}]

z - vertical coordinate (upwards positive) [m]

c - depth over which a decrease of a factor of 10 in K occurs [m]

The results are shown in Fig. 4.29 to Fig. 4.31. The underlying parameters are compiled in Tab. 4.6. Since the data as well as the fitted functions for Laxemar and Simpevarp seem to be similar, a function for the combined data sets is eventually developed. The parameters are also included in Tab. 4.6 and a comparison of data sets and functions for these two sites are depicted in Fig. 4.32.

Tab. 4.6 Parameters for the fitted functions for the three locations

Location	K_0 [m s^{-1}]	c [m]
Äspö	$1.7 \cdot 10^{-7}$	3000
Laxemar	$1.0 \cdot 10^{-7}$	400
Simpevarp	$0.5 \cdot 10^{-7}$	300
Laxemar and Simpevarp	$1.0 \cdot 10^{-7}$	330

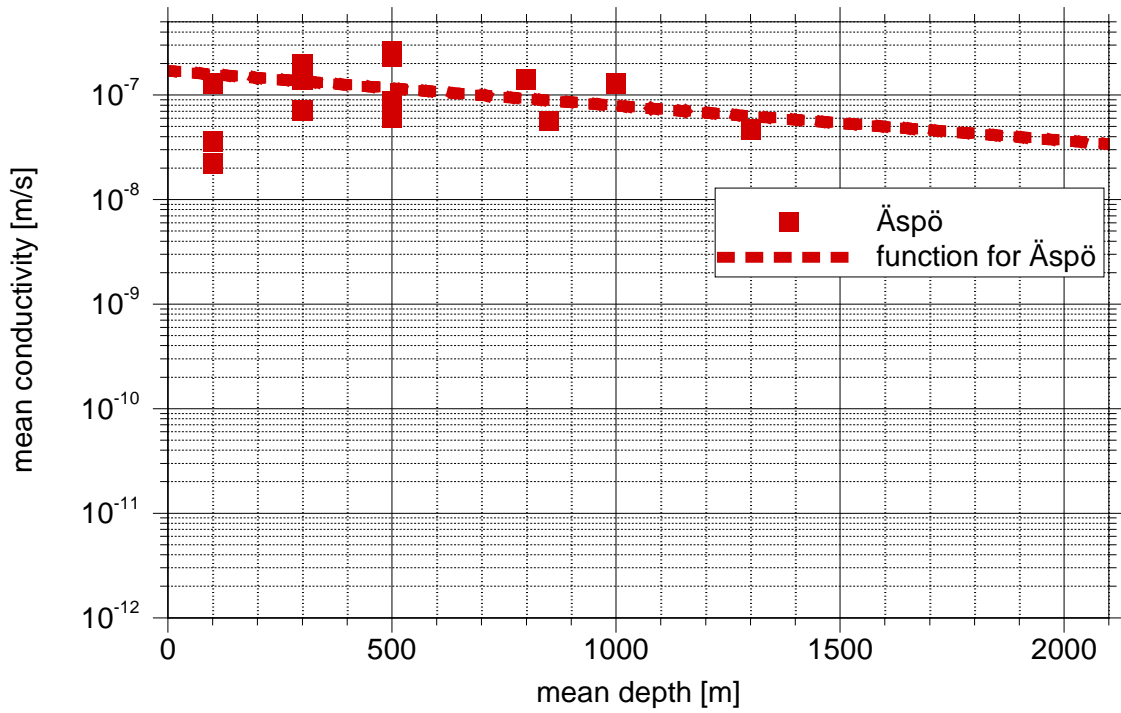


Fig. 4.29 Tentative function for the depth-dependent conductivities at Äspö

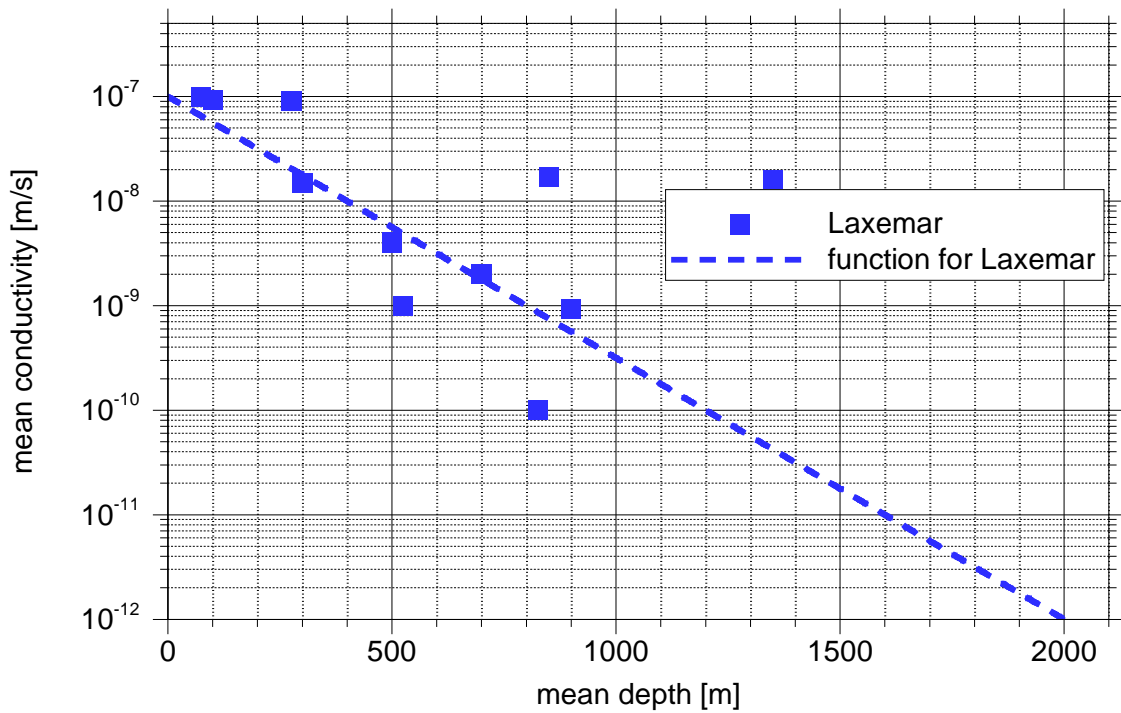


Fig. 4.30 Tentative function for the depth-dependent conductivities at Laxemar

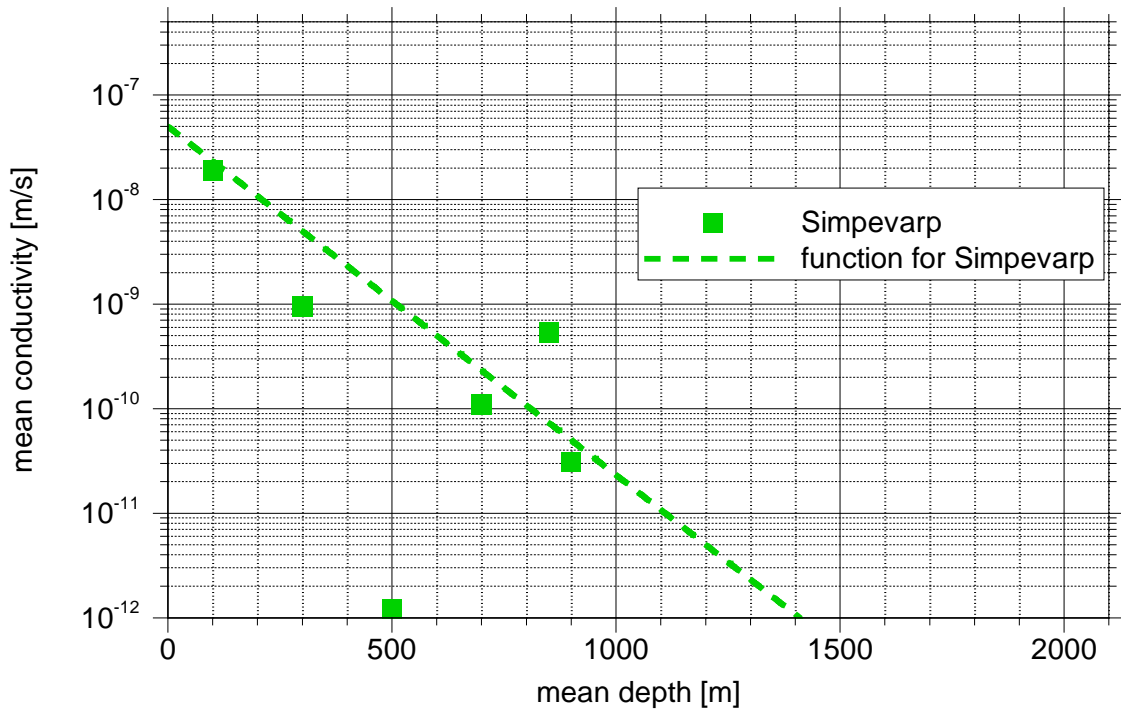


Fig. 4.31 Tentative function for the depth-dependent conductivities at Simpevarp

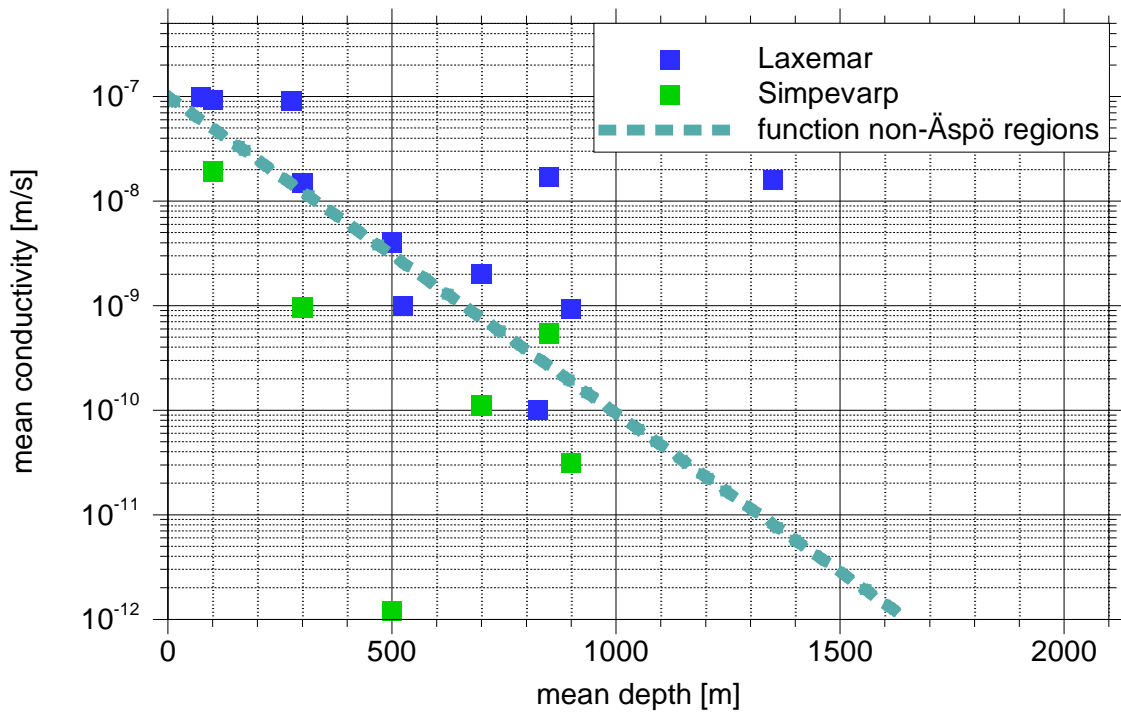


Fig. 4.32 Depth-dependent conductivities at Laxemar and Simpevarp

Generally, there is a huge scatter in the conductivity data which excludes the possibility of a identifying a differentiated hydraulic conductivity field. The data just allow to differentiate between the larger areas at Äspö, Laxemar and Simpevarp even more so as most of the data has already been processed beforehand by other authors. At all steps from measurement to published data, some kind of averaging was involved where it is not clear if the single data points in a borehole were equally distanced or which kind of average (arithmetic or geometric) has been used. The results derived from the published data have therefore to be considered with due care.

From a geohydrologic point of view the underground of Laxemar and Simpevarp is quite similar regarding the absolute conductivity value as well as its clear depth-dependence. This relation is only seriously defied by three data points. The two high values at Laxemar are related to measurements in boreholes of great depth, 0-1700 m and 1000-1700 m (see Fig. 4.33), where the value in the second case is additionally based on two locations only. The process of deriving the related mean for each of these two tests would therefore require closer inspection. The very low value at Simpevarp can only be explained by missing by chance any seriously conducting fracture network over the whole test section of 100 m.

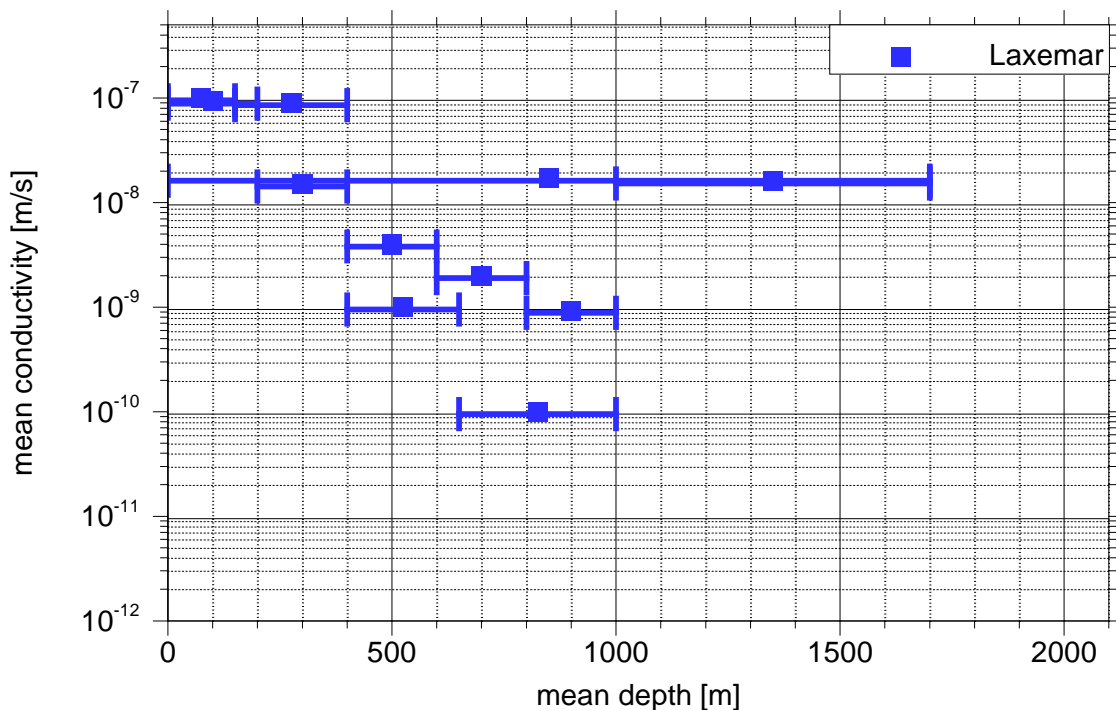


Fig. 4.33 Hydraulic conductivities and related test sections at Laxemar

The depth-dependence as quantified with eq. (4.4) together with the parameters in Tab. 4.6 and as illustrated in Fig. 4.32 appears to be a good approximation for Laxemar and Simpevarp. At Äspö, by contrast, the hydraulic conductivity does only change slightly with depth, if at all.

Fig. 4.24 shows that three different rock types dominate the Simpevarp and Laxemar area: Fine-grained dioritoid, Quartz monzodiorite and Ävrö granite. This could indicate that different hydraulic properties should be set for each unit. However, the conductivity values as listed in /RHÉ 06/ differ only about one order of magnitude between these three lithological units. Thus, the effect of depth on the hydraulic conductivity seems to be greater than the variability due to the rock type.

The values used for the analysis of conductivity mentioned above come from all three units e. g. /RHÉ 06/ and it is therefore assumed that the derived mean value and depth trend is applicable to the whole area around Simpevarp and Laxemar.

Contrary to Simpevarp and Laxemar, the geology of Äspö is dominated by Äspö diorite. According to Fig. 4.24 the spatial distribution at the surface of Äspö diorite is restricted to Äspö island. Data from boreholes show that also fine-grained granite and gabbro-dioritoid play an inferior role /CAR 17a/, /CAR 17b/, /CAR 17c/, /PET 17/. In some boreholes, Ävrö granodiorite is found as dominating rock type either in the upper part (e. g. in KAS03 /PET 17/) or in the bottom part (e. g. in KAS02 /CAR 17a/, KAS09, KAS12 /PET 17/). Ävrö granodiorite is not explicitly addressed in /RHÉ 06/ as an own rock type but seems to be subsumed under the rock type Ävrö granite. This corresponds to the information from /WAH 10/ that the term Ävrö granite is a loose field term used for a variety of rocks that vary in composition from granite to granodiorite and quartz monzodiorite.

The borehole data in /CAR 17a/, /CAR 17b/, /CAR 17c/, /PET 17/ do not reveal a clear picture about the geology at Äspö at great depth. In borehole KAS03 alternating sequences of Äspö diorite, fine-grained granite, gabbroid-dioritoid, and – above 303 m – of Ävrö granodiorite are found down to a borehole length of 900 m. The last 24 m, however, consist of Ävrö granodiorite. On the other hand, in KAS02 Ävrö granodiorite, gabbroid-dioritoid, and fine-grained granite are found in the upper 966 m and Äspö diorite is observed in the bottom 38 m. These findings leave open whether Äspö diorite continues in its spatial extent down to greater depth or whether the main diorite body is found in the upper 1,000 m. Many porosity data can be found in /RHÉ 08/.

Deformation zones

Deformation zones, also called fault zones, are defined in /RHÉ 06/ as deterministic large planar fracture zones that are generally, but not always, more conductive than the surrounding rock.

Apparently, deformation zones come in different sizes so that the choice of a relevant system of such zones depends among other things on the model size. For the SM it is exemplarily depicted in Fig. 4.34.

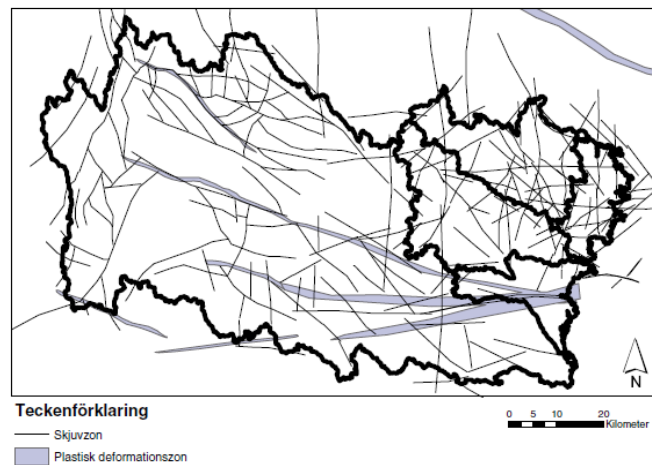


Fig. 4.34 Location of fault zones in the SM; from /ERI 10/

The also quite large RM1 has been treated like the SM except for a part of particular interest. Here, a much more detailed fault system has been incorporated which requires a certain adaption in order to accommodate a plausible transition from the coarse to the finer resolved fault system. The difficulties comprised the different density of fault zones in the two parts of the model as well as the fact that the fault zones had been treated as strictly vertical in SM but included subvertical to subhorizontal structures in the more detailed part of the model. Both fault systems are depicted in Fig. 4.35 and Fig. 4.36, respectively.

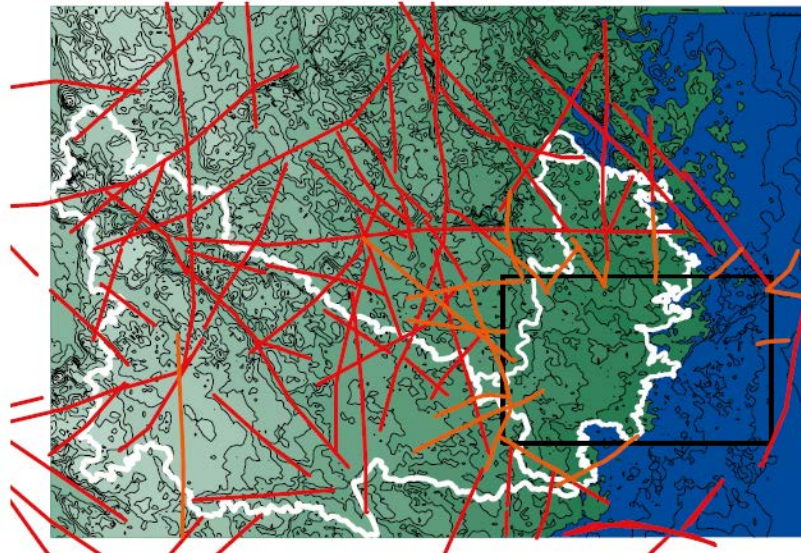


Fig. 4.35 Supra-regional fault zones in the RM1 and local zone of interest; from /HOL 08/

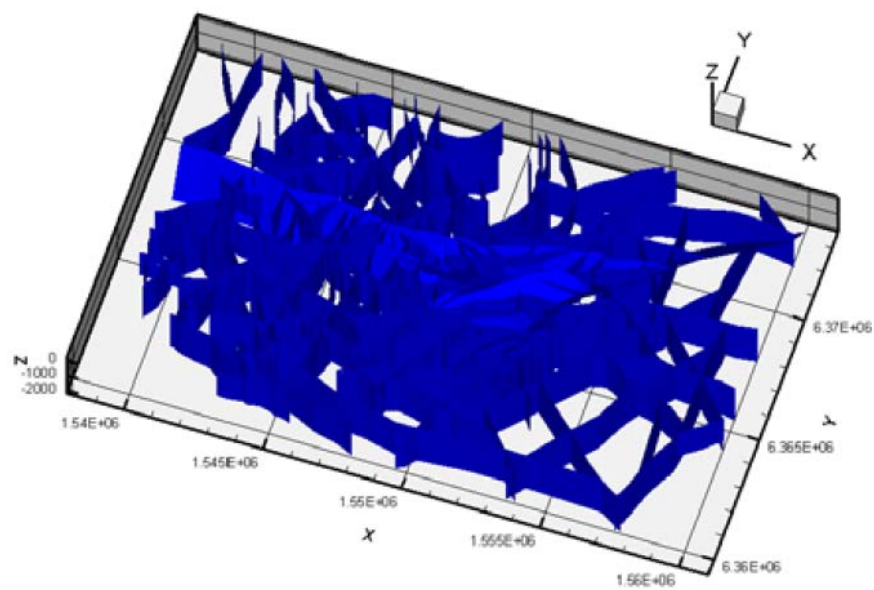


Fig. 4.36 Local fault zones in the RM1; from /HOL 08/

Major fault zones for the RM2 (and thus also for the ÄM) are depicted in /RHÉ 09a/ (see Fig. 4.37).

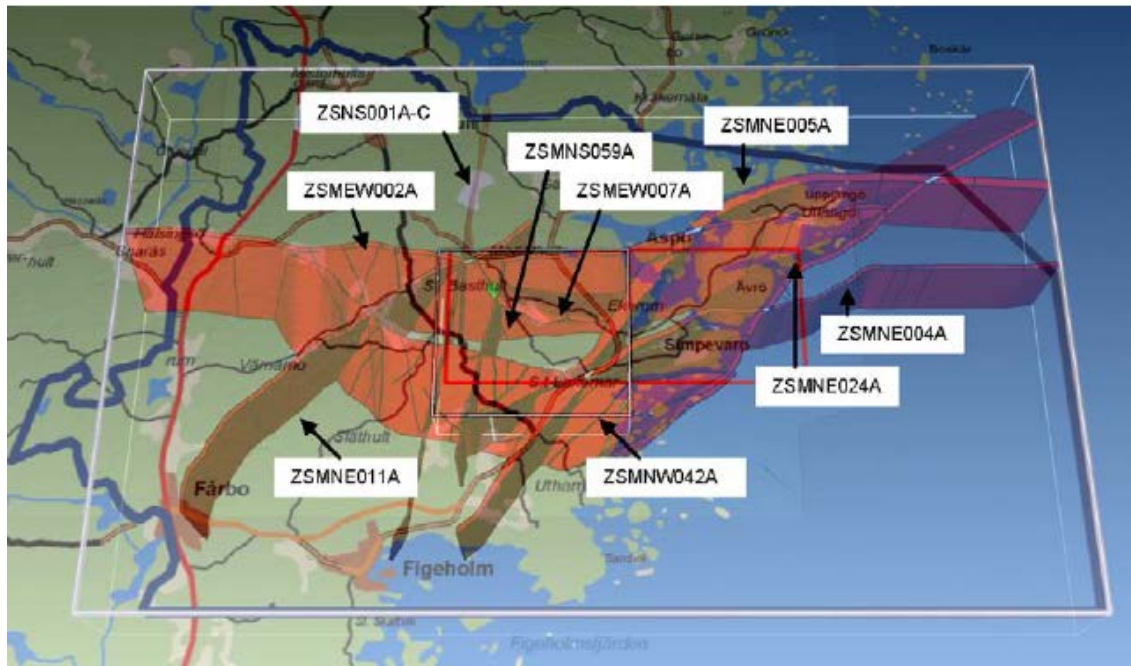


Fig. 4.37 Perspective view of some major fault zones; from /RHÉ 09a/

The thicknesses of the deformation zones inside the focused volume of RM1 are up to a few tens of metres. Since this focused volume coincides rather well with the RM2 and the ÄM, this information also applies to the RM2 and the ÄM. The thickness may vary, but it is judged to be of minor importance since transmissivity controls the flow in the deformation zones /RHÉ 09a/.

It has been shown that the hydraulic conductivity was about 100 times less in vertical boreholes compared to horizontal boreholes, indicating that subvertical fractures are the dominant conductive fractures at Äspö /RHÉ 09a/.

Mostly, the conductivity/transmissivity has been considered to decrease with depth but being constant in the horizontal direction. For the ÄM, however, the transmissivity has been treated as a lognormal distribution /SVE 08/ based on information from /VID 03/. Hydraulic conductivity decreases by a factor of 10 for every 400 metres and porosity and specific storage decrease by a factor 10 for every 800 metres.

/RHÉ 08/ lists in Appendix 3 site specific data for the deformation zones employed in the models for the Laxemar Site. Here, best choice transmissivity values are given as well as the estimated true thickness of the deformation zones ("Zone thickness"), elevation of the test section and mean values for the transmissivity. The evaluation methodology

with the principles for the choice of the best transmissivity values is explained in Section 7.1.2 in /RHÉ 08/.

/RHÉ 08/ derived deformation zone specific depth trends but also depth trends for groups of deformation zones depending on their orientation and size according to

$$T = 10^{(a+Bz)} \quad (4.5)$$

T - transmissivity [$\text{m}^2 \text{s}^{-1}$]

z - depth [m]

a, B - parameters

Most deformation zone specific depth trends are considered uncertain due to lack of data. In these cases, the use of the depth trends for groups of deformation zones are advised by /RHÉ 08/. The corresponding parameters are compiled in Tab. 4.7.

Tab. 4.7 Depth dependence of fault zones according to /RHÉ 08/

Model ID	Data type	Coeff. a	Coeff. B	Corr. coeff. r^2
DZ-R-19	T(1). Regional data, Zone E-W size < 2 km	-4.665	0.00263	0.95
DZ-R-20	T(1). Regional data, Zone E-W size > 2 km	-4.091	0.00187	0.773
DZ-R-21	T(1). Regional data, Zone NW-SE, N-S, NE- SW size < 2 km	-4.997	0.00250	0.83
DZ-R-22	T(1). Regional data, Zone NW-SE, N-S, NE- SW size > 2 km	-4.070	0.00274	0.83

T(1): Total transmissivity within a HCD. Regression based on mean values of $\log_{10}(T)$ for depth zones (4 data points)

/RHÉ 08/ suggests a lower limit for deformation zone transmissivity of $10^{-10} \text{ m}^2 \text{ s}^{-1}$ to avoid unrealistically low transmissivity values at great depths compared to the surrounding rock.

Boundary conditions

Different types of boundary conditions can be envisaged for the top boundary:

- Pressure boundary conditions that prescribe atmospheric pressure at the top of the model can be applied in a confined model if the position of the water table is known. However, the resulting groundwater recharge must be consistent with measured data (see next bullet point). /ERI 06/ and /HOL 08/ use a pressure boundary condition at the upper boundary of the model according to Fig. 4.38. Note that Eskers are highly permeable and are therefore removed from the topography by interpolation to estimate the groundwater surface. In /SVE 08/ the head is fixed at the ground surface as set by the numerical grid or at the sea bottom the head is fixed to the elevation of the sea at the time.

In a more sophisticated approach the difference in height between the top surface of a Digital Elevation Model (DEM) and the water table was used to calculate a modified pressure head /RHÉ 06/, /HAR 06/.

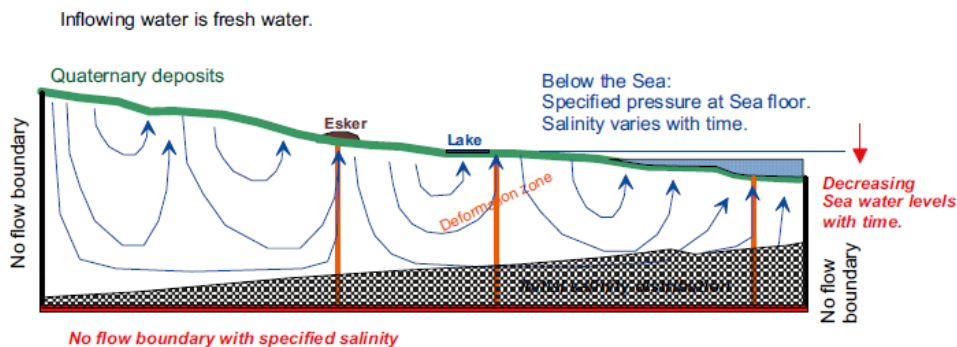


Fig. 4.38 Principal sketch of the boundary condition in SM and RM1; from /HOL 08/ after /ERI 06/

- Alternatively, a flux boundary condition can be used. Then the resulting pressure at the top of the model must be reasonably close to atmospheric pressure. The site-average long-term annual precipitation at the Laxemar site can be approximated to c. 600 mm/year /RHÉ 09a/. However, the precipitation is somewhat higher inland compared to coastal sites /WER 08/. Groundwater recharge is estimated to be in the order of 160–170 mm/year /WER 08/. The regional estimate is 150–180 mm/year /LAR 02/. For the ÄM 165 mm/year is specified /SVE 08/.

- In an unconfined model the position of the water table is calculated according to the measured groundwater recharge (see previous bullet point). In that case, the calculated position of the water table must reasonably well relate to measured data (see below).

Each of these approaches requires knowledge about the position of the water table. The relation of the water table to the surface topography as well as to the bedrock surface has been investigated by /WER 08/. The results show a strong correlation between the groundwater level and the ground-surface elevation while no relation of water table and rock surface depth could be shown (see Fig. 4.40). However, the elevation of the rock surface seems to be somewhat related to groundwater level / the ground-surface elevation “indicating that the ground-surface topography is a suitable indicator not only of groundwater levels in the QD but also of the topography of the rock surface”. It has to be mentioned, though, that elsewhere the water table has been found as deep as about 5 m below the rock surface /RHÉ 09a/. An example from /WER 05/ showing the water table elevation is shown in Fig. 4.39.

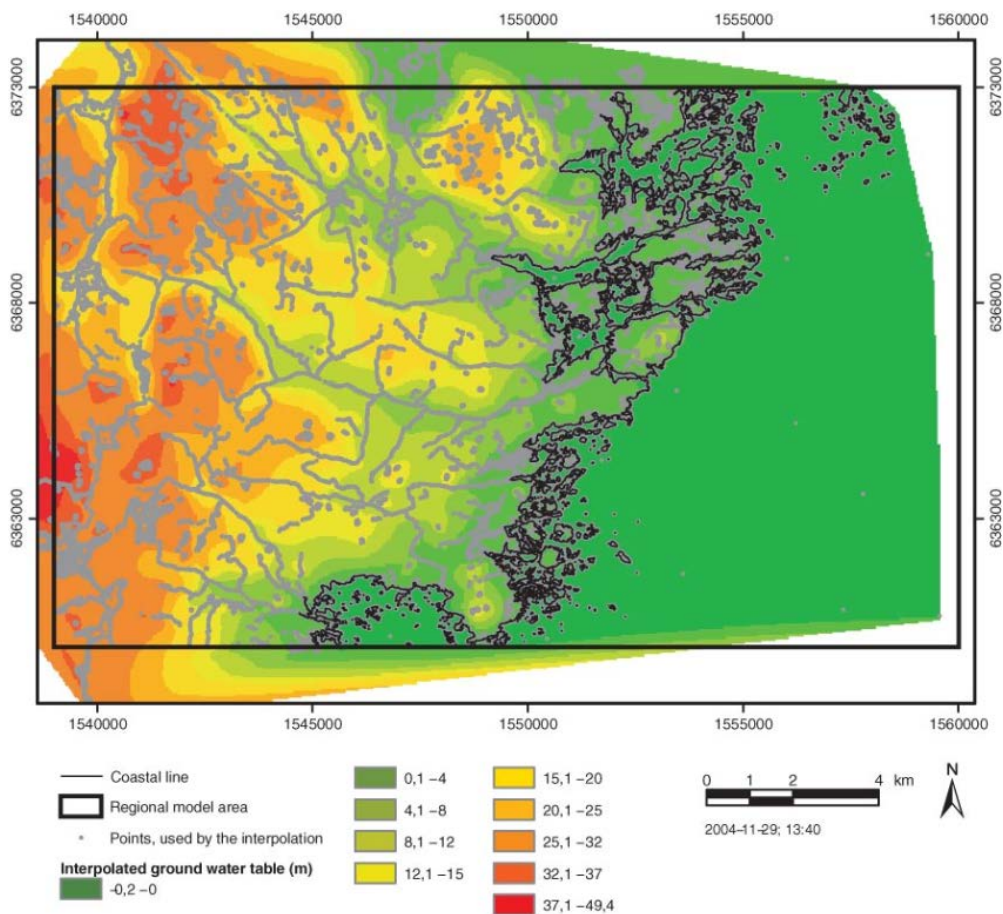


Fig. 4.39 Groundwater surface interpolated from measurements /WER 05/

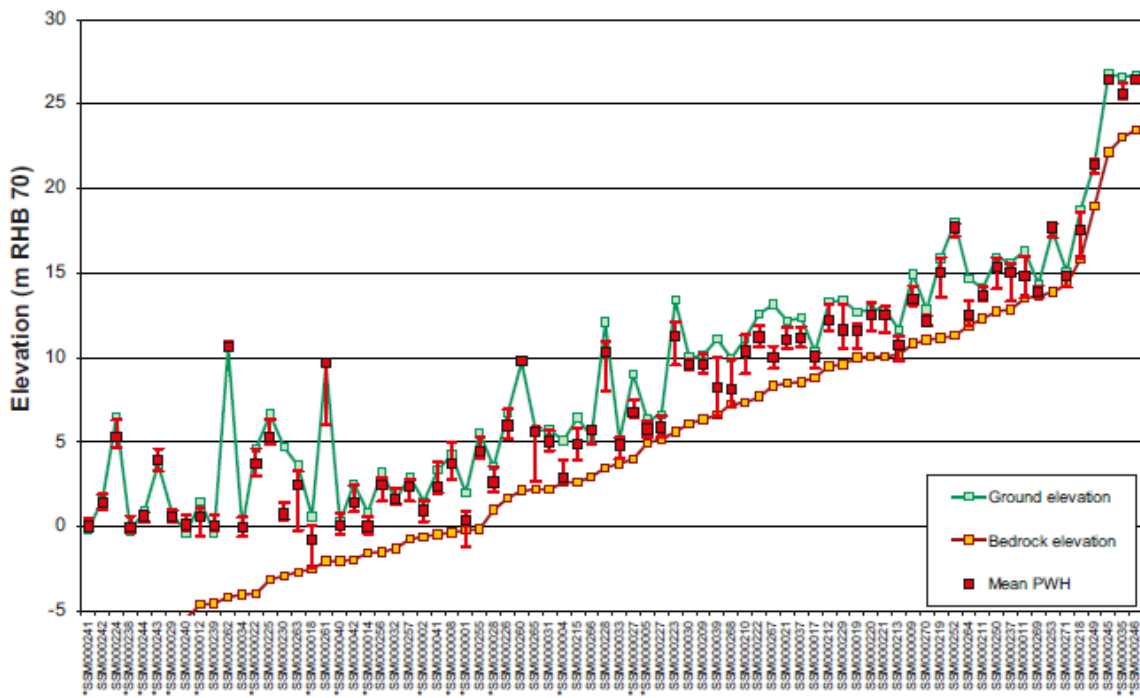


Fig. 4.40 Hydraulic heads used for calibration of the RM2; from /RHÉ 09a/

The position of rivers and lakes on top of the model are required as boundary conditions for confined models or as plausibility check for an unconfined model with a free water table. The required number of these features depends on the spatial resolution of the model. Fig. 4.41 for instance shows the rivers and lakes included in the SM /ERI 06/. The catchment area outlined top right in Fig. 4.41 is the relevant catchment area for lower scale models and shows just one river and one lake. BY contrast, many rivers and lakes appear in a finer resolved map of that area as depicted in Fig. 4.42. The relevance of these features thus depends on the actual model.

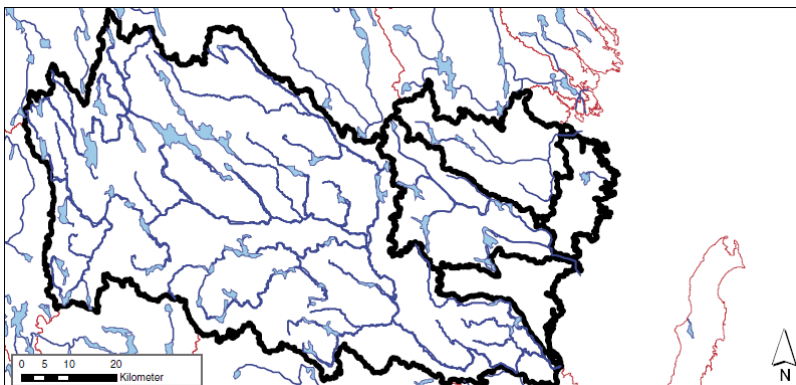


Fig. 4.41 Location of rivers and lakes for the SM; from /ERI 06/

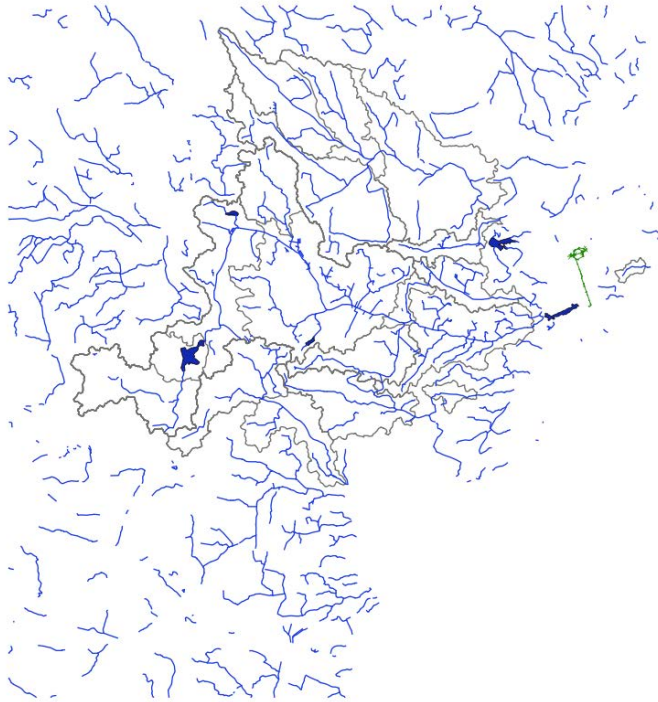


Fig. 4.42 Map of rivers and lakes; from /MOR 17/

As the lateral domain boundaries are chosen to coincide with water divides, a no-flow boundary condition can be assumed here. They can also be assigned the bottom as mentioned earlier.

At present, the shoreline displacement in the area is about +1.5 mm/year relative to mean sea level /PÁS 96/. As the simulation times will be in the range of years or maybe tens of years, the sea level will be assumed to be constant over the simulation period.

Initial conditions

It is commonly assumed that the flow field at Åspö was at steady state before the tunnels were drilled /MOR 17/. It is not entirely clear, though, if this also applies to the salinity.

Salinity

The salinity of the Baltic Sea at Åspö changes slowly with time (e. g. /ERI 06/). However, for the purpose at hand a constant value suffices. Generally, the salinity distribution in the Baltic Sea is characterized by horizontal as well as vertical gradients. As a comparison of maps from /ENG 15/ (Fig. 4.43) and /MOM 18/ (Fig. 4.44) shows, the salinity in

the surface waters (depth < 5 m) is in the same range (6.45 PSU) as the salinity at the sea bottom (5-7.5 PSU).

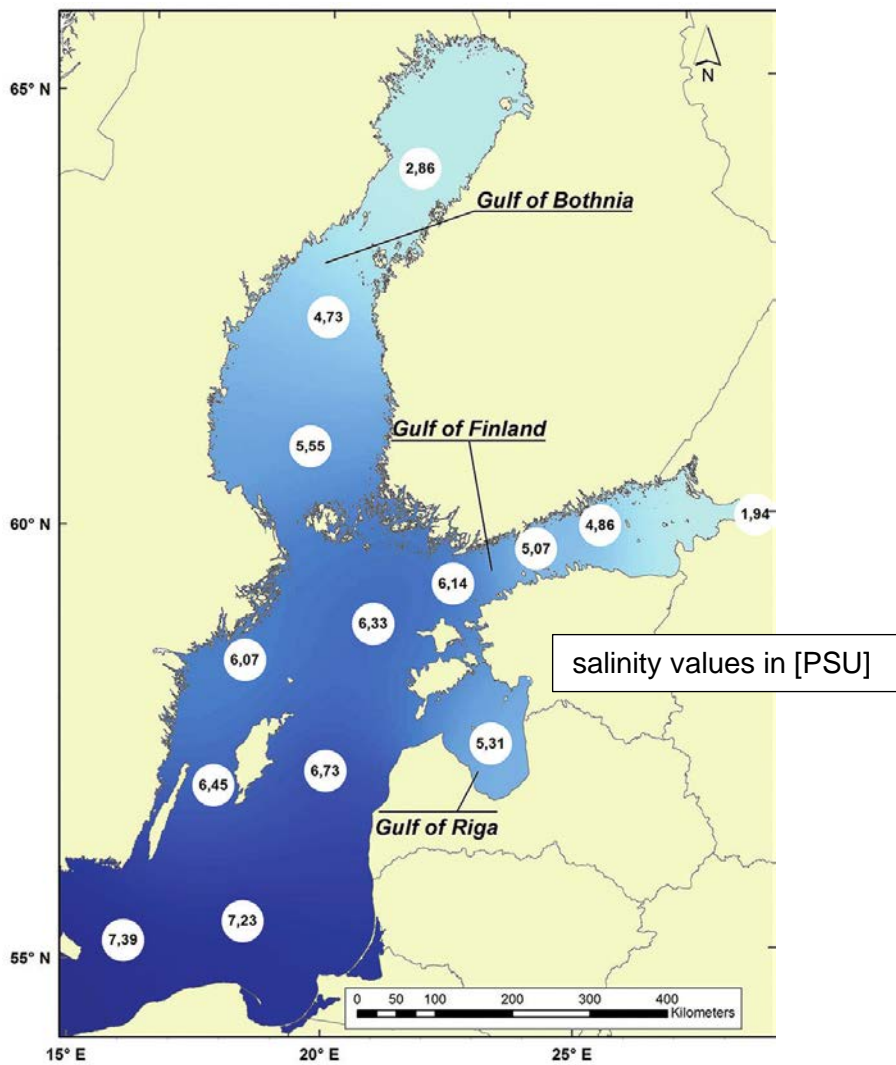


Fig. 4.43 Salinity at the surface (depth < 5 m) of the Baltic Sea; from /ENG 15/

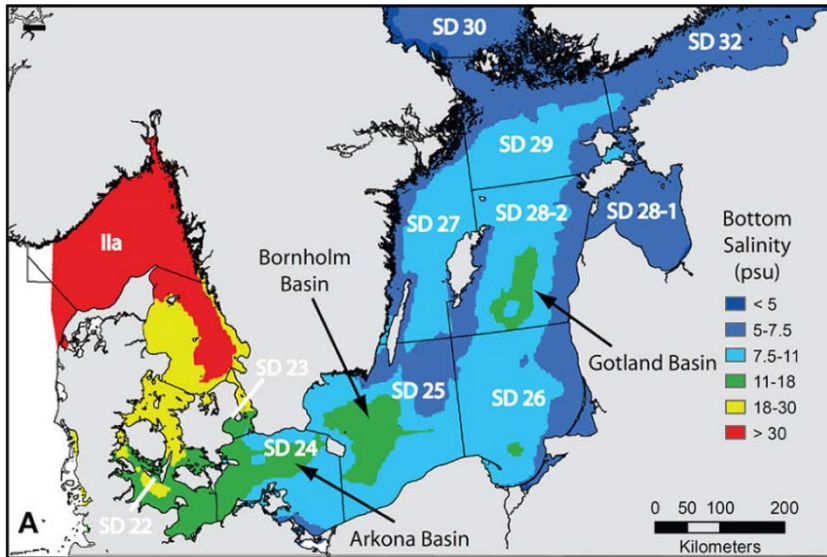


Fig. 4.44 Salinity in the deep waters in the Baltic Sea; from /MOM 18/

The results of an early investigation of the salinity in the groundwater from borehole tests are presented in /RHÉ 97/. The graphic in Fig. 4.45 depicting the salinity distribution below the island of Äspö shows a clear increase of salinity with depth. It also suggests upconing caused by the construction of the HRL. Finally, the effect of rainfall on the island of Äspö can clearly be observed in form of a freshwater lense. Note that salinity in Fig. 4.45 actually means the chloride content of the solution.

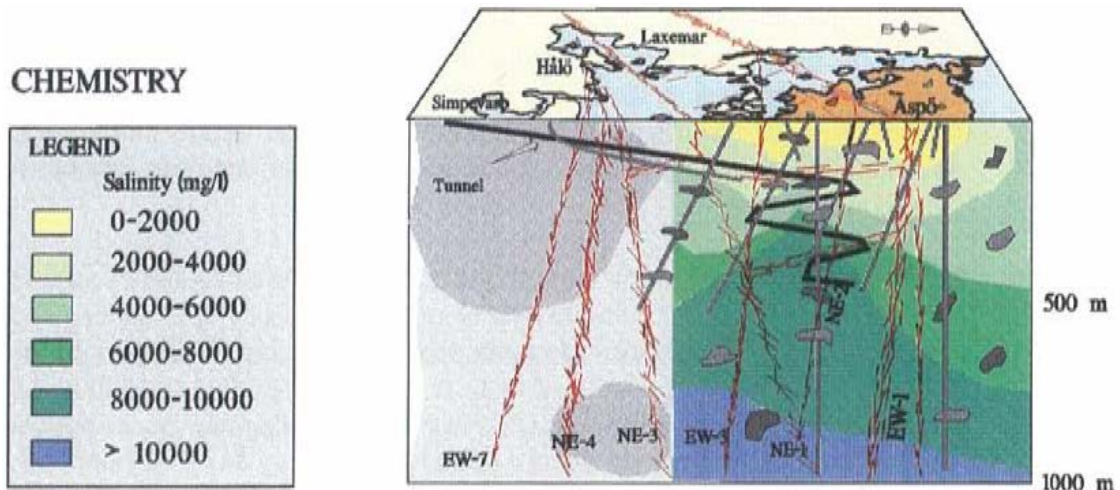


Fig. 4.45 Salinity in the Äspö area; from /RHÉ 97/

Data from Laxemar reaching deeper into the underground indicate that the salinity can be much higher than the range of 10 g/l indicated in Fig. 4.45. The profile for chloride

derived from the borehole KLX02, depicted in Fig. 4.46, shows a chloride concentration of about 50 g/l. It indicates the possibility of further increase of salinity at greater depths.

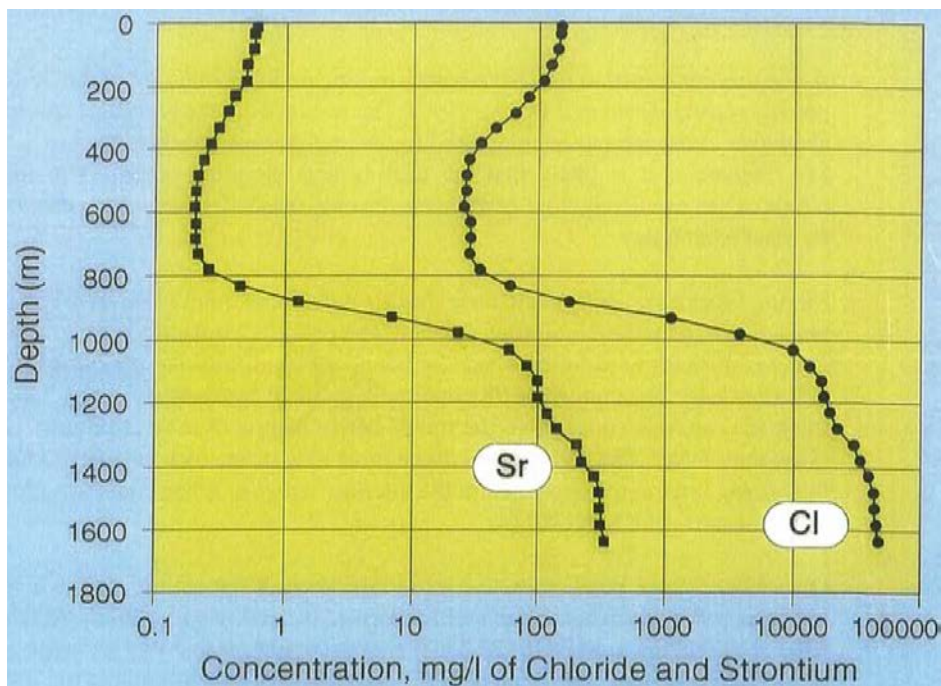


Fig. 4.46 Chloride profile along borehole KLX02 at Laxemar; from /RHÉ 97/

4.2.3 Pre-studies in a vertical cross-section for a regional-scale model

Section 4.2.1 and 4.2.2 offer background information on approaches to develop Äspö site descriptive models (SDMs). In the following, detailed information on and results of 2D pre-studies for regional-scale models (RMs) are illustrated and discussed which form the basis for 3D model approaches and set-ups presented in Section 4.2.4. 2D RMs were used to gain fundamental system and process understanding of the model area whereat valuable insight was collected which could be directly applied to 3D model development (cf. Sec. 4.2.4). In this study, the identifier RM refers to the catchments as illustrated in Fig. 4.20 including basin 12 and 13.

Model domain

The model domain as presented in Section 4.2.4, Fig. 4.58 also forms the basis for the 2D pre-studies. This approach offers the possibility to at least qualitatively compare results between 2D and 3D models eliminating the influence of differently set-up model

domains. Nevertheless, special attention has to be paid to hydrogeological parameterization and boundary conditions (BCs) when comparing model results.

The 2D model set up passed four steps of development (Fig. 4.47, Fig. 4.48). All 2D cross sections start in the far most NW corner of the domain running in SE-ward direction (Fig. 4.47). The cross sections originate directly at the boarder of the catchment area, cut through the island Äspö and, hence, the hard rock laboratory (HRL), to finally end at the shoreline (Fig. 4.47 B) or in the Baltic (Fig. 4.47 C – D). Cross section A as presented in Fig. 4.48 represents a generic model domain and is not related to geographic references.

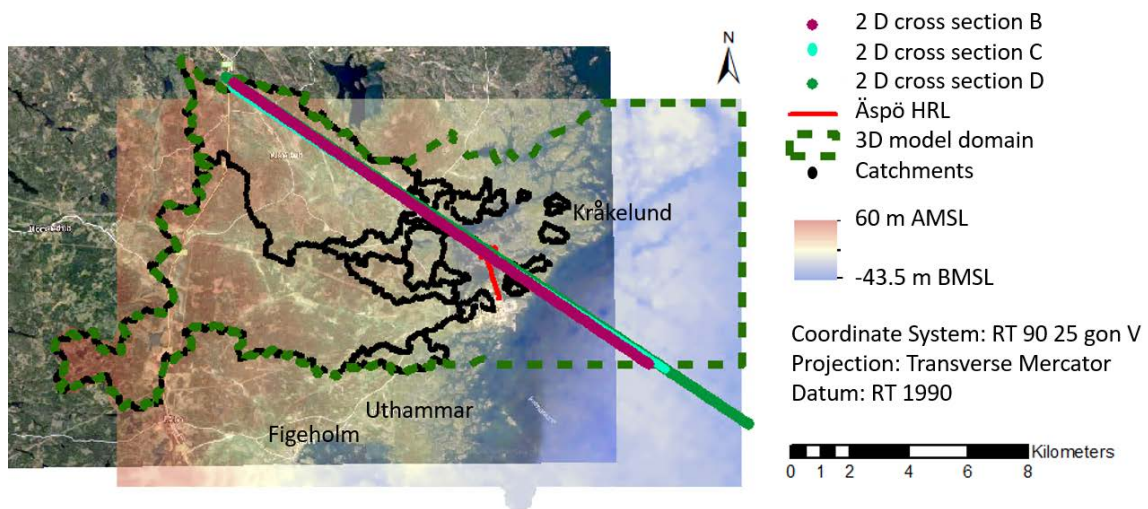


Fig. 4.47 2D cross sections B, C, D (dotted lines, cf. Fig. 4.48) in relation to the 3D model domain using a digital elevation model (DEM) as presented in detail in Section 4.2.4. Cross sections B – D illustrate different steps of development of the 2D RM, cf. Fig. 4.48. For orientation, the background map was obtained from google maps (<https://goo.gl/maps/UfjPHGR9bZQSw23fA>)

HRL – hard rock laboratory, Äspö

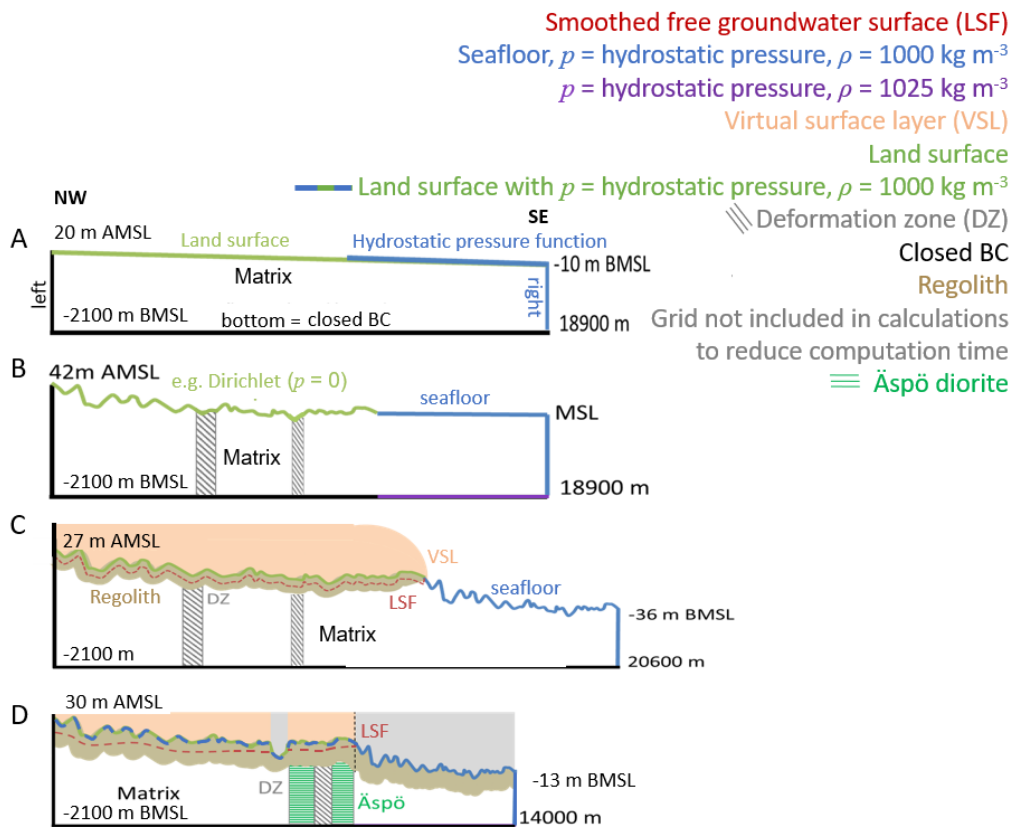


Fig. 4.48 A – D present the development of the 2D RMs to reach as close to nature conditions as possible but still being simplified enough to a manageable degree of complexity resulting in feasible computing times

BC – boundary condition, p – hydrostatic pressure (cf. Eq. (4.3), ρ – density [kg m^{-3}],
 LSF – level set function to define a free groundwater surface /SCH 12/

Each 2D RM is a further development of the previous one where each step is a more precise description of natural conditions of the area (cf. Fig. 4.48). While the model domain presented Fig. 4.48 A was set up as a “box” and was only used for first scoping calculations, the model domain in Fig. 4.48 B already comprised information on the land surface topography. The next step was to also include an approximation of the seafloor topography and a generic regolith layer to account for a higher permeability close to the land surface compared to the bedrock matrix beneath (cf. Fig. 4.48 C, Sec. 4.2.2). This set up was, e. g., used for first simulations with generic equidimensional deformation zones (DZ) to evaluate the influence of varying hydrogeological characteristics on the flow field. Furthermore, a free groundwater surface in the regolith layer (LSF) and a virtual surface layer were implemented where the latter one was only necessary for numerical reasons and does not influence results of model simulations in any way.

The last development of the model domain (cf. Fig. 4.48 D) included

- rivers,
- a more realistic implementation of the free groundwater surface (interrupted by, e. g., the archipelago),
- the island Äspö with its natural bedrock matrix conductivities that differ from the surrounding rock (cf. Sec. 4.2.2),
- and some refinements of the model set-up to reduce computing time.

Rivers were extracted from the DEM and included using geographic coordinates (east-ing, northing). The 2D model domains in Fig. 4.48 were triangulated where higher refine-ment was used for areas of high interest such as the regolith layer (Fig. 4.48 C and D) and, e. g., the transition zone between the land surface and the seafloor. Overall, simu-lation runs were based on 3'260 – 2'765'000 elements (cf. Tab. 4.8) for model domains illustrated in Fig. 4.48 whereat the number of elements increased with increasing degree of complexity.

Regolith

The regolith layer which was incorporated in the more sophisticated 2D RMs (Fig. 4.48) represents Quaternary deposits (QD) that are mainly located along topographical de-pressions and are often interrupted by outcrops of bedrock /VID 03/. The deposits are described to mainly consist of sandy to gravelly till /WER 05/. The thickness of the QDs vary from a few centimeters /RHE 08/ to up to 3 m /HOL 08/. For detailed information on QDs see Section 4.2.2.

Different approaches were followed to incorporate a thickness of the regolith layer being as close to nature as possible in this study. However, due to numerical difficulties the thickness of the regolith layer had to be defined to be at least 25 m in the RMs. For reasons of simplicity, the QD was defined to be evenly spread over the 2D model domain. This approach is comparable to /HOL 08/ who included QDs in their models using a thickness of 10 m for a RM (cf. Fig. 4.1). It is obvious that for both model approaches a highly overestimated value for the QD thickness was used. /HOL 08/ also justified this approach with numerical reasons. For pre-studies, the permeability of the QD was varied between 10^{-14} m^2 and 10^{-12} m^2 following /ERI 06/, /HOL 08/ and /KÄR 02/ (cf. Tab. 4.8, also Sec. 4.2.4).

Bedrock and deformation zones

Detailed information on bedrock characteristics, hydrogeological properties, and literature are provided in Sections 4.2.2 and 4.2.4. In Tab. 4.8 a summary of 2D RM simulations is presented including hydrogeological properties and model settings of relevant model features such as the bedrock (also referred to as matrix) and DZs which were considered as equidimensional features.

In agreement with the 3D model (Sec. 4.2.4), hydrogeological features of the bedrock were vertically extended from the land surface to the bottom of the model domain at -2100 m BMSL (cf. Fig. 4.48). Hydrogeological features in the RMs (e. g. DZs) have a generic character and do not necessarily correspond to geographic locations in nature. It was the aim to gain system and process understanding using 2D RMs. Therefore, generic approaches of model features seem feasible.

For generic simulations a permeability of $4.4\text{E-}16\text{ m}^2$ was assumed for the bedrock matrix. This value represents a mean value over all areas (Äspö, Laxemar, Simpevarp) and bore hole depths up to 1700 m which resulted from an in-house permeability data compilation based on /RHE 06/. Since the model domain covers up to -2100 m BMSL and all areas are at least partly considered in the domain this value seemed reasonable for generic 2D RM studies. Permeabilities for DZs were obtained from /RHE 09/ ($k_{\text{DZ}} = 1.7\text{E-}13\text{ m}^2$).

Precipitation

Precipitation was considered as groundwater recharge values in the current 2D simulations. For RM XI (cf. Tab. 4.8) groundwater recharge was derived from mean monthly precipitation time lines collected over 30 years at Oskarshamn (1961 – 1990, Fig. 4.49) /NYB 05/. In Fig. 4.49 a comparison between 30 year mean values and monthly mean annual precipitation 2004 is presented (from /NYB 05/). Groundwater was calculated from these values assuming a groundwater recharge rate of 1/10 with respect to precipitation. This assumption for 2D model simulations was agreed on by SKB during several discussions and workshops.

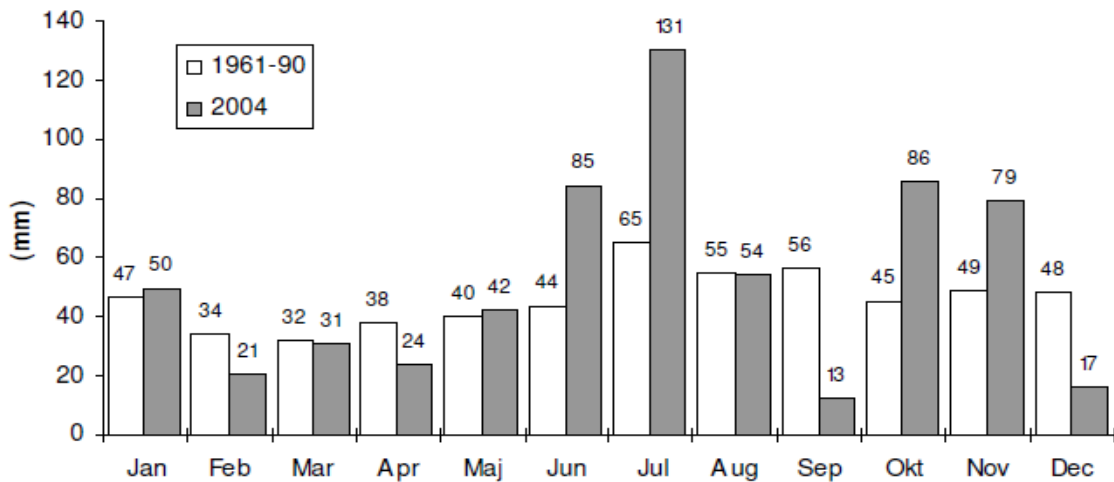


Fig. 4.49 Precipitation at Oskarshamn: Monthly values 2004 and monthly means from 1961 to 1990 /NYB 05/.

Boundary conditions and Salinity

In Tab. 4.8 a summary of boundary conditions and model settings for each simulation is provided. Together with Fig. 4.48, Tab. 4.8 shows the development of model approaches as well as the development of the complexity of model domains, and boundary conditions.

For all simulations, the left and the bottom boundary (cf. Fig. 4.48) were defined to be no-flow boundaries, hence, closed boundaries. The left boundary was chosen to be situated at the boarder of the catchment area allowing the latter assumption. Since /HOL 08/ assumed an upconing of salt water under the island Äspö which was described more precisely by /MOR 17/ to occur from about -1000 m BMSL the chosen conditions of a no-flow boundary at -2100 m BMSL seemed reasonable and also agree well with other literature as was shown in Section 4.2.2.

For most model runs the boundaries “seafloor” and “right” boundary (cf. Fig. 4.48) were defined using Equation (4.6)

$$h(x, y, t) = g \cdot \rho \cdot (-y) \quad (4.6)$$

- h hydrostatic pressure
- g gravitational acceleration ($g = 9.81 \text{ m s}^{-1}$)
- y depth (z) [m]
- ρ density of water [kg m^{-3}]

Equation (4.6) allows to define a hydrostatic pressure at the boundaries corresponding to the high BMSL and salt content of the considered water in the system. To account for brackish saltwater conditions similar to the Baltic a density of $\rho = 1025 \text{ kg m}^{-3}$ was used, for model set-ups that focused on freshwater systems in the aquifer a water density of $\rho = 1000 \text{ kg m}^{-3}$ was applied. To simulate the influence of deep groundwater which is reported to have a higher salt concentration compared to the Baltic Sea a density of $\rho = 1100 \text{ kg m}^{-3}$ was assumed /ERI 06/. To implement deep saline groundwater algorithm (4.7) was used.

$$c(x, y, t) = \text{if } x \geq 13450, \text{ then return 1, else return 0} \quad (4.7)$$

$$c(x, y, t) = \text{if } Y \geq 1900, \text{ then return 2, else return 0} \quad (4.8)$$

x distance [m] (here, “bottom” boundary, cf. Fig. 4.48)

$$1 \quad \rho = 1025 \text{ kg/m}^3 \triangleq c_{rel} = 1$$

$$2 \quad \rho = 1100 \text{ kg/m}^3 \triangleq c_{rel} = 1$$

$$0 \quad \rho = 1000 \text{ kg/m}^3 \triangleq c_{rel} = 0$$

c_{rel} relative concentration

(4.7) ascribes saline conditions to selected parts of the grid, here, to the area where $x \geq 13450 \text{ m}$ applies. Whereas, (4.8) defines saltwater conditions with elevated salt concentrations for the region of the grid where $y < -1900 \text{ m}$ is valid (cf. Fig. 4.48).

For most simulations the land surface was defined as a zero-pressure boundary (Dirichlet, $BC_p = 0$, cf. Tab. 4.8) allowing in and outflow of groundwater. For selected runs in and outflow of salt transport was also simulated (cf. Tab. 4.8, RM V, VI). The level set

function (LSF) simulates a free groundwater table in the model area. The free groundwater surface was defined to be situated -12.5 m beneath the boundary “land surface” (cf. Fig. 4.48) in the regolith layer. The initial position of the LSF (-12.5 m below land surface) represents a generic approach due to reasons of simplicity since the actual groundwater surface position varies with season and climate/weather conditions. Simulation results RM VII – RM XII (cf. Tab. 4.8) show the development of the application of the free groundwater surface with different model approaches (cf. Fig. 4.56).

Simulation runs

In Tab. 4.8 a summary of relevant development steps, simulations and hydrogeological parameters as well as boundary conditions is presented. Different generic approaches were developed to gain system and process understanding. Comparisons between cross-sections (RM I - RM III; RM VII, VIII, X; RM IX, VI), the influence of the topography (RM I and II), the free groundwater table (RM VII – RM X), different geological features (RM III, IV, IX), the influence of precipitation (RM XI), and salt transport were investigated (RM V and VI). To get an impression of the different geological units and the impact on the flow field permeabilities of typical rock matrices of Äspö, Laxemar, and Simpevarp were used (RM III).

Tab. 4.8 Summary of regional-scale model (RM) simulations including model settings and relevant hydrogeological settings

For RM IV and V the following porosities (θ [-]) were applied: $\theta_{IV} = 1.0E-04$, $\theta_V = 5.0E-03$. The following parameters are applicable to all simulations: longitudinal (D_L) and transversal (D_T) dispersivity: $D_L = 60$ m, $D_T = 20$ m following /RHE 09/; molecular diffusivity: $D_m = 1.0E-09$ m²/s after /KRO 10/, tortuosity [-]: $\tau = 1$, gravity acceleration: $g = 9.81$ m s⁻¹. LSF – level set function, k - permeability [m²]

RM ID	cross section ¹	Hydrogeological features	LSF ² (y/n)	Rivers (y/n)	Precipitation (y/n)	ρ [kg/m ³]	k [m ²]	BC (cf. Fig. 1.30)
RM I	A 3'264 elements	matrix	n	n	n	1000	4.4E-16 ³	left, bottom - closed; right, seafloor - type: Dirichlet ⁵ ($BC_p =$ cf. Eq. 1.3); land surface - type: Dirichlet ⁵ ($BC_p = 0$)
RM II	B 29'440 elements	matrix	n	n	n	1000	4.4E-16 ³	left, bottom - closed; right, seafloor - type: Dirichlet ⁵ ($BC_p =$ cf. Eq. 1.3); land surface - type: Dirichlet ⁵ ($BC_p = 0$)
RM III	B 18'832 elements	4 different bedrock matrices	n	n	n	1000	Äspö ³ 1.7E-14; Laxemar ³ 1.0E-14; Simpevarp ³ 0.5E-14; matrix ³ 4.4E-16	left, bottom - closed; right, seafloor - type: Dirichlet ⁵ ($BC_p =$ cf. Eq. 1.3); land surface - type: Dirichlet ⁵ ($BC_p = 0$)
RM IV	B 94'016 elements	matrix, DZ	n	n	n	1000	4.4E-16 ² , 1.7E-13 ¹⁰	left, bottom - closed; right, seafloor - type: Dirichlet ⁵ ($BC_p =$ cf. Eq. 1.3); land surface - type: Dirichlet ⁵ ($BC_p = 0$)
RM V	B 29'440 elements	matrix	n	n	n	1025	4.4E-16 ²	right, left, bottom - closed; seafloor - type: Dirichlet ⁵ ($BC_{c,rel} = 1^7$); seafloor - type: Dirichlet ⁵ ($BC_p =$ cf. Eq. 1.3); land surface - type: Dirichlet ⁵ ($BC_p = 0$, $BC_{c,rel} = 0$)
RM VI	B 29'440 elements	matrix	n	n	n	1100 ⁴	4.4E-16 ³	right, left - closed; bottom - type: Dirichlet ⁵ ($BC_{c,rel} = 1^8$, cf. Eq. 1.5); bottom - type: Dirichlet ⁵ ($BC_p = 0$); seafloor - type: Dirichlet ⁵ ($BC_p =$ cf. Eq. 1.3); seafloor - type: in/out ⁶ ($BC_c = 0$);

RM ID	cross section ¹	Hydrogeological features	LSF ² (y/n)	Rivers (y/n)	Precipitation (y/n)	ρ [kg/m ³]	k [m ²]	BC (cf. Fig. 1.30)
								land surface - type: Dirichlet ⁵ ($BC_p = 0$); land surface - type: in/out ⁶ ($BC_c \triangleq C_n = 0$)
RM VII	C 140'288 elements	matrix, regolith	y	n	n	1000	4.4E-16 ³ , 1.0E-14 ⁹	left, bottom - closed; right, seafloor - type: Dirichlet ⁴ ($BC_p =$ cf. Eq. 1.3); land surface - type: Dirichlet ⁴ ($BC_p = 0$)
RM VIII	C 2'765 T elements	matrix, regolith, DZ	y	n	n	1000	4.4E-16 ² , 1.0E-12 ⁹ , 1.7E-13 ¹⁰	left, bottom - closed; right, seafloor - type: Dirichlet ⁵ ($BC_p =$ cf. Eq. 1.3); land surface - type: Dirichlet ⁵ ($BC_p = 0$)
RM IX	D 294'016 elements	matrix, regolith	y	n	n	1000	4.4E-16 ³ , 1.0E-12 ⁹	left, bottom - closed; right, seafloor, land surface - type: Dirichlet ⁵ ($BC_p =$ cf. Eq. 1.3);
RM X	D 294'016 elements	matrix, regolith	y	y	n	1000	4.4E-16 ³ , 1.0E-12 ⁹	left, bottom - closed; right, seafloor, land surface - type: Dirichlet ⁵ ($BC_p =$ cf. Eq. 1.3);
RM XI	D 294'016 elements	matrix, regolith	y	y	y	1000	4.4E-16 ³ , 1.0E-12 ⁹	left, bottom - closed; right, seafloor, land surface - type: Dirichlet ⁵ ($BC_p =$ cf. Eq. 1.3);
RM XII	D 300'416 elements	matrix, regolith, Äspö, DZ	y	y	n	1000	4.4E-16 ³ , 1.0E-12 ⁹ , 1.7E-14 ³ , 6.7E-20 ¹⁰	left, bottom - closed; right, seafloor, land surface - type: Dirichlet ⁵ ($BC_p =$ cf. Eq. 1.3);

¹ cf. Fig. 4.48² /SCH 12/³ in house data compilation (cf. Sec. Tab. 4.6)⁴ /ERI 06/⁵ /SCH 16/⁶ in/out BC /FEI 99/⁷ $BC_{c\ rel} = 1 = 1025$ kg/m³, brackish salt concentration related to the Baltic⁸ $BC_{c\ rel} = 1 = 1100$ kg/m³⁹ cf. Sec. 4.2.3 (Regolith), /ERI 06/, /HOL 08/, /KÄR 02/¹⁰ /RHE 09/

Simulation results and discussion

For reasons of comparability, the presentation of flow fields were normalized to identical velocity ranges [m s^{-1}] if reasonable. Results of RMs are referred to as presented in Tab. 4.8.

A comparison of flow field simulations with different model approaches illustrates the development of the 2D RMs (Fig. 4.50). It was shown that due to the topography convection cells as presented in /HOL 08/ could also be observed in RMs of this study (Fig. 4.50 a) and b)). As expected, the main flow field followed the topographical gradient from the left (NW) to the right (SE) of the model domain. Within the regolith layer which was characterized by higher permeabilities compared to the bedrock matrix (Tab. 4.8) increased flow velocities were observed (Fig. 4.50 c)). Simulation RM IX (Fig. 4.50 c)) also showed that due to the free groundwater surface convection cells of the groundwater flow field that were mainly attributed to the topography levelled off. The archipelago which was represented by means of a fragmented free groundwater surface (cf. Fig. 4.48 D) allowed water to infiltrate without disturbing the main topographical driven flow direction. However, it should be mentioned that flow velocities at $y < -40$ m BMSL are extremely small with less than 1 mm a^{-1} (Fig. 4.50 c)). A detailed view of the regolith' layer flow field and its geographical orientation is provided in Fig. 4.56.

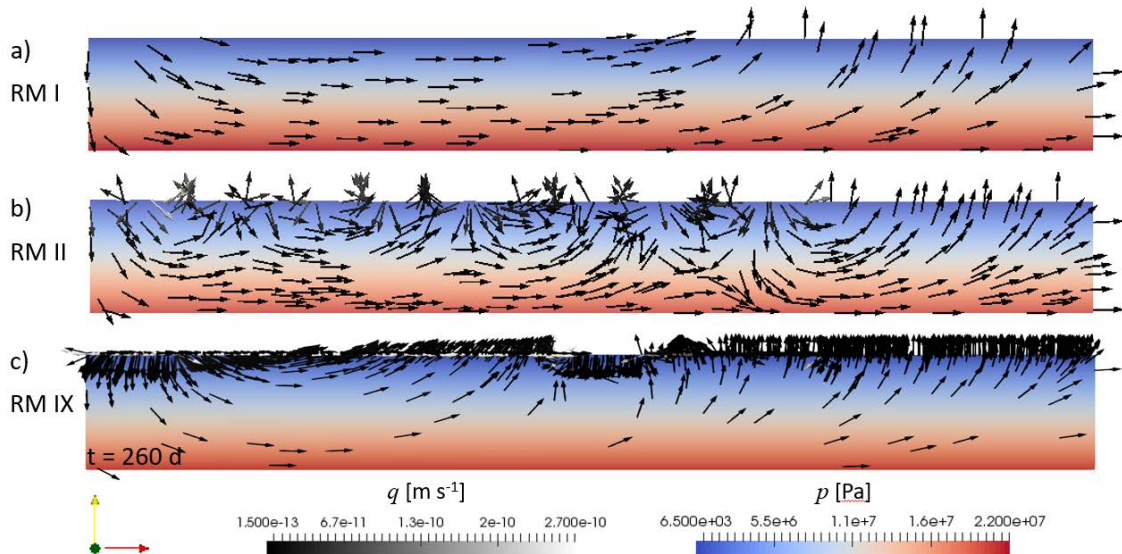


Fig. 4.50 Comparison of RM I, II, and VII to show the impact of topography (RM II) and a free groundwater surface in a 25 m regolith layer (RM VII)

Results of RM IX correspond to 260 d simulation time. Details on model domains and settings are provided in Fig. 4.48, Tab. 4.8. q – Darcy velocity [m s^{-1}], p – pressure [Pa]

From Fig. 4.50 b), c) it was also concluded that at approximately -1620 m BMSL the flow field started to level off following the bottom boundary in a parallel manner which reinforced the definition of the lower boundary at -2100 m BMSL. Additionally, flow velocities (q) were relatively slow at $y < 1620$ m BMSL beneath the land surface with q ranging between $6.5E-13 - 1.4E-11$ $m\ s^{-1}$ (Fig. 4.51 b)). In comparison, flow velocities at $y > -430$ m BMSL ranged between $6E-11 - 4E-10$ $m\ s^{-1}$ (Fig. 4.51 a)). Hence, it can be assumed that the bottom boundary did not influence simulation results in the upper parts of the model domain which were of higher interest, here.

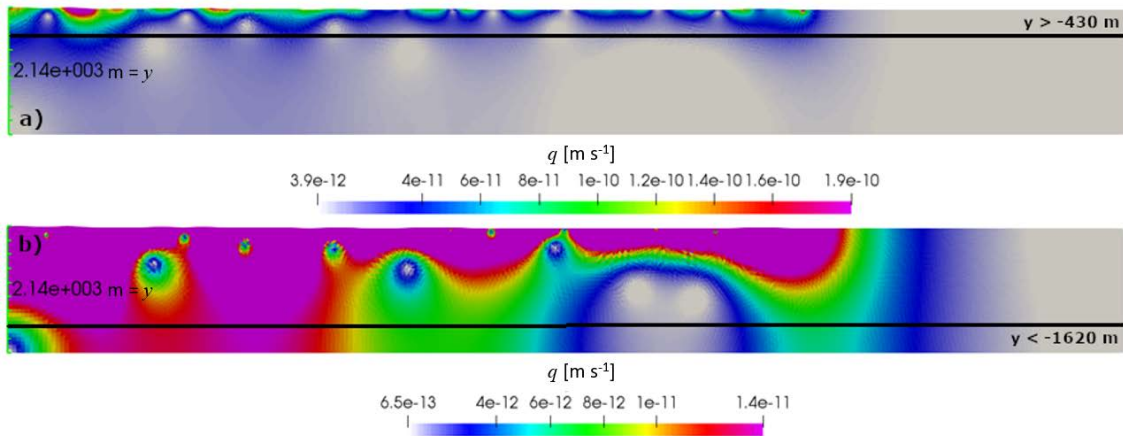


Fig. 4.51 Flow velocities of RM II with focus on $y > -430$ m BMSL (a) and $y < 1620$ m BMSL (b).

Details on model domains and settings are provided in Fig. 4.48, Tab. 4.8.

q – Darcy velocity [$m\ s^{-1}$], p – pressure [Pa]

In Fig. 4.52 the influence of different permeabilities on the flow field is illustrated. It is obvious that the higher the permeability, the faster the groundwater flows. Furthermore, it was shown that the transition between higher permeabilities to lower ones resulted in an upconing of water due to the higher flow resistance (cf. Fig. 4.52 b), Simpevarp \rightarrow Laxemar \rightarrow matrix). The comparison with a flow field simulation based on a uniform permeability (Fig. 4.52 a)) underlines this observation.

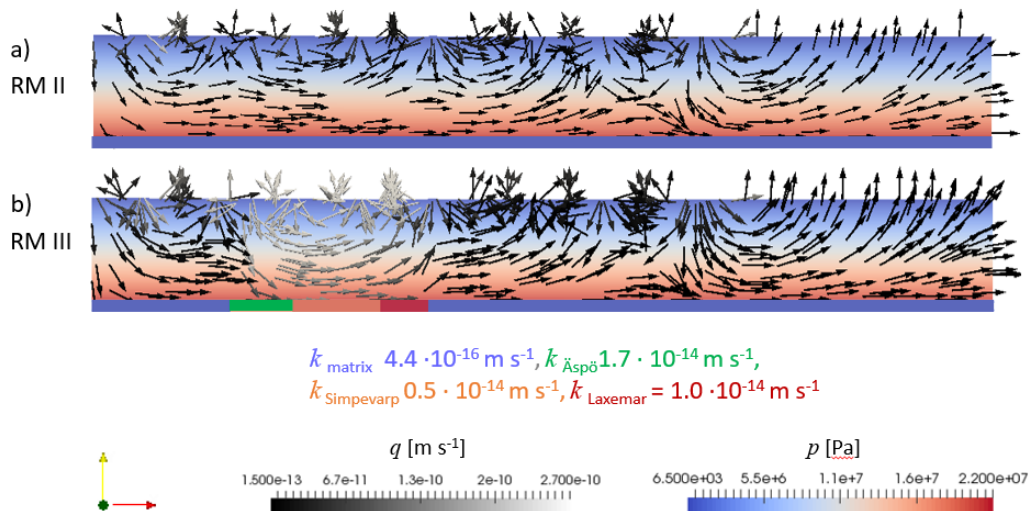


Fig. 4.52 Influence of permeabilities on the flow field (generic study)

Permeabilities typically found in the Äspö (green), Simpevarp (orange), and Laxemar (red) area and a mean value obtained from an in-house data compilation for matrix permeability (k - purple) were used (cf. Sec. 4.2.3, Bedrock and deformation zones, also cf. Tab. 4.6). Color coding at the bottom of a) and b) illustrate permeability values. Details on model domains and settings are provided in Fig. 4.48, Tab. 4.8. q – Darcy velocity [m s^{-1}], p – pressure [Pa]

Considering DZs in RM IV yielded similar results compared to observations made with RM III (cf. Fig. 4.52 and Fig. 4.54): Due to the heterogeneities of permeabilities in the hydraulically active DZs (higher permeabilities, hydraulic conductor domains) flow velocities increased and an upward flow direction was observed (upconing of groundwater). The change of flow direction in the flow field was induced due to the change of permeabilities from low permeabilities in the bedrock matrix ($k_{\text{matrix}} = 4.4\text{E-}16 \text{ m}^2$) to higher ones in the DZs ($k_{\text{DZ}} = 1.7\text{E-}13 \text{ m}^2$) and back to low k -values in the matrix.

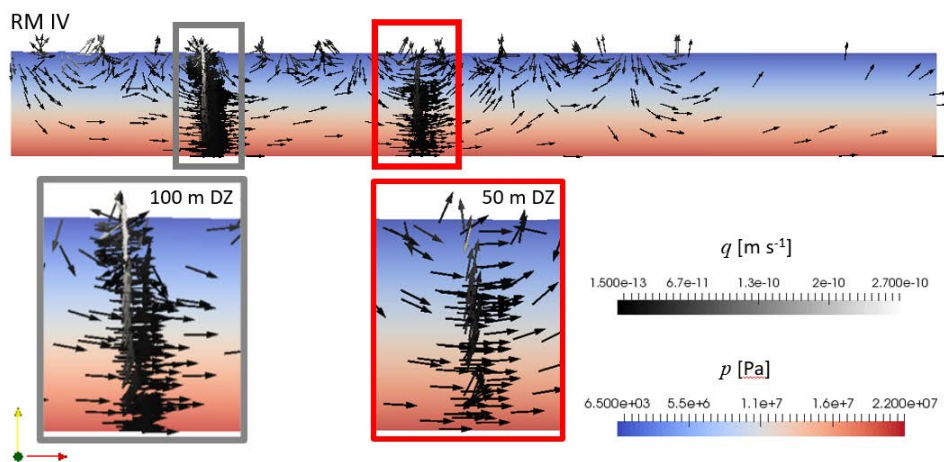


Fig. 4.53 Flow field simulation including equidimensional generic DZs.

Details provided in Fig. 4.47, Fig. 4.48, Tab. 4.8. q – Darcy velocity [m s^{-1}], p – pressure [Pa]

The influence of density-driven flow conditions on the flow field, hence, the transport of salt in the model area was investigated with two different generic model approaches based on model domain B (Fig. 4.48): The first approach started out with initial brackish water conditions (initial condition $\rho = 1025 \text{ kg m}^{-3}$) distributed over the right part of the model domain. Therefore (4.7) and (4.8) were used to define brackish water conditions for $x > 13'450 \text{ m}$ and hydrostatic pressure conditions for the seafloor and the right boundary. Boundary conditions were accordingly adapted (cf. Tab. 4.8). The transition between freshwater and saltwater conditions was defined at the shoreline in the model domain where $x = 13'450 \text{ m}$ applied. As illustrated in Fig. 4.54 the flow path of the saltwater conditions (red) was inverted compared to prior flow field simulations (cf. Fig. 4.52). The saltwater was transported from SE to NW of the model area which was based on the higher density of the brackish water. A dilution front occurred whereat a steady state between fresh- and saltwater conditions was approximately reached after 5,000 a simulation time.

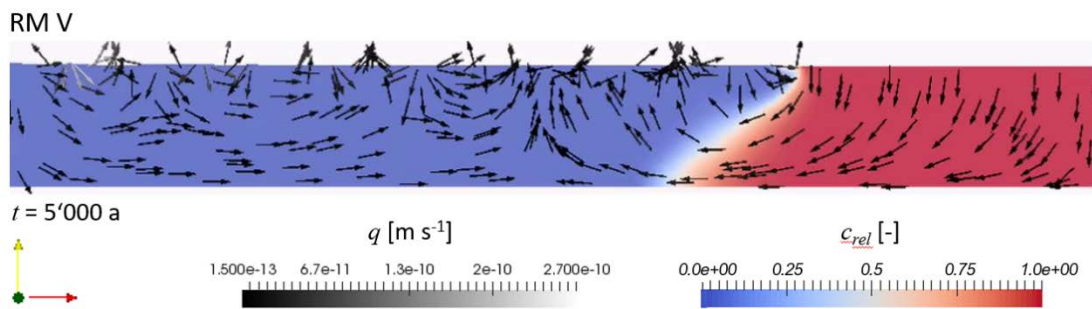


Fig. 4.54 Density-driven flow field simulation after 5'000 a simulation time.

Details on model domains and settings are provided in Fig. 4.48, Tab. 4.8. Porosity $\theta = 0.05$, viscosity $1.3\text{E-}03\text{-}1.75\text{E-}03 \text{ kg m}^{-1} \text{ s}^{-1}$ /KRO 10/, q – Darcy velocity [m s^{-1}], c_{rel} – relative concentration [-], $c_{rel} = 1 \triangleq 1'025 \text{ kg m}^{-3}$

The second approach to investigate saltwater transport in the model area followed suggestions from /ERI 06/. In /ERI 06/ saline deep groundwater compositions are postulated which were here applied in a generic approach with $\rho = 1'100 \text{ kg m}^{-3}$ (Tab. 4.8, RM VI). The bottom boundary was implemented as a closed boundary; where $y < -1'900 \text{ m}$ was valid a defined saltwater concentration was applied ($c_{rel} = 1 \triangleq 1100 \text{ kg m}^{-3}$). As shown in Fig. 4.55 the main flow field in the model domain was not influenced: Convections cells which were triggered by the topography were observed and the main flow field followed the topographical gradient from the left (NW) to right (SE) of the model domain. However, Fig. 4.55 also shows that the salt distribution stayed below $y < -1'500 \text{ m}$ and did not distribute over the entire domain which could be expected after 20'000 a simulation time. In Fig. 4.55 it is also illustrated that the salt distribution seems

to be depleted in the NW part of the model domain and accumulated in SE. This salt distribution can be explained with parallel flow paths at the bottom of the model domain as had already been observed in prior flow field simulations (cf. Fig. 4.50). Furthermore, since lateral dispersivities were defined to be larger compared to transversal dispersion lengths (cf. Tab. 4.8, where $D_L > D_T$) the density driven flow was rather orientated from NW-SW direction than from the bottom to the top of the model domain. In addition, realistic but small molecular diffusion coefficients ($D_m = 1.0E-09 \text{ m}^2 \text{ s}^{-1}$ /KRO 10/) and permeabilities of the homogeneous model domain ($k = 4.4E-16 \text{ m}^2$) did not enhance the transversal salt distribution either.

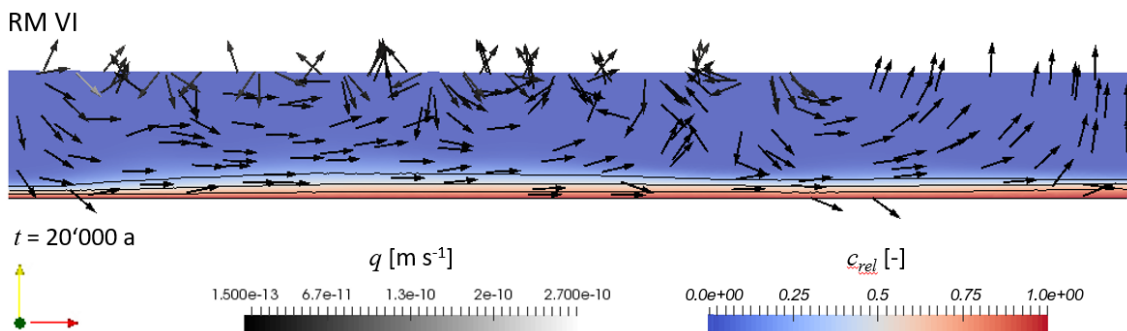


Fig. 4.55 Density-driven flow field simulation after 20'000 a simulation time.

Details on model domain and settings are provided in Fig. 4.48, Tab. 4.8. Porosity $\theta = 0.05$, viscosity $1.3E-03$ - $1.75E-03 \text{ kg m}^{-1} \text{ s}^{-1}$ /KRO 10/, q – Darcy velocity [m s^{-1}],
 c_{rel} – relative concentration [-], $c_{rel} = 1 \triangleq 1'100 \text{ kg/m}^3$ /ERI 06/

The development and approaches of the 2D model are briefly summarized in Fig. 4.56 and Fig. 4.57. In Fig. 4.56, differently implemented LSFs (RM VII, IX), the influence of receiving waters (RM IX), and precipitation (RM XI) on the free groundwater surface are illustrated by means of a close-up that is exaggerated 50 times for better visualization. Fig. 4.57 presents variations of permeabilities as realistically expected under the island Äspö also considering receiving waters (RM XII). The different model approaches develop from a truly generic model to more and more close to nature conditions (Fig. 4.56 RM VII – XI, Fig. 4.57 RM XII):

RM VII Results represent the steady state of the free groundwater surface after 500 a simulation time without receiving waters, precipitation or permeability variations. It is shown that (as expected) the LSF levels off and equilibrates approximately at sea level. Since no “disturbing” influences (e. g. precipitation, etc.) were included in model and since results represent steady state the flow velocity is orders of magnitudes smaller in the regolith layer compared to results

of RM IX-XII where steady state had not been reached within simulation time. Flow velocities are simulated to be $< 0.1 \text{ mm a}^{-1}$ indicating that no flow takes place at steady state as expected in a generic study without driving forces such as precipitation and/or rivers, etc. Hence, velocity values and flow direction should be interpreted as indicative rather than absolute since they might be prone to numerical bias.

RM IX Simulation results represent $t = 260 \text{ d}$. Due to the discontinuous LSF water is allowed to infiltrate from the archipelago (fjord) into the regolith layer which slightly influences the flow field. However, as has already been observed in RM VII flow velocities are extremely low where the LSF has reached equilibrium at sea level as e. g. in the area of Äspö. It can be assumed that the free groundwater surface would also level off at approximately sea level and flow velocities would further decrease if enough simulation time was allowed. The upward flow direction in the center of the model under the land surface is caused by the hydrostatic pressure boundary condition which results in pressure differences between the different positions of the LSF AMSL. Hence, since the groundwater surface lies below sea level at $t = 260 \text{ d}$ groundwater flows from regions with higher hydrostatic pressure to this area trying to reach steady state with respect to pressure conditions.

RM XI This approach represents a high degree of model complexity: a discontinuous LSF, receiving waters (arrows), and precipitation was included. Information on the precipitation timeline is provided in Section 4.2.3 (Precipitation). Results illustrate a simulation time of 42 days. It is shown that the groundwater surface cuts the land surface where rivers were implemented which allows infiltration as well as exfiltration (boundary condition: Eq. (4.6), /SCH 12/). The LSF has almost levelled off at sea level at the coastline of the archipelago which is expected since no receiving waters influence its location there. From site it is known that the free groundwater table can be situated only a few cm below the land surface on e. g. Äspö which is nicely represented by model results. Since precipitation and rivers were included the velocity field will always follow the geographic gradient and the hydrostatic pressure and, hence, the LSF will not level off at sea level as it did for RM VII and IX. The latter results also nicely represent realistic conditions. Since water table measurements undergo long-term climate changes as well as seasonal variations it has to be pointed out

that model results have not been verified with local head measurements, yet. This next model development step should be subject for future research.

RM XII In Fig. 4.57 RM XII ($t = 12$ d) is presented with and without 50 times exaggeration to visualize the influence of the naturally occurring Äspö permeability heterogeneities on groundwater flow and velocity in the regolith layer (A) and in the model domain (B). The development of the free groundwater surface, hence, LSF is comparable to RM XI (Fig. 4.56). Beneath Äspö the groundwater table has already reached sea level in the regolith layer after 12 d simulation time. The low permeability of the DZ (cf. Tab. 4.8) results in an upconing of groundwater as it acts as a barrier with high flow resistance. Simulated flow velocities in the 2D model are comparable to velocity ranges yielded with 3D simulations (Sec. 4.2.4 Simulation results) considering that the 3D model did not incorporate as complex features/influences as the 2D model (i. e. receiving water, free groundwater surface). In the 3D model velocities vary between $1.0 \cdot 10^{-8} \text{ m s}^{-1}$ and $1.6 \cdot 10^{-6} \text{ m s}^{-1}$ whereas the 2D model resulted in velocities in the regolith layer mainly ranging between $1.0 \cdot 10^{-8} \text{ m s}^{-1}$ and $1.2 \cdot 10^{-7} \text{ m s}^{-1}$ with maximum values reaching up to $4 \cdot 10^{-7} \text{ m s}^{-1}$ ($\approx 13 \text{ m a}^{-1}$).

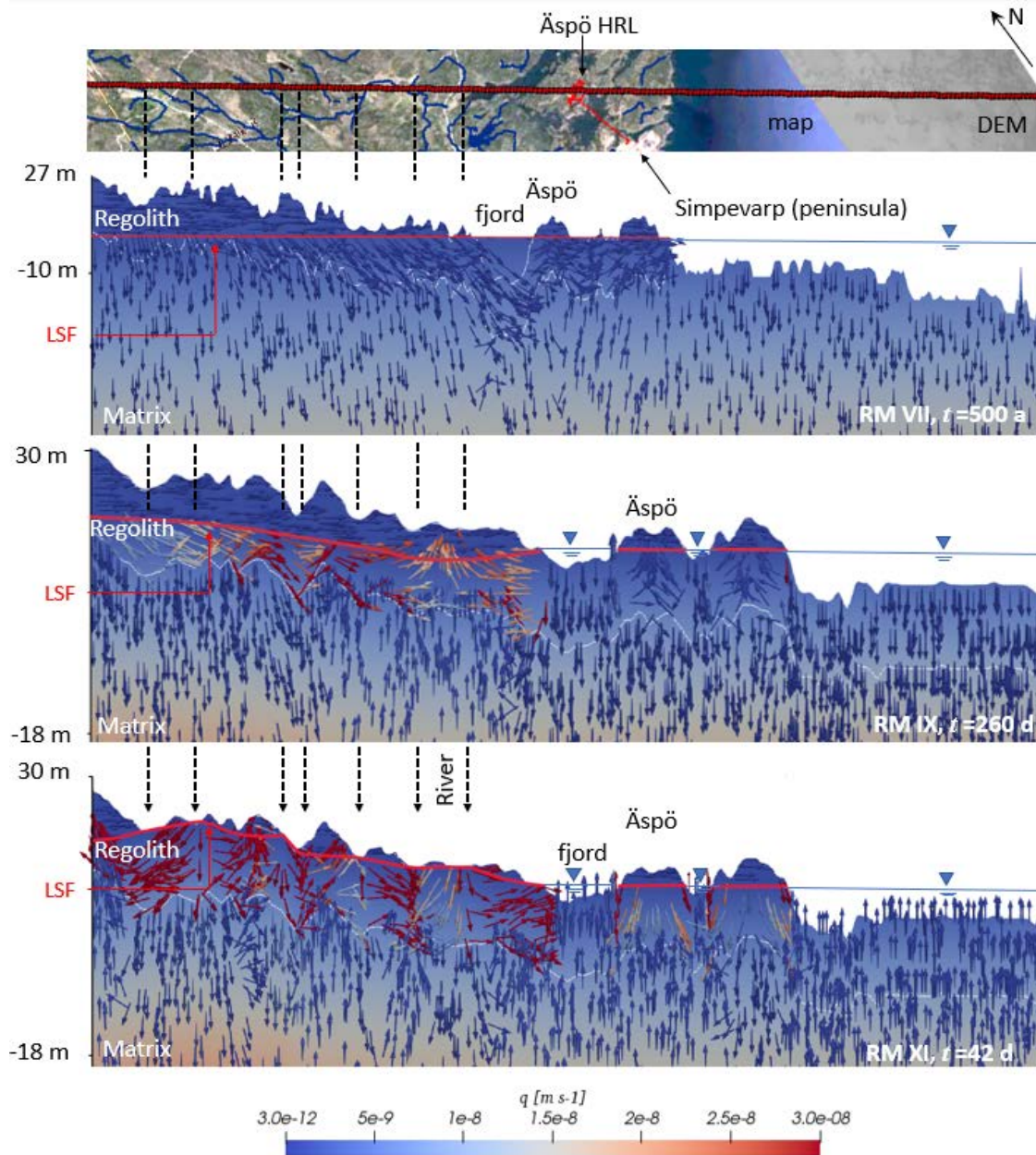


Fig. 4.56 Detailed view of the flow field in the regolith layer for two different cross sections (RM VII and RM IX, XI) and comparison of flow field simulations with a free groundwater table (RM VII, IX, XI) with (RM XI) and without (RM VII, IX) the influence of receiving waters, and precipitation (RM XI) 50x exaggerated

Top image offers a broad overview of the geographical location of receiving waters, the Äspö HRL, and the cross section for RM VII. Details on cross sections, model domains and settings are provided in Fig. 4.47, Fig. 4.48, Tab. 4.8. q – Darcy velocity [m s^{-1}], p – pressure [Pa]

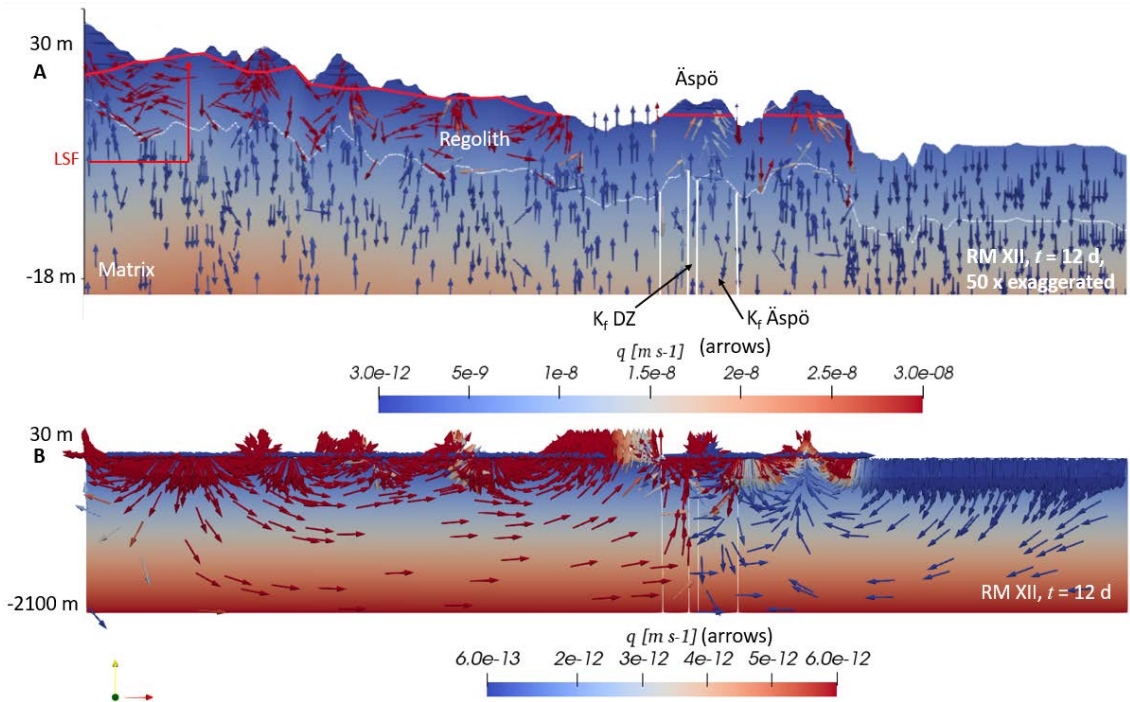


Fig. 4.57 Simulation results of RM XII, $t = 12$ d, A) 50 times exaggerated, B) overview of model domain. The model considers a regolith layer, rivers, and permeability variations as found on site under the island Äspö. The position of receiving waters is illustrated in Fig. 4.56 RM XI.

Details on cross sections, model domains and settings are provided in Fig. 4.47, Fig. 4.48, Tab. 4.8. q – Darcy velocity [m s^{-1}], p – pressure [Pa]

4.2.4 Regional-scale model in 3D

A confined three-dimensional regional-scale model was constructed and parameterized based on the experience gained during the pre-studies. The model represents an interim state to a regional model with a free groundwater surface.

Model domain

The model domain of the regional-scale model extends over about 23 km from the east to the west and about 12 km from the north to the south (cf. Fig. 4.58). The Äspö HRL is situated at the centre of the model and is at least 2 km off the boundary.

The horizontal model boundaries align as far as possible with catchment areas (cf. Fig. 4.20). Where not catchment areas were available, the model boundary intersects contour lines at approximately right angles or runs – in the transition zone from land to sea – in

the approximate middle of a bay or between islands. Offshore, no natural boundary is available, so that the model domain is set arbitrarily about 8 km from Äspö.

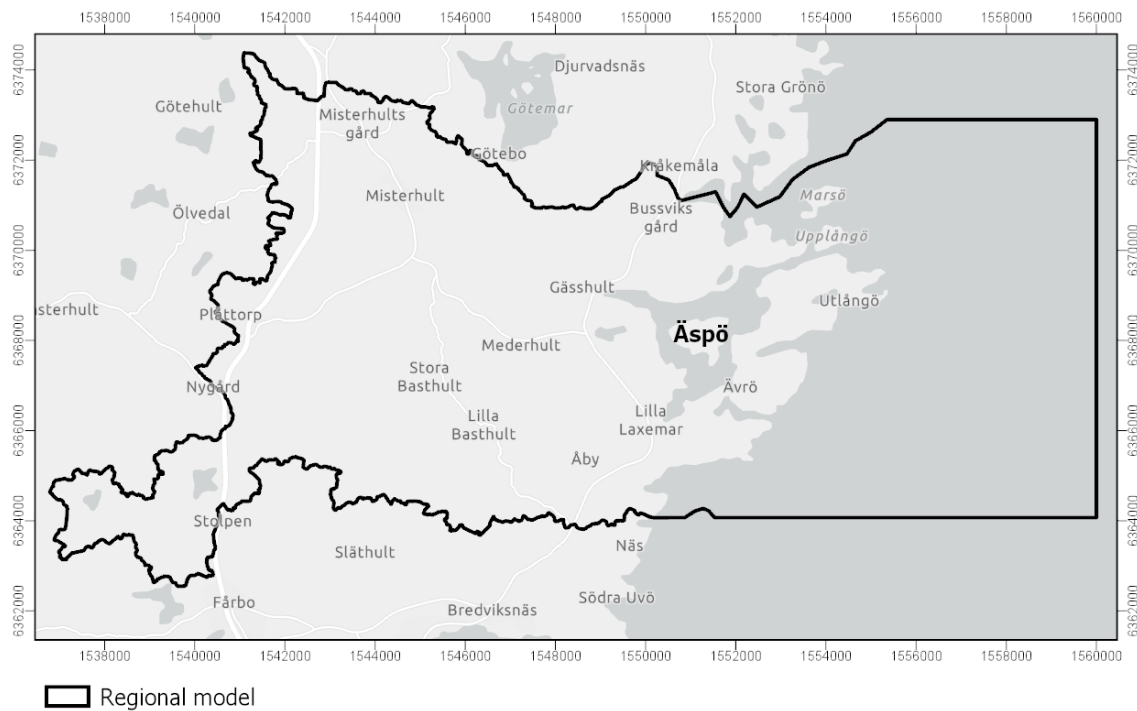


Fig. 4.58 Domain of the regional-scale model

A digital elevation model (DEM) on a 20 m x 20 m grid was provided by SKB as basis for the model topography (see Fig. 4.60). The DEM is accurate for the land surface, but the seafloor was only approximated. The original DEM was considered too rich in detail for the regional model. To reduce complexity, the grid was transformed to a resolution of 50 m x 50 m and an averaging filter was applied. A further simplification took place during the meshing process in which the element size determined the degree of smoothing.

The course of the coastline was of special interest as it is a characteristic of the model area. Moreover, the coastline plays an important role concerning the definition of boundary conditions as they differ between land surface and seafloor. It was considered essential to construct a well-defined border between land and sea based on the DEM, which is formed by raster values with $z = 0$ m. As the original DEM did not contain such data points, the values of certain grid cells were changed to zero. The resulting modification of the topography was considered acceptable.

Fig. 4.59 shows the original DEM and the topography formed by the mesh of the model. The comparison shows that the model surface is much less detailed than the original DEM. However, the main characteristics – e. g. the borderline between land and sea – are maintained in a simplified manner.

The model depth was set to 2,100 m which corresponds to the model depth of the ÄM.

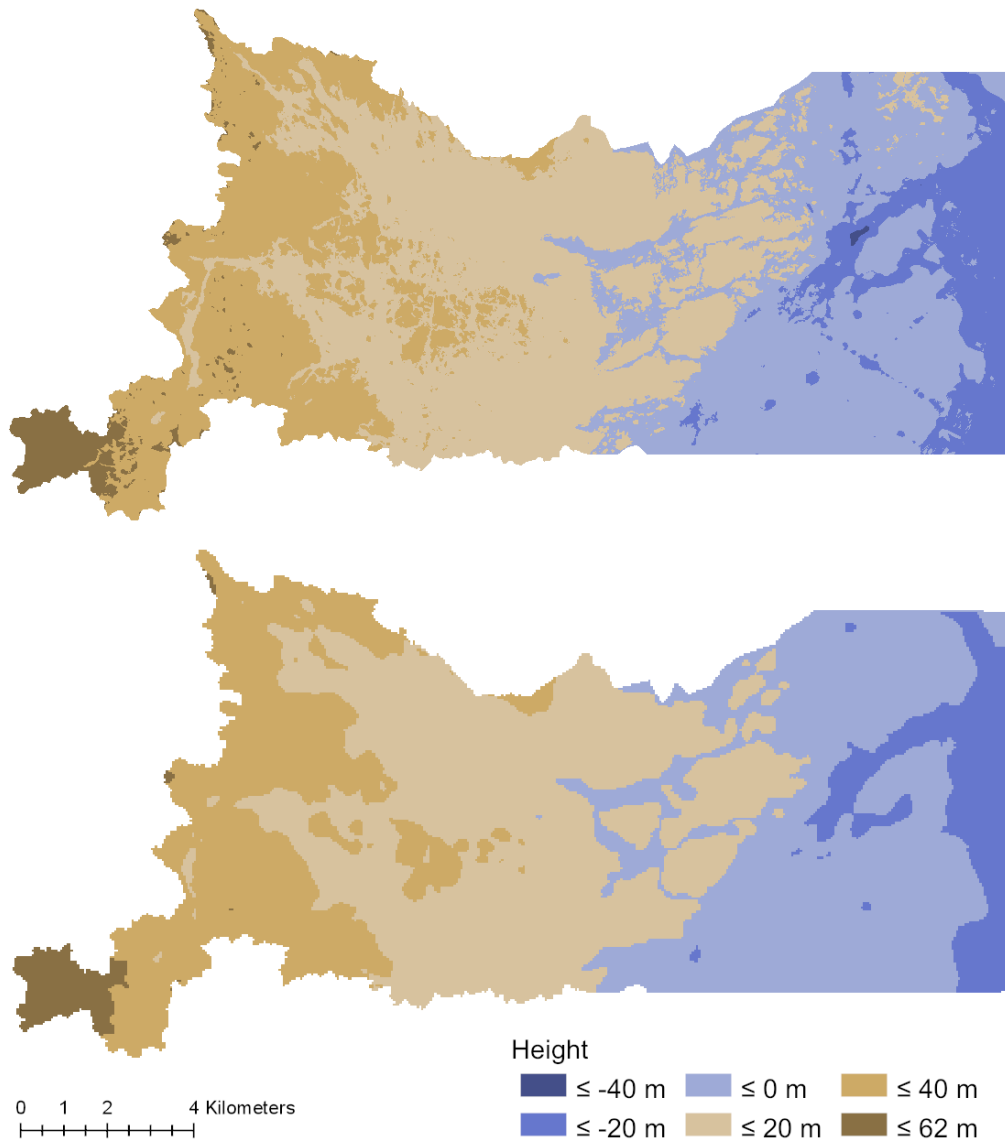


Fig. 4.59 Original DEM (above) and topography used in the regional model (below)

Regolith

The regolith is represented in the model by a uniform layer with a thickness of 25 m. The top of the regolith corresponds to the topographical surface and the layer extends over the whole model domain (see Fig. 4.60). In most areas, the thickness of 25 m lies far above the “true” thickness of the regolith. However, tests with the 2-dimensional model suggested to choose this high thickness to avoid problems with the free surface.

It was decided to use a permeability of 10^{-12} m² which is the mean value of the two soil types (glacifluvial deposits and glacial till) considered in /ERI 06/ and /HOL 08/.

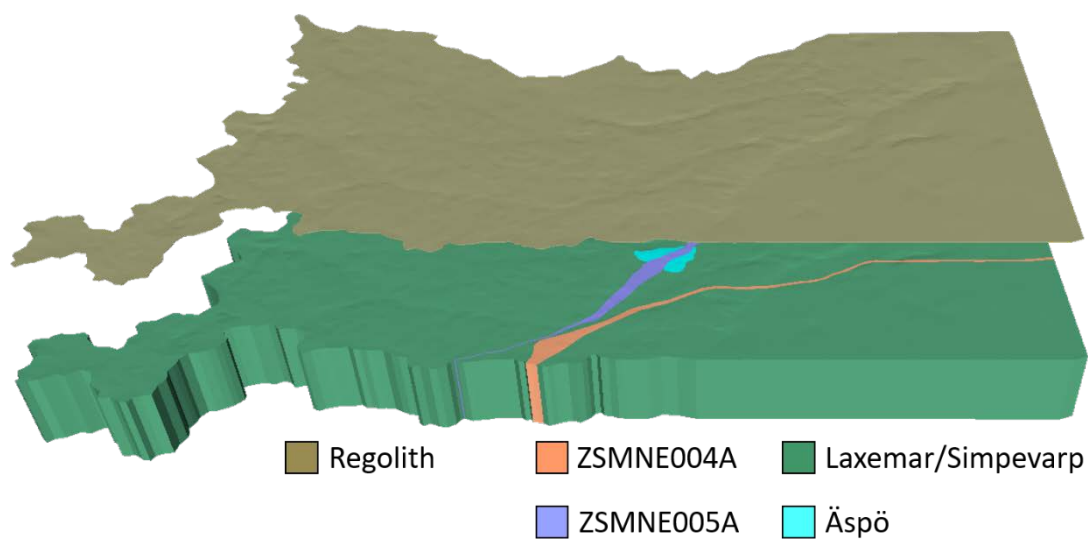


Fig. 4.60 Hydrogeological units of the regional-scale model

Bedrock

After the analysis of permeability data from literature (cf. Section 4.2.2, Section “Bedrock”) it was decided to divide the bedrock into two units only: “Äspö” and “Laxemar/Simpevarp” (see Fig. 4.60). The unit “Äspö” is almost identical to the island Äspö and corresponds horizontally to the lithological unit “Äspö diorite”. Its extent was estimated based on Fig. 4.24 and it was assumed that the diorite stretches vertically from the regolith to the bottom of the model. The unit “Äspö” is surrounded by the unit “Laxemar/Simpevarp” and cut by a deformation zones as described below.

The depth-dependent permeability functions described in Section 4.2.2, Section “Bedrock” are used with the parameters listed in Tab. 4.6 for the hydrogeological units “Äspö”

and “Laxemar/Simpevarp”. An overview over the depth trends for bedrock and deformation zones are shown in Fig. 4.61.

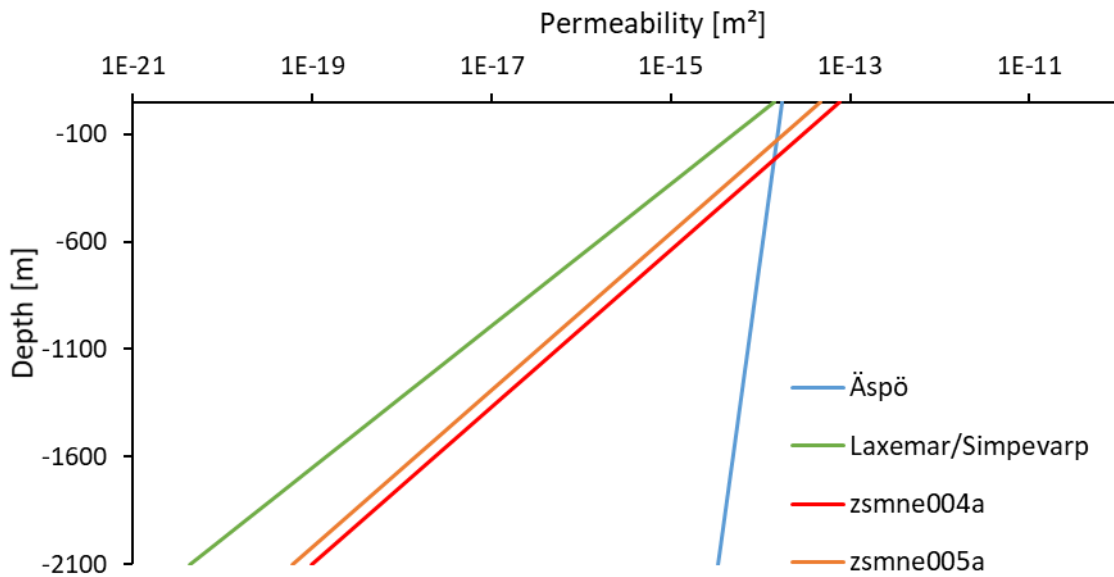


Fig. 4.61 Depth-dependent permeability for the hydrogeological structures used in the regional model

Deformation zones

The two dominant ductile deformation zones in the regional model area are considered in the model: ZSMNE004A and ZSMNE005 (Äspö shear zone) /WAH 08/ (see Fig. 4.60). The geometry of both deformation zones corresponds to /RHÉ 09a/ (cp. Fig. 4.37) except for minor changes due to smoothing during the mesh generation process. Both deformation zones are modelled with a vertical dip.

As the depth trends for transmissivity derived for ZSMNE004A and ZSMNE005A are considered uncertain by /RHÉ 08/, equation (4.5) is used with model DZ-R-22 in Tab. 4.7. Mean thicknesses of 150 m for ZSMNE004A and of 250 m for ZSMNE005A (/WAH 08/) are employed to compute the depth-dependent permeabilities for the deformation zones.

/RHÉ 08/ suggested a minimum transmissivity of 10^{-10} m²/s which corresponds to a minimum permeability of $6.7 \cdot 10^{-20}$ m² for ZSMNE004A and $4.0 \cdot 10^{-20}$ m² for ZSMNE005A, respectively. The permeabilities computed for the deformation zones do not fall below the respective minimum values within the model depth of 2,100 m (see Fig. 4.61).

Although /RHÉ 08/ suggests to model ZSMNE005a with a low conductive core and permeable sides, no horizontal anisotropy is considered for the regional model at the current state.

Boundary conditions

The bottom boundary and all vertical boundaries are closed except for the eastern side where the hydrostatic gradient is set so that water can leave and enter the model volume (see Fig. 4.62). The hydrostatic gradient was computed for fresh water as salinity is not considered in the presented model, and the pressure is zero at sea level. The same procedure was used to compute the pressure for the Dirichlet boundary condition at the seafloor on the top of the model.

At the land surface, the pressure is set to zero. This is not realistic, as the model surface is based on the topography and not on the groundwater table. However, the work presented here is only an interim step to a model with a free groundwater surface where the upper model surface only defines the volume in which the groundwater table may move (see Chapter 4.2.3).

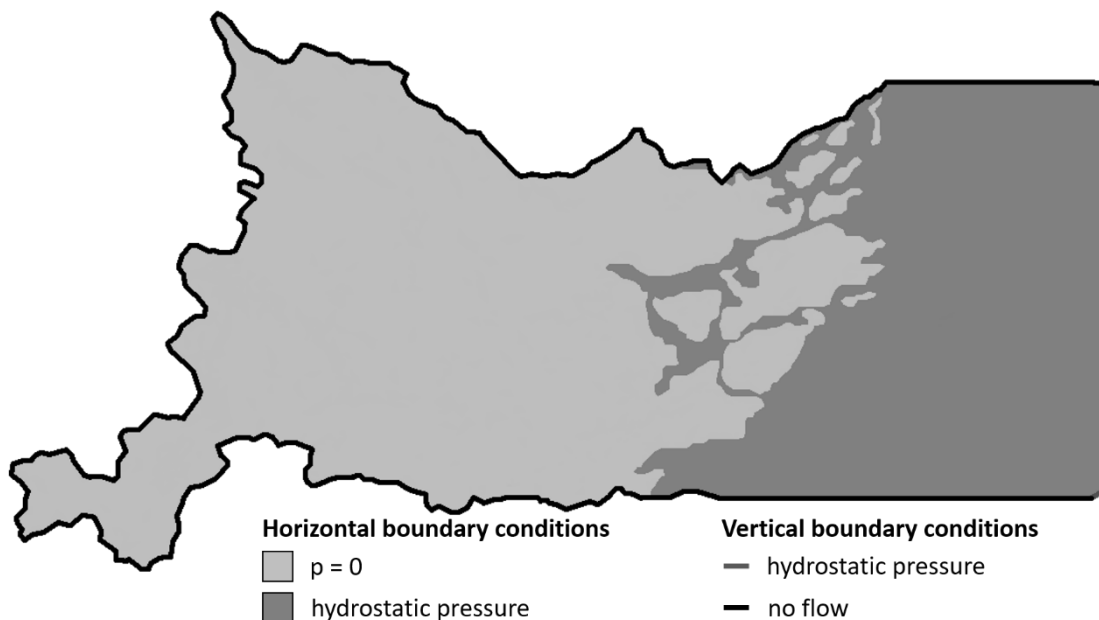


Fig. 4.62 Boundary conditions of the regional-scale model

Simulation results

In different reports of SKB, measured data such as groundwater heads or the drawdown caused by the Äspö HRL is used to evaluate and calibrate flow models (e. g. /RHÉ 09a/, /HAR 07/). This is not possible for the interim model presented here because the groundwater surface is predefined by the boundary conditions. Instead, it is attempted to assess the suitability of the model for the planned modelling work with a free groundwater surface based on the current simulation results.

The simulations with d³f++ using the set of parameters and boundary conditions described above yielded pressure and velocity distributions. The latter will be described and discussed in the following.

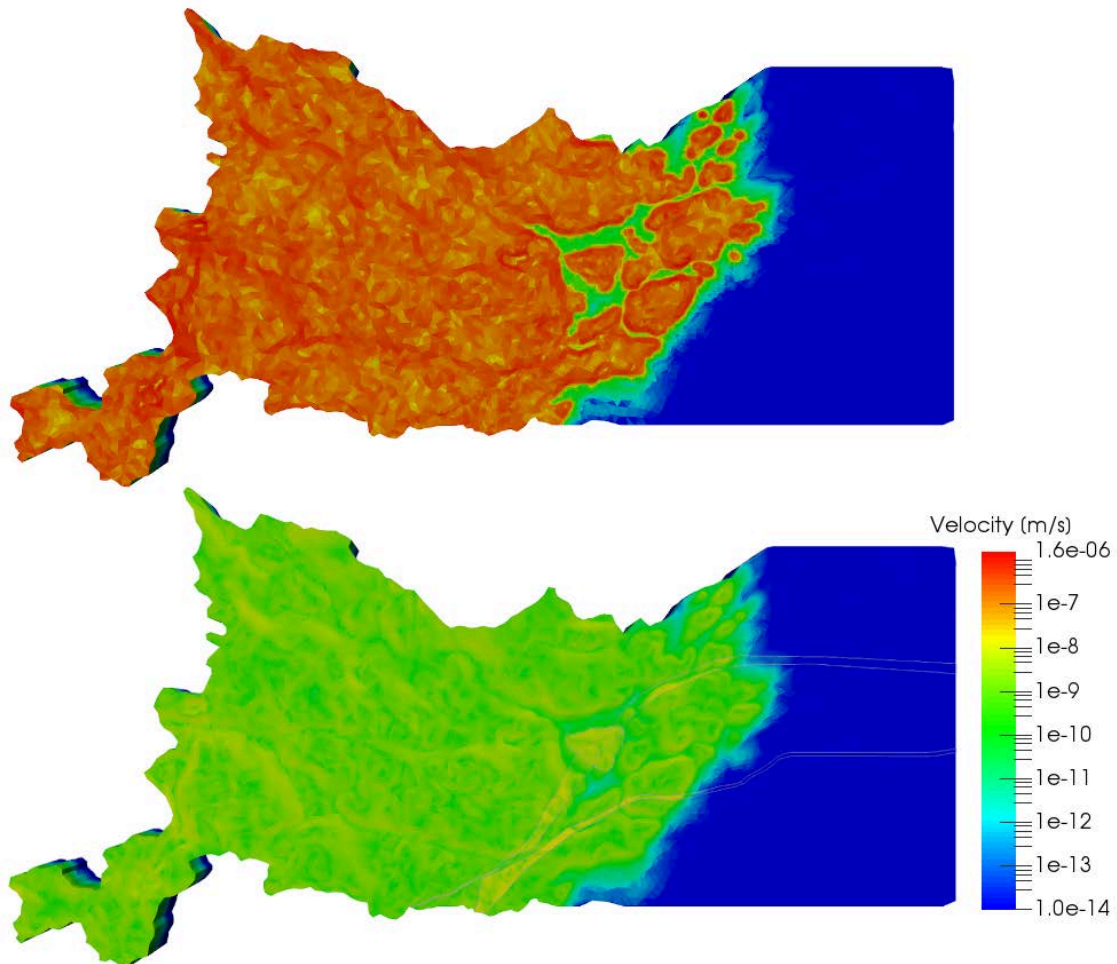


Fig. 4.63 Flow velocity at the model surface (above) and below the regolith (below)

Velocities at the top of the model vary from $4.0 \cdot 10^{-24} \text{ m s}^{-1}$ at the seafloor to $1.6 \cdot 10^{-6} \text{ m s}^{-1}$ on the land surface (see Fig. 4.63, upper figure). The range of the flow velocities shown in Fig. 4.63 was limited because here the flow patterns at the land surface are in focus where the velocity varies between $1.0 \cdot 10^{-8} \text{ m s}^{-1}$ and $1.6 \cdot 10^{-6} \text{ m s}^{-1}$. The velocity map does not show a large-scale trend but a small-scale pattern. Between the islands the flow velocity ranges between $1.0 \cdot 10^{-11} \text{ m s}^{-1}$ and $1.0 \cdot 10^{-9} \text{ m s}^{-1}$, and it decreases strongly towards the open sea.

This pattern is approximately the same below the regolith (see Fig. 4.63, bottom figure) which has – as stated above – a uniform thickness all over the model. However, the magnitude of the flow velocities is about two orders of magnitude smaller and the contrast between higher and lower velocities is less pronounced. Moreover, the deformation zones and Äspö can be distinguished as they show higher flow velocities than the surrounding unit “Laxemar/Simpevarp”. This does not apply for areas below the seafloor where no contrasts between the deformation zone and the surrounding bedrock can be seen.

Although flow velocities are higher in the deformation zones compared to the surrounding rock, the flow along the structures is inferior to the flow across them (not shown). Moreover, the flow directions arising in the regolith are retained in the deformation zones, but the flow is accelerated relative to the surrounding rock.

The flow velocity decreases strongly with depth (not shown). Thus, the main flow occurs in the upper 500 m. The highest flow velocity at the bottom of the model is reached in the unit “Äspö” with about $1.0 \cdot 10^{-10} \text{ m s}^{-1}$. In the surrounding unit “Laxemar/Simpevarp” reaches a maximum velocity of $5.0 \cdot 10^{-15} \text{ m s}^{-1}$.

As expected, the general flow directs from the hills to the valleys and from the land to the sea (not shown). High flow velocities occur along the valleys and at the border between land and sea. Very low flow velocities appear at the open sea. Moreover, no distinct flow direction can be distinguished in this part of the model.

A comparison with the slope of the model surface (see Fig. 4.64) shows that the magnitude of the flow velocity at the model surface corresponds strongly to the slope. The steeper it is the higher is the velocity. This is because stronger pressure gradients occur between the top boundary (where the pressure is set to zero) and the elements below.

This rule does not apply below the seafloor because here the hydrostatic pressure was set as boundary condition which inhibits strong pressure gradients at the top of the model.

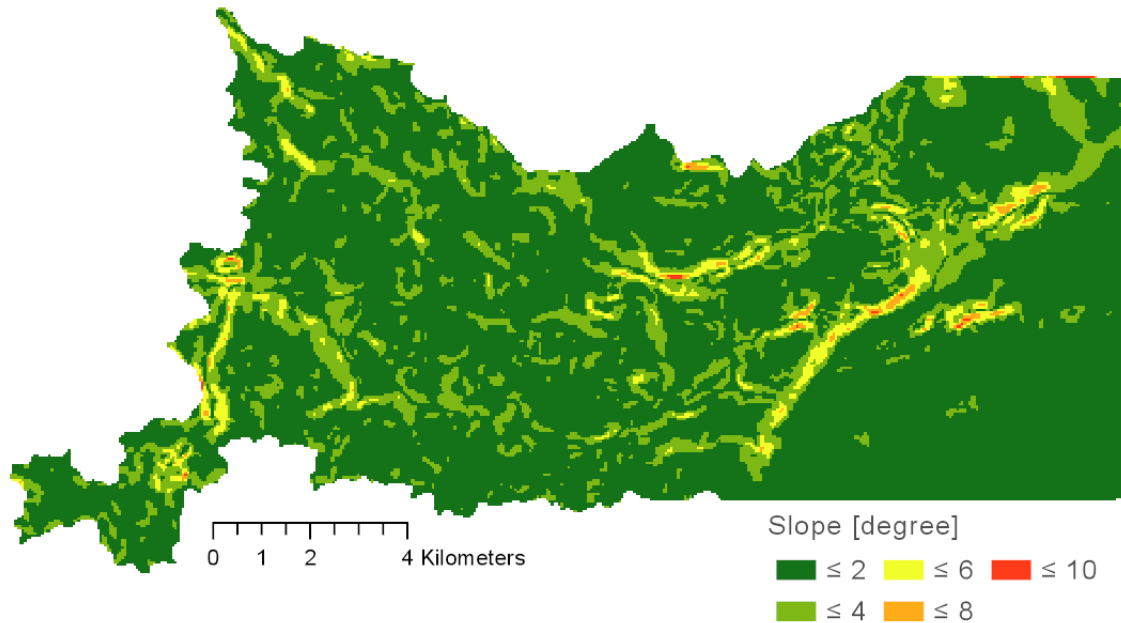


Fig. 4.64 Slope of the model surface in degrees

The model results show that distribution of the permeabilities has a strong influence on the flow velocities at large. This is shown by the higher flow velocities in the regolith compared to the bedrock or the differences in the flow velocities between the units “Äspö” and “Laxemar/Simpevarp”. The small-scale flow patterns, however, are mainly determined by the topography. Thus, the changes of the topography that were performed to obtain a defined coastline or the simplification and smoothing of the grid to reduce complexity might have a significant impact on the model results.

However, the actual model is only an interim stage on the way to a model with a free groundwater surface. It is not clear, how the free surface will behave in 3D, but it is sure that the topography will have a much smaller impact than it has in the actual model. Thus, the changes performed on the topography should be acceptable.

In the future model, also the Äspö HRL shall be considered and its impact on the groundwater surface and the flow field shall be analysed.

4.3 The WIPP Site, New Mexico

The Waste Isolation Pilot Plant (WIPP) is a repository for transuranic waste situated in a semi-arid region of southeastern New Mexico and western Texas, 42 km east of the City of Carlsbad, USA. The repository is located in a large, thick, Permian-age deposit of bedded salt, the Salado formation. This host rock formation is covered by flat bedded Permian halite, dolomite, anhydrite and clastic hydrogeological units as well as Triassic and Quaternary sandstone.

The aim of this work is examining groundwater flow in the overburden of the Salado formation, based on various studies performed by Sandia National Laboratories (SNL) /DAV 89/, /COR 96/, /COR 00/. These SNL studies in the past were mostly restricted to groundwater flow without regarding the density effects caused by dissolving salt. At the other hand, previous models of GRS that were considering density effects were restricted to 2d or small scale domains, see e. g. /KRO 96/. The three dimensional model presented here includes the overburden in the entire basin. The model region is based on /COR 00/ and extends to topographic features forming the boundaries of a regional groundwater flow system. It covers an area of about 6,000 km² and has a length of 112 km in north-south direction, a maximum width of 78 km in east-west direction and a depth of almost 700 m. The lateral model boundary is shown in Fig. 4.65.

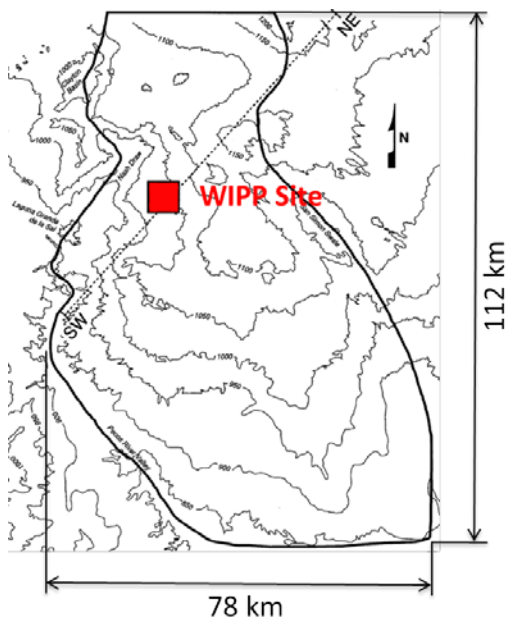


Fig. 4.65 Area of the WIPP-Site basin model after /COR 00/

4.3.1 Hydrogeological situation

The studied region is characterized by a smooth topographic relief, the elevation of the land surface ranges from about 850 m a. s. l. at the river Pecos to 1200 m in the north-eastern part. The geology is well documented in literature /DAV 89/. A schematic hydrogeological cross section of host rock and overburden is shown in Fig. 4.66.

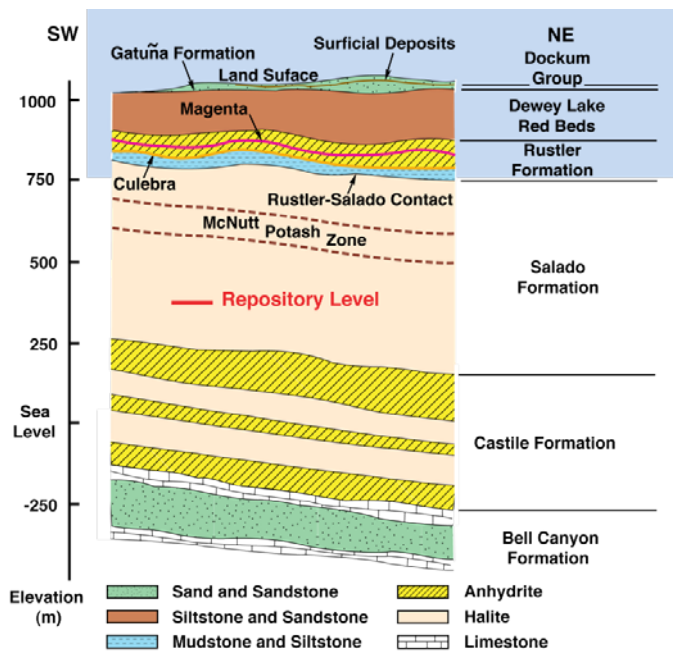


Fig. 4.66 WIPP-Site, schematic cross section (source: US DOE)

The lowest layer above the Salado, the Permian Rustler formation consists of anhydrite interbedded with dolomitic limestone, interlaminated dolomite and anhydrite, muddy halite, and clastics ranging from mudstone to fine-grained sandstone. It has a thickness of 100-150 m and is divided into five layers or members, /DAV 89/, see Fig. 4.67.

The lowest of these members, Los Medanos Member, consists of basal, fine-grained sandstone and mudstone overlain by interbeds of anhydrite, halite, and mudstone and has a thickness of 27 – 37 m. The basal, fine-grained sandstone forms the upper part of the Rustler-Salado contact zone. The anhydrite, halite and mudstone in the upper part of the Los Medanos Member are relatively impermeable and act as confining beds for the brine in the Rustler-Salado contact zone that is under artesian conditions.

The following Culebra Dolomite Member is a fine-textured, microcrystalline dolomite or dolomitic limestone. The Culebra has a thickness of approximately 8 meters over a very

large area, but there exist zones with a thickness of only 2 m or less. In some parts the Culebra Dolomite is extensively fractured, and the intensity of fracturing increases from east to west. First hydrologic field studies focused on the Culebra Dolomite. Because of its relatively high permeability in the vicinity of the WIPP site, the Culebra is considered an important potential pathway for the transport of radionuclides.

The Culebra Dolomite Member is overlain by the Tamarisk Member. East of the WIPP site the Tamarisk Member consists of about 55 meters of anhydrite and muddy halite. In the vicinity of the WIPP-Site and to the west in Nash Draw, the 20 to 30 meters of Tamarisk halite have been completely removed, leaving behind a 2- to 5-meter-thick mudstone residue, and the Tamarisk is almost impermeable. Westward toward Nash Draw, an increased permeability was observed, possibly due to fracturing. Here the Tamarisk is assumed to consist of two anhydrite layers, separated by a thin bedding of mudstone and halite, respectively, see Fig. 4.67.

The overlying Magenta Dolomite Member consists of dolomite and anhydrite with a thickness of about 7 m. It is partially fractured and has also relatively high permeabilities increasing from east to west, even though somewhat lower than in the Culebra. The Magenta is dry at several locations in central and northern Nash Draw, and it has been completely removed by erosion in southern Nash Draw.

The Forty-Niner Member is the youngest unit in the Rustler Formation. It consists of approximately 25 meters of low permeable anhydrite and muddy halite. In the vicinity of the WIPP site and to the west, the halite has been completely dissolved, leaving behind a 2- to 3-meter-thick residue of mudstone. In this basin model the Forty-niner member is assumed to consist of two anhydrite layers, separated by a thin bedding of mudstone and halite, respectively, see Fig. 4.67.

The Rustler Formation is overlain by the Permian Dewey Lake Red Beds, consisting of alternating beds of siltstone and fine-grained sandstone. In the eastern part of the basin it is 150 to 180 meters thick; whereas towards the west, it has increasingly been subject to erosion and is completely removed by erosion in the western part of the basin /DAV 89/. Here, the overlying, undifferentiated Triassic Rocks including the Dockum Group (Fig. 4.66) are combined with the Dewey Lake Red Beds to one layer of the hydrogeological model, see Fig. 4.67.

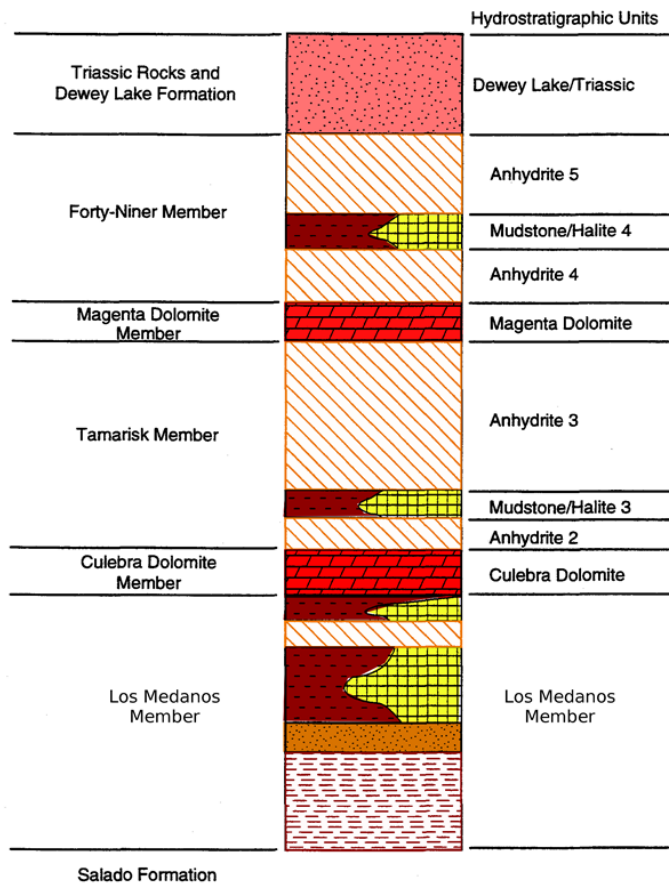


Fig. 4.67 Hydrostratigraphic units of the WIPP-Site basin-scale model /COR 96/

Based on geological data as well as on data from plant and animal remains, alternating climatic conditions are assumed throughout the Pleistocene Epoch with mean precipitation rates about twice that of the present /COR 00/. Up to 10,000 years in the past, precipitation is assumed to vary between 500 and 600 mm/year, decreasing rapidly to about 280 – 340 mm/year as the present values, whereas three peaks of 420 mm/a are supposed to have occurred 6,000, 4,000 and 1,500 years ago.

Because of the dry climates, groundwater recharge constitutes only a small percentage of precipitation, sinking from 2 mm/year 14,000 years ago to only 0 to 0.2 mm/year during the last 8,000 years, with periodic fluctuations throughout the Pleistocene and Holocene because following the assumption that maximum recharge occurs during cool wet periods /COR 00/, see Fig. 4.71. It is assumed that the groundwater table was near the land surface 14,000 years ago, while it is currently at a depth up to 150 m below especially in the north-eastern part of the model area /COR 00/.

4.3.2 Model description

The objective of the current modelling is to enhance the understanding of the groundwater flow dynamics in the basin in a time frame of tens of thousands of years, reproducing the development of the groundwater table from the late Pleistocene to the present and investigating the impact of density effects. This includes varying recharge rates while checking the position of the water table and the groundwater flow patterns. Finally, a comparison of the d^3f++ results with PFLOTRAN-simulations /LIC 14/ is planned.

The first small 3d density-driven flow model of the WIPP-Site region was presented by Davies using SUTRA /VOS 84/, /DAV 89/. In 1996, Corbet and Knupp presented a basin-scale groundwater model without regarding density effects, using the SNL-code SECOFL3D /COR 96/, /COR 00/.

The d^3f++ model presented here is directly based on the SECOFL3D input data provided by SNL. The geometrical data were received as raster data describing the 10 basal surfaces of the hydrogeological layers as well as the land surface. These 11 raster surfaces were converted into a 3d d^3f++ numerical grid using the ProMesh preprocessing tool (/SCH 16/, SCH 17/, www.promesh3d.com), see Fig. 4.68.

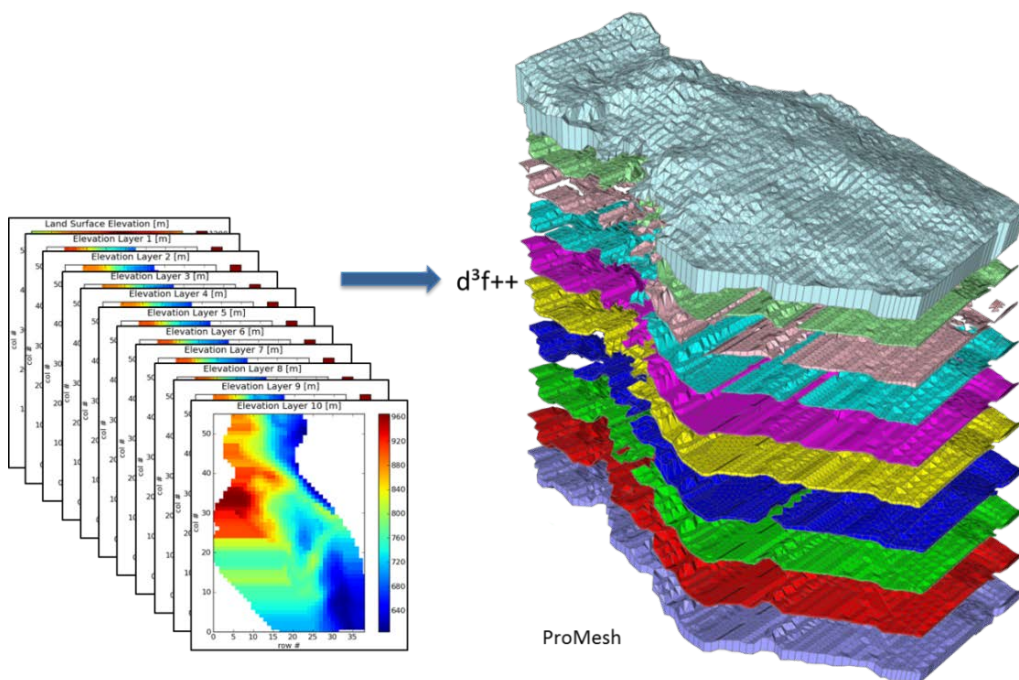


Fig. 4.68 Construction of the 3d d^3f++ model from 11 raster surfaces

The model domain has a depth of about 700 m and consists of 10 flat bedded layers with contrasts in their permeabilities of up to seven orders of magnitude, where the two main aquifers, the Culebra Dolomite and the Magenta Dolomite, have a thickness of only 2 m over huge areas. These characteristics combined with the large horizontal extension of the model domain evoke high numerical anisotropies.

For this reason, the d^{3f++} model restricts to only six layers as described on the left hand side of Fig. 4.67. The resulting geometry model is shown in Fig. 4.69.

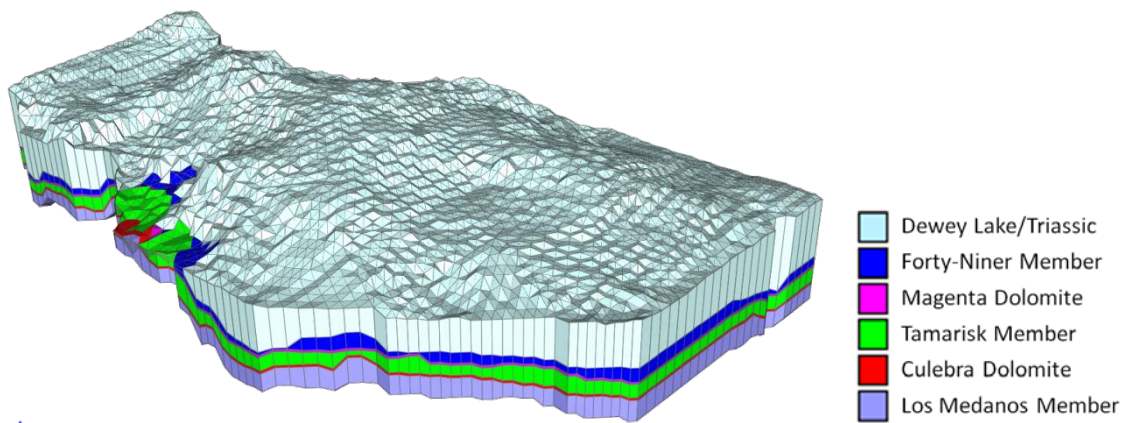


Fig. 4.69 WIPP-Site: 6 layers model, 50x exaggerated in vertical direction

The permeabilities and porosities used for each hydrogeological unit are compiled in Tab. 4.9. It has to be kept in mind that the permeabilities are not constant over the whole basin area within one layer. They are varying from lower values in the east, where the halite and limestone structures are still undisturbed, compared to the western, lower bedded areas, where formations and members are dissolved or strongly fractured, respectively. The permeability data in the d^{3f++} model are adopted from /COR 00/. Fig. 4.70 illustrates exemplarily the distribution of conductivities in the Culebra Dolomite and the formation above the Rustler. (To get the permeabilities, these values have to be multiplied by a factor of about 10^{-7} .)

As shown in Fig. 4.71, the recharge is assumed to decrease from 2.0 mm/year to 0.0 mm/year during the first 6000 years of model time, and during the last 8000 years three short-term periods occur with 0.2 mm/year. In the absence of information spatial variations of recharge are neglected.

Tab. 4.9 WIPP-site model: permeabilities and porosities

unit	permeability [m ²]	porosity
Dewey Lake/Triassic	10^{-14} - 10^{-12}	0.15
Forty-Niner Member	10^{-17} - 10^{-16}	0.14
Magenta Dolomite	10^{-17} - 10^{-12}	0.14
Tamarisk Member	10^{-21} - 10^{-18}	0.14
Culebra Dolomite	10^{-17} - 10^{-11}	0.15
Los Medanos Member	10^{-21} - 10^{-18}	0.1

The diffusion coefficient D_m is set to 10^{-9} m² s⁻¹ and the dispersion lengths are set to $\alpha_L = 10$ m and $\alpha_T = 1$ m (see equation (3.4)).

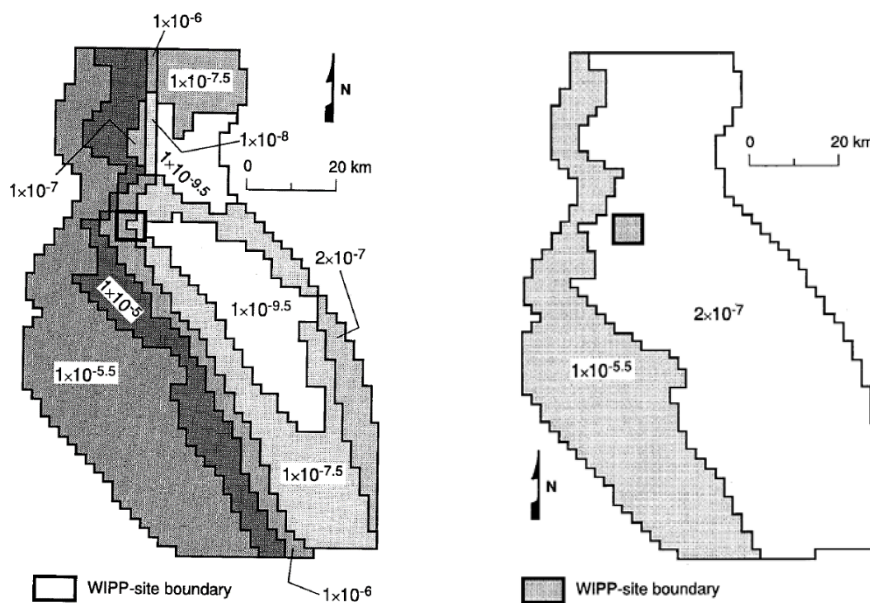


Fig. 4.70 WIPP-Site model: Distribution of hydraulic conductivities on example of the Culebra Dolomite (left) and the Dewey Lake/Triassic (right) after /COR 00/

4.3.3 Numerical model

Corbet and Knupp /COR 00/ used a computational grid consisting of only 18,000 hexahedrons. They started simulating groundwater flow about 14,000 years model time in the past in order to match the present groundwater flow regime, verifying their model among

other by pressure measurements and the current groundwater table. The objective of the d^{3f++} modelling is the reproduction of their results, but using a density-driven flow model.

The first step in model set up is the construction of the model geometry and the generation of the numerical grid. For models with thin layers, d^{3f++} usually works on triangle prism grids.

In former works the WIPP-Site model had provoked a lot of improvements of the preprocessor and grid generator ProMesh, see /SCH 16/ and /SCH 17/. The code d^{3f++} is using multigrid algorithms, see chapter 3. That means, the computational grid produced by the grid generator is used as a coarse grid and has to be refined several times during computation. To avoid high numbers of nodes in this coarse grid, a new refinement method was developed. By construction of special projectors within the multigrid algorithm, it is possible now to include the complete geometrical information of the original raster data in the grid refinement process, see section 2.2. That means using a coarse grid consisting of relatively few elements causes no loss of geometrical information on the finer grids while the grid quality remains good on all grid levels. The result was a coarse grid consisting of 54,200 prism elements enabling simulations up to multigrid level two. But the levelset method (see /FRO 12/, /SCH 12/), that is used in d^{3f++} for the modelling of the free groundwater surface, did not work stable on this grids for long model times. Therefore, to get long-term results also for free-surface-flow problems, the grid had to be further optimized. The result is the coarse grid consisting of 2,856 elements shown in Fig. 4.71. That means, the corresponding grid at level 1 and level 2 consists of 22,848 or 182,784 elements, respectively.

The bottom of the model and the lateral boundaries are assumed to be closed for groundwater flow. On the bottom boundary the concentration of saturated brine is prescribed as a Dirichlet boundary condition, where a Neumann-zero-condition is set for the salt concentration on the lateral boundaries. For the complete the upper boundary a groundwater recharge varying from about 2 mm 14,000 years ago to 0.1 mm in the present is defined, as shown in the upper part of Fig. 4.71, and freshwater concentration is assumed except of the leakage areas, where the concentration adopts the same value as inside the boundary. In the north-western region, the Nash Draw, a leaching boundary is developing with time. As an initial condition the salt concentration was set to zero in the whole model. As an initial condition the groundwater surface was placed about 10 m below ground surface (b.g.s.) as shown at the in Fig. 4.71 (right).

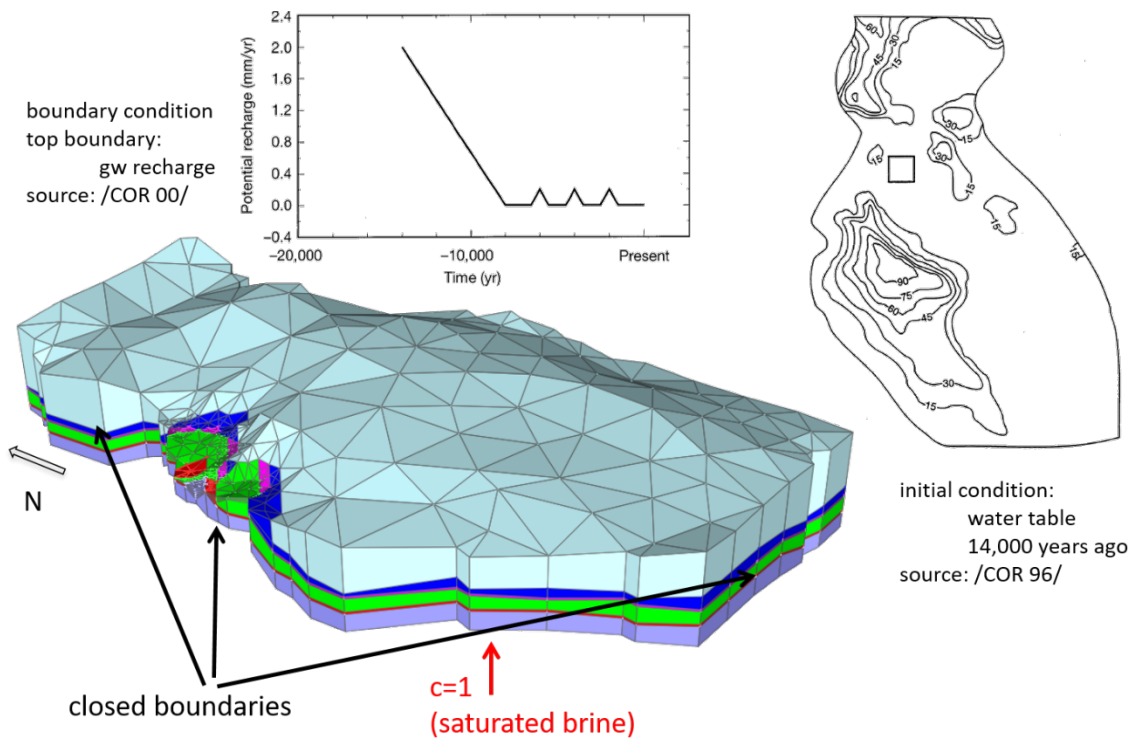


Fig. 4.71 WIPP-Site model with coarse grid and boundary conditions, 50 times exaggerated in vertical direction

4.3.4 Results

The simulations were performed at grid level 1 and grid level 2, whereas a model time of 14,000 years was only reached on level 1 up to now. Fig. 4.72 shows the distribution of the permeabilities in vertical direction and the corresponding velocities in a W-E-cutting plane with y coordinate at the position of the repository. It illustrates that the main groundwater flow takes part in the two thin main aquifers culebra dolomite and magenta dolomite. The flow directions are following the declining ground surface. Most of the groundwater flow leads to the west, where a discharge into the Nash Draw is observed. In the low permeable, central part of the model domain occur only small flow velocities.

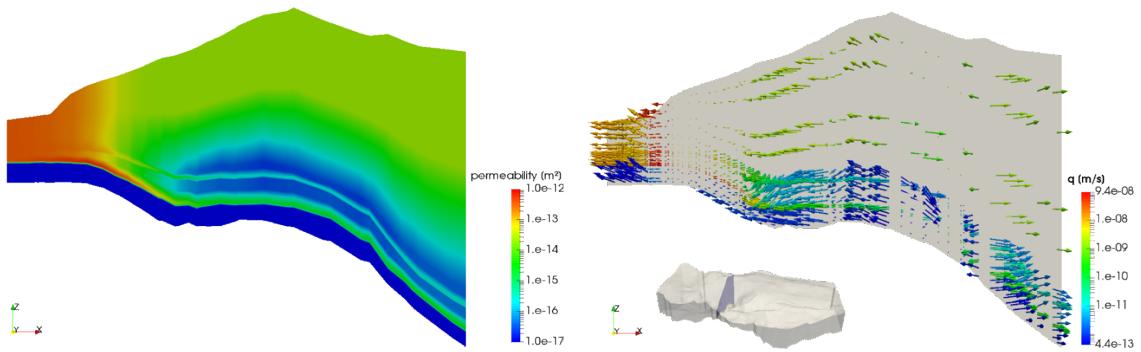


Fig. 4.72 Distribution of permeabilities (left) and velocity vectors (right) in a vertical W-E-cutting plane at the repository position

Fig. 4.73 compares the Darcy velocities in the main aquifer, the culebra dolomite, at the beginning of the simulation 14,000 years ago and today. It is obvious that the flow patterns are primarily following the slope of the terrain that is identical with the slope of the initial groundwater surface, that is shown in Fig. 4.75. The velocity values and directions are slightly varying with time, especially in the western part of the model, caused by smoothing and flattening of the free groundwater surface with model time.

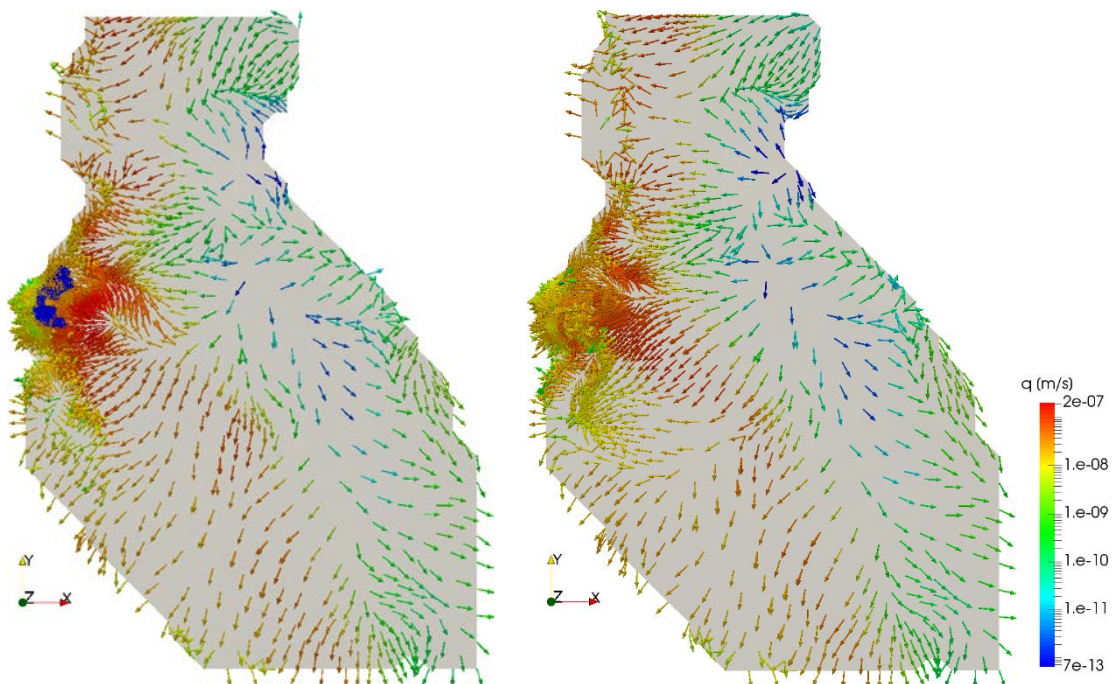


Fig. 4.73 Simulated velocity field in the culebra dolomite at the beginning of the simulation and after 14,000 years (right)

To handle free surface groundwater flow d3f++ is using a level set method, see /FRO 12/ and /SCH 12/. The implementation of this method still leads to restrictions of the time step size.

Another result, the development of the salt concentration, is shown in Fig. 4.74. In this graphic the variable c stands for the relative salt concentration with $c = c^{rel} = 1,197.2 \text{ kg/m}^3$. The left side shows the salt concentrations by isosurfaces. The salt is moving very slowly upwards with time. To illustrate the salt spreading, on the right side a logarithmic scale was chosen to show the salt spreading at a cross section. As expected, the salt moves much faster upwards in the west part where higher permeabilities occur and the main aquifers are touching ground surface.

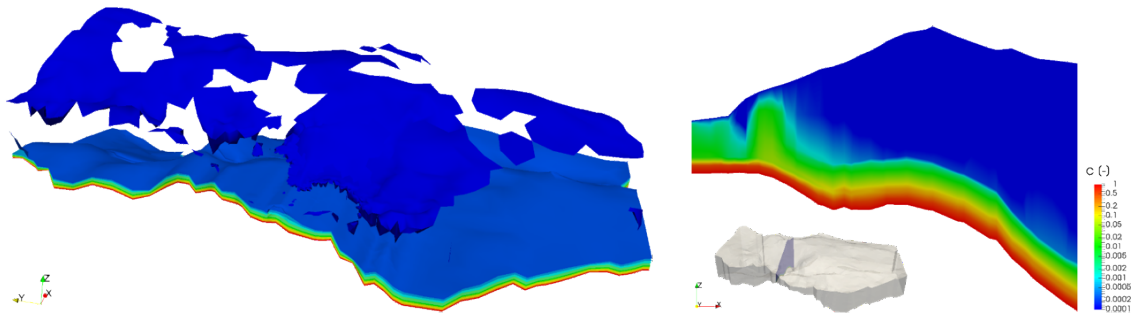


Fig. 4.74 Simulated relative salt concentration after 14,000 years;
left: isosurfaces in successive intervals of 0.1: $c=0$ (dark blue), $c=0.1$ (light blue), ..., $c=1$ (red)
right: W-E-cutting plane, c on log scale

The structure of the groundwater surface is strongly declining with time caused by decreasing recharge rates (see Fig. 4.71). Additionally, it is noticeably smoothed, because at initial state it was completely following the hilly ground surface. This rough structure disappears with advancing model time, and the water table is only following physical conditions. The water table is sinking at its formerly highest points, while it is touching ground surface in the lower lying areas close to the west and south-west boundary. In the related regions of the top boundary groundwater discharge areas are establishing and growing with time. In Fig. 4.75 (b) and (c) these areas appear as voids in the visualization because the simulated groundwater level lies outside of the model domain.

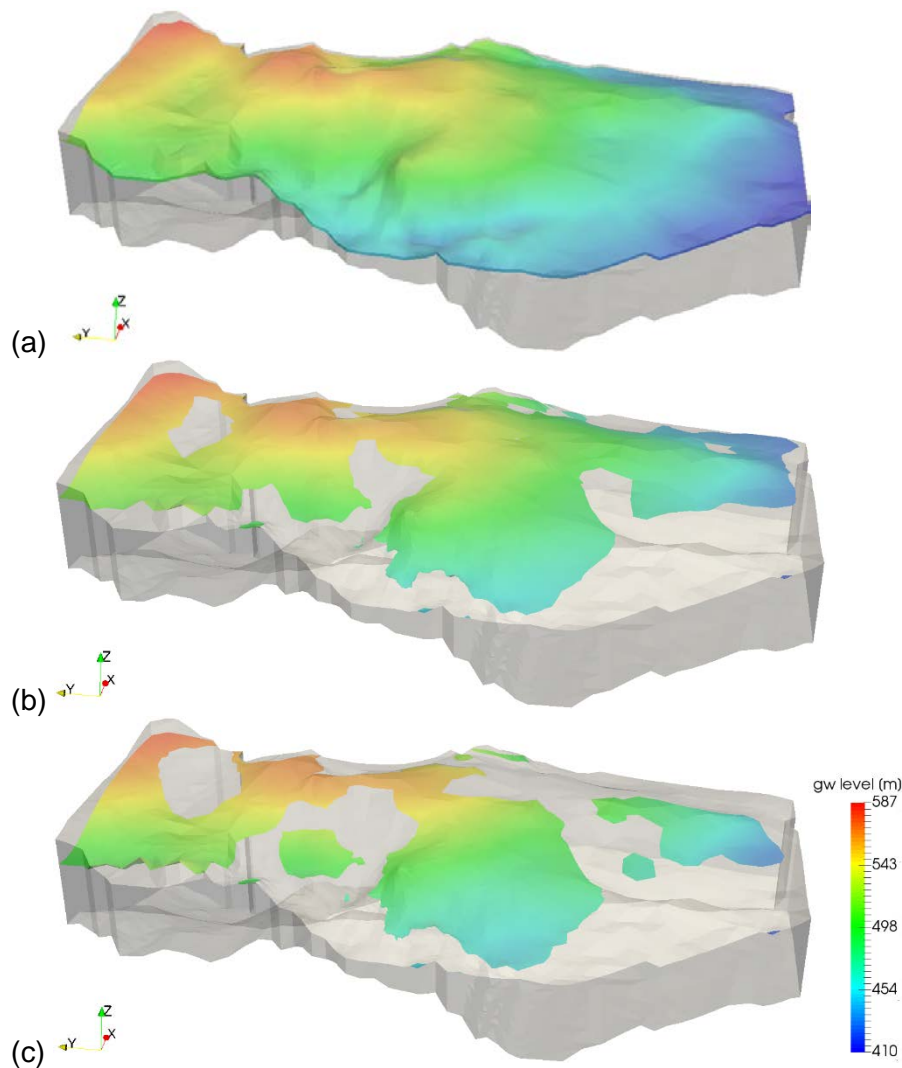


Fig. 4.75 Simulated situation off the groundwater surface at the initial state (a), after 2,000 years (b) and after 14,000 years (c)

4.3.5 Summary

The Waste Isolation Pilot Plant (WIPP) is a repository for transuranic waste situated in a semi-arid region east of Carlsbad, New Mexico, USA, in a thick, Permian-age deposit of bedded salt. The host rock formation is covered by flat bedded Permian halite, dolomite, anhydrite and clastic hydrogeological units as well as Triassic and Quaternary sandstone. The present model covers the whole overburden in the entire basin. The model domain has a horizontal extension of about 6,000 km², a depth of about 700 m and consists of flat-bedded layers with contrasts in their permeabilities up to seven orders of magnitude, where the two main aquifers have a mean thickness of only 2 m. These characteristics combined with the large horizontal extent of the model domain evoke high

numerical anisotropies. A second challenge is the large free groundwater surface with extremely low groundwater recharge rates as an upper boundary condition.

The objective of this work was to enhance the understanding of the groundwater flow dynamics in the basin in a time frame of tens of thousands of years, to show and to improve the ability of d^{3f++} to set-up a regional 3d model with a reasonable effort, to simulate density-driven groundwater flow correctly and, especially, to handle a free groundwater surface in such a big model, with density influence and over long time periods.

The d^{3f++} solvers work very efficient despite of the high anisotropies, but only if the free groundwater surface is neglected. In d^{3f++} levelset a method is used for the modelling of the free groundwater surface. Even though this method was substantially improved and stabilized and an implicit solver was implemented in the scope of this work, it is still limiting timestep length and leads to long computing times.

Modelling this strongly density-driven flow problem with high anisotropies and a large free groundwater surface was successful, even though the time step lengths are still not satisfying. This problem has to be overcome to get the results in reasonable computation times.

4.4 Čihadlo groundwater flow model, Czech Republic

In 2014, SÚRAO, the Czech Radioactive Waste Repository Authority launched a large-scale project aimed at acquiring the knowledge and know-how needed both to form an understanding of the various processes likely to occur within the repository system and to compile conceptual, mathematical and computational models describing the disposal system and predicting its development for safety assessment purposes. As part of this project, nine studies were conducted which were subsequently summarised in the form of safety reports on all candidate deep geological repository sites (Březový potok, Čertovka, Čihadlo, Hrádek, Horka, Janoch, Kraví hora, Magdaléna and Na Skalním). All candidate sites are situated in a crystalline rock environment.

In 2020 it is planned to reduce the number of potential sites to 4 preferred sites for the conducting of geological investigation work. The current schedule envisages that the Government will select a final and a reserve site in 2025. The actual construction of the repository will commence in 2050 with the start of operation of the facility expected in 2065 at the earliest.

In 2015, SURAO started a project in where regional geological and hydrogeological models were developed for the nine candidate sites mentioned above. Based on this a 3d flow- and transport modelling should be performed to describe the groundwater flow in the geosphere and to identify the main transport pathways. The Czech Geological Survey, the PROGEO consulting engineers, the Libereč Technical University, and ÚJV Řež are taking part in this project. SURAO provided successively site characterizing data to the project partners. The working groups participating build up groundwater flow and transport models based on different numerical codes, MODFLOW /HUG 17/, FEFLOW /WAS 10/ and FLOW123 (ÚJV in-house code, /JAN 19/), and they are exchanging their results at regular meetings. In the course of the German-Czech cooperation the GRS suggestion of setting-up a groundwater model for one of these sites also with d3f++ was appreciated, and the Čihadlo site was selected for this purpose. Čihadlo is situated in the south of Bohemia, about 100 km south-east of Prague, see Fig. 4.76.

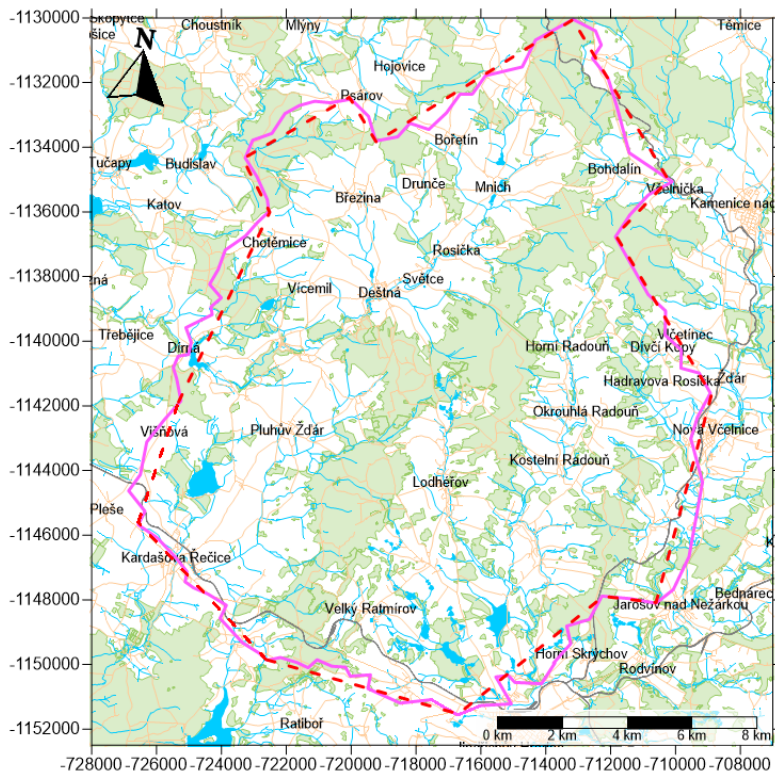


Fig. 4.76 Model areas (full line: FEFFLOW/MODFLOW, dotted line: Flow123); source: PROGEO

4.4.1 Hydrogeological model

The local rock units belong to the Moldanubicum of Southern Bohemia. Rocks identified in the area of the 3D regional model include the Monotonous Group, granitoids of the Moldanubian Plutonic Complex (Klenov Pluton) and sediments of the platform cover. The existing fault system is in general trending NE–E to SW–W or NW–SE. In the eastern part of the area faults and fault zones with N–S orientation are predominating. Their more abundant occurrence in the southeast of the area is due to the more intensive exploration works in the area.

The largest and most important fault zones occur in NW and SE parts of the model area. This includes faults oriented NE-SW and N-S exceeding 10 km in length, corresponding to the category 1 – regionally important fault zones (according to the SKB classification). The majority of the faults in this area are classified in category 2 – locally important fault zones with an extension 1 –10 km. Faults shorter than 1 km were classified as category 3. They mainly include fault zones without a preferred orientation in the southern part of the study area, see Fig. 4.77. Because of fault data insufficiency, an equivalent porous media (EPM) approach was chosen by PROGEO.

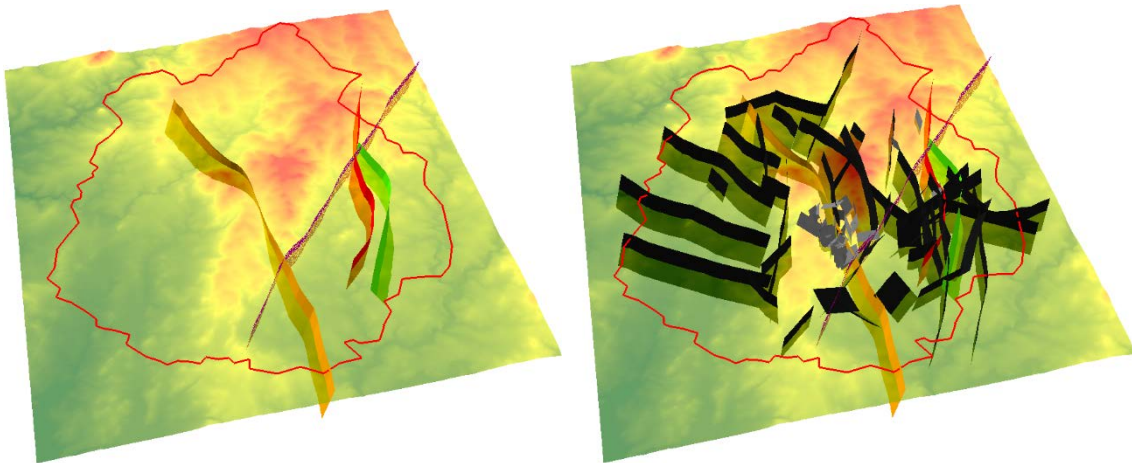


Fig. 4.77 Situation of faults in the model area; left: regional fault zones; right: regional (coloured), major (black) and minor faults (gray)

The Čihadlo model area is part of the Lužnice River catchment area and is drained by a huge river network. The total recharge is estimated to 100 mm a^{-1} .

The model covers an area of about 260 km^2 with a north-south extension of about 20 km . Because of lack of exploration data all assumptions concerning rock permeability are solely based on input assumptions and expert knowledge. On this base, PROGEO provided a hydrogeological structure model, consisting of 13 layers, including the conductivity values in a MODFLOW format. This model was adapted and imported to d^{3f++}, see Fig. 4.78. The permeabilities in the upper part of the matrix is varying between $5 \cdot 10^{-16} \text{ m}^2$ and $1 \cdot 10^{-15} \text{ m}^2$, the permeability of all fractures is set to $1 \cdot 10^{-13} \text{ m}^2$. The permeability of the covering sediment layer is set to $2 \cdot 10^{-15} \text{ m}^2$, s. a. Fig. 4.79.

The hydraulic conductivity is assumed to decrease with depth following

$$K(z) = K_0 \cdot 10^{\frac{-z}{c}} \quad (4.9)$$

where $K(z)$ is the hydraulic conductivity [m s^{-1}] at depth z and c a coefficient, $c = 400 \text{ m}$.

Additionally, PROGEO provided a digital relief map, river network data (see Fig. 4.78) and data of 73 groundwater gauges. Based on this data, a 3d hydrogeological model was set-up in d^{3f++}.

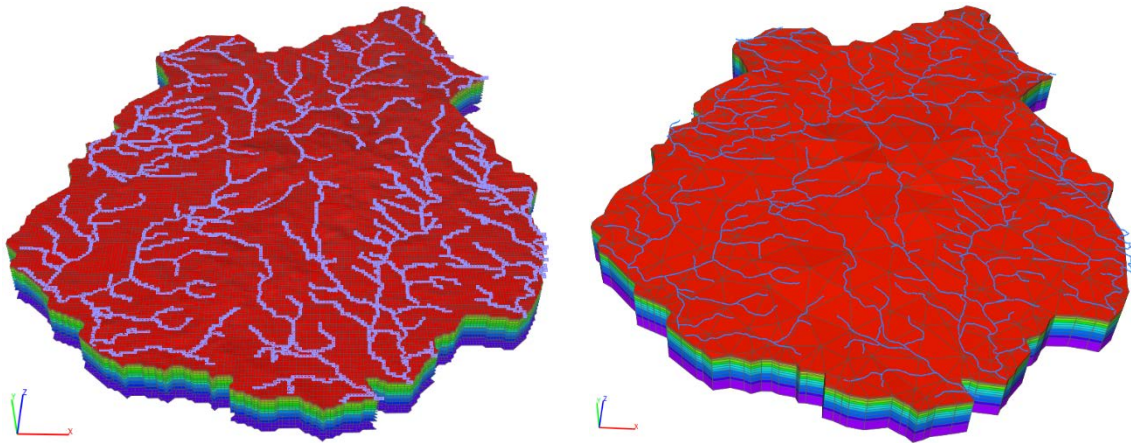


Fig. 4.78 Regional model Čihadlo; left: MODFLOW model, right: d³f++ model with river network

The lateral boundaries and the bottom of the model are assumed to be closed for groundwater flow. At the top boundary a constant groundwater recharge of 100 mm/year is defined as the only source of groundwater inflow. The rivers allow an outflow depending on their water level in relation to the local groundwater level. Following the suggestions of PROGEO, the initial state for the groundwater level was set to 10 m b. s. l.

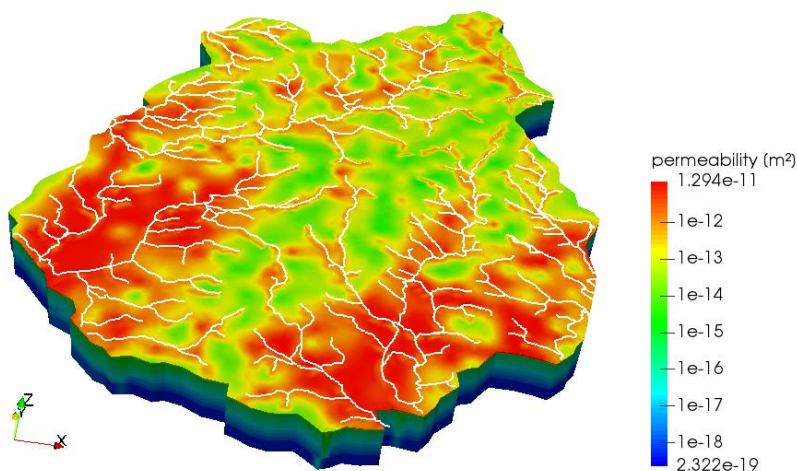


Fig. 4.79 Čihadlo model, permeability distribution

4.4.2 Results

The d³f++ numerical coarse grid consists of 40,911 elements. For the calibration process the grid was refined to grid level 2 with 2,618,304 elements. The groundwater model was calibrated comparing the simulated groundwater level with the measurements in 73 wells provided by PROGEO. Fig. 4.80 shows the differences as a diagram and their spatial

distribution. The resulting Nash-Sutcliffe-coefficient amounts 0,957. In Fig. 4.81 the spatial distribution of the deviations is illustrated.

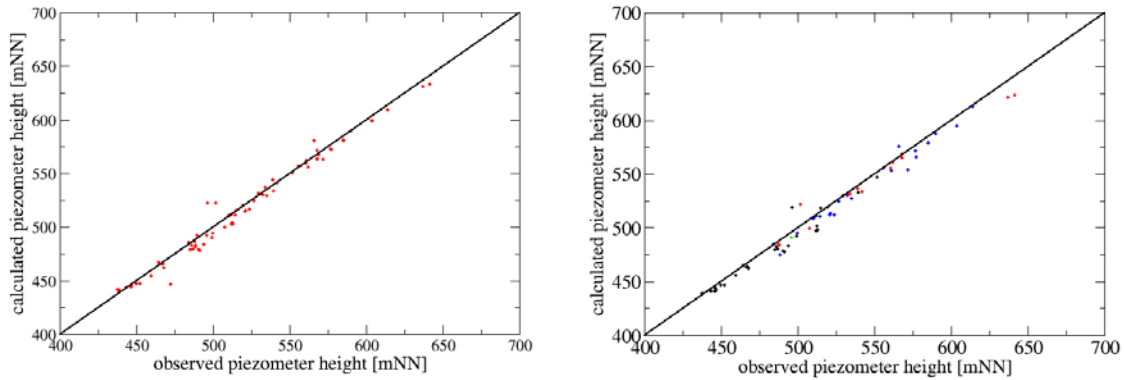


Fig. 4.80 Comparison of the simulated groundwater level with the measurements in m a. s. l.; left: MODFLOW, right: d3f++, point colors corresponding river catchment zones, s. a. Fig. 4.84

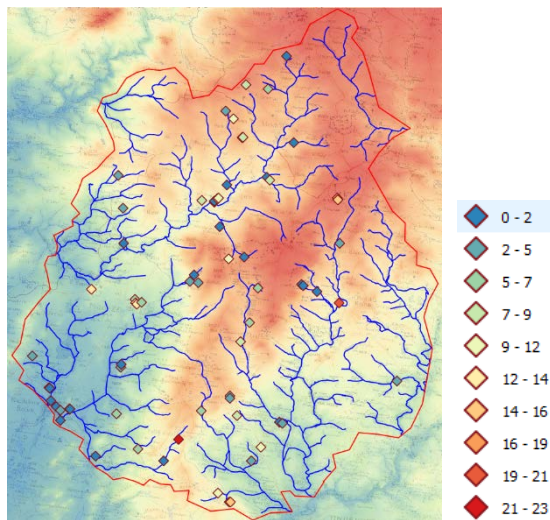


Fig. 4.81 Location of the measuring points and difference in m

Fig. 4.82 shows the steady state of the groundwater level and the flow field at the depth of the hypothetical repository. Obviously, near-surface groundwater flow is mainly directed to the rivers and especially to the south-west of the model area. This corresponds with the observation that the region is predominantly drained in direction of the Lužnice-river that is located there.

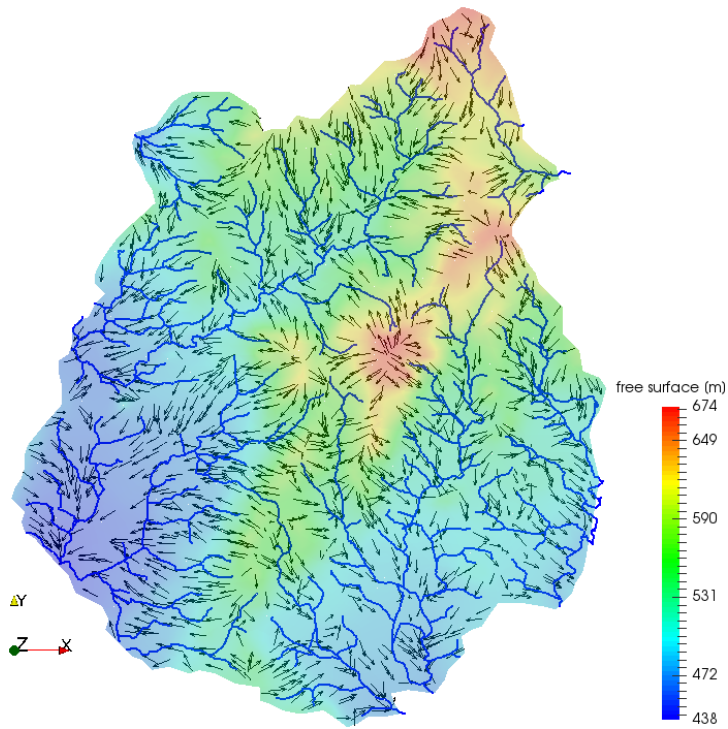


Fig. 4.82 Simulated groundwater level and velocity field at 0 m a. s. l.

One of the objectives of this works was to compare the results of d^3f++ with MODFLOW-results provided by PROGEO. Fig. 4.83. shows the simulated groundwater heads after calibration. The isolines are nearly identical.

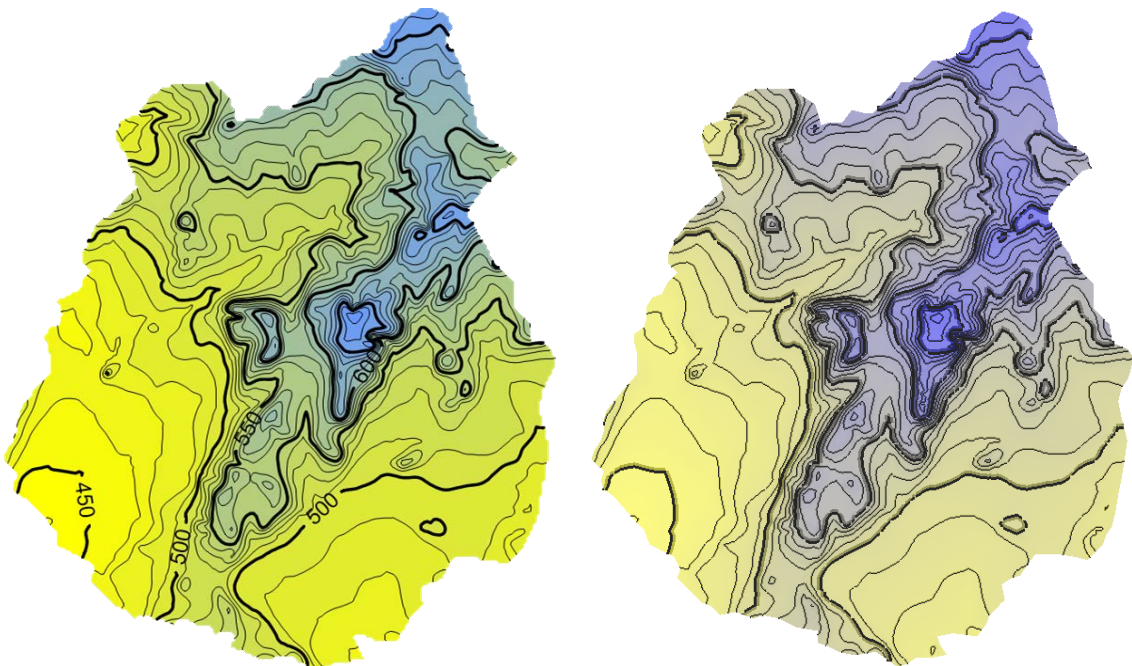


Fig. 4.83 Comparison of the calibrated groundwater heads, left: MODFLOW /PRO 20/, right: d^3f++ ; yellow: 438 m, blue: 674 m a. s. l. (different colorbars)

Within the scope of the benchmarking the position of the groundwater table, the results for the groundwater discharge into the rivers were provided by PROGEO. For this purpose 6 river catchment areas were distinguished, see Fig. 4.84. It is obvious that the near-surface flow patterns are mainly directed to the rivers. Fig. 4.84 shows also that there are some velocity vectors crossing the boundaries of the catchment areas. This may indicate that these areas are not optimally chosen. The simulated drainage rates of both codes as well as the corresponding groundwater recharge rates are compiled in Tab. 4.10. The drainage rates are slightly overestimated in comparison to the recharge rates by both codes in the same four catchment areas, while they are underestimated in area 2 and 5. MODFLOW and d³f++ show similar deviations.

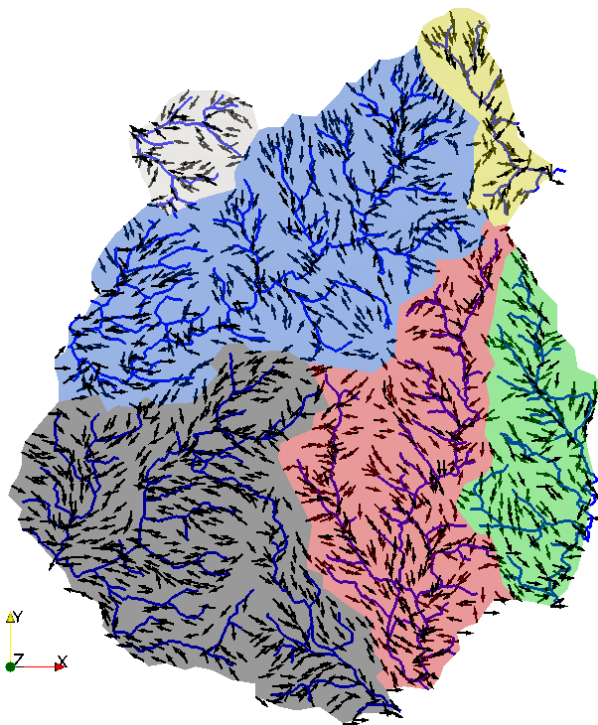


Fig. 4.84 Flow field in the upper layer and catchment areas of the rivers

Tab. 4.10 Comparison of recharge and river drainage

catchment area	river drainage [l/s]		gw recharge [l/s]
	d ^{3f++}	MODFLOW	boundary condition
1	239	242	234
2	159	166	170
3	91	91	86
4	42	39	35
5	234	232	241
6	41	36	31
sum	806	806	797

4.4.3 Discussion

Most of the differences in the results can be led back to the huge differences in the codes. Where d^{3f++} based on a Finite Volume discretisation, implemented in C++, MODFLOW is a Finite Difference Code, implemented in FORTRAN 90. This evokes differences in the numerical grids: The latter uses a fixed grid, consisting of 328,081 rectangular cells with an extension of 100 m x 100 m in horizontal direction. As just mentioned above d^{3f++} works with multigrid algorithms, the coarse grid consists of 40,911 triangle prism elements, that are refined to 327,288 elements at grid level 1 and 2,618,304 elements at grid level 2. Especially in the case of EPM modelling this different grid concepts lead to differences in the hydraulic conductivity distribution and, consequently, in the fracture representation. To meet the faults locations more exactly and to make the results comparable it would be advisable to use discrete fracture network models (DFN).

Additionally, both models provide a different interpretation of the free groundwater surface. MODFLOW provides groundwater heads calculated for the centroids of each model cell, whereas d^{3f++} uses a levelset method /FRO 12/, /SCH 12/ to simulate the exact position of the moving surface.

Another important difference in the model set-up between MODFLOW and d^{3f++}, that can be led back to the grid resolution, is the model resolution of the DEM. d^{3f++} starts with a coarse grid, only describing the hydrological structures. From the numerical point of view it is desirable that this coarse grid is as coarse as possible. In case of the Čihadlo model that means, that the resolution of the digital elevation model (DEM) is even worse than in the MODFLOW grid. Though the situation of the DEM, representing the upper

model boundary, has no physical importance for groundwater flow, there can occur some problems if the groundwater surface is touching the model boundary. To overcome this the recently developed raster layer projector method /REI 16/ was applied. This method allows that the geometric approximation of individual layer improves as the grid is refined. The grid refinement is not only restricted to the simple partition of the grid elements, it also processes the complete geometric information available in the original raster data. The application of this method to the Čihadlo model is illustrated in Fig. 4.85.

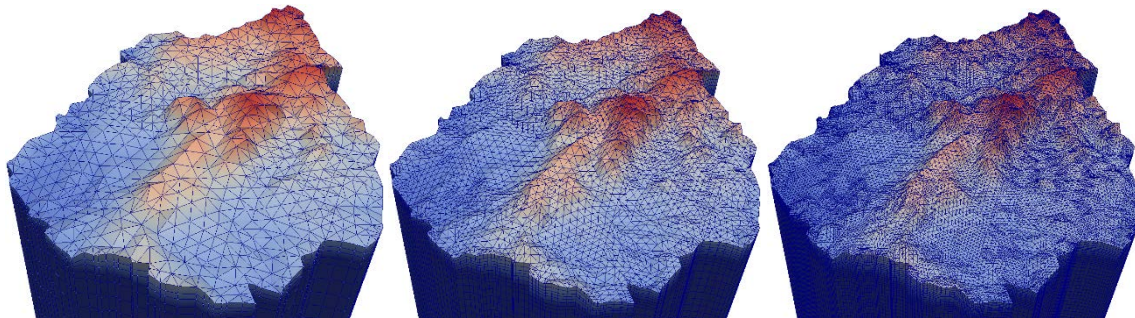


Fig. 4.85 Refinement of the top surface to grid level 1, 2 and 3 using the raster layer projector method (blue: 420 m, red: 682 m a. s. l.)

Finally, the main disadvantage of d^{3f}++ with respect to the Čihadlo groundwater model is, that there still doesn't exist an automatic calibration. This is one of the subjects of current works in the HYMNE-project (FKZ 02E11809A-B).

Nevertheless, at the end groundwater levels were met very well. At the other hand, river drainage is still slightly overestimated. This can be overcome only with the help of an automation.

5 Summary

The works described in this report were funded by the German Federal Ministry of Economics and Technology (BMWi) with the objective to improve and extend the tools for groundwater flow and transport modelling as an important element of long-term safety assessment for radioactive waste repositories.

The growing and varying demands on groundwater flow and transport modelling, such as growing extension and complexity of the models and the mapping of new physical processes in the equations, evoke constantly rising requirements for code enhancement and improvement.

With the objective to enable d^3f++ for the modelling of short-term field-scale experiments with pressure-influenced transient processes the flow equation was extended by a storage term. The new feature was successfully tested by comparing the results of a small 3d test case with the analytical solution. Further test cases will have to be provided in future projects.

3d model set-up and meshing of complex geometries for the purpose of scientific computing can be a challenging and time-consuming task. The quality of each individual grid element may be crucial for stability and efficiency of the numerical solvers especially in the case of unstructured grids and parallel multigrid solvers. To ease model set-up and to improve grid quality, functionality and visualisation of the interactive, graphical pre-processor ProMesh were extended and improved and new projectors for an intelligent grid refinement with better resolution of the model geometry were implemented.

The application of modern, parallelized numerical algorithms as well as the effective use of high-performance computers are essential for the simulation of density-driven groundwater flow and nuclide transport at regional scale. The growing extension and complexity of the models require a permanent development in speed-up and robustness of the solvers. For density-driven flow problems LIMEX -methods have been demonstrated as an attractive and efficient alternative to standard time-stepping strategy. In the scope of this works two versions of this methods were investigated, differing in the approximation of the Jacobian. Very promising results could be achieved for a modified Elder problem, the Saltpool problem and a vertical cross section through the Gorleben channel.

To improve the robustness of the linear multigrid solvers, different types of smoothers were implemented and tested, e. g. downwind numbering ILU and ILU_{β} . The coarse grid correction was improved by implementing a Galerkin projection and a special matrix dependent interpolation. Additionally, Filtering Algebraic Multi-Grid Methods (FAMG) were adapted to thermohaline flow and implemented in d^3f++ .

For non-linear problems like thermohaline groundwater flow and transport very fine grid resolutions are decisive to achieve a correct description of the non-linear behaviour. This implies the need for robust solvers in parallel. To obtain robust methods, an appropriate grid tailoring and adaptive anisotropic refinement methods are decisive. Ideas from computer graphics were adapted to get such an adaptive anisotropic refinement strategy. The generalization to thermohaline flow will be completed in the following project HYMNE (FKZ 02E11809A-B). Another field of work was the parallelization of downward numbering. These algorithms have been applied very successfully for serial computations also in d^3f++ . Using them in parallel, requires a special type of load balancing, the partitioning has to follow the streamlines. The algorithms for this were developed and implemented, and first tests provided good results. This issue is to be pursued in the HYMNE project.

d^3f++ was originally developed for the modelling of confined aquifers. Subsequently, levelset methods were adapted and implemented to enable the code for the modelling of a free groundwater surface. In the last years free surfaces are gaining more and more importance, particularly in groundwater modelling at a regional scale. Therefore some works were done for a substantially stabilization of the levelset method, and new algorithms using so called virtual elements and PLIC-reconstruction for a better description the free surface were applied. Mainly motivated by the Čihadlo test case, also the implementation of river drainage was improved and stabilized.

A short review of various concepts of diffusion and sorption of radioactive nuclides in crystalline rock is presented. As a result of this process a two-zone approach is used for modelling the transport of four different tracers in Task 9b of the SKB Task Force on Groundwater Flow and Transport of Solutes.

In the scope of this work d^3f++ was applied to three 3d groundwater flow models at regional scale, in porous media as well as in crystalline rock. The first of them is the Äspö Site Descriptive Model (SDM) over an area of about 250 km², situated in fractured granite, covered by a thin sedimental layer. A lot of effort had to be spent into data enquiry,

and a couple of 2d pre-studies were performed. Finally, a 3d model was successfully set-up.

The second application was the Waste Isolation Pilot Plant (WIPP) site, a repository for transuranic waste in bedded salt in New Mexico. The model covers an area of about 6,000 km² and is characterized by thin sedimental layers and high salt concentrations strongly influencing fluid density.

As the last application the Čihadlo candidate site in the Czech Republic was modeled, covering an area of about 260 km² in granite with a huge system of fault zones. Following the work of the PROGEO colleagues, an equivalent porous media (EPM) approach was chosen. The result was a well calibrated model, and groundwater heads as well as river discharge in 6 catchment zones are corresponding very well with the results of PROGEO.

In summary, the range of applications of d^{3f++} has been enlarged not only to pressure-influenced transient processes but also to density-driven flow models with free groundwater surface and river discharge at a regional scale. Efficiency, robustness and stability of the numerical solvers could be substantially improved and the code has become more user-friendly by advancing the preprocessor and the grid generator. Finally, the application of d^{3f++} to three regional-scale models from the field of radioactive waste disposal, in sedimentary as well as crystalline rock, contributes to the qualification of the code and to a growing confidence in groundwater modelling as part of long-term safety assessment.

Generally, the increasing capability of the code opens up doors to an increasing variety of applications on all scales of research for radioactive waste repositories. The scope begins at the centimeter to decimeter scale of laboratory tests, continues to the meter to tens of meter scale of in-situ experiments, up to the repository scale for predictions of the long-term performance, and further up to the scale of tens of kilometers for site selection purposes. This work thus contributes in various ways substantially to the ongoing development of tools for the assessment of long-term safety of geological repositories for radioactive waste for all three potential host rocks presently considered in Germany.

References

- /ALC 81/ Alcouffe, R. E., Brandt, A., Dendy, J. E, Painter, J. W.: The multigrid method for the diffusion equation with strongly discontinuous coefficients. *SIAM J. Sci. Stat. Comp.* 2, 430-454, 1981.
- /BAS 94/ Bastian, P.: Parallele adaptive Mehrgitterverfahren. Dissertation, Universität Heidelberg, 1994.
- /BAS 94a/ P. Bastian, G. Wittum, On robust and adaptive multi-grid methods, in: Hemker, P. W.; Wesseling, P. (Ed.), *Multigrid methods IV: Proceedings of the Fourth European Multigrid*, Vol. 116 of International series of numerical mathematics, Birkhäuser, Basel, 1994, pp. 1–17.
- /BEA 87/ Bear, J. and Verruijt, A.: *Modelling Groundwater Flow and Pollution*. D. Reidel Publishing Company, Dordrecht, 1987.
- /BEY 95/ Bey, J., Wittum, G.: Downwind numbering: robust multigrid for convection-diffusion problems. *ICA-Bericht N95/2*, ICA, Stuttgart 1995.
- /BEY 97/ Bey, J., Wittum, G.: Downwind numbering: robust multigrid for convection-diffusion problems. *Applied Numerical Mathematics*, 23 (1) S.177-192, doi 10.1016/S0168-9274(96)00067-0, Februar 1997.
- /CAR 59/ Carslaw, H.S. and Jaeger, J.C.: *Conduction of Heat in Solids*, Oxford 1959.
- /CAR 17a/ Carlsten, S., Strähle, A., Wahlgren, C.-H., Hultgren, P., Stenberg, L., Mattson, H.: Äspö site descriptive model, Geological single-hole interpretation of KAS02, SKB Report P-14-14, Svensk Kärnbränslehantering AB, Stockholm, 2017.
- /CAR 17b/ Carlsten, S., Strähle, A., Wahlgren, C.-H., Hultgren, P., Stenberg, L., Mattson, H.: Äspö site descriptive model, Geological single-hole interpretation of KAS04, KAS06 and KAS08, SKB Report P-14-15, Svensk Kärnbränslehantering AB, Stockholm, 2017.

- /CAR 17c/ Carlsten, S., Strähle, A., Wahlgren, C.-H., Hultgren, P., Stenberg, L., Mattson, H.: Äspö site descriptive model, Geological single-hole interpretation of KAS07, KA1755A and KC0045F, SKB Report P-14-16, Svensk Kärnbränslehantering AB, Stockholm, 2017.
- /COR 96/ Corbet, T., Krupp, P.: The role of regional groundwater flow in the hydrogeology of the Culebra member of the Rustler formation at the Waste Isolation Pilot Plant (WIPP), Southeastern New Mexico, SAND96-2133, Albuquerque, 1996.
- /COR 00/ Corbet, T.: A groundwater-basin approach to conceptualize and simulate post-Pleistocene subsurface flow in a semi-aride region, southeastern New Mexico and western Texas, USA; Hydrogeology Journal 8:310-327, 2000.
- /DAV 66/ Davies, S. N. and de Wiest, R. J. M.: Hydrogeology. John Wiley & Son, 1966.
- /DAV 89/ Davies, P., Variable-density ground-water flow and paleohydrogeology in the Waste Isolation Pilot Plant (WIPP) region, southeastern New Mexico, USGS Open File Report 88-490, USA, 1989.
- /DEU 87/ Deuffhard, P., Nowak, U., Extrapolation integrators for quasilinear implicit ODEs, in: P. Deuffhard, B. Engquist (Eds.), Large scale scientific computing, Birkhaeuser, pp. 37–50, 1987.
- /DEU 02/ Deuffhard, P., Bornemann, F., Scientific Computing with Ordinary Differential Equations, Springer, 2002.
- /DEU 12/ Deuffhard, P., M. Weiser, M., Adaptive Numerical Solution of PDEs, de Gruyter, 2012.
- /DIE 14/ Diersch, H.-J. G., FEFLOW – Finite element modeling of flow, mass and heat transport in porous and fractured media, Springer, 2014, Berlin Heidelberg, XXXV, 996p., ISBN 978-3-642-38738-8, ISBN 978-3-642-38739-5 (eBook), doi:10.1007/978-3-642-38739-5.

- /EMS 97/ Emsley, S., Olsson, O., Stenberg, L., Alheid, H.-J., Falls, S.: ZEDEX – A study of damage and disturbance from tunnel excavation by blasting and tunnel boring, SKB Technical Report TR-97-30, Svensk Kärnbränslehantering AB, Stockholm, 1997.
- /ENG 15/ Engstrom-Ost, J., Rasic, I.S., Brutemark, A., Rancken, R., Simić, G.S., Laugen, A.T.: Can *Cylindrospermopsis raciborskii* invade the Baltic Sea? *Environmental Reviews*. 23. 10.1139/er-2014-0062, 2015.
- /ERI 06/ Ericsson, L.O., Holmén, J., Rhén, I., Blomquist, N.: Storregional grundvattenmodellering – fördjupad analys av flödesförhållanden i östra Småland. SKB Report R-06-64, Svensk Kärnbränslehantering AB, Stockholm, 2006.
- /ERI 10/ Ericsson, L.O., Holmén, J.: Storregional grundvattenmodellering – en känslighetsstudie av några utvalda konceptuella beskrivningar och förenklingar. SKB report R-10-43, Svensk Kärnbränslehantering AB, Stockholm, 2010.
- /FEH 18/ Fehrs, K.: Gitterpartitionierung für konvektionsdominierte Probleme. G-CSC-Bericht , Goethe Center for Scientific Computing (G-CSC), Universität Frankfurt, 2018.
- /FEI 99/ Fein, E., Schneider, A. (ed.): *d^{3f}* – Ein Programmpaket zur Modellierung von Dichteströmungen, BMWi, Gesellschaft für Anlagen- und Reaktorsicherheit (GRS) gGmbH, GRS-292, Köln, ISBN 3-923875-97-5, 1999.
- /FOR 00a/ Forsmark, T., Rhén, I.: Äspö Hard Rock Laboratory, Prototype Repository, Hydrogeology – Injection test campaign 1, SKB Report IPR-00-20, Svensk Kärnbränslehantering AB, Stockholm, 2000.
- /FOR 00b/ Forsmark, T., Rhén, I.: Äspö Hard Rock Laboratory, Prototype Repository, Hydrogeology – Deposition- and lead-through boreholes: Inflow measurements, hydraulic responses and hydraulic tests, SKB Report IPR-00-33, Svensk Kärnbränslehantering AB, Stockholm, 2000.

- /FOR 01/ Forsmark, T., Rhén, I.: Äspö Hard Rock Laboratory, Prototype Repository, Hydrogeology – Injection test Campaign 2, flow measurement of DA3575G01, ground water salinity, ground water leakage into G-, I-, and J-tunnels, SKB Report IPR-01-31, Svensk Kärnbränslehantering AB, Stockholm, 2001.
- /FRA 15/ Fransson, Å., Åkesson, M., Andersson, L.: Bentonite Rock Interaction Experiment Characterization of rock and installation, hydration and dismantling of bentonite parcels. Report R-14-11 (draft), Swedish Nuclear Fuel and Waste Management Company (SKB), Stockholm, 2014.
- /FOL 07c/ Follin, S., Johansson, P.-O., Hartley, L., Jackson, P., Roberts, D., Maršić, N.: Hydrogeological conceptual model development and numerical modelling using CONNECTFLOW, Forsmark modelling stage 2.2. SKB Report R-07-48, Svensk Kärnbränslehantering AB, Stockholm, 2007.
- /FRO 12/ Frolkovič, P.: Application of level set method for groundwater flow with moving boundary, *Adv. Wat. Res.* 2012.
- /GIN 01/ Ginzburg, I., Wittum, G: Two-phase flows on unstructured grids with spline volume tracking. *Journal of Computational Physics*, 166 (2): S.302-335, 2001.
- /GUS 88/ K. Gustafsson, M. Lundh, G. Söderlind, Api stepsize control for the numerical solution of ordinary differential equations, *BIT Numerical Mathematics* 28 (2) (1988) 270–287.
- /GUS 91/ Gustafson, G., Liedholm, M., Rhén, I., Stanfors, R., Wikberg, P.: Äspö Hard Rock laboratory, Predictions prior to excavation and the process of their validation, SKB Report TR-91-23, Svensk Kärnbränslehantering AB, Stockholm, 1991
- /HAC 89/ Hackbusch, W.: On first and second order box schemes. *Computing*, 41: S.277-296, doi.org/10.1007/BF02241218, 1989.
- /HAC 96/ Hackbusch, W., Probst, Th.: On first and second order box schemes. *Computing*, Preprint: Kiel, 1996.

- /HAI 02/ E. Hairer, G. Wanner, Solving Ordinary Differential Equations II, Springer Heidelberg Dordrecht London New York, 2002.
- /HAR 06a/ Hartley, L., Hunter, F., Jackson, P., McCarthy, R., Gylling, B., Marsic, N.: Regional hydrogeological simulations using CONNECTFLOW. Preliminary site description Laxemar subarea – version 1.2, SKB Report R-06-23, Svensk Kärnbränslehantering AB, Stockholm, 2006.
- /HAR 07/ Hartley, L., Jackson, P., Joyce, S., Roberts, D., Shevelan, J., Swift, B., Gylling, B., Marsic, N., Hermanson, J., Öhman, J.: Hydrogeological pre-modelling exercises, Site descriptive modelling SDM-Site Laxemar. SKB Report R-07-57, Svensk Kärnbränslehantering AB, Stockholm, 2007.
- /HEI 95/ Heisig, M., Lieckfeldt, R., Wittum, G., Mazurkevich, G., Lee, G.: Non steady-state descriptions of drug permeation through stratum corneum. I: the biphasic, brick-and-mortar model. ICA-Bericht N95/3, ICA: Stuttgart, 1995.
- /HEI 96/ Heisig, M., Lieckfeldt, R., Wittum, G., Mazurkevich, G., Lee, G.: Non steady-state descriptions of drug permeation through stratum corneum. I: the biphasic, brick-and-mortar model. Pharmaceutical Research 13(3): S.421-426, 1996.
- /HOE 16/ Höllbacher, S.: Voll gekoppelte Modellierung zur direkten numerischen Simulation partikulärer Fluide. Dissertation, Informatik, Universität Frankfurt, 2016.
- /HOE 19a/ Höllbacher, S., Wittum, G.: Rotational test spaces for a fully-implicit FVM and FEM for the DNS of particulate flow. Journal of Computational Physics, 393, S.186-213, doi.org/10.1016/j.jcp.2019.05.004, Sept. 2019.
- /HOE 19b/ Höllbacher, S., Wittum, G.: Gradient-consistent enrichment of finite element spaces for the DNS of fluid-particle interaction. Journal of Computational Physics, 401, 109003.doi:10.1016/j.jcp, 2019.

- /HOE 20/ Höllbacher, S., Wittum, G.: A sharp interface method using enriched finite elements for elliptic interface problems . Submitted for publication, 2020.
- /HOL 08/ Holmén, I. G. (ed.): Premodelling of the importance of the location of the upstream hydraulic boundary of a regional flow model of the Laxemar-Simpevarp area - Site descriptive modelling - SDM-Site Laxemar, SKB Report R-08-60, Svensk Kärnbränslehantering AB, Stockholm, 2008.
- /HUG 17/ Hughes, J.D., Langevin, C.D., and Banta, E.R., 2017, Documentation for the MODFLOW 6 framework: U.S. Geological Survey Techniques and Methods, book 6, chap. A57, 40 p., <https://doi.org/10.3133/tm6A57>.
- /JAN 19/ Jankovský, F., Zuna, M., Havlová, V., Fisher, C., Kulenkampff, J., Kottowski, J., Polak, M., Hokr M., Cernik, M.: Contaminant migration in fractured rocks: insights from tracer tests in core scale Geophysical Research Abstracts, Vol. 21, EGU2019-10839, 2019.
- /JOB 16/ Jobmann, M. (ed.): Site-specific evaluation of safety issues for high-level waste disposal in crystalline rocks. Final Report. TEC-28-2015-AB, 2016.
- /JOH 02/ K. Johannsen, W. Kinzelbach, S. Oswald, G. Wittum, The saltpool benchmark problem – numerical simulation of saltwater upconing in a porous medium, *Advances in Water Resources* 25 (2002) 335–348.
- /JOH 03/ K. Johannsen, On the validity of the Boussinesq approximation for the Elder problem, *Computational Geosciences* 7 (2003) 169–182.
- /JOH 04/ Numerische Aspekte dichtegetriebener Strömung in porösen Medien. Habilitationsschrift, Heidelberg, 2004.
- /KÄR 02/ Kärnbränslehantering, S.: Simpevarp – site descriptive model version 0, SKB Report R-02-35, Svensk Kärnbränslehantering AB, Stockholm, 2002.

- /KEE 05/ S. Keesmann, U. Noseck, D. Buhmann, E. Fein, A. Schneider, Modellrechnungen zur Langzeitsicherheit von Endlagern in Salz- und Granitformationen, Tech. rep., Gesellschaft für Anlagen- und Reaktorsicherheit (2005).
- /KRÖ 91/ Kröhn, K.-P.: Simulation von Transportvorgängen im klüftigen Gestein mit der Methode der Finiten Elemente. Bericht 29/1991, Institut für Strömungsmechanik und Elektronisches Rechnen im Bauwesen, Universität Hannover, 1991.
- /KRO 10/ Kröhn, K.-P.: State Variables for Modelling Thermohaline Flow in Rocks. Summary report, FKZ 02 E 10477 (BMW), Gesellschaft für Anlagen- und Reaktorsicherheit (GRS) gGmbH, GRS-268, Köln, ISBN 978-3-939355-44-1, 2010.
- /KRÖ 17/ Kröhn, K.-P.: Hydraulic Interaction of Engineered and Natural Barriers – Task 8b-8d,8f of SKB. Summary report, FKZ 02 E 11213 and 02 E 11102 (BMW), Gesellschaft für Anlagen- und Reaktorsicherheit (GRS) gGmbH, GRS-430, Köln, 2017.
- /KRÖ 18a/ Kröhn, K.-P.: Hydraulic Interaction of Engineered and Natural Barriers – Task 8e of SKB. Summary report, FKZ 02 E 11213 (BMW), Gesellschaft für Anlagen- und Reaktorsicherheit (GRS) mbH, GRS-431, Köln, 2018.
- /KRÖ 18b/ Kröhn, K.-P. and Lanyon, B.: Observations of Hydraulic and Transport „Skin Effects“ SKB Task Force Workshop Prague 2016. FKZ 02 E 11476A (BMW), Gesellschaft für Anlagen- und Reaktorsicherheit (GRS) mbH, GRS-504, Köln, 2018.
- /KUL 02/ Kull, H. (ed.), Helmig, R., Jacobs, H., Jockwer, N., Kröhn, K.-P., Zimmer, U.: Two-Phase-Flow Experiment in the Fractured Crystalline Rock of the Äspö Hard Rock laboratory. Final report FKZ 02 E 9027 8 (BMFT), Report GRS-183, GRS Braunschweig, 2002.
- /LAN 01/ J. Lang, Adaptive Multilevel Solution of Nonlinear Parabolic PDE Systems - Theory, Algorithm, and Applications, Springer, 2001.

- /LI 74/ Li, Y.-H., Gregory, S.: Diffusion of ions in sea water and in deep-sea sediments. *Geochimica et Cosmochimica Acta*, 1974, Vol. 38, pp. 703-714, Pergamon Press, 1974.
- /LIC 14/ Lichtner, P. C., Hammond, G. E., Lu, C., Karra, S., Bisht, G., Andre, B., Mills, R. T., and Kumar, J.: PFLOTRAN user manual: A massively parallel reactive flow and transport model for describing surface and subsurface processes. <http://www.pflotran.org/> 2014.
- /LIE 91a/ Liedholm, M. (Ed.): Äspö Hard Rock Laboratory, Conceptual modeling of Äspö, Technical Notes 1 – 17, General geological, Hydrogeological and Hydrochemical information, SKB Progress Report 25-90-16a, Svensk Kärnbränslehantering AB, Stockholm, 1991
- /LIE 91b/ Liedholm, M. (Ed.): Äspö Hard Rock Laboratory, Conceptual modeling of Äspö, Technical Notes 18 – 32, General geological, Hydrogeological and Hydrochemical information, SKB Progress Report 25-90-16a, Svensk Kärnbränslehantering AB, Stockholm, 1991
- /LUB 95/ C. Lubich, A. Ostermann, Linearly implicit time discretization of nonlinear parabolic equations, *IMA J. Numer. Anal.* 15 (1995) 555–583.
- /MOM 18/ Momigliano, P., G.P.J., Jokinen, H., Merilä, J.: *Platichthys solemdali* sp. nov. (Actinopterygii, Pleuronectiformes): A New Flounder Species From the Baltic Sea. *Frontiers in Marine Science*, Vol. 5, 2018, <https://doi.org/10.3389/fmars.2018.00225>.
- /MOR 17/ Mansueto, M.: personal communication, 2017.
- /NAE 07/ Nägel, A., Falgout, R. D., Wittum, G.: Filtering algebraic multigrid and adaptive strategies, *Comput Vis Sci*, Volume 11, Number 3, May 2008.
- /NAE 15/ A. Nägel, A. Vogel, G. Wittum, Evaluating linear and nonlinear solvers for density driven flow, *Computer Methods in Applied Mechanics and Engineering* 292 (2015) 3–15.

- /NAE 19/ A. Nägel, D. Logashenko, J. B. Schroder, U. M. Yang, Aspects of Solvers for Large Scale Coupled Problems in Porous Media, *Transport in Porous Media*, vol. 130, No. 1, pp. 363-390, DOI: 10.1007/s11242-019-01323-w, 2019.
- /NIG 70/ Nigrini, A.: Diffusion in rock alteration system. I. Prediction of limiting equivalent ionic conductances at elevated temperatures. *Amer. J. Sci.* 269, 65-91, 1970. (cited in /Li 74/)
- /NIL 89/ Nilsson, L.: Hydraulic Tests at Äspö and Laxemar. Evaluation, SKB Report PR-25-88-14, Svensk Kärnbränslehantering AB, Stockholm, 1989
- /NIL 10/ Kersti Nilsson, Johan Byegård, Eva Selnert, Henrik Widestrand, Sanne Höglund, Erik Gustafsson: Long Term Sorption Diffusion Experiment (LTDE-SD) - Results from rock sample analyses and modelling. SKB-report R-10-68, Svensk Kärnbränslehantering AB, Stockholm, 2010.
- /NOS 12/ Noseck, U., Brendler, V., Flügge, J., Stockmann, M., Britz, S., Lampe, M., Schikora, J., Schneider, A.: Realistic integration of sorption processes in transport codes for long-term safety assessments, Final Report GRS-297, BMWi-FKZ 02E10548. Gesellschaft für Anlagen- und Reaktorsicherheit (mbH), Braunschweig, (2012).
- /NUE 16/ G. Nützmann, H. Moser, *Elemente Einer Analytischen Hydrologie*. Springer, Berlin (2016).
- /NYB 05/ Nyberg, G. Jonsson, S. Wass, E.: Äspö Hard Rock Laboratory – Hydro monitoring program, Report 2004, IPR-05-26, 2005.
- /NYM 08/ Nyman, H., Sohlenius, G., Strömngren, M., Brydsten, L.: Depth and stratigraphy of regolith, Site descriptive modelling SDM-Site Laxemar. SKB Report R-08-06, Svensk Kärnbränslehantering AB, Stockholm, 2008.
- /OSW 04/ S. E. Oswald, W. Kinzelbach, Three-dimensional physical benchmark experiments to test variable-density flow models, *Journal of Hydrology* 290 (2004) 290 (2004) 22–42.

- /PÁS 96/ Pässe, T.: A mathematical model of the shore level displacement in Fennoscandia. SKB Report TR-96-24, Svensk Kärnbränslehantering AB, Stockholm, 1996.
- /PET 17/ Petersson, J., Wahlgren, C.-H., Curtis, P., Hultgren, P., Mattsson, H., Carlsten, S.: Äspö site descriptive model, Simplified geological single-hole interpretation of drill cores from the period 1988-2002, SKB Report P-14-12, Svensk Kärnbränslehantering AB, Stockholm, 2017.
- /PRO 20/ PROGEO, personal communication
- /REI 14/ Reiter, S., Vogel, A., Heppner, I., Rupp, M., Wittum, G.: A Massively Parallel Geometric Multigrid Solver on Hierarchically Distributed Grids. *Computing and Visualization in Science*, 16 (4), pp 151-164, December 2014/ROB 59/Robinson, R.A., Stokes, R.H.: *Electrolyte Solution*, 2nd Ed., 571 pp., Butterworths, 1959. (cited in /Li 74/)
- /REI 16/ Reiter, S., Logashenko, D., Vogel, A., Wittum, G.: Mesh generation for thin layered domains and its application to parallel multigrid simulation of groundwater flow", *Computing and Visualization in Science*, accepted 2016.
- /RHÉ 97/ Rhén, I. (ed.), Gustafson, G., Stanfors, R., Wikberg, P.: Äspö HRL - Geoscientific evaluation 1997/5. Models based on site characterization 1986-1995. SKB Report TR-97-06, Svensk Kärnbränslehantering AB, Stockholm, 1997.
- /RHÉ 97a/ Rhén, I., Bäckbom, G. (ed.), Gustafson, G., Stanfors, R., Wikberg, P.: Äspö HRL – Geoscientific evaluation 1997/2, Results from pre-investigations and detailed site characterization, Summary report, SKB Technical Report TC-97-03, Svensk Kärnbränslehantering AB, Stockholm, 1997
- /RHÉ 97b/ Rhén, I., Gustafson, G., Wikberg, P.: ÄSPÖ HRL – Geoscientific evaluation 1997/4, Results from pre-investigations and detailed site characterization, Comparison of predictions and observations, Hydrogeology, groundwater chemistry and transport of solutes, SKB Report TR-97-05, Svensk Kärnbränslehantering AB, Stockholm, 1997

- /RHÉ 97c/ Rhén, I., Gustafson, G., Wikberg, P.: ÄSPÖ HRL – Geoscientific evaluation 1997/4, SKB Report TR-97-06, Svensk Kärnbränslehantering AB, Stockholm, 1997
- /RHÉ 06/ Rhén, I., Forsmark, T., Forssman, I., Zetterlund, M.: Evaluation of hydrogeological properties for Hydraulic Conductor Domains (HCD) and Hydraulic Rock Domains (HRD), Laxemar subarea – version 1.2, SKB Report R-06-22, Svensk Kärnbränslehantering AB, Stockholm, 2006.
- /RHÉ 08/ Rhén, I., Forsmark, T., Hartley, L., Jackson, P., Roberts., D., Swan, D., Gylling, B.: Hydrogeological conceptualization and parameterization, Site descriptive modelling SDM-Site Laxemar, SKB Report R-08-78, Svensk Kärnbränslehantering AB, Stockholm, 2008.
- /RHÉ 09/ Rhén, I., Forsmark, T., Hartley, L., Joyce, S., Roberts, D., Gylling, B., Marsic, N.: Bedrock hydrogeology: Model testing and synthesis – Site descriptive modelling, SDM-Site Laxemar, SKB Report R-08-91, Svensk Kärnbränslehantering AB, Stockholm, 2009.
- /RHÉ 09b/ Rhén, I., Hartley, L.: Bedrock hydrogeology Laxemar, Site descriptive modelling SDM-Site Laxemar. SKB report R-08-92, Svensk Kärnbränslehantering AB, Stockholm, 2009.
- /RUP 20/ Rupp, M.: Ein filterndes algebraisches Mehrgitterverfahren mit Anwendungen in der Strukturmechanik. Unpublished manuscript, G-CSC, Universität Frankfurt, 2020.
- /SCH 99/ C. Schwarz, Dichteabhängige Strömungen in homogenen und heterogenen porösen Medien, Ph.D. thesis, Eidgenössische Technische Hochschule Zürich (1999).
- /SCH 12/ Schneider, A. (ed.): Enhancement of d^{3f} und r^{3t} (E-DuR). FKZ 02 E 10336 (BMWi), final report, Gesellschaft für Anlagen- und Reaktorsicherheit (GRS) gGmbH, GRS-292, Braunschweig, 2012.
- /SCH 13/ Schneider, A. (ed.), Representation of inhomogeneities in the flow and transport codes d^{3f} and r^{3t}, GRS 311, Braunschweig, 2013.

- /SCH 13a/ Schäfer, T., Noseck, U., Huber, F. (eds.): Colloid/nanoparticle formation and mobility in the context of deep geological nuclear waste disposal (Project KOLLORADO-2; Final Report), KIT Scientific Report 7645, 2013.
- /SCH 16/ Schneider, A. (ed.): Modeling of Data Uncertainties on Hybrid Computers (H-DuR). FKZ 02 E 11062A (BMWi), final report, Gesellschaft für Anlagen- und Reaktorsicherheit (GRS) gGmbH, GRS-392, Braunschweig, 2016.
- /SCH 17/ Schneider, A., Gehrke, A., Kröhn, K.-P., Zhao, H.: Qualification of the Code d^{3f++}. FKZ 02E11213 (BMWi), final report, Gesellschaft für Anlagen- und Reaktorsicherheit (GRS) gGmbH, GRS-448, Braunschweig, 2017.
- /SIN 17/ Sindalooovskiy, L.N.: Aquifer Test Solutions. Springer, 2017.
- /SOH 08/ Sohlenius, G. and Hedenström, A.: Description of regolith at Laxemar-Simpevarp, Site descriptive modelling SDM-Site Laxemar. SKB Report R-08-05, Svensk Kärnbränslehantering AB, Stockholm, 2008.
- /STE 11/ Stepniewski, M.: Approximation glatter Ränder und Volumengittergenerierung zur alternativen Erzeugung von 3D-Gitterhierarchien für Mehrgitterverfahren. University Heidelberg. Diploma thesis, Mathematik, 2011.
- /STE 14/ Stepniewski, M.: Volumengittergenerierung in der Computational Neuroscience. Spezialthema zur Vorlesung Modellierung und Simulation 3, G-CSC, Universität Frankfurt, 2014.
- /STE 20/ Stepniewski, M., and Queisser, G. A subdivision based geometric multigrid method. Submitted to Computing and Visualization in Science (2020).
- /SVE 08/ Svensson, U., Vidstrand, P., Neretnieks, I., Wallin, B.: Towards a new generation of flow and transport models for the Äspö Hard Rock Laboratory, Main results from the project Äspömodels 2005, SKB Report R-08-74, Svensk Kärnbränslehantering AB, Stockholm, 2008.

- /SVE 12/ Svensson, U.: Task 8 Modelling a one m³ block of granite. Presentation at the 28th Meeting of the Task Force on Groundwater and Transport of Solutes, Berlin, 2012./SIM 58/Simpson, J.H., Carr, H.Y.: Diffusion and nuclear spin relaxation in water. Phys. Rev. 2nd Series, 1201-1202, 1958. (cited in /Li 74/)
- /TAR 72/ Tarjan, R.: Depth-first search and linear graph algorithms. SIAM Journal on Computing, 1(2), S.146-160, DOI: 10.1137/0201010, Juni 1972.
- /VOG 14/ Vogel, A., Reiter, S., Rupp, M., Nägel, A., Wittum, G.: UG 4 - A Novel Flexible Software System for Simulating PDE Based Models on High Performance Computers. Computing and Visualization in Science, 16 (4), pp 165-179, 2014.
- /VOS 87/ C. I. Voss, W. R. Souza, Variable Density Flow and Solute Transport Simulation of Regional Aquifers Containing a Narrow Freshwater-Saltwater Transition Zone, Water Resources Research 23 (10) (1987) 1851–1866.
- /VID 03/ Vidstrand, P.: Äspö Hard Rock Laboratory, Update of the hydrogeological model 2002. Report IPR-03-35, Svensk Kärnbränslehantering AB (SKB), Stockholm, 2003.
- /VIL 07a/ Vilks, P.: Forsmark site investigation – Rock matrix permeability measurements on core samples from borehole KFM01D. Report P-07-162, Svensk Kärnbränslehantering AB (SKB), Stockholm, 2007.
- /VIL 07b/ Vilks, P.: Oskarshamn site investigation, Rock matrix permeability measurements on core samples from borehole KLX03, SKB Report P-07-204, Svensk Kärnbränslehantering AB (SKB), Stockholm, 2007.
- /WAG 00/ Wagner, C.: Ein algebraisches Mehrgitterverfahren – Entwicklung und Anwendung auf einen Sanierungsfall. Habilitationsschrift, Mathematische Fakultät, Universität Heidelberg, 2000.
- /WAG 97/ Wagner, C.; Wittum, G.: Adaptive Filtering. Numerische Mathematik, 78(2), 305-328, 1997.

- /WAH 08/ Wahlgren, C.-H., Curtis, P., Hermanson, J., Forssberg, O., Öhman, J., Fox, A., La Pointe, P., Drake, H., Triumpf, C.-A., Mattsson, H., Thunehed, H., Juhlin, C.: Geology Laxemar, Site descriptive modelling SDM-Site Laxemar. SKB Report R-08-54, Svensk Kärnbränslehantering AB, Stockholm, 2008.
- /WAH 10/ Wahlgren, C.-H.: Oskarshamn site investigation, Bedrock geology - overview and excursion guide, SKB Report R-10-05, Svensk Kärnbränslehantering AB (SKB), Stockholm, 2010.
- /WER 05/ Werner, K., Bosson, E., Berglund, S.: Description of climate, surface hydrology, and near-surface hydrogeology, Simpevarp 1.2. SKB Report R-05-04 Svensk Kärnbränslehantering AB (SKB), Stockholm, 2005.
- /WER 08/ Werner, K., Öhman, J., Holgersson, B., Rönback, K., Marelius, F.: Meteorological, hydrological and hydrogeological monitoring data and near-surface hydrogeological properties data from Laxemar- Simpevarp, Site descriptive modelling SDM-Site Laxemar. SKB Report R-08-73, Svensk Kärnbränslehantering AB, Stockholm, 2008.
- /WID 10a/ Widestrand., H., Byegård., J., Selnert., E., Skålberg., M., Höglund., S., Gustafsson., E.: Äspö Hard Rock Laboratory. Long Term Sorption Diffusion Experiment (LTDE-SD). Supporting laboratory program – Sorption diffusion experiments and rock material characterisation. With supplement of adsorption studies on intact rock samples from the Forsmark and Laxemar site investigations. SKB R-10-66, Svensk Kärnbränslehantering AB, Stockholm, 2010.
- /WID 10b/ Widestrand., H., Byegård., J., Kronberg., M., Nilsson., K., Höglund., S., Gustafsson., E.: Äspö Hard Rock Laboratory. Long Term Sorption Diffusion Experiment (LTDE-SD). Performance of main in-situ experiment and results from water phase measurements. SKB R-10-67, Svensk Kärnbränslehantering AB, Stockholm, 2010.

- /WIK 91/ Wikberg, P., Gustafson, G., Rhén, I., Stanfors, R.: Äspö Hard Rock Laboratory. Evaluation and conceptual modelling based on the pre-investigations 1986-1990, SKB Report TR-91-22, Svensk Kärnbränslehantering AB, Stockholm, 1991
- /WIK 18/ Wikipedia: https://de.wikipedia.org/wiki/Datei:Baltic_sea_bottom_salinity_and_distribution_of_Platicthys_populations_-_fmars-05-00225-g001.jpg. 2018. (from /MOM 18/)
- /WIT 89/ Wittum, G.: On the robustness of ILU-smoothing. SIAM Journal on Scientific and Statistical Computing, 10(4), S.699-717, doi.org/10.1137/0910043, 1989.
- /W3S 19/ <http://w3sdesign.com/?gr=b07&ugr=proble>

Table of figures

Fig. 2.1	Comparison of results from d^{3f++} and a referring analytical solution.....	12
Fig. 2.2	Edge operations	20
Fig. 2.3	Face-Split executed on the left triangle The resulting triangulation (right) features one new vertex, three new edges and two new triangles.....	20
Fig. 2.4	Several visibility configurations for a tetrahedrization of the Stanford Bunny in a box Left: Clip-plane; Middle: Clip-plane and hidden subset; Right: Hidden elements	22
Fig. 3.1	Diffusion from salt dome (2D) with SuperLU preconditioner:.....	34
Fig. 3.2	Diffusion from salt dome (2D) with multigrid preconditioner:	35
Fig. 3.3	Modified Elder (3D) with SuperLU:.....	39
Fig. 3.4	Modified Elder (3D) with multi-grid:	40
Fig. 3.5	Saltpool problem (3D): Simulated results for (a) the solution at the end of experiment; (b) breakthrough curve at outlet (for all simulations).	41
Fig. 3.6	Saltpool problem (3D) with multi-grid:	42
Fig. 3.7	Gorleben problem (2D):.....	44
Fig. 3.8	Gorleben problem (2D) – initial phase:.....	45
Fig. 3.9	Gorleben problem (2D):.....	48
Fig. 3.10	Gorleben problem:.....	49
Fig. 3.11	Gorleben problem (2D): Time step size [yrs] vs. time [yrs] for LIMEX 2reduced (omitting derivatives w. r. t. convection and diffusion).....	50
Fig. 3.12	Repeated refinements of an initial set of control vertices x_0 (far left) yields a sample subdivision surface $x_\infty := \lim_{j \rightarrow \infty} x_{j+1} = \lim_{j \rightarrow \infty} S_j$ of a reconstructed 3D nucleus geometry (far right), /STE 20/	54
Fig. 3.13	Reconstruction of a neuron nucleus using subdivision surfaces using the subdivision surface method /STE 14/.....	55
Fig. 3.14	Box portion of an elements corner.....	57
Fig. 3.15	Segment vector and center of mass.....	58

Fig. 3.16	Dependence of the number of iteration steps on the number of partitions due to wrong partitioning. The parallelisation then has no gain /FEH 18/.....	62
Fig. 3.17	Number of iteration steps for different partitioners of the 2d channel, /FEH 18/	63
Fig. 3.18	Partitions used for the results from Fig. 3.17 /FEH 18/.....	63
Fig. 3.19	Scheme of the domain of a partially saturated aquifer: Ω_1 is the unsaturated and Ω_2 the saturated parts separated by the phreatic surface Γ (blue line); the dotted lines are the boundaries of the geological layers.....	64
Fig. 3.20	Schematic numerical treatment of the free surface.....	66
Fig. 3.21	Simulated position of the phreatic surface in the Cihadlo problem at $t \approx 1.5$ years; color: z-coordinate; white lines: channels; green points: measurements. The plot is scaled by 10 in z-direction.....	67
Fig. 3.22	Simulated position of the phreatic surface and the salt mass fraction field in the WIPP problem at $t \approx 453.3$ years; the upper isosurface presents the phreatic surface (color: z-coordinate); the lower ones correspond to $\omega = 0.01, 0.25, 0.5, 0.75, 0.99$. The plot is scaled by 100 in z-direction.....	68
Fig. 3.23	Construction of the flat top basis functions.....	69
Fig. 3.24	Approximation of the free surface by the flat-top basis functions for a test problem.....	69
Fig. 3.25	PLIC reconstruction (grey) and subsequent spline reconstruction (smooth line).....	70
Fig. 4.1	Location of the LTDE-Experiment; from /WID 10a/	71
Fig. 4.2	Borehole instrumentation and test section design; from /WID 10b/	72
Fig. 4.3	Test sections, close-up from Fig. 4.2; modified from /WID 10b/	72
Fig. 4.4	Drill pattern of the overcored inflow reservoir	73
Fig. 4.5	Slicing pattern of the drill cores	74
Fig. 4.6	$^{226}\text{Ra}^{2+}$ tracer profile found to be characteristic for the LTDE	75
Fig. 4.7	Examples for the transition function for a normalised depth	80
Fig. 4.8	$^{226}\text{Ra}^{2+}$ tracer profile, detection limits and subsample partitioning	82

Fig. 4.9	Best model fit of a homogeneous model to the ^{36}Cl -data from the D-cores.....	83
Fig. 4.10	Fit of the two-zone model to ^{36}Cl -data from the A-cores; initial fit	84
Fig. 4.11	Fit of the two-zone model to ^{36}Cl -data from the A-cores	85
Fig. 4.12	Fit of the two-zone model to $^{22}\text{Na}^+$ -data from the A-cores	86
Fig. 4.13	Fit of the two-zone model to $^{137}\text{Cs}^+$ -data from the A-cores	86
Fig. 4.14	Fit of the two-zone model to $^{133}\text{Ba}^{2+}$ -data from the A-cores	87
Fig. 4.15	Fit of the two-zone model to ^{36}Cl -data from the D-cores.....	88
Fig. 4.16	Fit of the two-zone model to $^{22}\text{Na}^+$ -data from the D-cores	88
Fig. 4.17	Fit of the two-zone model to $^{137}\text{Cs}^+$ -data from the D-cores	89
Fig. 4.18	Fit of the two-zone model to $^{133}\text{Ba}^{2+}$ -data from the D-cores.....	89
Fig. 4.19	Model areas for SM (top left), RM1 (top right), RM2 (lower left) and ÅM (lower right); from /ERI 06/, /HOL 08/, /RHÉ 09a/, and /SVE 08/.....	95
Fig. 4.20	Overlay of catchment areas in the coastal region; from /WER 05/ and /MOR 17/	96
Fig. 4.21	Map of ground-surface topography in the area of RM2; from /RHÉ 09a/	97
Fig. 4.22	Conceptual understanding of the underground at a typical valley at Laxemar; from /RHÉ 09b/	98
Fig. 4.23	North-west and west-east cross-section through the valley in Fig. 4.22, the graphics are exaggerated by a factor of 20 in the vertical direction; from /RHÉ 09b/.....	98
Fig. 4.24	Map of lithological units from /WAH 10/	100
Fig. 4.25	3D-view of lithological units in the SM; from /ERI 10/	101
Fig. 4.26	Lithological units in the model for RM2; from /WAH 08/	101
Fig. 4.27	Depth-dependent hydraulic conductivities for all three locations	103
Fig. 4.28	Depth-dependent hydraulic conductivities separately for the three locations	104
Fig. 4.29	Tentative function for the depth-dependent conductivities at Äspö.....	105
Fig. 4.30	Tentative function for the depth-dependent conductivities at Laxemar ...	105

Fig. 4.31	Tentative function for the depth-dependent conductivities at Simpevarp	106
Fig. 4.32	Depth-dependent conductivities at Laxemar and Simpevarp	106
Fig. 4.33	Hydraulic conductivities and related test sections at Laxemar.....	107
Fig. 4.34	Location of fault zones in the SM; from /ERI 10/	109
Fig. 4.35	Supra-regional fault zones in the RM1 and local zone of interest; from /HOL 08/	110
Fig. 4.36	Local fault zones in the RM1; from /HOL 08/.....	110
Fig. 4.37	Perspective view of some major fault zones; from /RHÉ 09a/	111
Fig. 4.38	Principal sketch of the boundary condition in SM and RM1;.....	113
Fig. 4.39	Groundwater surface interpolated from measurements /WER 05/	114
Fig. 4.40	Hydraulic heads used for calibration of the RM2; from /RHÉ 09a/.....	115
Fig. 4.41	Location of rivers and lakes for the SM; from /ERI 06/	115
Fig. 4.42	Map of rivers and lakes; from /MOR 17/.....	116
Fig. 4.43	Salinity at the surface (depth < 5 m) of the Baltic Sea; from /ENG 15/ ..	117
Fig. 4.44	Salinity in the deep waters in the Baltic Sea; from /MOM 18/	118
Fig. 4.45	Salinity in the Äspö area; from /RHÉ 97/.....	118
Fig. 4.46	Chloride profile along borehole KLX02 at Laxemar; from /RHÉ 97/.....	119
Fig. 4.47	2D cross sections B, C, D (dotted lines, cf. Fig. 4.48) in relation to the 3D model domain using a digital elevation model (DEM)	120
Fig. 4.48	A – D present the development of the 2D RMs to reach as close to nature conditions as possible but still being simplified enough to a manageable degree of complexity resulting in feasible computing times.....	121
Fig. 4.49	Precipitation at Oskarshamn: Monthly values 2004 and monthly means 1961 – 1990 /NYB 05/.....	124
Fig. 4.50	Comparison of RM I, II, and VII to show the impact of topography (RM II) and a free groundwater surface in a 25 m regolith layer (RM VII).....	129
Fig. 4.51	Flow velocities of RM II with focus on $y > - 430$ m BMSL (a) and $y < 1620$ m BMSL (b).....	130

Fig. 4.52	Influence of permeabilities on the flow field (generic study)	131
Fig. 4.53	Flow field simulation including equidimensional generic DZs.	131
Fig. 4.54	Density-driven flow field simulation after 5'000 a simulation time.	132
Fig. 4.55	Density-driven flow field simulation after 20'000 a simulation time.	133
Fig. 4.56	Detailed view of the flow field in the regolith layer for two different cross sections (RM VII and RM IX, XI) and comparison of flow field simulations with a free groundwater table	136
Fig. 4.57	Simulation results of RM XII, $t = 12$ d: A) 50 times exaggerated, B) overview of model domain..	137
Fig. 4.58	Domain of the regional-scale model.....	138
Fig. 4.59	Original DEM (above) and topography used in the regional model (below).....	139
Fig. 4.60	Hydrogeological units of the regional-scale model	140
Fig. 4.61	Depth-dependent permeability for the hydrogeological structures used in the regional model.....	141
Fig. 4.62	Boundary conditions of the regional-scale model.....	142
Fig. 4.63	Flow velocity at the model surface (above) and below the regolith (below).....	143
Fig. 4.64	Slope of the model surface in degrees.....	145
Fig. 4.65	Area of the WIPP-Site basin model after /COR 00/	146
Fig. 4.66	WIPP-Site, schematic cross section (source: US DOE)	147
Fig. 4.67	Hydrostratigraphic units of the WIPP-Site basin-scale model /COR 96/	149
Fig. 4.68	Construction of the 3d d ^{3f++} model from 11 raster surfaces.....	150
Fig. 4.69	WIPP-Site: 6 layers model, 50x exaggerated in vertical direction.....	151
Fig. 4.70	WIPP-Site model: Distribution of hydraulic conductivities on example of the Culebra Dolomite (left) and the Dewey Lake/Triassic (right) after /COR 00/	152
Fig. 4.71	WIPP-Site model with coarse grid and boundary conditions, 50 times exaggerated in vertical direction	154

Fig. 4.72	Distribution of permeabilities (left) and velocity vectors (right) in a vertical W-E-cutting plane at the repository position.....	155
Fig. 4.73	Simulated velocity field in the culebra dolomite (left) and the magenta dolomite (right) after 5,000 years	155
Fig. 4.74	Simulated relative salt concentration after 5,000 years; left: isosurfaces in successive intervals of 0.1: c=0 (dark blue), c=0.1 (light blue), ..., c=1 (red) right: W-E-cutting plane, c on log scale.....	156
Fig. 4.75	Simulated situation of the groundwater surface at the initial state, after 2,000 years and after 5,000 years	157
Fig. 4.76	Model areas (full line: FEFFLOW/MODFLOW, dotted line: Flow123); source: PROGEO	160
Fig. 4.77	Situation of faults in the model area; left: regional fault zones; right: regional (coloured), major (black) and minor faults (gray)	161
Fig. 4.78	Regional model Čihadlo; left: MODFLOW model, right: d ^{3f++} model with river network.....	162
Fig. 4.79	Čihadlo model, permeability distribution.....	162
Fig. 4.80	Comparison of the simulated groundwater level with the measurements in m a. s. l.; left: MODFLOW, right:d ^{3f++} , point colors corresponding river catchment zones, s. a. Fig. 4.84.....	163
Fig. 4.81	Location of the measuring points and difference in m	163
Fig. 4.82	Simulated groundwater level and velocity field at 0 m a. s. l.	164
Fig. 4.83	Comparison of the calibrated groundwater heads, left: MODFLOW /PRO 20/, right: d ^{3f++} ; yellow: 438 m, blue: 674 m a. s. l. (colorbar not identic).....	164
Fig. 4.84	Flow field in the upper layer and catchment areas of the rivers,.....	165
Fig. 4.85	Refinement of the top surface to grid level 1, 2 and 3 using the raster layer projector method (blue: 420 m, red: 682 m a. s. l.	167

List of tables

Tab. 3.1	Diffusion from salt dome (2D):	36
Tab. 3.2	Modified Elder (3D):.....	38
Tab. 3.3	Saltpool problem (3D) with multigrid: Iteration counts (for time stepping and linear solver), and CPU time.....	43
Tab. 3.4	Gorleben problem (2D): Mesh statistics after uniform refinement.....	43
Tab. 3.5	Gorleben problem (2D) – initial phase:.....	46
Tab. 4.1	Thickness of slices according to slicing plan	74
Tab. 4.2	Timeline of the experiment, period lengths and resulting model times	74
Tab. 4.3	Fitting parameters for the model results depicted in Fig. 4.10 to Fig. 4.14	85
Tab. 4.4	Fitting parameters for the model results depicted in Fig. 4.15 to Fig. 4.18	87
Tab. 4.5	Relation of test-scales and the resulting hydraulic conductivity	102
Tab. 4.6	Parameters for the fitted functions for the three locations	104
Tab. 4.7	Depth dependence of fault zones according to /RHÉ 08/	112
Tab. 4.8	Summary of regional-scale model (RM) simulations including model settings and relevant hydrogeological settings.....	127
Tab. 4.9	WIPP-site model: permeabilities and porosities	152
Tab. 4.10	Comparison of recharge and river drainage	166

A Appendix: Data for modelling the LTDE

A.1 Tracer data

Tab. A.1 Grouping of tracer materials according to sorption mechanisms

Ion	appearance	an-/cationic	comments
<i>non-sorbing</i>			
³⁶ Cl ⁻	predominately as anionic Cl ⁻	✓	anion exclusion?
<i>ion exchange</i>			
²² Na ⁺	predominately as cationic Na ⁺	✓	
¹³³ Ba ²⁺	?		
¹³⁷ Cs ⁺	predominately in cationic form	✓	
²²⁶ Ra ²⁺	totally as cationic Ra ²⁺	✓	
<i>surface complexation</i>			
⁵⁷ Co ²⁺	both anionic and cationic	(✓)	
⁶³ Ni ²⁺	predominately as cationic Ni ²⁺	✓	
¹⁰⁹ Cd ²⁺	Only 3% as cationic Cd ²⁺	✓	Heavy metal
^{110m} Ag ⁺	Only 4% as non-charged AgCl		
¹⁵³ Gd ³⁺	complex speciation chemistry		
<i>electrochemical reduction dependent</i>			
²³⁷ Np ³⁺	sensitive to the redox potential		

Note the comment in /WID 10a/ with respect to elements sorbing by surface complexation: "These elements show a tendency not to reach sorption equilibrium after 186 days ...".

Tab. A.2 Tracer half-lives

Ion	Half-life
$^{36}\text{Cl}^-$	301 000 a
$^{22}\text{Na}^+$	2.602 a
$^{133}\text{Ba}^{2+}$	10.51 a
$^{137}\text{Cs}^+$	30.17 a
$^{226}\text{Ra}^{2+}$	1602 a
$^{57}\text{Co}^{2+}$	271.79 d
$^{63}\text{Ni}^{2+}$	100.1 a
$^{109}\text{Cd}^{2+}$	462.6 d
$^{110\text{m}}\text{Ag}^+$	249.79 d
$^{153}\text{Gd}^{3+}$	241.6 d
$^{237}\text{Np}^{3+}$	$2.144 \cdot 10^6$ a

Tab. A.3 K_d -values evaluated in batch experiments; from /WID 10a/

Sorted by sorption categories		Sorted by K_d -values	
Ion	K_d [m^3/kg]	Ion	K_d [m^3/kg]
$^{36}\text{Cl}^-$	~ 0	$^{36}\text{Cl}^-$	~ 0
$^{22}\text{Na}^+$	$2.90 \cdot 10^{-04}$	$^{22}\text{Na}^+$	$2.90 \cdot 10^{-04}$
$^{133}\text{Ba}^{2+}$	$2.10 \cdot 10^{-03}$	$^{237}\text{Np}^{3+}$	$8.20 \cdot 10^{-04}$
$^{137}\text{Cs}^+$	$2.20 \cdot 10^{-02}$	$^{133}\text{Ba}^{2+}$	$2.10 \cdot 10^{-03}$
$^{226}\text{Ra}^{2+}$	$7.50 \cdot 10^{-03}$	$^{109}\text{Cd}^{2+}$	$5.07 \cdot 10^{-03}$
$^{57}\text{Co}^{2+}$	$4.97 \cdot 10^{-02}$	$^{226}\text{Ra}^{2+}$	$7.50 \cdot 10^{-03}$
$^{63}\text{Ni}^{2+}$	$1.54 \cdot 10^{-02}$	$^{63}\text{Ni}^{2+}$	$1.54 \cdot 10^{-02}$
$^{109}\text{Cd}^{2+}$	$5.07 \cdot 10^{-03}$	$^{137}\text{Cs}^+$	$2.20 \cdot 10^{-02}$
$^{110\text{m}}\text{Ag}^+$		$^{57}\text{Co}^{2+}$	$4.97 \cdot 10^{-02}$
$^{153}\text{Gd}^{3+}$		$^{110\text{m}}\text{Ag}^+$	
$^{237}\text{Np}^{3+}$	$8.20 \cdot 10^{-04}$	$^{153}\text{Gd}^{3+}$	

Data for diffusion coefficients had to be compiled and processed. Details are given right after Tab. A.4.

Tab. A.4 Diffusion coefficients

Ion	appearance	an-/cationic	Self-diffusion coefficient at 15 °C [10 ⁻¹⁰ m ² /s]
³⁶ Cl ⁻	predominately as anionic Cl ⁻	✓	15,8
²² Na ⁺	predominately as cationic Na ⁺	✓	10,3
¹³³ Ba ²⁺	?		6,5
¹³⁷ Cs ⁺	predominately in cationic form	✓	16,4
²²⁶ Ra ²⁺	totally as cationic Ra ²⁺	✓	6,8
⁵⁷ Co ²⁺	both anionic and cationic	(✓)	5,2
⁶³ Ni ²⁺	predominately as cationic Ni ²⁺	✓	5,3
¹⁰⁹ Cd ²⁺	Only 3% as cationic Cd ²⁺	✓	5,5
^{110m} Ag ⁺	Only 4% as non-charged AgCl		13,0
¹⁵³ Gd ³⁺	complex speciation chemistry		
²³⁷ Np ³⁺	sensitive to the redox potential		

Starting point for deriving the diffusion coefficients is the Nernst expression /ROB 59/:

$$D_j^0 = \frac{RT \lambda_j}{|Z_j| F^2} \quad (\text{A.1})$$

D_j^0 - limiting tracer- or self-diffusion coefficient of ion j

λ_j^0 - limiting equivalent conductivity of ion j

Z_j - absolute value of charge of ion j

R - gas constant

T - absolute temperature

F - Faraday constant

An estimation of λ_j^0 at 25 °C can be given by an empirical formula after /NIG 70/ (for temperatures between 60° and 300 °C another formula is proposed by /NIG 70/.):

$$\lambda_j^0 = 10.56 + 90.72 \log Z_j + 42.95 \frac{\gamma_j}{Z_j} \quad (\text{A.2})$$

γ_j - crystal ionic radius of ion j

Stokes-Einstein relation for self-diffusion of water reads

$$\left(\frac{D^0 \eta^0}{T}\right)_{T_1} = \left(\frac{D^0 \eta^0}{T}\right)_{T_2} \quad (\text{A.3})$$

η^0 - viscosity of water

and has been shown to hold for a temperature range of 0-100 °C /SIM 58/. For ions „diffusing slower than the fluoride ion“, this equation holds also „fairly well in the temperature range relevant to the ocean“ /Li 74/. For faster diffusing ions another equation is proposed by /Li 74/:

$$(D^0 \eta^0)_{T_1} = (D^0 \eta^0)_{T_2} \quad (\text{A.4})$$

The diffusion coefficients as a function of ionic potential at 25 °C are depicted in Fig. A.1 and compiled in Tab. A.5. The higher the ionic potential, the larger is the hydration shell, and the lower is the diffusion coefficient. The data given in Tab. A.4 are linearly interpolated from the data in Tab. A.5 assuming an ambient temperature of 15 °C. Note that the diffusion coefficients differ by less than a factor of 4.

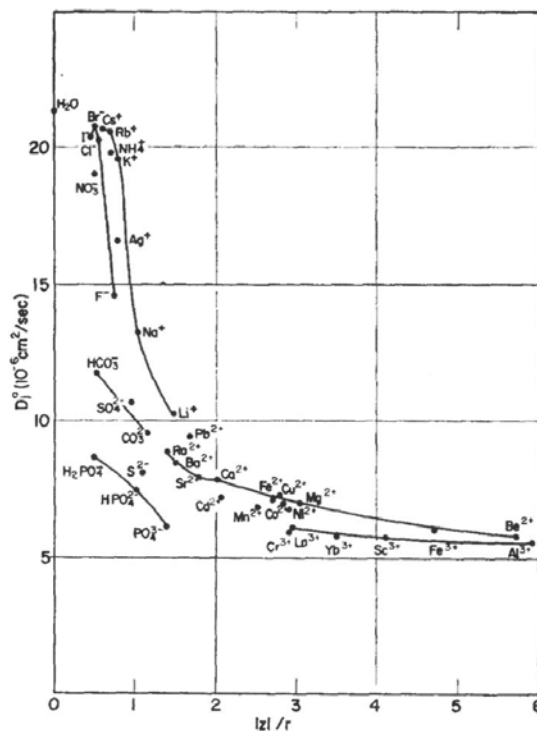


Fig. A.1 Tracer- or self-diffusion coefficient as a function of ionic potential at 25 °C; from /Li 74/

Tab. A.5 Diffusion coefficients after /Li 74/

Ion	Self-diffusion coefficient [10^{-10} m ² /s]		
	0 °C	18 °C	25 °C
³⁶ Cl ⁻	10,1	17,1	20,3
²² Na ⁺	6,27	11,3	13,3
¹³⁷ Cs ⁺	10,6	17,7	20,7
¹³³ Ba ²⁺	4,04	7,13	8,48
²²⁶ Ra ²⁺	4,02	7,45	9,89
¹⁰⁹ Cd ²⁺	3,41	6,03	7,17
²³⁷ Np ³⁺			
⁵⁷ Co ²⁺	3,41	5,72	6,99
⁶³ Ni ²⁺	3,11	5,81	6,79
¹¹⁰ Ag ⁺	8,5	14	16,6
¹⁵³ Gd ³⁺			
¹⁹ F		12,1	14,6

A.2 Experimental data during the tests

The tracer concentration in the injection volume for the solution containing the tracers was monitored over time. The data are visualized in Fig. A.2. Note that the units in which the concentrations for the tracers are given vary.

While some of the tracer concentrations are more or less constant over the whole active period of the experiment, some show a dramatic decrease. In Tab. A.6 the tracers together with minimum and maximum concentration value are listed. Looking at the ratio between maximum and minimum concentration, the tracers can be divided into 3 groups: ratio < 2 (³⁶Cl⁻, ²²Na⁺, ¹³³Ba²⁺, ²³⁷Np³⁺), ratio between 2 and 5 (²²⁶Ra²⁺, ¹³⁷Cs⁺, ⁶³Ni²⁺, ¹⁰⁹Cd²⁺), and ratio > 100 (^{110m}Ag⁺, ⁵⁷Co²⁺, ¹⁵³Gd³⁺). The temporal development of concentrations in the reservoir is depicted in Fig. A.3 where the activity is plotted over time in a logarithmic and a linear scale.

While the tracers from the first group qualify for approximating the initial value in the reservoir by a constant (with a view to boundary conditions of a numerical model) it appears to be less justifiable in case of the second and to be certainly not appropriate for the third group. However, a significant loss in concentration can be observed over the first ten days. Therefore also the concentration after this time and the related ratio are listed in Tab. A.6. These ratios are significantly smaller and should allow for using these

reduced values as a constant boundary condition in case of the second group of tracers. But a large error is possibly related to applying this procedure to the third group since a large amount of tracer would be lost in the numerical model.

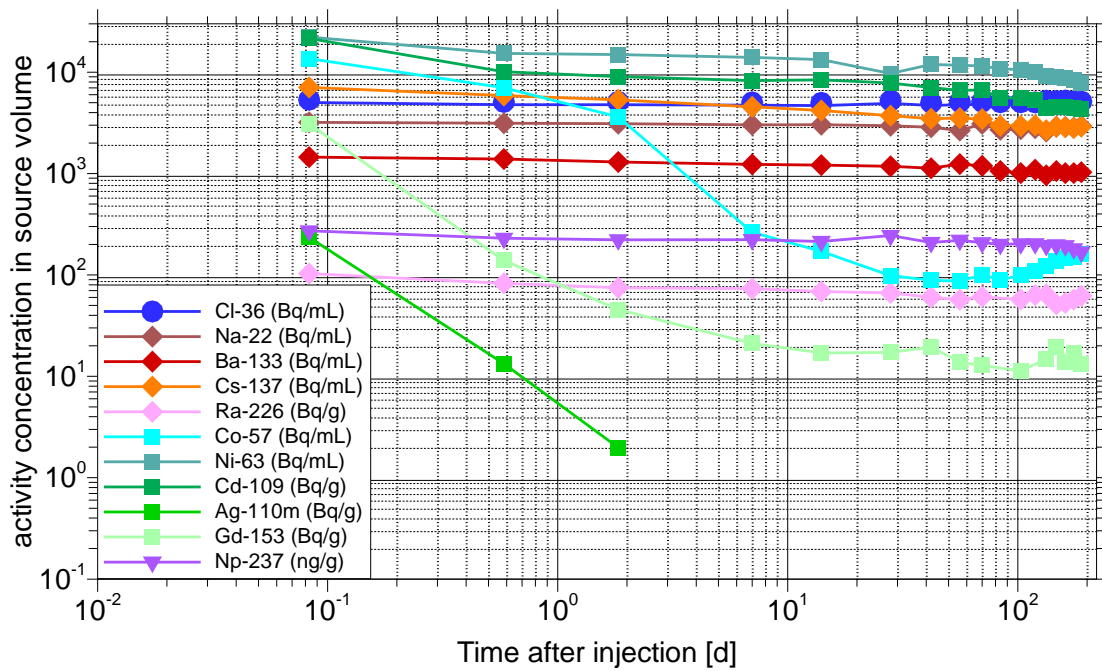


Fig. A.2 Tracer concentrations in the injection volume over time

Tab. A.6 Characteristic data on tracer concentrations in the injection volume

Ion	Maximum concentration	Minimum concentration	Ratio	Concentration after 10 days	Ratio	Unit
³⁶ Cl ⁻	5350	4980	1.1	5009	1.0	Bq/mL
²² Na ⁺	3200	2600	1.2	3025	1.2	Bq/mL
¹³³ Ba ²⁺	1450	960	1.5	1220	1.3	Bq/mL
¹³⁷ Cs ⁺	7070	2680	2.6	4360	1.7	Bq/mL
²²⁶ Ra ²⁺	103	51.3	2.0	70.85	1.4	Bq/g
⁵⁷ Co ²⁺	13600	87.0	156.3	210.7	2.4	Bq/mL
⁶³ Ni ²⁺	22200	7900	2.8	13635	1.7	Bq/mL
¹⁰⁹ Cd ²⁺	21524	4310	5.0	8312	1.9	Bq/g
^{110m} Ag ⁺	235	1.98	118.7	-	-	Bq/g
¹⁵³ Gd ³⁺	3084	11.3	272.0	18.88	1.7	Bq/g
²³⁷ Np ³⁺	272	168	1.6	218.3	1.3	ng/g

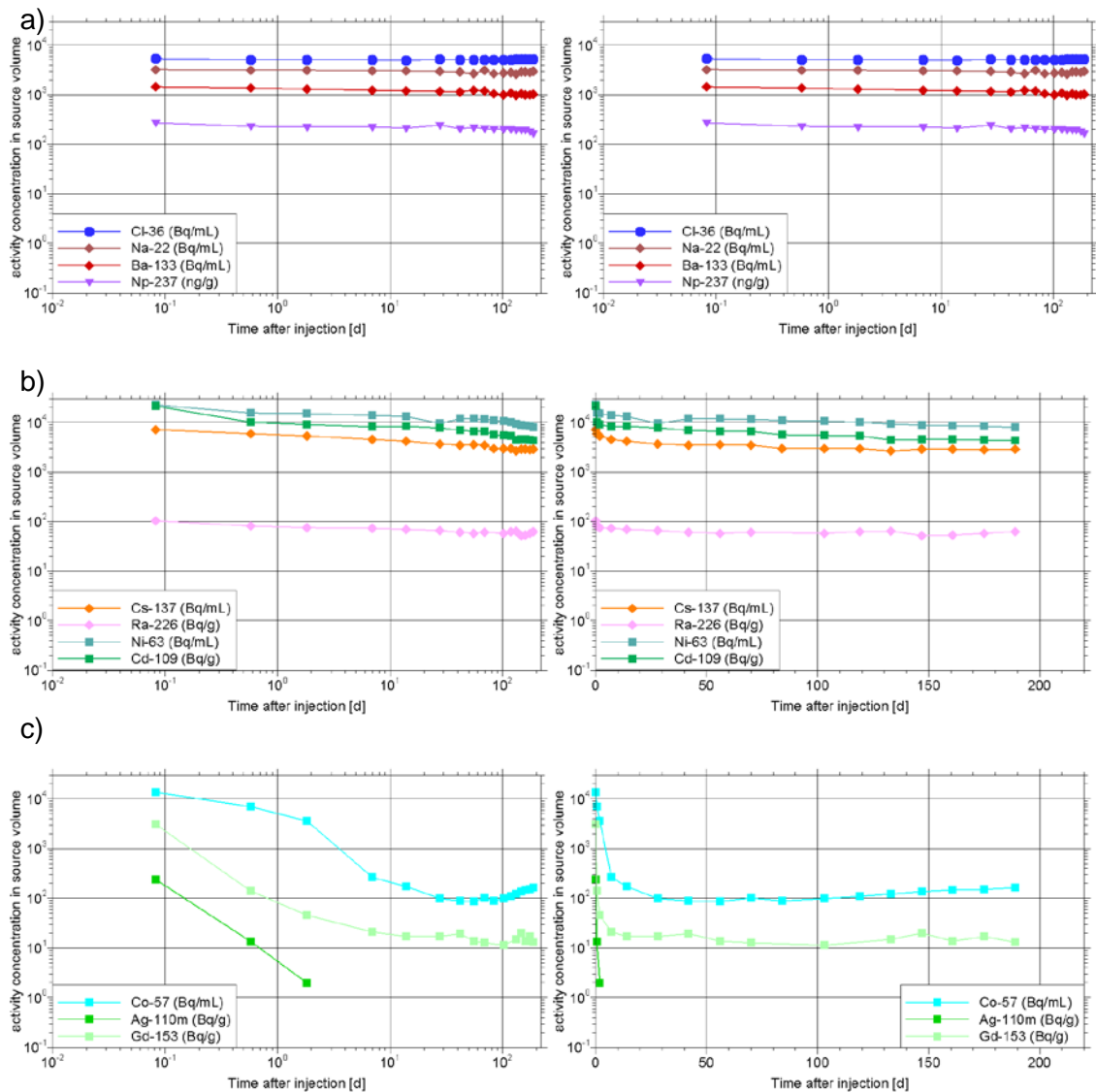
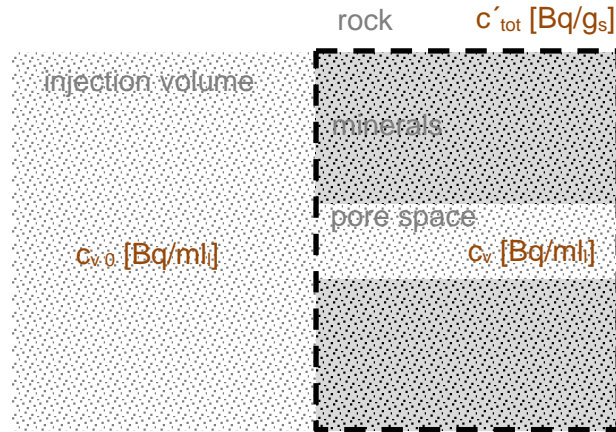


Fig. A.3 Tracer concentrations in the injection volume over time sorted after ratio; a) ratio < 2; b) ratio between 2 and 5; c) ratio > 100; time on the x-axis in a logarithmic scale on the left hand side, linear on the right hand side

A.3 Conversion of tracer concentration units

While the tracer concentration in the injection volume is measured in Becquerel per volume of solution or per mass of solution, the concentration profiles in the samples are given in Becquerel per mass of rock. This is a practical unit as determination of tracer mass is done on the rock sample. Input for the numerical transport model can only be the monitored solution based concentrations. As a result the model provides the tracer concentrations related to the groundwater in the pore space of the rock. In order to compare model results with the measurements, the groundwater related concentration must

be transformed into a rock related concentration. This situation is sketched in Fig. A.4 together with the symbols for the different concentrations. In terms of Fig. A.4 the task is to derive c'_{tot} from the numerically calculated concentration c_v in the rock.



- $c_{v,0}$ - tracer concentration of the solution in the injection volume [Bq / ml]
- c'_{tot} - activity measured in the rock after termination of the test [Bq / g_{rock}]
- c_v - tracer concentration of the solution in the rock [Bq / ml]

Fig. A.4 Relevant concentrations in the experiment

The basic relation between solute concentration and sorbed solute mass reads

$$c' = K_d \rho_l c \quad (\text{A.5})$$

c - Solute concentration related to mass of solution [g_c / g_l]

ρ_l - Solution density [g_l / ml_l]

K_d - Distribution coefficient [ml_l / g_{rock}]

c' - Solute concentration related to solid mass [g_c / g_{rock}]

The distribution coefficient in (A.5) is defined as

$$K_d = \frac{c'}{c_v} \quad (\text{A.6})$$

c_v - Solute concentration related to the volume of the solution [g_c / ml_l]

with

$$c_v = \rho_l c \quad (\text{A.7})$$

The total activity as measured in the laboratory is the sum of solute in the water and adsorbed solute mass. While the sorbed mass concentration c' is already given in [Bq / g_rock], the unit for the tracer concentration c_v still in the solution must be transformed to the same dimensions. For this purpose, c_v is multiplied by the porosity in order to relate the solute mass to the bulk volume of the rock and then divided by the bulk rock density to relate the resulting expression to the rock mass:

$$c'_v = c_v \frac{\Phi}{\rho_s} \quad (\text{A.8})$$

c'_v - Equivalent sorbed solute mass [g_c / g_s]

ρ_s - Rock bulk density [g_s / ml_s]

Φ - Porosity [ml_l / ml_s]

The total activity is then calculated as

$$c'_{tot} = c' + c'_v \quad (\text{A.9})$$

which can be expressed as a function of the solute concentration c_v with the help of eq. (A.6) and (A.8) as

$$c'_{tot} = c_v \left(K_d + \frac{\Phi}{\rho_s} \right) \quad (\text{A.10})$$

Explanation of indices:

c - solute

l - solution (liquid)

s - solid

A.4 Experimental data after the tests

The activity data of the determined profiles for the drill cores that were provided with the task description included many entries like “< x”. These entries were interpreted as a detection limit for a specific subsample. The detection limits thus formed a distribution by themselves. Evaluation of these distributions alone as well as investigating their relation to the activity distributions proved to be quite revealing.

A characteristic example is given by the data for $^{226}\text{Ra}^{2+}$. Fig. A.5 shows the detection limits for $^{226}\text{Ra}^{2+}$ which seem – on a closer look – to form sections at different levels. In Fig. A.6 a dashed line is added to visualise the levels. Only in the first 5 mm there might

be rather a gradient than a level. The subsample sizes are indicated as well by short vertical blue lines. The long vertical red lines, by contrast, separate sections of different subsample sizes showing clearly that the detection limits are correlated with the sample sizes. Similar observations even if not always as conclusive as in the case of $^{226}\text{Ra}^{2+}$ were made in case of the other tracers as well.

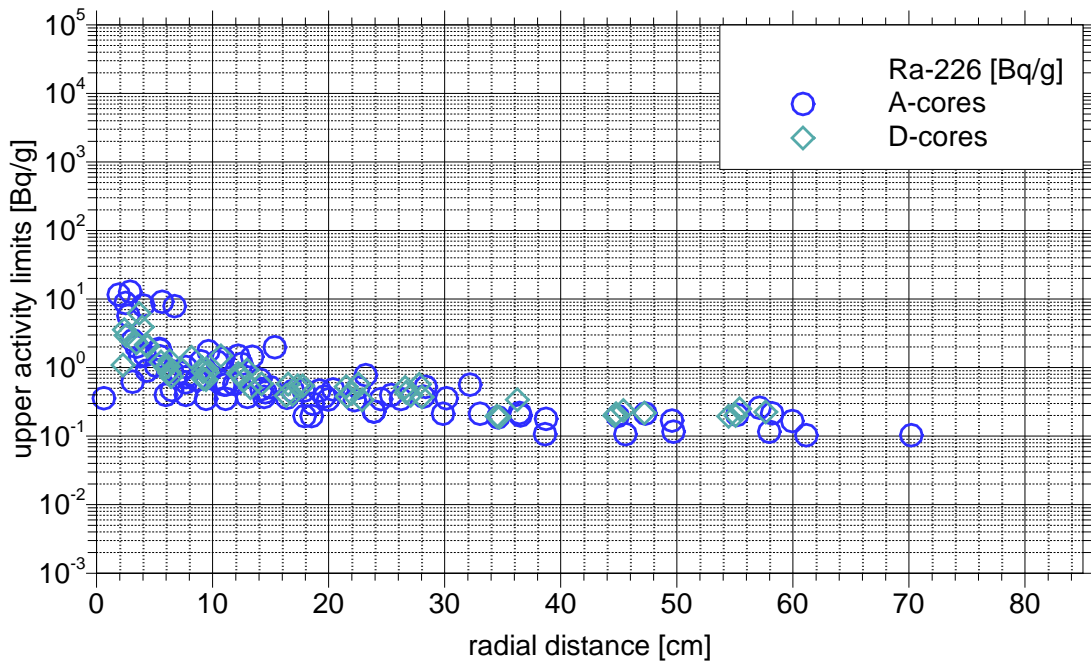


Fig. A.5 Detection limits for $^{226}\text{Ra}^{2+}$ from A- and D-cores

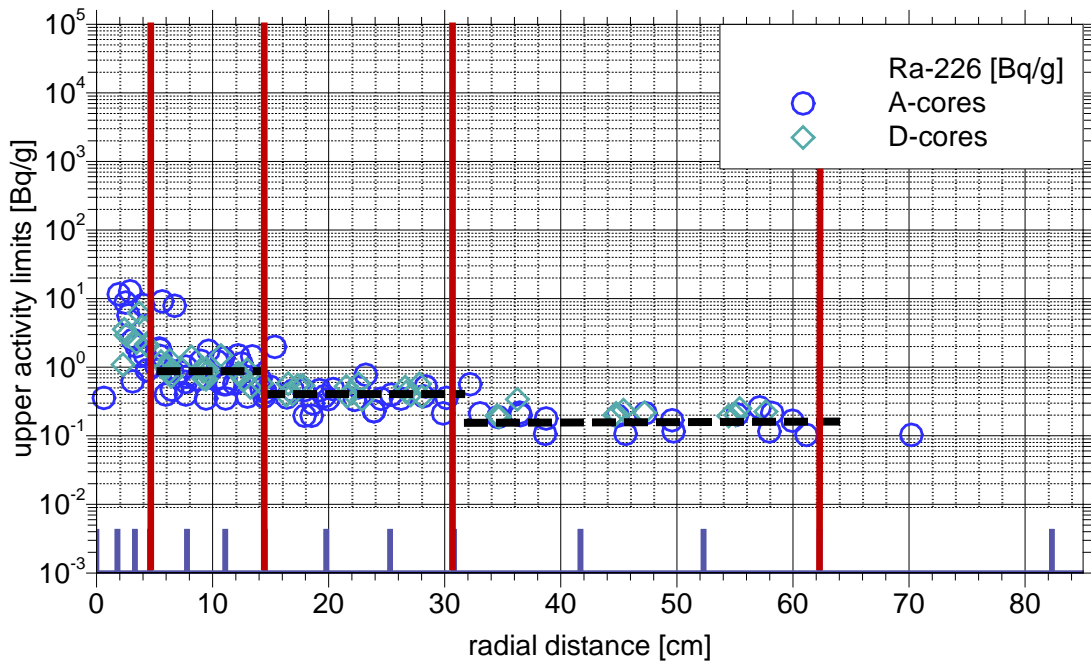


Fig. A.6 Detection limits for $^{226}\text{Ra}^{2+}$ from A- and D-cores and subsample sizes

The relation of detection limits and sample sizes cannot come as a total surprise. It proves to become important, though, in the comparison of activity data and detection limits. Exemplarily, the activity data for $^{226}\text{Ra}^{2+}$ together with the related detection limits are shown in Fig. A.7. In this case there is no difference between data and detection limits beyond a depth of 2.5 mm into the drill core. Consequently, the activity data shows a certain drop in level at about 30 mm which coincides with the drop in detection limits and the increase in sample size. Interpretation of activity data thus requires in general close inspection of the relation to the detection limits.

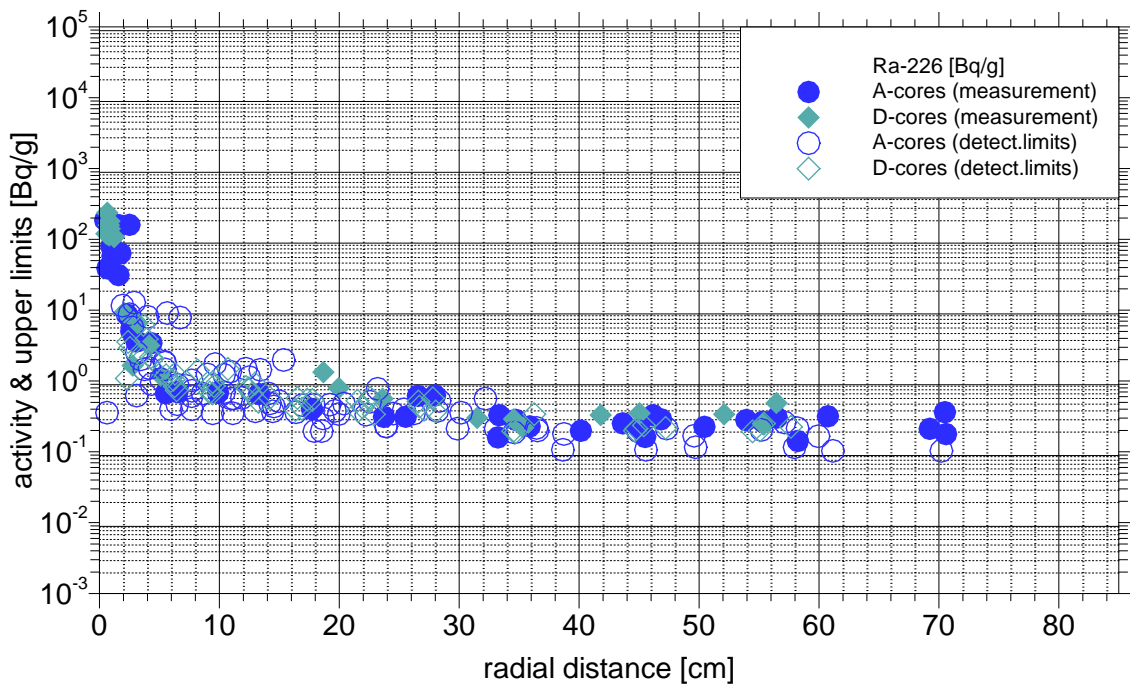


Fig. A.7 Activity data and detection limits for $^{226}\text{Ra}^{2+}$ from A- and D-cores

Activity data and detection limits were thus compared for all tracers that are relevant for Task 9b. In general, all tracer data are clearly above the detection limits within the first few millimeters into the drill core. However, only few tracer data proved to be significant beyond this margin. The comparison allowed for discriminating four groups of tracers (examples for each group are given in Fig. A.8):

- (1) Data points clearly above the cloud of detection limits ($^{22}\text{Na}^+$, $^{36}\text{Cl}^-$, $^{137}\text{Cs}^+$)
- (2) Data points “swimming” on top of the cloud of detection limits ($^{57}\text{Co}^{2+}$, $^{133}\text{Ba}^{2+}$)
- (3) Data points inside the cloud of detection limits ($^{109}\text{Cd}^{2+}$, $^{110\text{m}}\text{Ag}^+$, $^{153}\text{Gd}^{3+}$, $^{226}\text{Ra}^{2+}$)
- (4) Data points just for the first few millimeters ($^{63}\text{Ni}^{2+}$, $^{237}\text{Np}^{3+}$)

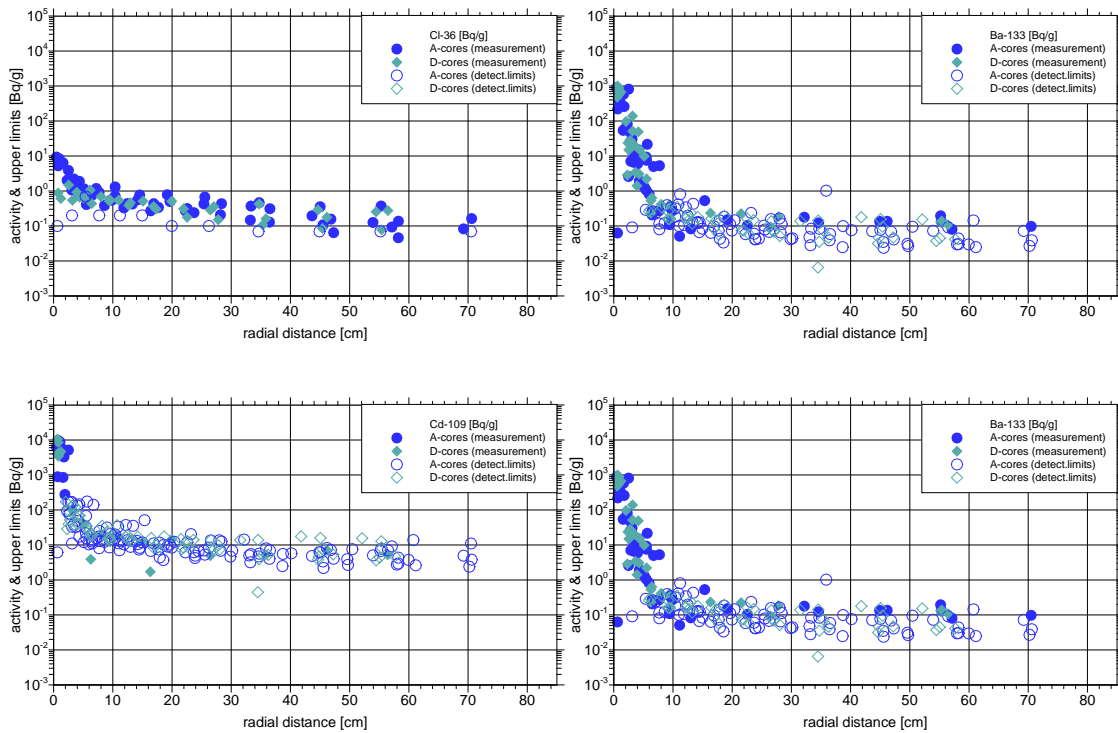


Fig. A.8 Activity and detection limits; groups (1) to (4) from top left to bottom right

It appears that only data from group (1) is entirely and only data from group (2) at least partly reliable and useful. Therefore only the tracers $^{22}\text{Na}^+$, $^{36}\text{Cl}^-$, $^{137}\text{Cs}^+$, and $^{133}\text{Ba}^{2+}$ will be addressed further on. Work on $^{57}\text{Co}^{2+}$ was dropped due to time limitations.

Separating the data for the A-cores from the data for the D-cores reveals a striking difference in the concentration distributions for $^{36}\text{Cl}^-$ and $^{22}\text{Na}^+$ as illustrated in Fig. A.9 to Fig. A.12. While most concentration distributions show a knee at about 5 mm this is not the case for $^{36}\text{Cl}^-$ and $^{22}\text{Na}^+$ -data from the D-cores. There is no curious change in the profiles and the boundary concentration is considerably lower in case of $^{36}\text{Cl}^-$ and noticeably lower in case of $^{22}\text{Na}^+$. This observation alone seems to call for different models for A- and D-cores. Additionally, it should be kept in mind that the surfaces of the A-cores are in principle different from those of the D-cores as they show a fracture coating while the surface of the D-cores may have been influenced by a borehole disturbed zone (BDZ). Be that as it may, the matrix parameters for A- and D-cores should nevertheless be the same and relate basically to undisturbed conditions.

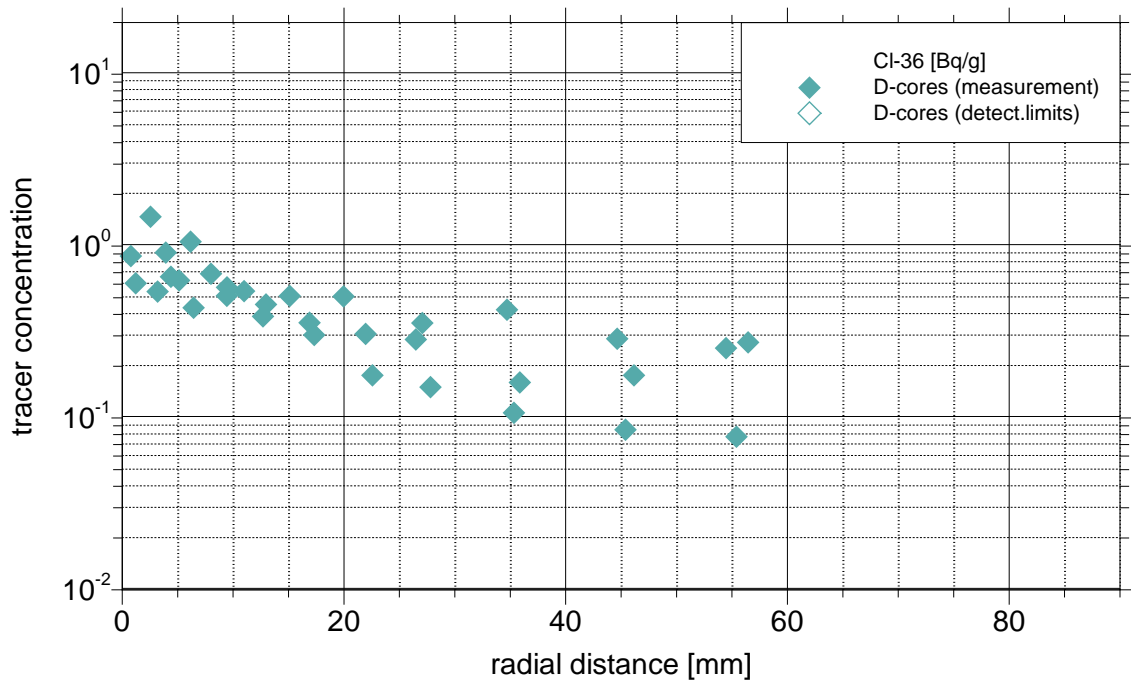
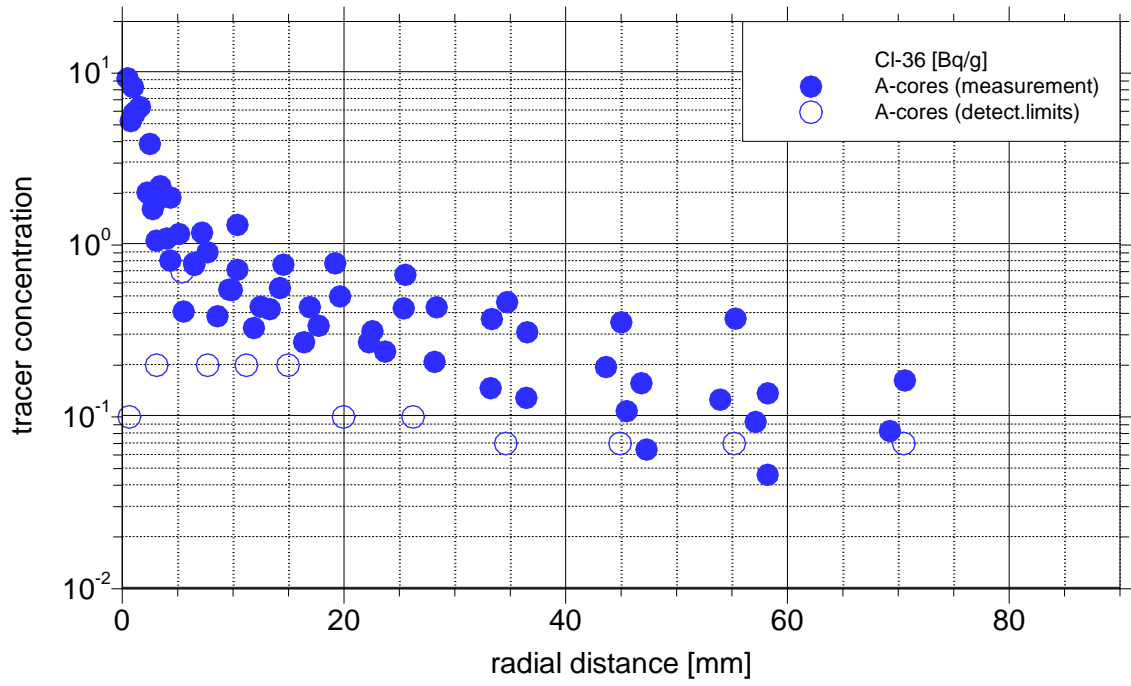


Fig. A.9 Activity and detection limits for ^{36}Cl ; A-cores (top) and D-cores (bottom)

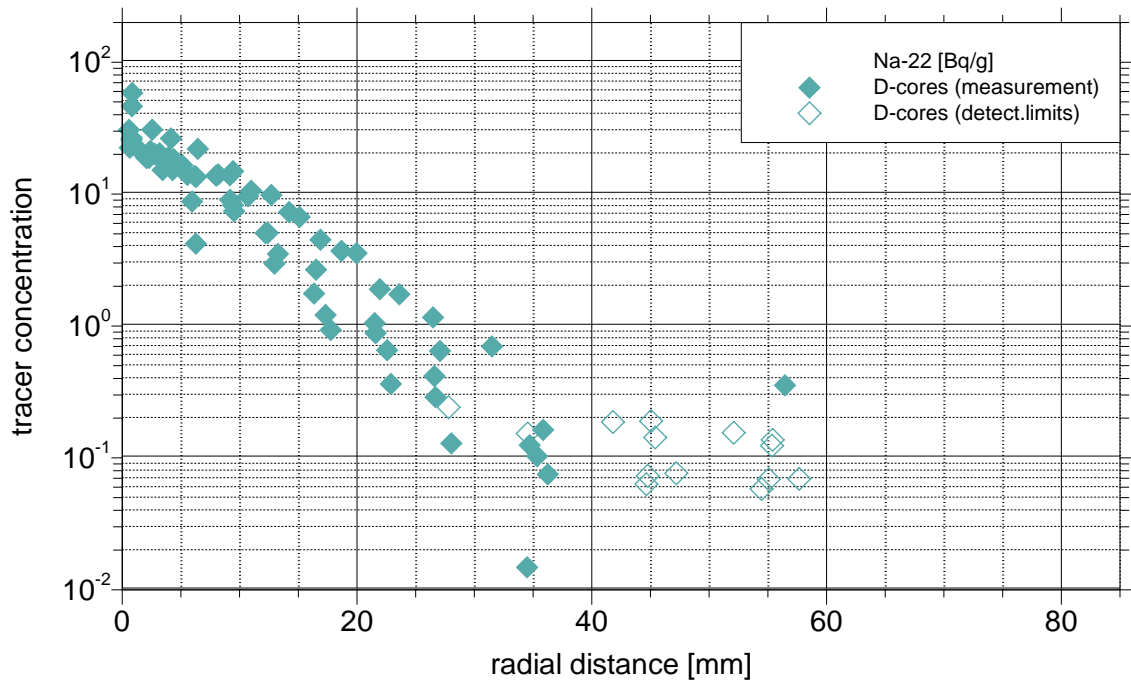
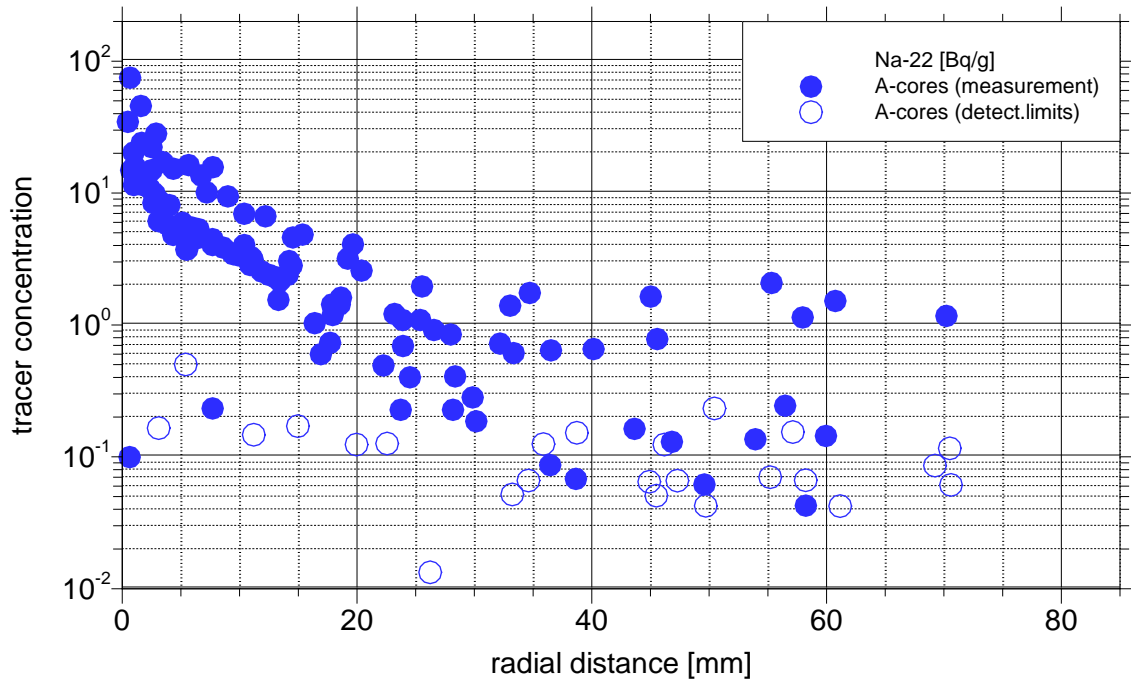


Fig. A.10 Activity and detection limits for $^{22}\text{Na}^+$; A-cores (top) and D-cores (bottom)

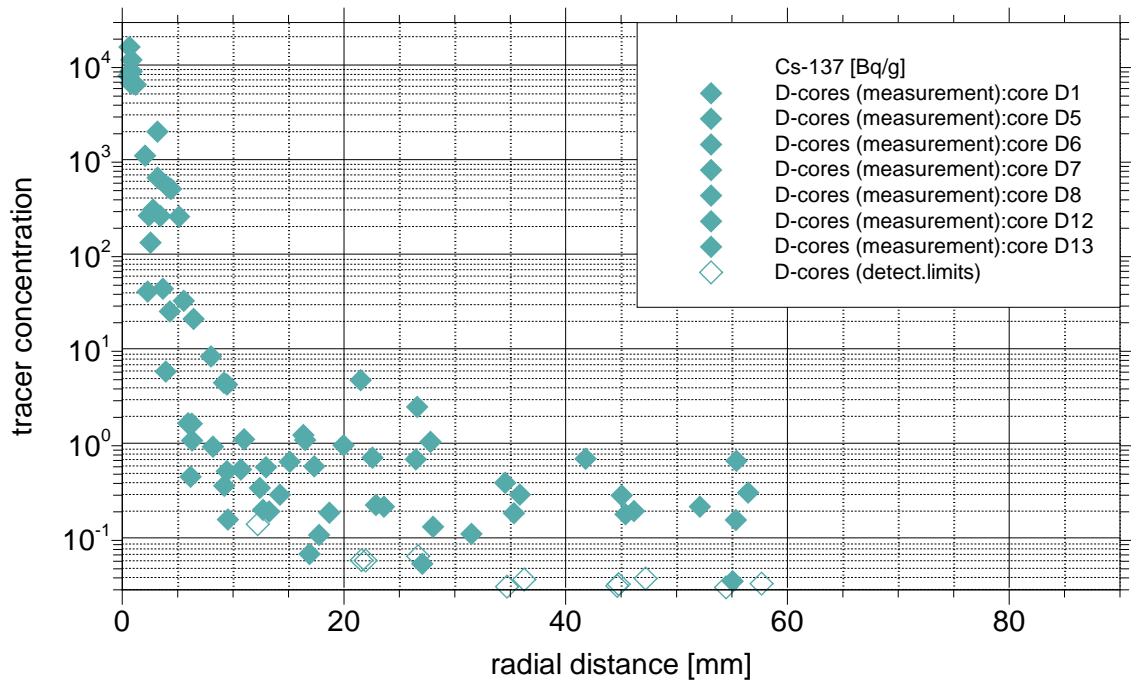
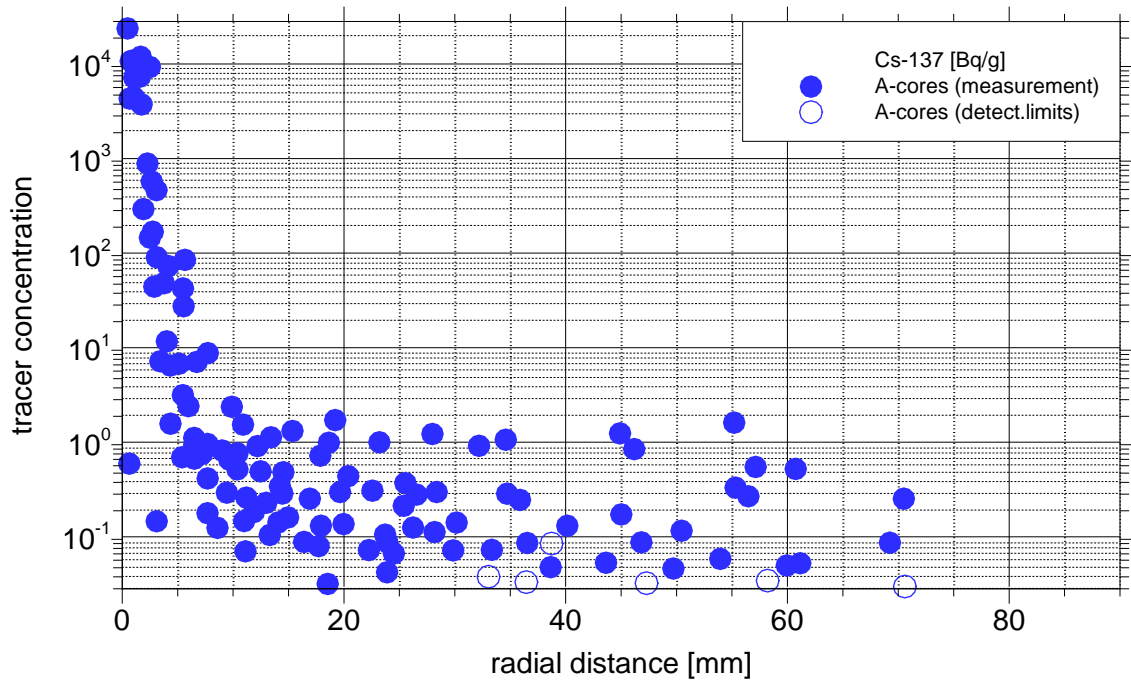


Fig. A.11 Activity and detection limits for $^{137}\text{Cs}^+$; A-cores (top) and D-cores (bottom)

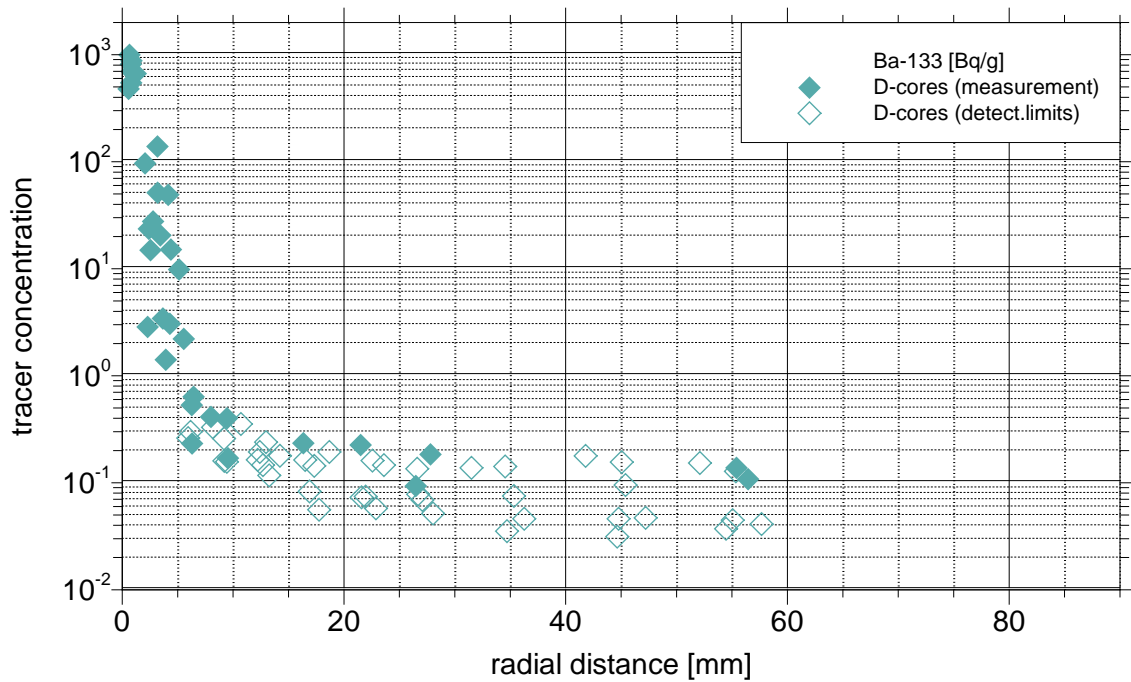
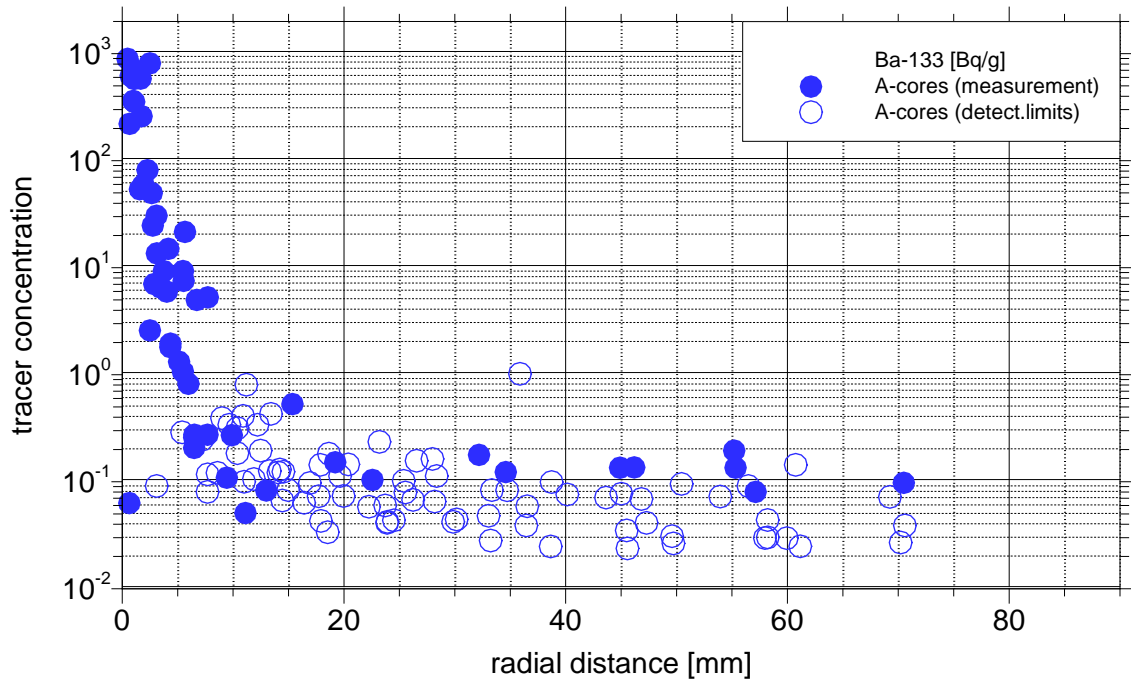
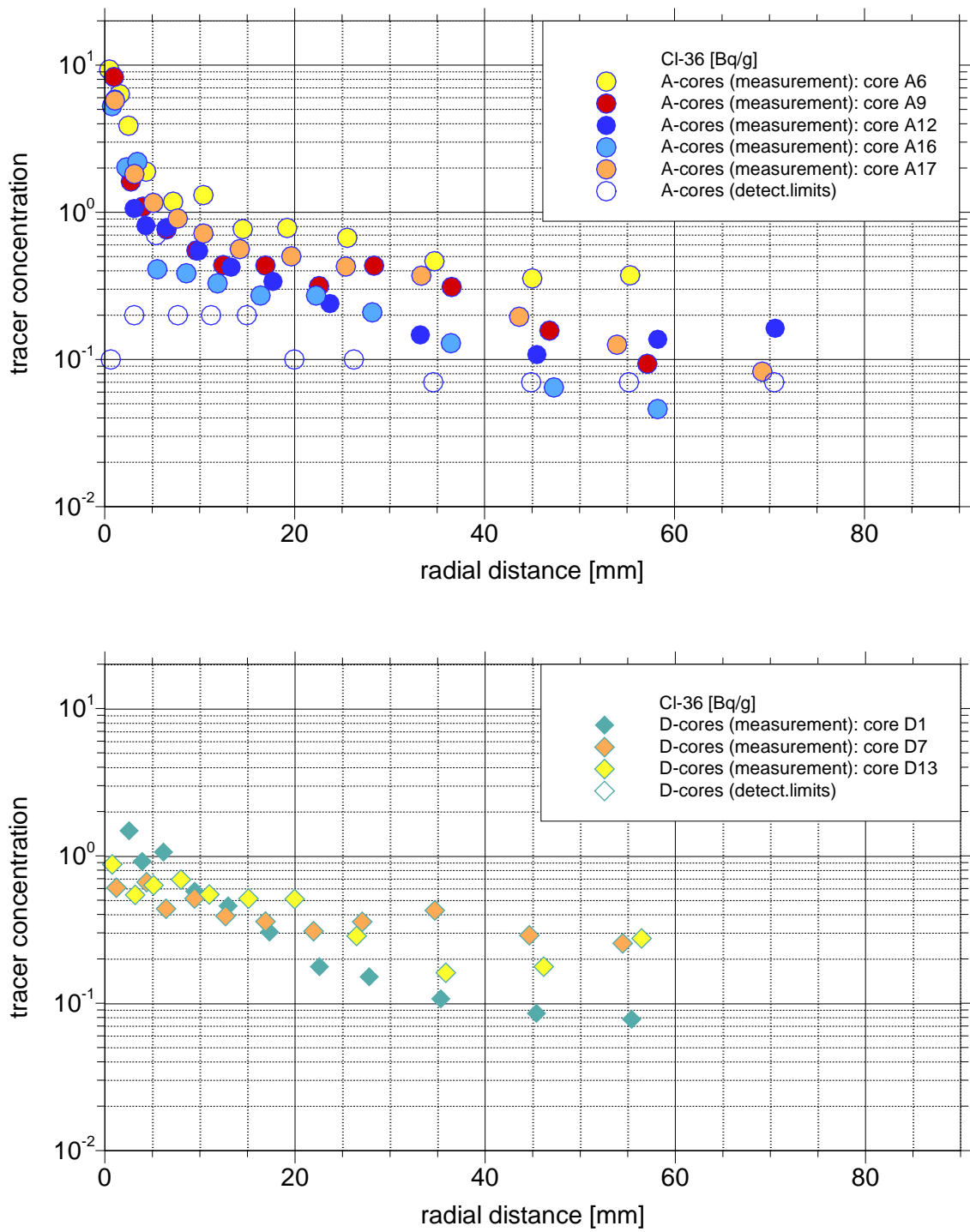


Fig. A.12 Activity and detection limits for $^{133}\text{Ba}^{2+}$; A-cores (top) and D-cores (bottom)

Examining Fig. A.9 to Fig. A.12 more closely, an interesting visualisation artefact has been discovered. Looking for instance at the ^{36}Cl -data in Fig. A.9, the data for both core types (A and D) have a comparatively broad bandwidth thereby provoking the impression of a large uncertainty in the individual data points. However, Fig. A.13 shows the same

data as Fig. A.9 but the data from the different drill cores are marked with different colours. This results in the quite different impression that the curves from specific drill cores show quite clear trends but the trends differ from each other, in other words, there is much less data scatter within a drill core than between the cores. This is illustrated by Fig. A.14 where the coloured symbols are connected with thick lines of the same colour. Apparently, there is already considerable local variation of material properties in the matrix on the scale of the LTDE.



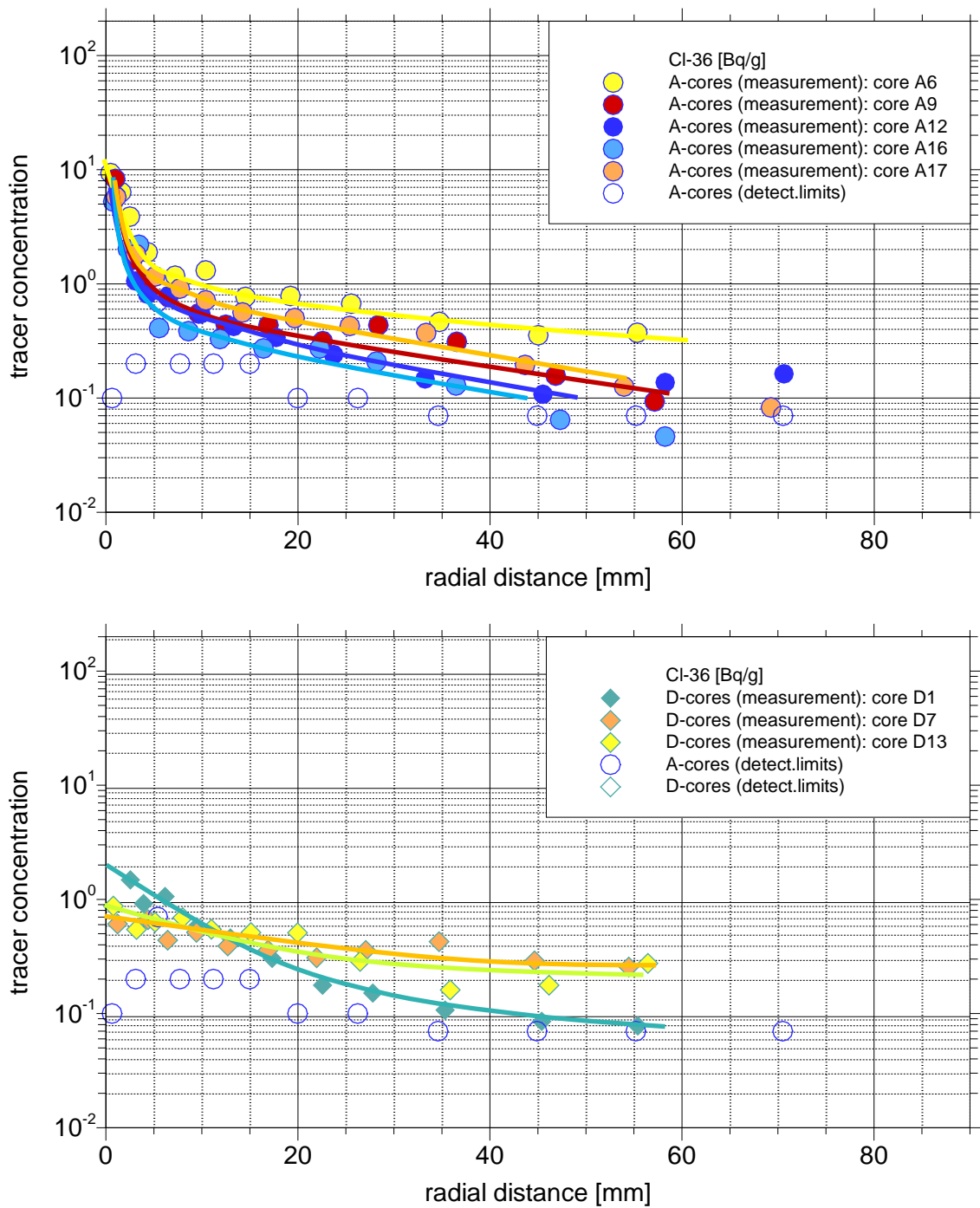


Fig. A.14 Activity distributions and trends in individual drill cores for ^{36}Cl ; A-cores (top) and D-cores (bottom)

**Gesellschaft für Anlagen-
und Reaktorsicherheit
(GRS) gGmbH**

Schwertnergasse 1
50667 Köln
Telefon +49 221 2068-0
Telefax +49 221 2068-888

Boltzmannstraße 14
85748 Garching b. München
Telefon +49 89 32004-0
Telefax +49 89 32004-300

Kurfürstendamm 200
10719 Berlin
Telefon +49 30 88589-0
Telefax +49 30 88589-111

Theodor-Heuss-Straße 4
38122 Braunschweig
Telefon +49 531 8012-0
Telefax +49 531 8012-200

www.grs.de

**Goethe Zentrum für
wissenschaftliches Rechnen
Goethe-Universität Frankfurt**
Kettenhofweg 139
60325 Frankfurt am Main

www.g-csc.de